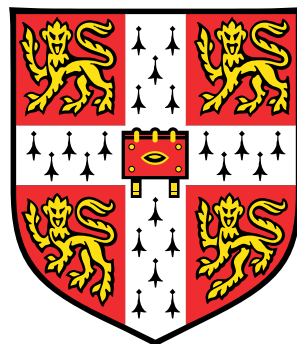


Multi-scale multiphase modelling of granular flows



Krishna Kumar Soundararajan

Department of Engineering
University of Cambridge

This dissertation is submitted for the degree of

Doctor of Philosophy

Draft - v1.0

Wednesday 17th September, 2014 – 02:00

Abstract

Geophysical hazards usually involve flow of dense granular solids and water as a single-phase system. Understanding the mechanics of granular flow is of particular importance in predicting the run-out behaviour of debris flows. The dynamics of a homogeneous granular flow involve three distinct scales: the microscopic scale, the meso-scale, and the macroscopic scale. Conventionally, granular flows are modelled as a continuum because they exhibit many collective phenomena. Recent studies, however, suggest that a continuum law may be unable to capture the effect of inhomogeneities at the grain scale level, such as orientation of force chains, which are micro-structural effects. Discrete element methods (DEM) are capable of simulating these micro-structural effects, however they are computationally expensive. In the present study, a multi-scale approach is adopted, using both DEM and continuum techniques, to better understand the rheology of granular flows and the limitations of continuum models.

The collapse of a granular column on a horizontal surface is a simple case of granular flow, however a proper model that describes the flow dynamics is still lacking. In the present study, the generalised interpolation material point method (GIMPM), a hybrid Eulerian – Lagrangian approach, is implemented with Mohr-Coloumb failure criterion to describe the continuum behaviour of granular flows. The granular column collapse is also simulated using DEM to understand the micro-mechanics of the flow. The limitations of MPM in modelling the flow dynamics are studied by inspecting the energy dissipation mechanisms. The lack of collisional dissipation in the Mohr-Coloumb model results in longer run-out distances for granular flows in dilute regimes (where the mean pressure is low). However, the model is able to capture the rheology of dense granular flows, such as run-out evolution of slopes subjected to impact loading, where the inertial number $I < 0.1$.

The initiation and propagation of submarine flows depend mainly on the slope, density, and quantity of the material destabilised. Certain macroscopic models are able to capture simple mechanical behaviours, however the complex physical mechanisms that occur at the grain scale, such as hydrodynamic instabilities and formation of clusters, have largely been ignored. In order to describe the mechanism of submarine granular flows, it is important to consider both the dynamics of the solid phase and the role of the ambient fluid. In the present study, a two-dimensional coupled Lattice Boltzmann LBM – DEM technique is developed

to understand the micro-scale rheology of granular flows in fluid. Parametric analyses are performed to assess the influence of initial configuration, permeability, and slope of the inclined plane on the flow. The effect of hydrodynamic forces on the run-out evolution is analysed by comparing the energy dissipation and flow evolution between dry and immersed conditions.

Table of contents

Table of contents	5
List of figures	9
List of tables	13
Nomenclature	13
1 Granular flows	15
1.1 Introduction	15
1.2 Modelling the granular flows	17
1.2.1 Kinetic theory	18
1.2.2 Shallow-water approximation	19
1.2.3 Rheology	21
1.3 Studies on granular flows	26
1.3.1 Granular column collapse	27
1.3.2 Flow on inclined plane	32
1.3.3 Saturated and submerged granular flows	34
1.4 Summary	35
2 Numerical modelling of granular flows	37
2.1 Introduction	37
2.2 Continuum modelling of granular flows	37
2.3 Material Point Method (MPM)	40
2.3.1 Discrete formulation of the governing equations	42
2.3.2 Boundary conditions	44
2.3.3 Solution scheme	46

3 Particulate modelling of granular flows	51
3.1 Introduction	51
3.2 Discrete Element Method	52
3.2.1 The Forces	54
3.2.2 Numerical algorithm and integration scheme	58
3.2.3 Boundary conditions	65
3.2.4 Particle Assembling Methods	67
3.2.5 Voronoi Tesselation	70
4 Multi-scale modelling of dry granular flows	71
4.1 Introduction	71
4.2 Granular column collapse	72
4.2.1 Numerical set-up	73
4.2.2 Deposit morphology	78
4.2.3 Flow evolution and internal flow structure	79
4.2.4 Energy dissipation mechanism	88
4.2.5 Role of initial grain properties	90
4.3 Slopes subjected to impact loading	94
4.3.1 Numerical procedures	102
4.3.2 Evolution of pile geometry and run-out	103
4.3.3 Decay of kinetic energy	105
4.3.4 Effect of friction	113
4.3.5 Effect of material points	116
4.3.6 Comparison with granular column collapse	116
4.4 Summary	116
5 Numerical modelling of fluid–grain interactions	125
5.1 Fluid simulation using lattice Boltzmann method	125
5.1.1 Formulation	127
5.1.2 Lattice Boltzmann - Multi-Relaxation Time (LBM-MRT)	131
5.1.3 Boundary conditions	134
5.2 Validation of the lattice Boltzmann method	137
5.3 Turbulence in lattice Boltzmann method	141
5.4 Coupled LBM and DEM for fluid-grain interactions	144
5.4.1 Draft, kiss and tumbling: Sedimentation of two grains	151
5.5 GP-GPU Implementation	154

Table of contents	7
6 Underwater granular flows	161
6.1 Submarine granular flows down incline plane	161
6.1.1 Effect of initial density	162
6.1.2 Effect of permeability	170
6.1.3 Summary	175
7 Conclusions and future work	177
7.1 Introduction	177
7.2 Outline of future research	177
7.2.1 Multi-scale simulations of granular flows	178
7.2.2 Developments in Material Point Method	179
7.2.3 The I rheology	180
7.2.4 Homogenization of granular flows	181
References	183

Draft - v1.0

Wednesday 17th September, 2014 – 02:00

List of figures

1.1	Particle size range and their predominant characteristics	16
1.2	Illustration of the Savage-Hutter model	20
1.3	Plane stress at a constant pressure	22
1.4	Dependence of frictional coefficient μ with dimensionless shear rate I	23
1.5	Variation of dimensionless parameters for various flow regimes	24
2.1	Multi-scale modelling of granular materials	38
2.2	Typical discretization of a domain in MPM	41
2.3	Cell crossing noise	45
2.4	Illustration of the MPM algorithm for particles occupying a single cell in the background grid	48
3.1	Calculation of normal force	55
3.2	Verlet list	60
3.3	Checking the validity of Verlet list	62
3.4	Verlet integration scheme	64
3.5	A 2D simulation cell ω with its basis vectors in an absolute frame	66
3.6	(a)Ballistic deposition: first contact followed by steepest descent; (b) small-scale periodic sample (Radjai and Dubois, 2011)	69
3.7	Voronoi tessellation to average bulk properties	70
4.1	Schematic of experimental configuration for 2-D collapse in a rectangular channel, (Lajeunesse et al., 2004)	73
4.2	DEM sample characteristics	75
4.3	Periodic shear test	77
4.4	Normalised final run-out distance for columns with different initial aspect ratio	80
4.5	Normalised final collapse height for columns with different initial aspect ratio	81
4.6	Velocity profile of a granular column collapse (' $a' = 0.4 \& t = \tau_c$)	83
4.7	Velocity profile of a granular column collapse (' $a' = 0.4 \& t = 3 \times \tau_c$)	84

4.8	Velocity profile of a granular column collapse (' $a' = 6$ & $t = \tau_c$)	86
4.9	Velocity profile of a granular column collapse (' $a' = 6$ & $t = 3 \times \tau_c$)	87
4.10	Flow evolution of granular column collapse	89
4.11	Energy evolution of granular column collapse	91
4.12	Flow evolution of granular column collapse using $\mu(I)$ rheology	92
4.13	Evolution of inertial number with time for columns with ' $a' = 0.4$ and ' $a' = 6$ '	93
4.14	Effect of density on run-out evolution ' $a' = 0.8$	95
4.15	Effect of density on energy evolution $a = 0.8$	96
4.16	Evolution of local packing density ' $a' = 0.8$	97
4.17	Effect of density on run-out evolution ' $a' = 0.8$ (poly-dispersity 'r' = 6)	98
4.18	Snapshots of granular column collapse $t = 6\tau_c$	99
4.19	Effect of density on energy and packing fraction evolution ' $a' = 0.8$ (poly-dispersity 'r' = 6)	100
4.20	Effect of density on run-out behaviour and energy evolution ' $a' = 0.6$	101
4.21	Periodic shear test using CD (?).	104
4.22	Snapshots of MPM simulations of the evolution of granular pile subjected to a gradient impact energy.	106
4.23	Snapshots of CD simulations of the evolution of granular pile subjected to a gradient impact energy (?).	107
4.24	Run-out behaviour of a pile subjected a gradient impact energy	108
4.25	Evolution of kinetic energy with time	110
4.26	Evolution of vertical and horizontal kinetic energy with time	111
4.27	Evolution of kinetic energy in the x component of the velocity field normalized by the available kinetic energy at the end of the transient as a function of normalized time.	112
4.28	Decay time and run-out time as a function of the normalised kinetic energy E_{kx0}	114
4.29	Effect of friction on the run-out behaviour	115
4.30	Effect of input velocity distribution on the run-out behaviour	117
4.31	Snapshots of MPM simulations of the evolution of granular pile subjected to a gradient impact energy $E_0 = 61\ mgd$	118
4.32	Snapshots of DEM simulations of the evolution of granular pile subjected to a gradient impact energy $E_0 = 61\ mgd$	119
4.33	Evolution of run-out with time for varying material points per cell.	120
4.34	Evolution of kinetic with time for varying material points per cell	121
4.35	Evolution of run-out and duration of flow for varying material points per cell.	122
4.36	Comparison of column collapse with slope subjected to impact loading.	123

5.1	The lattice Boltzmann discretisation and D2Q9 scheme	127
5.2	Illustration of the streaming process on a <i>D2Q9</i> lattice	129
5.3	Illustration of the collision process on a <i>D2Q9</i> lattice	130
5.4	Half-way bounce back algorithm for the <i>D2Q9</i> model	135
5.5	Velocity profile: LBM Simulation of a laminar flow through a channel.	138
5.6	Finite Volume mesh used in the CFD analysis of laminar flow through a channel.	139
5.7	Velocity profile: CFD analysis of laminar flow through a channel.	139
5.8	Development of the Poiseuille velocity profile in time: comparison between LBM simulation, CFD simulation and the analytical solution. Time is made dimensionless by H/U_0	140
5.9	LBM simulation of velocity profile for a laminar flow through a pipe with an obstacle at $L/4$	141
5.10	CFD simulation of velocity contour for a laminar flow through a pipe with an obstacle at $L/4$	141
5.11	LBM and CFD simulation of a flow around an obstacle.	142
5.12	Kármán vortex street	145
5.13	Bounce back boundaries for different values of δ	149
5.14	Time series of draft, kiss and tumble of two grains during sedimentation in a viscous fluid.	152
5.15	Time history of two circular grains during sedimentation.	153
5.16	Schematics of a heterogeneous CPU/GPU system.	155
5.17	GPU scalability with increase in LBM nodes	159
6.1	Underwater granular collapse set-up	162
6.2	Evolution of run-out with time (dense)	163
6.3	Evolution of Kinetic Energy with time (dense case)	164
6.4	Flow morphology at critical time for different slope angles (dense)	165
6.5	Evolution of run-out with time (loose)	166
6.6	Flow morphology at critical time for different slope angles (loose)	167
6.7	Evolution of Kinetic Energy with time (loose)	168
6.8	Evolution of packing density with time	169
6.9	Evolution of run-out with time for different permeability (loose slope 5°)	171
6.10	Evolution of height with time for different permeability (loose slope 5°)	172
6.11	Evolution of Kinetic Energy with time for different permeability (loose slope 5°)	173
6.12	Evolution of packing density with time for different permeability (loose slope 5°)	174
7.1	Identification of dynamic solid-fluid boundary	180

Draft - v1.0

Wednesday 17th September, 2014 – 02:00

List of tables

4.1	Material properties of glass ballotini (Lajeunesse et al., 2004)	73
4.2	Micro-mechanical parameters used in DEM simulations	76
4.3	Parameters used in continuum simulations	78
4.4	DEM simulation of simple shear test (?)	102
5.1	LBM parameters used in simulating laminar flow through a circular pipe. . .	137
5.2	Computed Strouhal number for fluid flows with different Reynolds number .	146
5.3	GPU vs CPU parallelisation	158

Draft - v1.0

Wednesday 17th September, 2014 – 02:00

Chapter 1

Granular flows

1.1 Introduction

A granular material is a conglomeration of large number of discrete solid particles of sizes greater than $1\mu m$ whose behaviour is governed by frictional contact and inelastic collisions. A schematic representation of the size range of the granular materials is presented in figure 1.1. Granular materials, characterized by interaction between individual particles, lie between two extremes scales: the molecular-scale range predominated by electrostatic force, i.e. Van der Waals forces, and the continuum scale which is described by the bulk property of the material. In various soil classification systems adopted in soil mechanics, sand is classified as a granular material having particle sizes greater than $75\mu m$. Particle size of $75\mu m$ is an important transition point, where the frictional effect starts to dominate the material behaviour and the effect of the electrostatic Van der Waals forces diminishes. The extent of the particle size range of the granular materials from the molecular size to a continuum scale indicates that they have a complex behaviour, demonstrating a mix of particle-like and continuum-like behaviour. The physics of non-cohesive granular assemblies is intriguing. Despite being ubiquitous in nature, granular materials are the most poorly understood materials from a theoretical standpoint. For such a poorly understood area, the flow of granular materials has a surprising range of geo-hazard predictions and industrial applications. For years, granular materials have resisted theoretical development, demonstrating non-trivial behaviour that resembles solid and/or fluid-like behaviour under different circumstances. Even in the simplest of situations, granular materials can exhibit surprisingly complex behaviour. Macroscopically, the complex mix of solid and fluid-like behaviour can be illustrated by a simple example; while one walks on the beach, the solid-like behaviour of soil becomes evident as it supports one's weight, but if we scoop a handful of soil and allow it to run through the fingers, the fluid-like nature becomes obvious. Microscopically this complex behaviour has various reasons. The range of

the particle size gives rise to complex interactions between grains constituting the granular media. Unlike other micro-scale particles, granular particles are insensitive to thermal energy dissipation (Mehta, 2011), because the thermal energy dissipation in a granular material is several orders of magnitude smaller in comparison with the energy dissipation due to interaction between the grains. The thermal energy scales are small when compared to the energy required to move grains. The granular material reaches the static equilibrium quickly due to its dissipative nature, unless an external source of energy is constantly applied (Choi, 2005). Our knowledge of the behaviour of granular assemblies is restricted to two extremes: the solid-like behaviour of dense granular assemblies that resist the shearing force by undergoing plastic deformations, and the fluid-like flow behaviour characterized by high shear rates. Granular media are *a priori* simple systems made of solid particles interacting through their contacts. However, they still resist our understanding and no theoretical framework is available to describe their behaviour (Pouliquen et al., 2006). The strong dependency of the behaviour of granular material on its surrounding environment makes it difficult to have a unified theoretical framework. When strongly agitated, the granular material behaves like a dissipative gas, and kinetic theories have been developed to describe this regime (Popken and Cleary, 1999; Xu et al., 2003). On the other hand, during slow deformations, the quasi-static regime is dominated by steric hindrance and friction forces are often described using plasticity theories. In between the two regimes, the material flows like a fluid, and the particles experience enduring contacts, which is incompatible with the assumptions of the kinetic theory (Pouliquen et al., 2006) that describes the dilute regime of a granular flow. Typical granular flows are dense and hence a fundamental statistical theory is not appropriate to describe their properties. Moreover, during the process of granular flow, the material can exist in all the above-mentioned states, which further complicates our understanding of granular flows.

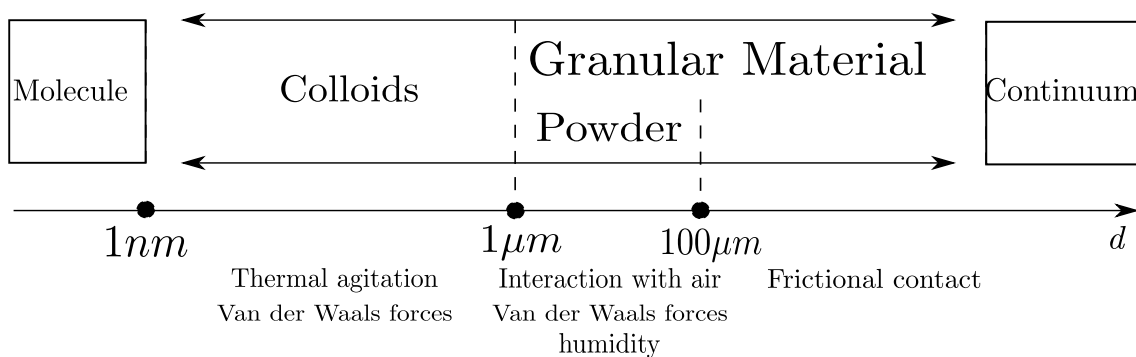


Figure 1.1 Particle size range and their predominant characteristics

1.2 Modelling the granular flows

Granular flows can be classified into three different regimes (Jaeger et al., 1996): the dense slow quasi-static regime characterized by long duration between contacts and particle interaction via frictional contact (Roux and Combe, 2002); the rapid and dilute flow regime characterized by particles moving freely between successive collisions (Goldhirsch, 2003); and an intermediate fluid-like regime in which the material is dense but still flows like a fluid and the particles interact both by collision and through friction (Midi, 2004; Pouliquen and Forterre, 2002). Transfer of particle kinetic energy and momentum within a rapidly flowing granular medium occurs during these collisions (Popken and Cleary, 1999). Different approaches have been used to model granular flows at different scales of description. The dynamics of a homogeneous granular flow involve at least three distinct scales: (1) the *Microscopic scale* characterized by small time and length scales representing contact/particle interactions, (2) the *Mesoscopic scale*, where particle rearrangements, development of micro-structures and shear rates have a dominant influence on the granular flow behaviour, and (3) the *Macroscopic scale* which involves large length scales that are related to geometric correlations at even larger scales. The interesting issue is whether one should consider or neglect a particular scale while modelling the granular dynamics (Radjai and Richefeu, 2009). However, the difficulty in modelling the granular flows originates from the fundamental characteristics of the granular matter such as negligible thermal fluctuations, highly-dissipative interactions, and a lack of separation between the microscopic grain scale and the macroscopic scale of the flow (Goldhirsch, 2003).

Granular flow modelling began as early as 1776 with Coulomb's paper describing the yielding of granular material as a frictional process (Coulomb, 1776). Although it was not about granular flows, *per se*, the prediction of soil failure for Civil engineering applications describes the onset of structural collapse leading to catastrophe (Campbell, 2006). Mohr-Coulomb's yield criterion along with a flow rule from metal plasticity is sufficient to describe the behaviour of granular flow as a continuum process, without considering the interaction of individual particles. Advanced models based on the critical state concept (Schofield and Wroth, 1968) provides further insight into continuum description of granular flows. According to the critical state theory, the 'under consolidated' or loose soil tends to increase in density upon shearing, while the dense 'over consolidated' soil dilates when sheared, until it reaches the critical state. As dense granular flow involves large shear stresses, it is reasonable to assume that the shearing occurs at the critical state. Large applied stress can cause the granular particles to deform at the grain scale and squeeze them into the inter-particle pores. However, the critical state is independent of the applied stress. In granular flows, the applied stress during the actual flow is less in comparison with the stress on the soil underneath a structure, where the soil is subjected to large shear strains. It is therefore reasonable to assume that the flow

is incompressible and takes place at the critical state (Campbell, 2006). The main limitation of the continuum approach is the assumption that the friction angle, ϕ is a constant material parameter, which is found to vary by a factor of 3, violating the fundamental assumption of quasi-static flow theories (Potapov and Campbell, 1996). Although the mechanism of dense granular flow is attributed to the bulk friction, it is the formation of force chains and the rearrangement of internal structure of the granular assembly that causes friction-like behaviour. Experiments (Savage and Sayed, 1984; Savage, 1984) and computer simulations (Campbell and Brennan, 1985) indicate a weak relation between the bulk friction and the packing density, due to the micro-structural rearrangement of particles (Campbell, 1986). As the packing density increases, the particles tend to arrange themselves in a regular order when sheared. In order to understand the development of micro-structure, it is important to look at the particle-level interactions. Bagnold (1954) was the first to try and model granular materials as individual particles. Bagnold's theory of motion of individual particles in a shear flow and inter-particle friction inducing random velocities is reminiscent of the thermal motion of molecules in the kinetic theory of gases. The two common approaches in modelling the granular flow: the kinetic theory and the shallow water theory, are discussed below.

1.2.1 Kinetic theory

The gas kinetic theory assumes that the particles interact by instantaneous collisions, which implies only binary (two-particle) collisions. The particles are modelled using a single coefficient of restitution, to represent the energy dissipated by the impact normal to the point of contact between the particles, and for the most part, the surface friction or any other particle interactions tangential to the point of contact are ignored (Campbell, 1990). Jenkins and Savage (1983) extended the kinetic theory for thermal fluids to idealized granular mixtures to predict the rapid deformation of granular material by including energy dissipation during collision for nearly inelastic particles. Savage and Jeffrey (1981) extended the kinetic theory to predict simple shear flow behaviour for a wide range of coefficients of restitution. The kinetic theory is capable of predicting the shear flow behaviour only for mixtures composed of particles with identical density and size (Iddir and Arastoopour, 2005), however real systems are composed of particles that vary in size, and segregation of particles can occur.

The kinetic theory is valid for dispersed granular flows (Ng et al., 2008), however ? observed that the numerical simulations of dense granular flow based on kinetic theory were poor in comparison with the experimental data on fluidized bed expansion. Confined granular flows are usually dense, because of their mechanism of energy dissipation and their tendency to form clusters. The dense granular flows lie in an intermediate regime, where both the grain inertia and the contact network has significant influence on the flow behaviour (Pouliquen and Forterre,

2002). Thus, a part of the force is transmitted through the force network, which contradicts
the two basic assumptions in the kinetic theory, i.e. binary collision and molecular chaos. For
dense granular flow conditions, the total stress transmission in the flow regime is the sum of the
rate-dependent (collision-transition) and the rate-independent (friction) components (Ng et al.,
2008). Addition of frictional stress component (?) to the kinetic theory improves the ability of
the model to predict the dense granular flows. The main advantage of kinetic theories is that
they can be used to derive deterministic constitutive laws to describe the behaviour of granular
flows in a theoretical framework (Jenkins and Savage, 1983). Kinetic theories formulated on
the assumption of solid phase stress as a viscous response have limitations when applied to
granular flows. A viscous material produces no force unless it is in motion, hence the kinetic
theory based on viscous solid phase cannot explain the static force exerted by the granular
materials on the walls, as observed in experiments. The addition of a frictional component to
the kinetic theory improves its prediction of granular flows. However, the frictional component
that is based on long-duration contact is added to the instantaneous collision contact term. Also,
the rapid-flow models based on gas kinetic theory assume that the molecular collisions are
elastic, which means that they do not dissipate energy (Campbell, 2006), which is in contrast to
the reality. Finally, the important assumption of gas kinetic theory is molecular chaos, which
assumes no correlation between the velocities or positions of the colliding particles, which is
not true especially in a dense granular flow where the particles interact many times with their
neighbours and a strong correlation between their velocities is inevitable.

1.2.2 Shallow-water approximation

The Navier-Stokes equation in fluid mechanics is capable of describing the dynamics of fluid
flow under different conditions. However, the proposed models for granular flows tend to be
specialized for a particular situation. By drawing a simple analogy from fluid dynamics one can
model granular flows as non-Newtonian fluids using a variant of the Navier-Stokes equation;
one such approach is the depth-averaged shallow-water equation, which has been applied
to solve granular flow dynamics with a reasonable amount of success. The Savage-Hutter
model (Savage and Hutter, 1991), is a depth-average continuum-mechanics based approach
which consists of hyperbolic partial differential equations to describe the distribution of the
depth and the topography of an avalanching mass of cohesion-less granular media (Hutter et al.,
2005). This approach is based on the assumption that the horizontal length scale is very large
in comparison with the vertical length scale, which allows us to neglect the horizontal partial
derivatives relative to the vertical partial derivatives. Field observations indicate an aspect
ratio of 10^{-3} to 10^{-4} for natural avalanches (?). By neglecting the vertical length scale, the

² continuum equation for conservation of mass and momentum can be written as:

³ $\partial_x u + \partial_y v = 0$ (1.1)

⁴ $\partial_t u + u \partial_x u + v \partial_y u = (\nabla \cdot \sigma)_x + F_x$ (1.2)

⁶ The continuum equation requires determining the components of the stress tensor and a suitable
⁷ constitutive law. *Savage-Hutter (SH) model* uses the Mohr-Coulomb law to describe the
⁸ constitutive relation. The conservation of mass and momentum in the SH model is based on
⁹ the assumption of granular flow as an incompressible fluid flow, which means that throughout
¹⁰ the avalanche, the density of the avalanching material remains constant. Although [Hutter et al.](#)
¹¹ ([1995](#)) observed the density of the granular flow to remain almost constant in a flow down a
¹² curved chute, the destructive nature of landslides and avalanches restricts us from inferring a
¹³ conclusive result. The SH model involves the following assumptions: (1) Coulomb-type sliding
¹⁴ takes place with a bed friction angle δ , (2) Mohr-Coulomb frictional behaviour occurs inside
¹⁵ the material with internal angle of friction, $\phi \geq \delta$, and (3) the velocity profile is assumed to be
¹⁶ uniform throughout the avalanche depth. The granular flow over a rigid plane inclined at an
¹⁷ angle, θ is shown in figure 1.2. The mass and momentum balance in the SH model is written
as:

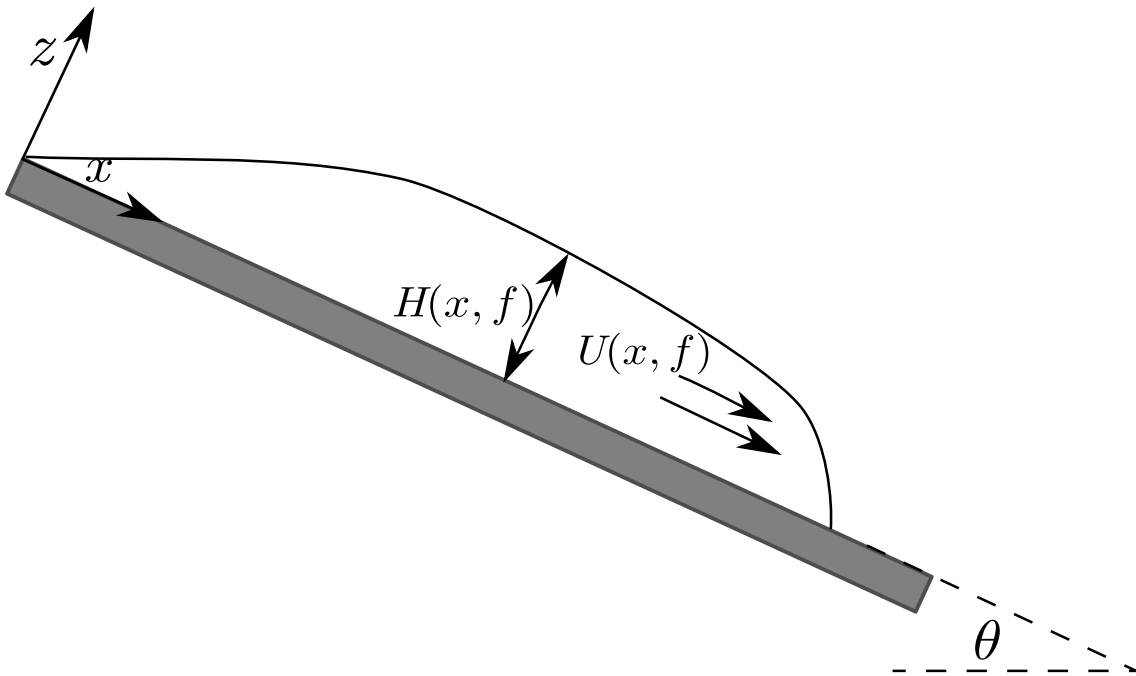


Figure 1.2 Illustration of the Savage-Hutter model

18

$$\frac{\partial H}{\partial T} + \frac{\partial}{\partial X}(HU) = 0 \quad (1.3) \quad 1$$

$$\frac{\partial U}{\partial T} + U \frac{\partial U}{\partial X} = (\sin \theta - \tan \delta sgn(U) \cos \theta) - \beta \frac{\partial H}{\partial X} \quad (1.4) \quad 2 \\ 3$$

where capital letters denote non-dimensional quantities with respect to the typical horizontal and vertical length scales (L^*, H^*) and the time scale $\sqrt{L^*/g}$. The key feature in the shallow water approximation is the Mohr-Coulomb constitutive law, which is applied at the free surface and at the base, to describe the granular flow. Comparison of the model with the post-calculation of Madlein avalanche in Austria indicates that the Coulomb basal friction is insufficient and requires an additional viscous component. The SH model's predictions were not satisfactory for granular flows down gentle slopes of inclination angle $\leq 30^\circ$, where granular materials exhibit a different behaviour (Hutter et al., 2005). 4
5
6
7
8
9
10
11

1.2.3 Rheology

12

Rheology is the science of flow of materials with solid and fluid characteristics. In practice, rheology is principally concerned with describing the mechanical behaviour of those materials that cannot be described by the classical theories, by establishing an empirical relation between deformation and stresses. Consider a granular assembly of particles having diameter d and density ρ_d under a confining pressure P (see figure 1.3). If the material is sheared at a constant shear rate, $\dot{\gamma} = V_w/L$ is imposed by the relative movement of the top plate with a velocity V_w . In the absence of gravity, the force balance implies that the shear stress, $\tau = \sigma_{xy}$, and normal stress, $P = \sigma_{xx}$, are homogeneous across the cell. This configuration is the simplest configuration to study the rheology of granular flow, i.e. to study the effect of the strain rate, $\dot{\gamma}$, and pressure, P on the volume and shear stress, τ . Even though the granular materials have been extensively researched at microscopic level, the continuum representation of granular materials in terms of conservation of mass and momentum is still an area of concern (Daniel et al., 2007; Midi, 2004). The prediction of rheology of granular materials even in the simplest case is complicated as they exhibit rate-dependent behaviour and no single constitutive equation is able to describe the behaviour over a range of shear stress rates. Da Cruz et al. (2005) developed a very famous rheology for granular flows, that is based on the simple two-dimensional shear in the absence of gravity and establishes that the flow regime and rheological parameters scale with a dimensionless number that represents the relative strength of inertia forces with respect to the confining pressure (Daniel et al., 2007), along the lines of Savage and Hutter (1991). The 13
14
15
16
17
18
19
20
21
22
23
24
25
26
27
28
29
30
31

shear stress, τ , is proportional to the confining pressure, P , and is written as:

$$\tau = P\mu(I) \quad (1.5) \quad 33$$

1

2 The friction coefficient μ depends on the single non-dimensional parameter I , expressed as:

$$I = \frac{\dot{\gamma}d}{\sqrt{P\rho_p}} \quad (1.6) \quad 34$$

3 The parameter I can be interpreted in terms of different time scales controlling the grain flow.
4 If the particles are rigid, i.e. neglecting the elastic properties of the particles, then I is the only
5 non-dimensional parameter in the problem. Hence, the shear stress, τ , has to be proportional
6 to the pressure, P , times a function of I . Comparing the shape of the function $\mu(I)$ with the
7 experimental results of flow down an inclined plane, Jop et al. (2006) observed that the frictional
8 coefficient increases from a minimal value of μ_s to an asymptotic value of μ_2 , when the value
9 of I increases. The variation of friction coefficient with I is shown in figure 1.4. To formulate
10 a complete constitutive model, it is essential to describe the volumetric behaviour. Based
11 on the dimensional analysis, it can be argued that the volume change is also a function of
12 dimensionless parameter I and that it also depends on the maximum and the minimum possible
13 void ratios and the time for microscopic rearrangement of particles.

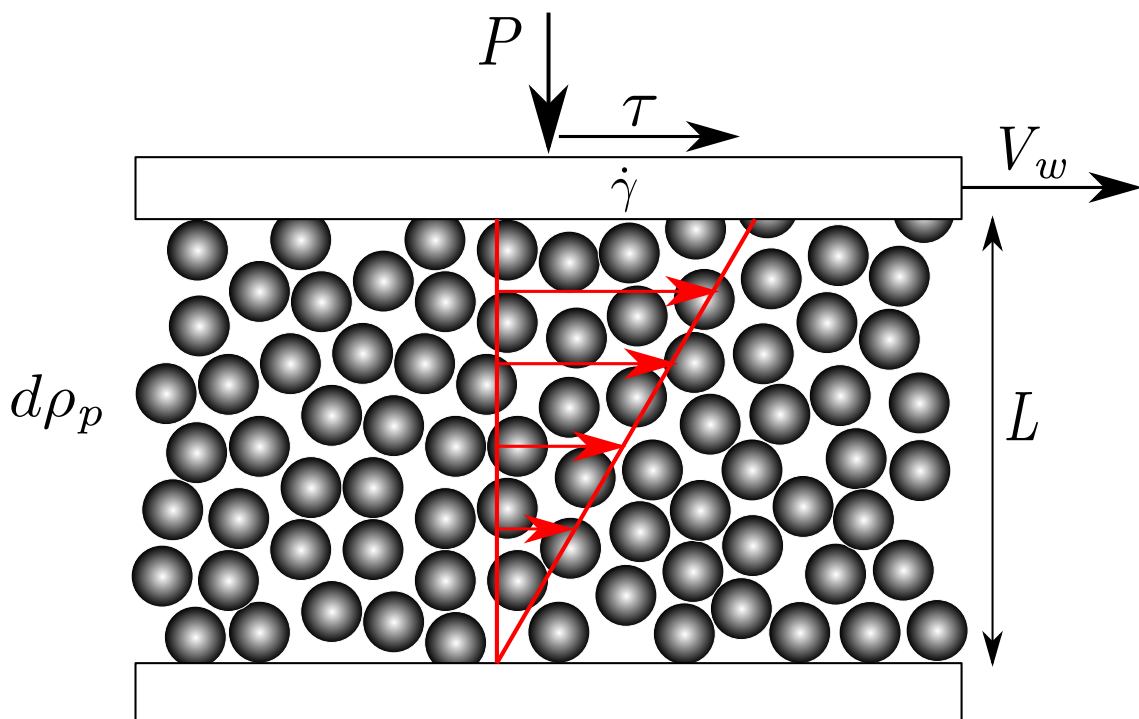


Figure 1.3 Plane stress at a constant pressure

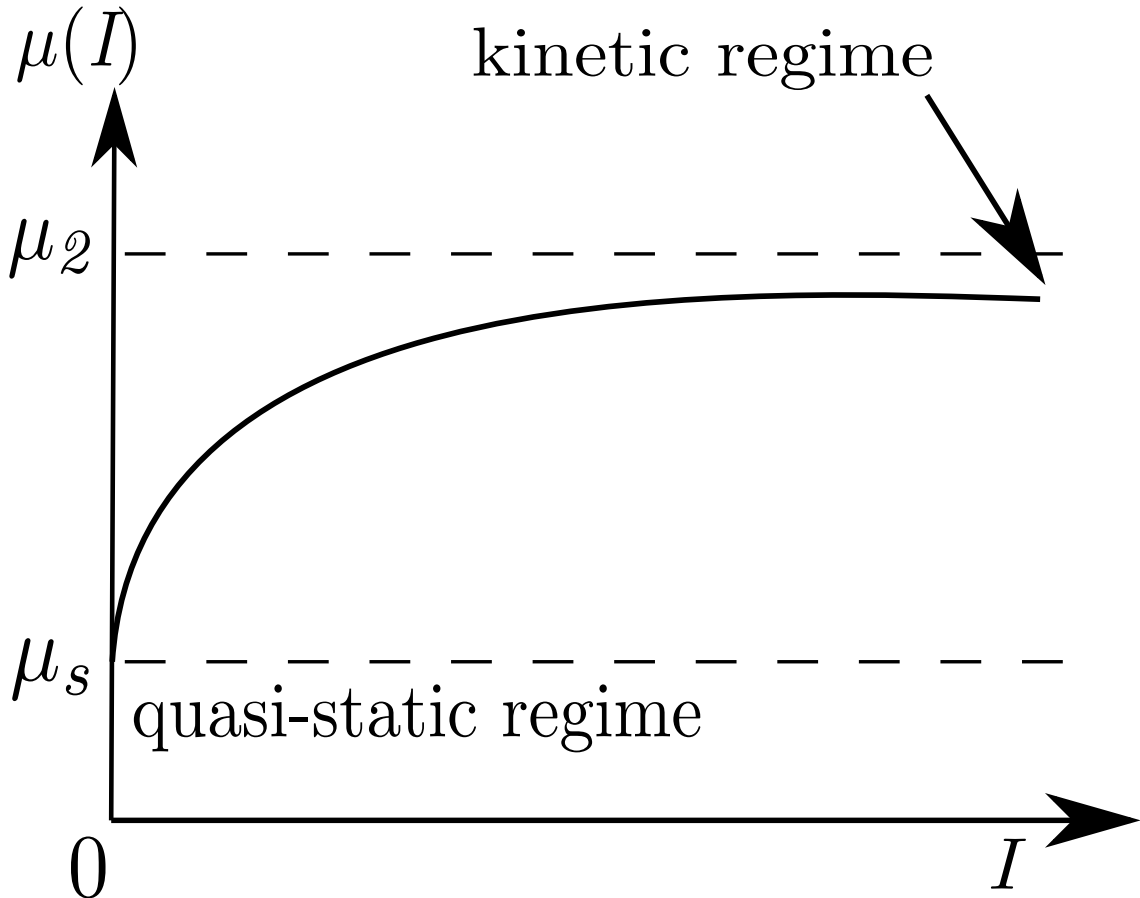


Figure 1.4 Sketch of dependence of frictional coefficient μ with dimensionless shear rate I , reproduced after [Pouliquen et al. \(2006\)](#)

¹⁵ In general, the flow regimes can be classified based on the dimensionless number I ([Da](#)
¹⁶ [Cruz et al., 2005](#)). Dilute or “collisional” flow occurs for $I > 10^{-1}$ and the particle collision
¹⁷ is chiefly binary, accompanied by additional “bounce-back” akin to gases ([Kamrin, 2008](#)). In
¹⁸ the dilute flow regime, the particles are rarely in long-duration contacts and can be described
¹ by dissipative Boltzmann kinetics. The “quasi-static” regime occurs at the other extreme of
² the spectrum, $I < 10^{-3}$, where the intermittent motion is prevalent. The inertial time is always
³ small enough for the particles to align to a dense compaction, without significant collisional
⁴ dissipation. The frictional sliding and stick-slip dynamics dominate the dissipation mechanism.
⁵ The moderate-flow regime is observed for I between 10^{-3} and 10^{-1} , characterized by faster
⁶ flows, with a high rate of contact formation and more energy dissipation per impact. In this
⁷ regime, I has a one-one relationship with μ and is large enough for rate dependence, but small
⁸ enough for the flow to remain dense. Moderate flows also exhibit the property of *shearing*
⁹ *dilation*, where an increase in the normalized flow rate causes the steady-state packing fraction

to decrease, which is different from *shear dilation*, which refers to a decrease in the packing density as a function of total shear. Flows which are too slow to be moderate still undergo shear dilation due to geometric packing constraints, but shearing dilation occurs only in faster flows due to rate effects (Kamrin, 2008). figure 1.5 shows the variation of frictional coefficient μ and packing fraction ϕ with dimensionless number I for various flow regimes.

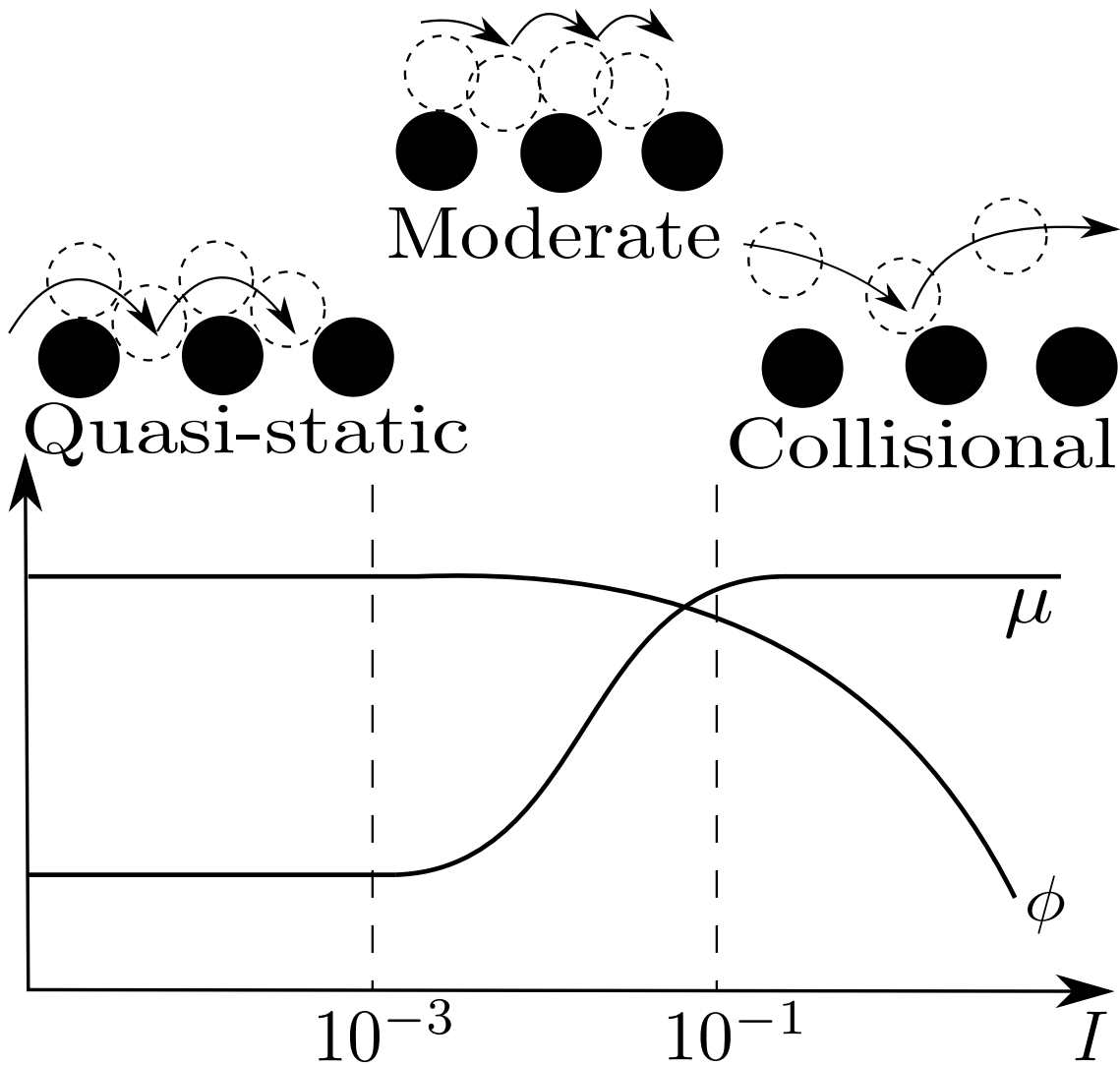


Figure 1.5 Variation of dimensionless parameters through the various flow regimes under simple shearing, reproduced after (Kamrin, 2008)

Campbell (2002) described the “Moderate regime” as an elastic granular flow regime, where the inter-particle stiffness governs the overall flow behaviour of the granular assembly. At high concentration, the stresses are proportional to the contact stiffness, and the streaming stiffness is negligible. When a dense granular assembly is sheared, the force chains that transmit the forces continue to rotate until it becomes unstable and collapses. As the force-chain

rotates, the granular material tend to dilate, however it is restricted due to the constant volume constraint; instead, the rotation compresses the chain, generating an elastic response (Campbell, 2006). Campbell (2002) divided the flow into the elastic and the inertial regimes. In the Elastic regime, the force is transmitted principally through the deformation of force chains with a natural stress scaling of $\tau d/k$. The force chain forms when the particles are sheared at the rate of $\dot{\gamma}$, and hence the rate of chain formation is proportional to the shear rate $\dot{\gamma}$. This transition regime can be explained using the force-chain concept. The lifetime of a force chain is proportional to $1/\dot{\gamma}$, consequently the product of rate of formation and the lifetime of the force chain is independent of $\dot{\gamma}$, and the stresses generated are quasi-static. However at higher shear rates, the elastic forces in the chain have to absorb the additional inertial force of the particles, requiring extra force to rotate the chain proportional to the shear rate. Even though the particles are locked in force chains, the forces generated must reflect the particle inertia. The ratio of elastic to inertial effects is governed by a dimensionless parameter:

$$k^* = \frac{k}{\rho d^3 \dot{\gamma}^2} \quad (1.7)$$

where $k/\rho d^3 \dot{\gamma}^2 = (\tau/\rho d^2 \dot{\gamma}^2)/(\tau d/k)$ is the ratio of Bagnold's inertial to the elastic stress scaling. The important dimensionless parameter is k^* , which is a measure of inertially-induced deformation, reflects the relative effects of elastic to inertial forces, i.e. at large k^* , the elastic forces dominate and at small k^* , inertial forces dominate (Campbell, 2006). Campbell (2002) observed a strong correlation between the coefficient of friction and the dimensionless parameter, k as the flow progresses through different regimes, similar to the observation made by Kamrin (2010).

Constitutive laws, which describe the dilatancy and friction, allow us to deduce the dependency of pressure and shear stress on shear rate and solid fraction. In contrast to the observation of Campbell (2002), Da Cruz et al. (2005) found that the elastic stiffness has little effect on the constitutive law, for values greater than 10^4 , however that it does affect the coordination number. Da Cruz et al. (2005) also observed that the microscopic friction coefficient, μ , has a significant influence on the dilatancy, and the solid fraction remains a linearly-decreasing function of I . The frictional properties of the material are found to control the solid fraction, from the critical state to the collisional regime (Da Cruz et al., 2005). Although the rheology tends to describe the behaviour of granular flows, the mechanism of granular flows was found to vary with time, position and feedback mechanism (Iverson, 2003). Rheology summarizes the mechanical behaviour at scales smaller in comparison with the Representative Elemental Volume (REV), for a substance modelled as a continuum. Rheology-based descriptions are generally restricted to homogeneous materials that exhibit time-independent behaviour, hence

are unsuitable for describing granular flows where the stress history has a significant effect on the flow dynamics. The estimation of debris flow yield strength highlights the limitation of rheologies which do not consider the development of strength with evolution of time and space. Johnson (1965) emphasized that debris yield strength is predominantly a frictional phenomenon analogous to the Coulomb strength of granular soils, and that strength consequently varies with effective normal stress. Treatment of yield strength as an adjustable rheological property contradicts the basic understanding that the strength evolves as the debris-flow motion progresses. Frictional behaviour implies no explicit dependence of shear resistance on shear rate, whereas rheological formulas commonly used to model debris flows generally include a viscous component that specifies a fixed functional relationship between shear resistances and shear rate. Although rate-dependent shear resistance is observed in debris flows, its magnitude and origin indicate that it is ancillary rather than essential (Iverson, 2003).

The two main modelling techniques that are commonly employed to describe the granular flow are the continuum approach and the discrete element approach. The continuum approach involves treating granular assembly as a continuum and describing its response using constitutive laws, while the discrete approach involves considering the individual particles of the granular material and applying Newton's laws of motion to describe the deformation of the granular material. These approaches are adopted in the present study and detailed discussions are provided in the subsequent chapters.

1.3 Studies on granular flows

The flow of dense granular material is a common phenomenon in engineering predictions, such as avalanche, landslides, and debris-flow modelling. Despite the huge amount of research that has gone into describing the behaviour of granular flow, a constitutive equation that describes the overall behaviour of a flowing granular material is still lacking. To circumvent this difficulty, depth-averaged constitutive equations have been employed along with an empirical friction coefficient and a velocity profile deduced from experiments (Iverson, 2003; Midi, 2004; Pouliquen, 1999). Although this approach has been successful to a certain extent in predicting geophysical flows (Hutter et al., 1995; Pouliquen and Chevoir, 2002), it presents two important shortcomings (Lajeunesse et al., 2005). First, the depth-average method is true only if the thickness of the flowing layer is thin in comparison with the lateral dimension, and second, the empirical laws are deduced from experiments performed under steady-flow conditions. These cast doubts on the validity of the depth-averaged approach. Two simple granular flow studies, granular column collapse and granular flow down an inclined plane, have been carried out by various researchers to understand the flow behaviour.

1.3.1 Granular column collapse

Lube et al. (2005) and Lajeunesse et al. (2004) have carried out experimental investigation on the collapse behaviour of a granular column on a horizontal plane. Both the experiments involved filling a cylinder of height H_i and radius R_i with granular material of mass m . The granular column is then released *en masse* by quickly removing the cylinder, thus allowing the granular material to collapse onto the horizontal surface, forming a deposit having a final height H_f and radius R_f . Although the experiment is simple and attractive allowing us to explore the limitations of depth-average modelling techniques, a constitutive law that could describe the entire flow behaviour is still lacking. The primary aim of these experiments was to determine the scaling laws for the run-out distance.

Deposit morphology

Lajeunesse et al. (2005) observed that the flow dynamics and the final deposit remain independent of the volume of granular material that is released, but depend only on the initial aspect ratio ‘ a ’ of the granular column. The experiment was carried out to understand the effect of the geometrical configuration on the run-out, the mechanism of initiation of the flow, the evolution of flow with time, and to understand how such complex flow dynamics could produce deposits obeying simple power laws. Lube et al. (2005) explored the effect of density and shape of grains on flow dynamics, whereas Lajeunesse et al. (2004) worked with glass beads to study the influence of bead size and substrate properties on the deposit morphology. Surprisingly, both drew the striking conclusion that the flow duration, the spreading velocity, the final extent of the deposit, and the fraction of energy dissipated during the flow can be scaled in a quantitative way independent of substrate properties, bead size, density, and shape of the granular material and released mass, M (Lajeunesse et al., 2005). Lube et al. (2005) scaled the run-out distance as:

$$\frac{R_f - R_i}{R_f} \approx \begin{cases} 1.24a, & a \lesssim 1.7 \\ 1.6a^{1.2}, & a \gtrsim 1.7 \end{cases} \quad (1.8)$$

while Lajeunesse et al. (2004) scaled run-out as:

$$\frac{R_f - R_i}{R_f} \approx \begin{cases} 1.35a, & a \lesssim 0.74 \\ 2.0a^{1.2}, & a \gtrsim 0.74 \end{cases} \quad (1.9)$$

Quasi-two-dimensional collapse of a granular column on a horizontal surface (Lajeunesse et al., 2005) reveals that the geometric configuration influences the scaling of the run-out distance.

- ₁₂ The run-out in a quasi-two-dimensional collapse of a granular column in a rectangular channel,
₁₃ is scaled as:

$$\frac{R_f - R_i}{R_f} \approx \begin{cases} 1.2a, & a \lesssim 2.3 \\ 1.9a^{2/3}, & a \gtrsim 2.3 \end{cases} \quad (1.10)$$

₁₄ At large aspect ratios, the run-out is well represented by a simple power-law dependence. The
₁₅ exponent is found to vary with the channel width: $\Delta R/R_i \approx \lambda a^{0.65}$ for narrow channels and
₁₆ $\Delta R/R_i \approx \lambda a^{0.9}$ for wide channels. The constant of proportionality λ is found to vary with
₁₇ the internal friction angle of the granular material, which contradicts the findings of previous
₁₈ authors, especially Lube et al. (2005) who found that the scaling of run-out is independent
₁₉ of the granular material, perhaps due to a narrow range of experimental materials (Staron
₂₀ et al., 2005). However, scaling found for quasi-two-dimensional experiments in the narrow gap
₂₁ configuration gives similar results as (Lube et al., 2005) and roughly a scaling of $R_f/(R_f - R_i) \propto$
₂₂ $a^{2/3}$. Numerical simulations of granular column collapse by Zenit (2005) and Staron et al.
₂₃ (2005) yielded similar scaling of run-out with aspect ratio ‘ a ’, unlike other authors, Zenit (2005)
₂₄ did not observe any transition in the run-out behaviour of a granular column collapse with
₂₅ the aspect ratio ‘ a ’. The origin of the exponents is still under discussion. No model has yet
₂₆ achieved a comprehensive explanation of the dependence of the complex-collapse dynamics on
₂₇ simple power laws. However, it was observed that a simple friction model cannot effectively
₂₈ describe the collapse dynamics. Staron et al. (2005) explained the mechanism of spreading
₂₉ using an initial potential energy approach. For higher aspect ratios, the free fall of the column
₃₀ controls the dynamics of the collapse and the energy dissipation at the base is attributed to the
₃₁ coefficient of restitution. Thus, the initial potential energy stored in the system is dissipated
₃₂ by sideways flow of material and the mass ejected sideways is found to play a significant role
₃₃ in the spreading process, i.e. as ‘ a ’ increases, the same fraction of initial potential energy
₁ drives an increasing proportion of initial mass against friction, thus explaining the power-
₂ law dependence of the run-out distance on ‘ a ’. Taking advantage of the similarity between
₃ granular slumping and the classical “*dam break*” problem in fluid mechanics, ? solved both
₄ the axis-symmetric and two-dimensional granular-collapse problem using the shallow-water
₅ approximation. Although the results of the shallow-water approximation have good agreement
₆ with experimental results, the shallow-water approximation overestimates the run-out distance
₇ for columns with aspect ratio ‘ a ’ greater than unity. The shallow-water equation does not take
₈ into account the effect of vertical acceleration (Lajeunesse et al., 2005), which has been found
₉ to play a significant role in controlling the collapse dynamics Staron et al. (2005), thus resulting
₁₀ in overestimation of run-out. The evolution of the scaled deposit height H_f/R_i with the aspect
₁₁

1
2
3
4
5
6
7
8
9
10
11
12

ratio ‘ a ’ for axis-symmetric collapse ([Lajeunesse et al., 2005](#)) is given as:

$$H_f/R_i \approx \begin{cases} a, & a \lesssim 0.74 \\ 0.74, & a \gtrsim 0.74 \end{cases} \quad (1.11) \quad \begin{matrix} 14 \\ 15 \end{matrix}$$

and for two-dimensional collapse:

$$H_f/R_i \approx \begin{cases} a, & a \lesssim 0.7 \\ a^{1/3}, & a \gtrsim 0.7 \end{cases} \quad (1.12) \quad \begin{matrix} 17 \\ 18 \end{matrix}$$

The scaling of the final collapse height is found to be similar with the experimental results of [Lube et al. \(2005\)](#) and [Balmforth and Kerswell \(2005\)](#), and the numerical simulation of [Staron et al. \(2005\)](#). Numerical simulation of granular column collapse ([Lacaze et al., 2008](#); [Staron et al., 2005](#)) showed a transition in the flow behaviour at ‘ a ’ ≥ 10 , which was not observed in granular collapse experiments ([Balmforth and Kerswell, 2005](#); [Lajeunesse et al., 2004](#); [Lube et al., 2005](#)). In the depth-averaged shallow-water model, which integrates over the depth, the emphasis was on capturing the scaling of the final deposit, rather than trying to reproduce the internal structure of the flow. The shallow-water model captures well the final deposit scaling for lower aspect ratios, however fails to capture the flow dynamics for granular columns with higher aspect ratios, where the flow is governed mainly by the vertical collapse of the granular column as a whole. The run-out distance predicted is clearly erroneous in the collapse regime where there is a sudden drop in efficiency by which the initial potential energy of the system is converted into the kinetic energy for spreading. Even a more sophisticated basal drag law will not be sufficient to model the mechanism of granular column collapse realistically using the shallow-water approximation (?).

3 Flow dynamics

The variation of final scaled deposit with aspect ratio ‘ a ’ shows a transition in the run-out behaviour for an aspect ratio of 1.7, indicating a transformation in the spreading process or the collapse mechanism. To understand the collapse mechanism, it is insufficient to study only the final scaled profile, and hence the entire flow process should be analysed. [Lajeunesse et al. \(2005\)](#) observed the flow regime and deposit morphology for a quasi-two-dimensional granular collapse in a rectangular channel. The flow phenomenology of a granular column collapse in a rectangular channel was surprisingly similar to that observed in the axis-symmetric collapse ([Lajeunesse et al., 2004](#); [Lube et al., 2005](#)), depending mainly on the initial aspect ratio ‘ a ’. The flow dynamics involve spreading of granular mass by avalanching of flanks producing

¹³ a truncated cone for $a \lesssim 0.74$ and a cone for $a \gtrsim 0.74$; the transition of flow dynamics occurs
¹⁴ as the value of ‘ a ’ is increased. The evolution of the deposit height remains independent of the
¹⁵ flow for $a \lesssim 0.7$, however it exhibits significant dependence on the geometrical configuration
¹⁶ for $a \gtrsim 0.7$. In rectangular channels, the effect of sidewall on the run-out behaviour was
¹⁷ observed; the surface velocity profile between the sidewalls is that of a plug flow with a high
¹⁸ slip velocity at the wall and low shear along the direction transverse to the flow. Systematic
¹⁹ measurements indicate that the ratio of the maximum surface velocity to the surface velocity at
²⁰ the wall is between 1.2 and 1.4. [Lajeunesse et al. \(2005\)](#) observed that the difference between
²¹ the evolution of H_f in the axis-symmetric geometry and in the rectangular channel is not an
²² experimental artefact due to the side wall friction, but is a *geometrical effect*.

²³ Understanding the internal flow structure will provide an insight into the complex collapse
²⁴ dynamics. For smaller values of aspect ratio ‘ a ’ ≤ 0.7 , the flow is initiated by a failure at
²⁵ the edge of the pile along a well-defined fracture surface above which material slides down
²⁶ and below which the grains remain static. The grains located above the fracture move “*en*
²⁷ *masse*” and most of the shear is concentrated along this surface forming a “*truncated-cone-like*”
²⁸ deposit with a central motionless plateau. For columns with larger aspect ratios, the flow is still
²⁹ initiated by failure along a well-defined surface, an inclined plane in two-dimensional geometry
³⁰ or a cone in the axis-symmetric case. However, the initial height of the column is much higher
³¹ than the top of the failure surface, causing a vertical fall of grains until they reach the summit
³² where they diverge along the horizontal direction, dissipating a lot of kinetic energy, resulting
³³ in a final conical deposit. Interestingly, the final deposit height coincides with the summit of
³⁴ the failure surface in the axis-symmetric geometry, whereas in the rectangular channel, the
³⁵ deposit summit always lies above the top of the failure surface ([Lajeunesse et al., 2005](#)).

³⁶ Identification of the static region is an important task, as it is a prime component in
¹ describing the collapse mechanism. Regardless of the experimental configuration, for all values
² of ‘ a ’ the flow is initiated by rupture along a well-defined failure surface and the failure angle
³ remains of the order of 50° to 55° . The failure angle is consistent with an interpretation of
⁴ *active Coulomb failure*, which leads to a failure angle $\phi_f = 45^\circ + \delta/2$, where δ is the internal
⁵ friction angle of the granular material. Estimating the internal friction angle of glass beads from
⁶ the angle of repose as 22° , the failure angle is estimated as 56° , which is in good agreement
⁷ with the experimental findings. Contrary to the suggestion of [Lajeunesse et al. \(2004\)](#), the
⁸ fracture angle was found to have no direct effect on the transition between truncated cone and
⁹ conical deposit occurring at aspect ratio ‘ a ’ of 0.7 ([Lajeunesse et al., 2005](#)). ? observed the
¹⁰ onset of instability, when the neutrally stable plane waves makes an angle of ϕ_I with the major
¹¹ principle stress axis. The onset of instability triggers unstable plane waves in a narrow wedge of
¹² 56° to 65° , which corresponds to the angle of shear bands: this observation matches well with

the failure angle observed in the granular flow. A rate-dependent constitutive relationship (Jop et al., 2006) for dense granular flows indicates the angle of shear-band orientation depends on the inertial number I . For small to moderate values of I , the orientation of shear bands is found to vary from the Roscoe and the Coulomb solutions to a unique admissible angle (Lemiale et al., 2011). Daerr and Douady (1999) observed active Coulomb-type yielding in transient surface flows for granular materials having a packing density of 0.62 to 0.65. The comparison of initial and final areas indicates a change in the packing; the initial area is systematically smaller than the final area. This change in packing is typical of granular slumping in a channel and reflects that the pile, which initially had a relatively close packing, expanded (by about 10%) as the flow progressed, to form the final deposit (Balmforth and Kerswell, 2005).

A critical time τ_c is defined as the transition time at which the flow is fully developed. The velocity field then depends on the position of grains along the pile, see Lajeunesse et al. (2005). In the front, the flow involves the entire thickness of the pile and corresponds to a plug flow in the horizontal direction. In the region above the static core, the flow is locally parallel to the failure surface and has an upper linear part and a lower exponential tail near the static bed (Lajeunesse et al., 2005). The velocity flow profile is similar to that of a steady granular flow (Midi, 2004). As the pile spreads, interface separation occurs as the flow diverges and the static region starts to move inwards; this effect is predominant in the case of granular flows in a rectangular channel. The typical velocity observed at the front of the ejecting mass is $v = \sqrt{2gR_i}$. The flow evolution as per Staron et al. (2005) involves three stages. The first stage involves conversion of the initial potential energy of the grains into vertical motion, resulting in downwards acceleration of grains. In the second stage, the grains undergo collision with the base and/or neighbouring grains, and their vertical motion is converted into horizontal motion.

- ¹ In the final stage, the grains eventually leave the base area of the column and flow sideways.
- ² The typical time required for the flow to cease and form the final deposit, from the instant of
- ³ its release, is $T = \sqrt{2H_i/g}$ (Staron et al., 2005). While plotting the variation of normalized
- ⁴ potential and kinetic energy with normalized time, Staron et al. (2005) observed that the flow
- ⁵ ceases when the normalized time t/T_0 is 2.5, i.e. the flow is assumed to have stopped when the
- ⁶ total normalized energy is almost zero. This observation is consistent with the experimental
- ⁷ results of Lube et al. (2005) and Lajeunesse et al. (2005). The transition of the flow occurs
- ⁸ when the normalized time t/T_0 is 1.0 or at critical time τ_c , which is defined as the time at which
- ⁹ the flow is fully mobilized.

¹⁰ Comments on modelling

- ¹¹ In order to have a detailed understanding of the final profile of the collapsed granular column, it
- ¹² is important to solve the collapse problem as an *initial-value problem* (Balmforth and Kerswell,

¹³ 2005), beginning from the instant of release and extending to the time when the material
¹⁴ finally ceases to flow, forming the final deposit. As the process of granular collapse involves
¹⁵ collective dynamics of collisions and momentum transfer, the prediction of the trajectory of
¹⁶ a single grain is difficult. In fact, there are quantitative disagreements between theory and
¹⁷ experiments; the final shapes are reproducible, but not perfectly. Some of the disagreement
¹⁸ arises because the experiments did not have exactly the same amount of materials; it is indeed
¹⁹ difficult to fill the pile with exactly the same amount of material, which results in differences in
²⁰ packing. However, the theoretical errors are due to the incapability of the models to capture
²¹ the physics that governs the flow dynamics (Balmforth and Kerswell, 2005). Shallow water
²² models fail to account for the vertical acceleration, which is responsible for the momentum
²³ transfer and, in turn, the spreading process. This restricts the shallow water model to capture
²⁴ the mechanism of collapse until the critical time τ_c . Surprisingly, shallow-water models capture
²⁵ certain experimental aspects for columns with lower aspect ratios (Balmforth and Kerswell,
²⁶ 2005; Mangeney et al., 2010; ?), even though the contrast between surface flows and the static
²⁷ region is important in this range of aspect ratio. Thus, the assumption of plug flow in the
²⁸ horizontal direction is not critical in capturing the run-out behaviour, especially if the basal
²⁹ friction coefficient is used as a fitting parameter (Lajeunesse et al., 2005).

³⁰ Simple mathematical models based on conservation of horizontal momentum capture the
³¹ scaling laws of the final deposit, however they fail to describe the initial transition regime,
³² indicating that the initial transition has negligible effect on the run-out, which is incorrect.
³³ Models based on the initial potential energy show promise, but the effect of material properties,
³⁴ such as basal friction and coefficient of restitution, on the run-out behaviour is still unclear
³⁵ and produces non-physical run-outs. The famous $\mu(I)$ rheology predicts well the normalized
1 run-out behaviour in comparison with the experimental results, for lower aspect ratios. The
2 spreading dynamics is found to be similar for the continuum and particle approaches; however,
3 the rheology falls short in predicting the run-out distance for higher aspect ratios. Unlike Lube
4 et al. (2005), many researchers (Balmforth and Kerswell, 2005; ?) observed strong dependency
5 of material properties on the run-out distance, moistening the materials or the sides of the
6 channel even by a small amount leads to markedly different results. ? observed that the
7 friction has little effect on the run-out for granular column collapse for high aspect ratios,
8 which are driven mainly by the free vertical fall of grains. The initial conditions have a
9 significant impact on the overall behaviour of the granular system, indicating the significance
10 of the triggering mechanism in case of the natural flows (?). Numerical investigations, such
11 as Molecular Dynamics techniques, allow us to evaluate quantities which are not accessible
12 experimentally, thus providing useful insight into the flow dynamics. Subsequent chapters

discuss the methodology and modelling of granular column by continuum- and discrete-element approaches. 13
14

1.3.2 Flow on inclined plane

Studies on the flow of granular materials down inclined planes are important to understand the mechanism of geophysical hazards, such as granular avalanches, debris flows and submarine landslides. Large scale field tests on dry and saturated granular materials were carried out to capture the mechanism of granular flows down an inclined plane (Denlinger and Iverson, 2001; Okada and Ochiai, 2008). The granular material stored in a reservoir at the top of the inclined plane is released by opening a gate; the material flows down and develops into a dense granular flow. A variant of this experiment is the experiment on fluidized beds which involves an initial bed of granular material of thickness ‘ h ’ which is inclined gradually until the granular material flows. When the plane inclination reaches a critical angle, θ_{start} , the material starts to flow and reaches a sustained flow until the inclination is decreased down to a second critical angle, θ_{stop} (Midi, 2004). The occurrence of two critical angles indicates the hysteretic nature of granular materials. Reciprocally, the critical angle thresholds can be interpreted in terms of critical layer thicknesses $h_{stop}(\theta)$ and $h_{start}(\theta)$. The measurement of $h_{stop}(\phi)$ is easier as it corresponds to the thickness of the deposit remaining on the plane once the flow has ceased. Three regions can be observed: a region where no flow occurs, ($h < h_{stop}(\theta)$), a sub-critical region where both static and flowing layers can exist ($h_{stop}(\theta) < h < h_{start}(\theta)$) and a region where flow always occurs, ($h > h_{start}(\theta)$). In the flow regime, i.e. ($h > h_{start}(\theta)$), the flow is steady and uniform for moderate inclination, but accelerates along the plane for large inclinations (Midi, 2004). The critical angle controlling the flow behaviour tends to increase when the thickness of the bed decreases (Daerr and Douady, 1999; Pouliquen and Chevoir, 2002), which can be attributed to the non-trivial finite-size effects and/or boundary effects that are not well understood (Forterre and Pouliquen, 2008).

Fast moving granular flows can undergo a motion-induced self-fluidization process under the combined effects of front instabilities setting on at large values of the Froude number which are responsible for extensive air entrainment, and small deflation rates associated with small incipient fluidization velocities and longer collapse time of the bed solids. Self-fluidization results in enhanced mobility of the solids, causing an inviscid flow to an extent that may largely exceed the establishment of a “*granular liquid*” state in purely granular flow (Bareschino et al., 2008). It is understood that, for a granular material to flow, it has to exceed a certain critical threshold, i.e. the friction criterion: the ratio of shear stress to normal stress. As there is no internal stress scale for a granular material, granular materials exhibit solid-fluid transition behaviour based on the friction criterion (Forterre and Pouliquen, 2008). The stress

ratio in the flowing regime above the static bed indicates the solid-to-fluid transition is a yielding phenomenon and can be described by Mohr-Coulomb-like failure criterion ([Zhang and Campbell, 1992](#)). This is in contrast to the mechanism of behaviour of other complex fluids, where there is an internal stress scale linked to the breakage of microscopic structure. From a microscopic point of view, the strength of the granular materials is due to the internal friction between grains, but packed frictionless materials still exhibit macroscopic friction.

Constitutive laws based on Plasticity-theories relate the micro-structure to the macroscopic behaviour ([Roux and Combe, 2002](#)), which provide useful insight into the mechanism of granular flow. However, at present they are limited to initiation of deformation and do not predict the quasi-static flow. Material Point Method simulation of granular flow down an inclined plane ([??](#)) captures the flow behaviour in the initial stages, however it exhibits inconsistent behaviour when the granular material ceases to flow. This may be due to the application of small deformation theory to a large deformation problem and to the use of zero dilation. In the case of flow down an inclined plane, the only control parameter is the flow rate, Q , and uniform, steady flows are possible if the system is confined between walls. The additional friction induced by the lateral walls has a significant effect on the flow and causes localization at the free surface. The $\mu(I)$ friction law captures the velocity profile and the localization at the free surface. However, the model fails to capture the transition from a continuous flow to an avalanching regime as the flow rate is decreased ([Pouliquen et al., 2006](#)). The flow can cause strong Coulomb shear stresses to develop on a plane normal to the basal flow boundary. The stresses dissipate energy as the flow encounters obstructions: models that lack multi-dimensional momentum transport or Coulomb friction cannot represent this energy dissipation and lodging.

1.3.3 Saturated and submerged granular flows

Geophysical hazards, such as debris flows and submarine landslides, usually involve flow of granular solids and water as a single-phase system. The momentum transfer between the discrete and continuous phases significantly affects the dynamics of the flow as a whole ([Topin et al., 2011](#)). Although certain macroscopic models were able to capture simple mechanical behaviours ([Peker and Helvacı, 2007](#)), the complex physical mechanisms occurring at the particle scale, such as hydrodynamic instabilities, formation of clusters, collapse, and transport ([Topin et al., 2011](#)), have largely been ignored. In particular, when the solid phase reaches a high volume fraction, the strong heterogeneity arising from the contact forces between the particles, and the hydrodynamic forces, are difficult to integrate into the homogenization process involving global averages ([Topin et al., 2011](#)). In two-phase models ([Pitman and Le, 2005](#)), the momentum transfer between the particles and the suspension fluid depends on the

momentum equations of both the phases. In case of mixture theory based models (Meruane et al., 2010), the shear-induced migration and particles collisions are considered in an average sense. In order to describe the mechanism of saturated and/or immersed granular flows, it is important to consider both the dynamics of the solid phase and the role of the ambient fluid (Denlinger and Iverson, 2001; Iverson, 1997). The dynamics of the solid phase alone are insufficient to describe the mechanism of granular flow in a fluid; it is important to consider the effect of hydrodynamic forces that reduce the weight of the solids inducing a transition from dense-compacted to dense-suspended flows, and the drag interactions which counteract the movement of the solids (Meruane et al., 2010). Cassar et al. (2005) carried out experimental investigation on the flow of dense granular material down an inclined plane fully-immersed in water. The velocities observed in the submarine case were found to be a magnitude smaller than the dry condition. However, $\mu(I)$ rheology for dry dense flows captures the behaviour of dense submarine granular flows, if the inertial time scale in the rheology is replaced with a viscous time scale. In the case of dry granular flows, the parameter I is defined as the ratio between the time taken for a particle to fall into the hole, t_{micro} , and the meantime, t_{mean} , which is inversely related to the shear rate. Pitman and Le (2005) observed that if the fluid inertial effects are small enough, then a simpler model can be adopted. Hence, assuming that the fluid velocity is low enough for the contact interaction between particles to be significant, the time taken by the particle to fall into a hole, t_{micro} , is then controlled by the viscosity of the ambient fluid. Thus, the dimensionless parameter can be modified to incorporate the viscous time to describe granular flow in a fluid (Pouliquen et al., 2005).

The constitutive law is found to be valid only for the steady uniform regime; unsteady phenomena such as the triggering of avalanches result in coupling between the granular particles and the ambient fluid and are much more complex to model. Transient regimes characterized by change in solid fraction, dilation at the onset of flow and development of excess pore pressure, result in altering the balance between the stress carried by the fluid and that carried by the grains, thereby changing the overall behaviour of the flow (Denlinger and Iverson, 2001). The $\mu(I)$ rheology seems to predict well the flow of granular materials in the dense regime. However, the transition to the quasi-static regime where the shear rate vanishes is not captured by the simple model. Also, shear band formation observed under certain flow configurations is not predicted. The flow threshold or the hysteresis characterizing the flow or no-flow condition is not correctly captured by the model, which can be due to the discrepancies between the physical mechanism controlling the grain level interactions, clustering, and vortex formations. When the scale of the system is larger than the size of the structure, a simple rheology is expected to capture the overall flow behaviour, however the size of the correlated motion is the same as that of the system, causing difficulties in modelling the flow behaviour (Pouliquen et al., 2005).

Hence, it is essential to study the behaviour of granular flows at various scales, i.e. microscopic, meso-scale and at continuum level, in order to develop a constitutive model that captures the entire flow process.

8
9
10

1.4 Summary

11
12
13
14
15
16
17
18
19
20
21
22
23

Granular flow involves three distinct regimes: the dense quasi-static regime, the rapid and dilute flow regime, and an intermediate regime. Many models, such as the shallow-water approximation, kinetic theory approach, and rheologies based on shear rate, have captured the basic flow dynamics, but have failed to describe the complete mechanics of the granular flow. The dynamics of homogeneous granular flow involve at least three different scales, making it difficult to describe the mechanics of granular flow by simple theories. It is important to describe the granular dynamics as an initial-value problem, beginning from the instance of its initiation to the time at which the material ceases to flow, forming a final deposit. During this process, the granular materials undergo phase transition, in addition to the transition in their flow dynamics. Most theoretical models are incapable of capturing these transition regimes. Experimental conditions are too difficult to reproduce precisely, resulting in inherent inconsistencies in the results. Discrete numerical approaches, such as Molecular Dynamics, allow us to evaluate

- ¹ quantities which are not accessible experimentally, thus providing useful insight into the flow
- ² dynamics, thereby enabling us to develop better constitutive laws. Subsequent chapters discuss
- ³ the continuum and particle-scale modelling of granular flows.

4 Chapter 2

5 Numerical modelling of granular flows

6 2.1 Introduction

7 The dynamics of a homogeneous granular flow involve at least three distinct scales: the
8 *microscopic scale*, which is characterised by the contact between grains, the *meso-scale* that
9 represents micro-structural effects such as grain rearrangement, and the *macroscopic scale*,
10 where geometric correlations can be observed (see figure 2.1). Conventionally, granular flows
11 are modelled as a continuum because they exhibit many collective phenomena. However, on
12 a grain scale, the granular materials exhibit complex solid-like and/or fluid-like behaviour.
13 Recent studies, however, suggest that a continuum law may be unable to capture the effect
14 of inhomogeneities at the grain scale level, such as orientation of force chains, which are
15 micro-structural effects. Discrete element methods (DEM) are capable of simulating these
16 micro-structural effects, however they are computationally expensive. In the present study,
17 a multi-scale approach is adopted, using both DEM and continuum techniques, to better
18 understand the rheology of granular flows and the limitations of continuum models.

19 2.2 Continuum modelling of granular flows

20 The most powerful way of modelling the granular assembly is through numerical techniques. It
21 is important to argue, why it is acceptable to model the granular materials as a continuum. At
22 the outset, it may even appear for some reasons why such a treatment is objectionable. Most
obvious is the fact that the micro-constituents of granular matter, i.e. the individual grains are
not small enough to warrant a continuum description (Kamrin et al., 2007). Typical continuum
laws are only expected to apply when there is a strong separation of scales, i.e. separation
of the micro-scale from the macro-scale, in the flow geometry. Continuum mechanics relies

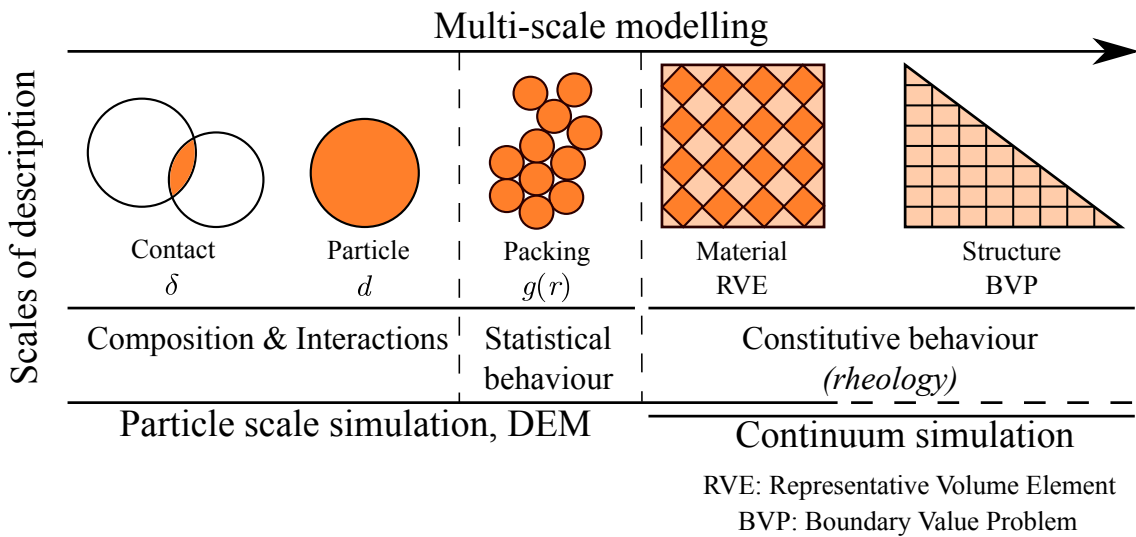


Figure 2.1 Multi-scale modelling of granular materials

on the fundamental notion of a representative volume element, in which properties averaged over discrete particles exhibit deterministic relationships. Recent works on granular materials suggest that a continuum law may be incapable of revealing in-homogeneities at the particle-scale level, such as force chains (?). Granular materials exhibit many collective phenomenon (Jaeger et al., 1996). However, no continuum model is still capable of describing the parabolic flow, the plug flow (Rycroft et al., 2006) and the occurrence of localized shear bands in the granular materials. This is in contrast to the hydrodynamics of dilute granular materials and the molecular fluids for which accurate continuum models can be systematically derived, by averaging over particle collisions in an idealized element (Jenkins and Savage, 1983). The fundamental question is how to model granular materials which exhibit complex phenomenon, meaningfully.

The oldest approach involves modelling the granular material as a rigid solid, which behaves as an ideal Coulomb material and undergoes failure if the ratio of the shear stress to the normal stress in any plane reaches a critical value of the Coulomb internal friction coefficient μ . The stress is determined based on the mechanical equilibrium of the system along with the hypothesis of *incipient yield*, i.e. the yield criterion is attained everywhere at all times. In limit-state Mohr-Coulomb plasticity, these conditions are assumed to hold even if the wall allows for a plastic yielding, due to the assumption of coaxiality (?). The fundamental assumption of a limit-state stress field at incipient yield everywhere is questionable. Granular flows can contain regions lying within the yield surface. For example, in the case of a granular column collapse the central cone remains stagnant, and thus cannot be considered as yielded. In fact, discrete-element simulations show that the grains in this region essentially remain static (Staron

et al., 2005). The coaxiality feature of Mohr-Coulomb plasticity is useful in describing the debris flow. Granular material deforms solely based on the alignment of the principle plane. In general, the major principle plane is usually vertical due to gravity, and the coaxiality rule requires the material to expand horizontally, which is the case for granular column collapse. However, the coaxiality can be troubling depending on the circumstances, for example, in a slow dense granular flow through a silo, the principle plane remains vertical and the coaxiality requires the granular material to expand horizontally, thus making it geometrically impossible for the granular material to converge and exit through the orifice. Depending on the boundary conditions, Mohr-Coulomb plasticity can result in discontinuity or jumps in the velocity and stress fields (Rycroft et al., 2006). Advanced elasto-plastic models based on *critical state*

1 theories provide a better representation of granular flows in quasi-static regime, but they fail

2 to capture the mechanism of rapid granular flows which involves rate dependent behaviour.

3 Another continuum based model is the partial fluidization model, which uses a set of equations

4 that describes the flow velocity and the shear stresses along with a auxiliary order parameter to

5 predict the granular flow behaviour. The order parameter of the granular media controls the

6 size of the viscous-like contribution to the stress tensor, and describes the transition between

7 the flowing and the static components of the granular system (Aranson and Tsimring, 2001).

8 A constitutive model, which considers the solid fraction as the main microscopic parameter

9 for describing dense granular flow was proposed by Josserand et al. (2004). The stress in

10 the granular material is divided into rate-dependent part representing the rebound-less impact

11 between grains, and a rate-independent part associated with longer contacts, i.e. quasi-static

12 regime. Although, the model captures shear localization behaviour, it fails to describe the

13 granular flow behaviour at rough boundaries.

14 Granular materials are composed of distinct grains, which displace independently from one
15 another and interact only at contact points. It is assumed that the deformations of individual
16 grains are negligible in comparison with the deformation of the granular assembly as a whole.

17 The latter deformation is primarily due to the movement of the grains as a rigid body. Therefore,
18 it can be argued that precise modelling of particle deformation is not necessary to obtain a good
19 approximation of the overall mechanical behaviour. An Eulerian grain-level continuum model

20 describes the response of individual grains to the applied loads. However, continuum mechanics

21 solves over the whole domain using initial and boundary conditions appropriate for the problem.

22 Hence, continuum models are still widely used to solve engineering problems associated with
23 granular materials and flows. Conventional mesh based approaches, such as Finite Element
24 Method or Finite Difference Method involves complex re-meshing and remapping of variables,
25 which causes additional errors in simulating large deformation problems (Li and Liu, 2002).

26 Mesh free methods such as Material Point Method are not constrained by the mesh size and

²⁷ mesh distortion, and hence can be effectively used in simulating large deformation problems,
²⁸ such as debris flow and submarine landslides.

²⁹ 2.3 Material Point Method (MPM)

¹ Material Point Method (MPM) ([Sulsky et al., 1994, 1995](#)) is a particle based method that
² represents the material as a collection of *material points*, and their deformations are deter-
³ mined by *Newton's laws of motion*. [Sulsky et al. \(1994\)](#) extended the Particle-in-Cell (PIC)
⁴ method ([Harlow, 1964](#)) to computational solid mechanics by taking advantage of the combined
⁵ Eulerian-Lagrangian approach. Material Point Method is a hybrid Eulerian-Lagrangian ap-
⁶ proach, which uses moving material points, and computational nodes on a background mesh.
⁷ This approach is very effective particularly in the context of large deformations ([??](#)). Although,
⁸ not derived directly from what is classically considered as mesh-free or mesh-less methods,
⁹ MPM is still considered as a mesh-free approach, primarily because the initial discretization of
¹⁰ the material does not involve a polygonal tessellation, as in Finite Element Method. However,
¹¹ MPM utilizes a background mesh to perform differentiation, integration, and to solve equations
¹² of motions ([Steffen et al., 2008](#)). The background mesh can be of any form, however for
¹³ computational efficiency a Cartesian lattice is adopted. A typical 2D discretization of a solid
¹⁴ body is shown in figure [2.2](#).

¹⁵ The grey-shaded circles are the material points (X_p , where 'p' represents a material point)
¹⁶ and the computational nodes are the points of intersection of the grid (denoted as X_i , where
¹⁷ i represents a computational node). The Material Point Method involves discretizing the
¹⁸ domain Ω with a set of material points. The material points are assigned an initial value of
¹⁹ position, velocity, mass, volume, and stress denoted as \mathbf{x}_p , v_p , m_p , \mathbf{V}_p and σ_p . Depending on
²⁰ the material being simulated, additional parameters, like pressure, temperature, etc., should be
²¹ specified at the material points. The material points are assumed to be within the computational
²² grid, which is assumed to be a Cartesian lattice for convenience (see figure [2.2](#)). At every
²³ time step t_k , the MPM computation cycle involves projecting the data, such as position, mass,
²⁴ and velocity from the material points to the computational grid using standard nodal basis
²⁵ functions, called *shape functions*, derived based on the position of particle with respect to the
²⁶ grid. Gradient terms are calculated in the computational grid and the governing equation, i.e.
²⁷ the equation of motion, is solved and the updated position and velocity values are mapped back
²⁸ to the material points. The mesh is reinitialized to its original state and the computational cycle
is repeated.

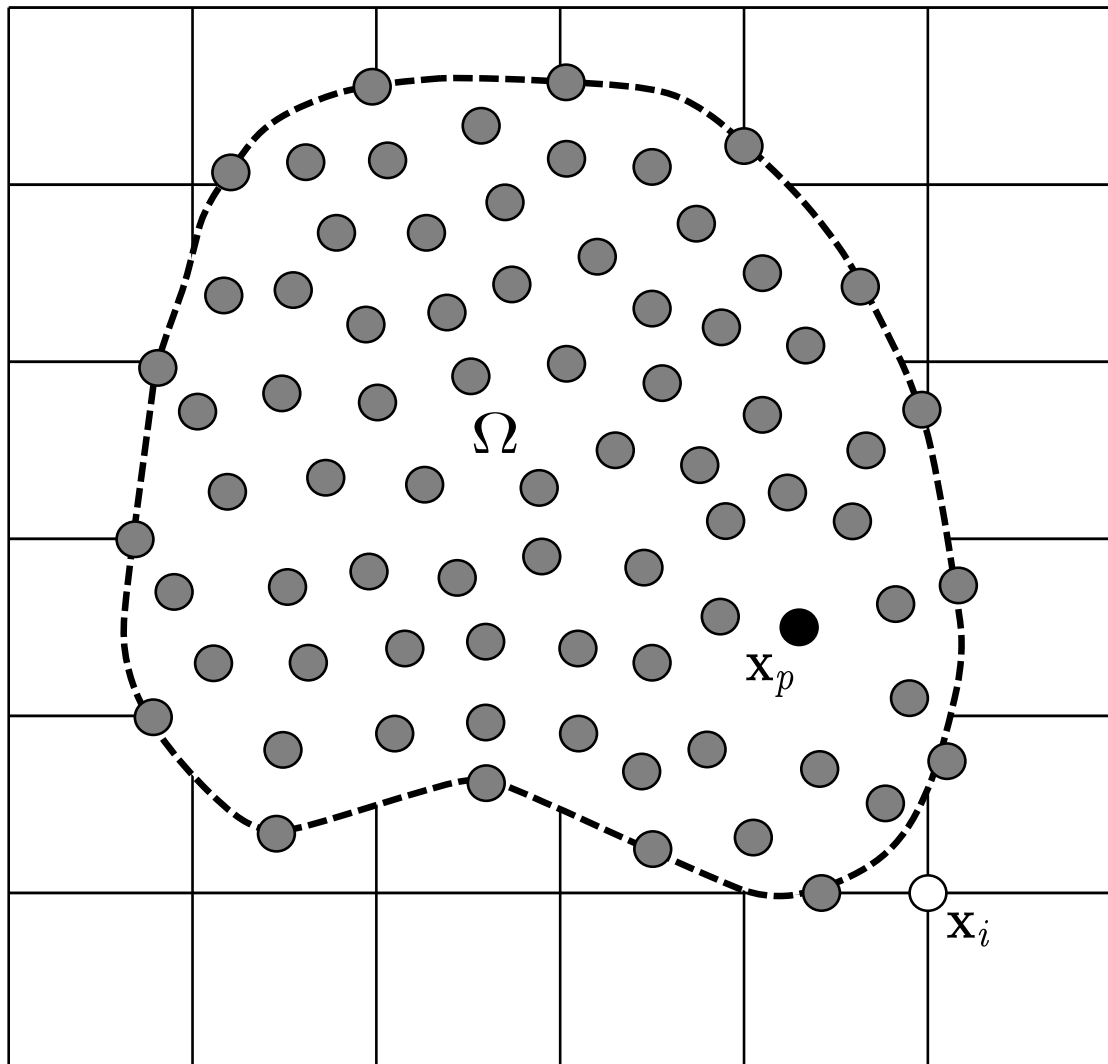


Figure 2.2 Typical discretization of a domain in MPM. The dotted line represents the boundary of the simulated object Ω and each closed point represents a material point used to discretize Ω . The square mesh represents the background grid. Each square in the background grid is a grid cell, and grid nodes are located at the corners of grid cells.

2.3.1 Discrete formulation of the governing equations

2

The governing differential equation for a continuum is derived from the conservation of mass and momentum.

3

4

$$\frac{\partial \rho}{\partial t} \rho \Delta \cdot v = 0 \quad (2.1) \quad 5$$

and

$$\rho a = \Delta \cdot \sigma + \rho b \quad (2.2) \quad 6$$

7

8

where $\rho(\mathbf{x}, t)$ is the mass density, $\mathbf{v}(\mathbf{x}, t)$ is the velocity, $\mathbf{a}(\mathbf{x}, t)$ is the acceleration, $\sigma(\mathbf{x}, t)$ is the Cauchy's stress tensor, and $\mathbf{b}(\mathbf{x}, t)$ is the body force. The vector \mathbf{x} represents the current position of any material point in the continuum, at time t . MPM discretizes the continuum body into finite number of material points N_p . Let \mathbf{x}_p^t ($p = 1, 2, \dots, N_p$) denote the current position of material point p at time t . Each material point, at any given time t , has an associated mass m_p^t , density ρ_p^t , velocity v_p^t , Cauchy stress tensor σ_p^t , strain ϵ_p^t , and other necessary internal state variables based on the adopted constitutive model. These material points provide a Lagrangian description of the continuum body, since material points have a fixed mass at all times, eq. 2.1 is satisfied. The data from the material points are mapped on to the nodes of the computational grid, where the discrete form of eq. 2.2 is described. The weak form of eq. 2.2 is obtained by multiplying eq. 2.2 with a test function $w(\mathbf{x}, t)$.

$$\int_{\Omega} \rho \mathbf{w} \cdot a d\Omega = - \int_{\Omega} \rho \sigma^s : \Delta w d\Omega + \int_{\partial\Omega_t} w \cdot \tau dS + \int_{\Omega} \rho w \cdot \mathbf{b} d\Omega \quad (2.3) \quad 20$$

21

where σ^s is the specific stress (i.e. stress divided by mass density, $\sigma^s = \sigma/\rho$), Ω is the current configuration of the continuum, τ is the traction. eq. 2.3 is obtained by applying the divergence theorem, similar to the standard procedure adopted in Finite Element Methods (Chen and Brannon, 2002; Sulsky et al., 1994, 1995). The differential volume and the surface elements are denoted by $d\Omega$ and dS , respectively.

22

23

24

25

26

As the whole continuum is discretized into a finite set of material points, the mass density can be written as:

27

28

$$\rho(\mathbf{x}, t) = \sum_{p=1}^{N_p} M_p \delta(x - x_p^t) \quad (2.4)$$

1

2

3 where δ is the Dirac delta function. Substituting [eq. 2.4](#) in [eq. 2.3](#), the sum of quantities of
4 material points can be evaluated as:

$$5 \quad \sum_{p=1}^{N_p} M_p [w(x_p^t, t) \cdot \mathbf{a}(x_p^t, t)] = \sum_{p=1}^{N_p} M_p [-\boldsymbol{\sigma}^s(x_p^t, t) : \Delta w|_{x_p^t} \\ 6 \quad + w(x_p^t, t) \cdot \boldsymbol{\tau}^s(x_p^t, t) h^{-1} + w(x_p^t, t) \cdot b(x_p^t, t)] \quad (2.5)$$

8 where h is the thickness of the boundary layer. It can be noted from [eq. 2.5](#) that the interactions
9 between different material points are reflected only through the gradient terms. In MPM, a
10 background computational mesh is used to calculate the gradient terms. The computational
11 mesh is constructed using 2-node cells for 1-D, 4-node cells for 2-D, and 8-node cells for
12 3-D problems. These elements are used to define the standard nodal basis functions, $N_i(\mathbf{x})$,
13 associated with the spatial nodes $x_i(t), i = 1, 2, \dots, N_n$, where N_n represents the total number of
14 mesh nodes. The nodal basis functions are assembled by using the conventional finite-element
15 shape functions ([Chen and Brannon, 2002](#)). The co-ordinates of any material point in a cell can
16 be represented by

$$17 \quad x_p^t = \sum_{i=1}^{N_n} x_i^t N_i(\mathbf{x}_p^t) \quad (2.6) \\ 18$$

19 Similarly the nodal displacements, velocity and acceleration of any material point in a cell are
20 represented using the basis functions. Thus, the test function has to be of the form:

$$21 \quad w_p^t = \sum_{i=1}^{N_n} w_i^t N_i(\mathbf{w}_p^t) \quad (2.7) \\ 22$$

23 [eq. 2.6](#) and [2.7](#) ensures that the associated vectors are continuous across the cell boundary.
24 However, the gradient of these functions are not continuous, due to the use of linear shape
25 functions. Substituting, [eq. 2.6](#) and [2.7](#) into [eq. 2.5](#), the weak form of the equation of motion
26 reduces to:

$$27 \quad \sum_{j=1}^{N_n} m_{ij}^t \mathbf{a}_j^t = \mathbf{f}_i^{int,t} + \mathbf{f}_i^{ext,t} \quad (2.8) \\ 28$$

29 where the nodal mass, m_{ij}^t is represented as:

$$30 \quad m_{ij}^t = \sum_{p=1}^{N_p} M_p N_i(x_p^t) N_j(x_p^t) \quad (2.9) \\ 31$$

The nodal internal force, $\mathbf{f}_i^{int,t}$ and the nodal external force, $\mathbf{f}_i^{ext,t}$ are defined as:

$$\mathbf{f}_i^{int,t} = - \sum_{p=1}^{N_p} M_p \mathbf{G}_{ip}^t \cdot \boldsymbol{\sigma}_p^{s,t} \quad 1$$

$$\mathbf{f}_i^{int,t} = - \sum_{p=1}^{N_p} M_p \mathbf{b}_p^t N_i(\mathbf{x}_p^t) + \sum_{p=1}^{N_p} M_p N_i(\mathbf{x}_p^t) \tau_p^{s,t} h^{-1} \quad 2 \\ 3 \\ 4 \quad (2.10)$$

where $\mathbf{G}_{ip}^k = \Delta N_i(x)|_{x=X_p^t}$. The nodal accelerations are obtained by explicit time integration of eq. 2.8. To obtain stable solutions, the time step used in the analysis should be less than the critical time step, which is defined as the ratio of the smallest cell size to the wave speed (Chen and Brannon, 2002). The boundary conditions are enforced on the cell nodes and the nodal velocities are obtained by solving the equation of motion at each node. The strain increment for each material point is determined using the gradients of the nodal basis functions. The corresponding stress increments are computed using the adopted constitutive law. After all the material points have been completely updated, the computational mesh is discarded, and a new mesh is defined for the next time step.

2.3.2 Boundary conditions

The Material Point Method uses standard shape functions, similar to those used in the Finite Element Methods, hence the essential and the natural boundary conditions can be applied to the background grid nodes in the same way as in the traditional FEM. The free surface boundary conditions are satisfied, as MPM is formulated in the weak form. Implementation of traction boundary conditions requires a set of material points to represent the boundary layer. ? proposed a friction interaction for the planar boundary condition, using Coulomb's friction criterion. The nodal accelerations were considered to include the frictional effects instead of the forces, as the forces are proportional to the corresponding accelerations. The static and kinematic frictions are applied tangential to the nodal boundary. Friction forces are applied, only if the particles are in contact. The normal velocity and acceleration on the boundary plane is zero. The shape functions used in the MPM are continuous, and hence penetration between bodies are handled automatically without the need for any supplemental contact algorithm (Chen and Brannon, 2002). In the MPM, the continuum body deforms and moves in an arbitrary computation grid and all the boundary conditions are carried by the boundary particles. If a boundary particle is present in a cell, then the cell boundary becomes a part of the continuum body, and the cell size represents the thickness of the boundary. However, in certain cases both the boundary particle and an interior particle can be found in a cell, in

which case the cell is still treated as a boundary cell, and the interior particle temporarily acts as a boundary particle. To avoid numerical errors, it is essential to consider smaller cell size along the boundary ([Chen and Brannon, 2002](#)).

In the MPM simulations, numerical noises are observed when the material points crosses the cell boundaries during deformation of the material, this is termed as cell crossing noise. If a material point is located very close to the cell boundary, it results in discontinuous nature of the gradient of the weighing function causing a force imbalance on the grid ([Bardenhagen and Kober, 2004](#)). This results in large non-physical acceleration values resulting in separation of material points from the continuum ([Sulsky et al., 1995](#)). figure 2.3 illustrates the problem of cell crossing noise. The main reason for the occurrence of cell crossing noise is the use of piecewise linear shape functions. However, this problem, which is predominant when using fine mesh size, can be overcome by changing the order of arithmetic operation as proposed by [Sulsky et al. \(1995\)](#). To overcome the problem of cell crossing noise, [Bardenhagen and Kober \(2004\)](#) proposed an alternate method called the Generalized Interpolation Material Point Method that uses smoother shape functions and a larger influence region for each grid node. This approach minimizes the cell crossing noise. However, special attention is required to simulate the boundaries in the Generalized Interpolation Material Point Method (GIMP).

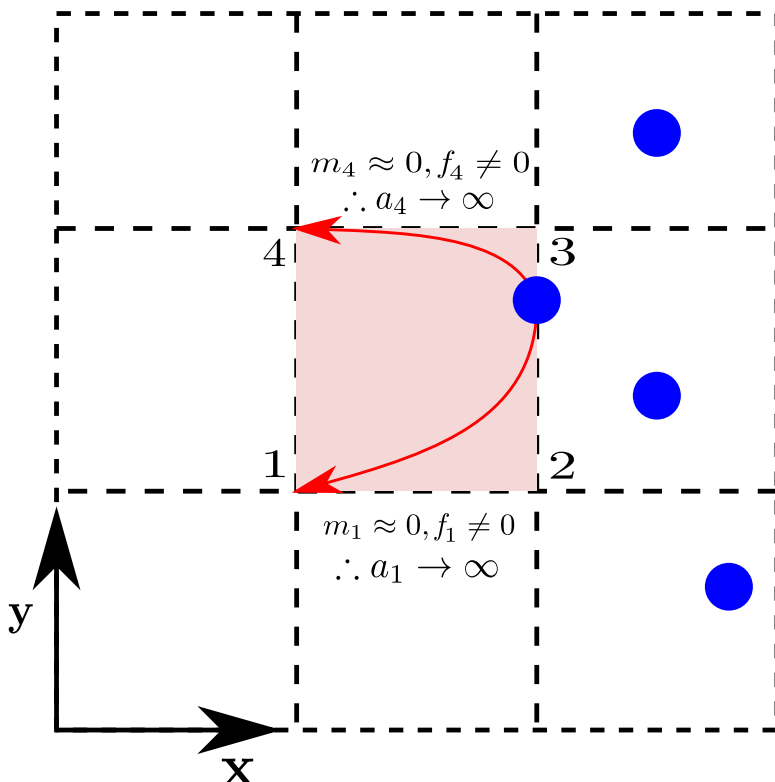


Figure 2.3 Cell crossing noise

2.3.3 Solution scheme

A step-by-step solution scheme for Material Point Method (?) is described below. It involves three stages: preprocessing, computation, and post-processing:

Preprocessing

- A continuum body is discretized into a finite set of material points corresponding to the original configuration of the body. The number of material points corresponds to the resolution of the mesh size adopted in Finite Element Method. The material points are followed throughout the deformation of the material, which gives a Lagrangian description of the motion.
- An arbitrary computational grid is initialized to describe the natural coordinates of the material points. For the purpose of simplicity, a Cartesian grid is usually adopted.
- The state variables (mass/density, velocity, strain, stress, other material parameter corresponding to the adopted constitutive relation) are initialized at every material point.

Computation scheme

- For each material point, the mapping of the properties from the particles to the cell nodes is accomplished using the shape functions computed from the particle position. The nodal mass matrix is obtained as:

$$m_i^k = \sum_{p=1}^{N_p} M_p N_{ip}^k \quad (2.11)$$

where m_i^t is the mass at node i at time t , M_p the particle mass, N_i the shape function associated with node i , and x_p^t the location of the particle at t .

- The nodal velocity is obtained by mapping the particle velocity to the nodes using the shape functions:

$$v_i^k = \sum_{p=1}^{N_p} m_p v_p^t N_{ip}^t / m_i^t \quad (2.12)$$

- Strain increment $\Delta\epsilon_p^{t+1}$ for particle is then computed as:

$$\Delta\epsilon_p^{t+1} = \frac{\Delta t}{2} \sum_{i=1}^{N_n} \mathbf{G}_{ip}^t \mathbf{v}_i^t + (\mathbf{G}_{ip}^t \mathbf{v}_i^t)^T \quad (2.13) \quad \begin{matrix} 9 \\ 10 \end{matrix}$$

- The stress increment for the particle $\Delta\sigma_p^{t+1}$ is computed from the strain increment using the constitutive model adopted in the simulation

$$\Delta\sigma_p^{t+1} = \mathbf{D} : \Delta\epsilon_p^{t+1} \quad (2.14) \quad \begin{matrix} 13 \\ 14 \end{matrix}$$

- The stress and the strain of the material points are updated based on:

$$\begin{aligned} \sigma_p^{t+1} &= \sigma_p^t + \Delta\sigma_p^{t+1} \\ \epsilon_p^{t+1} &= \epsilon_p^t + \Delta\epsilon_p^{t+1} \end{aligned} \quad (2.15) \quad \begin{matrix} 16 \\ 17 \\ 18 \end{matrix}$$

- The material point density is then updated as:

$$\rho_p^{t+1} = \frac{\rho_p^t}{\{1 + \text{tr}(\Delta\epsilon_p^{t+1})\}} \quad (2.16) \quad \begin{matrix} 20 \\ 21 \end{matrix}$$

- Then the nodal acceleration is computed using the equation of motion as:

$$\mathbf{a}_i^t = (\mathbf{f}_i^{int,t} + \mathbf{f}_i^{ext,t}) / m_i^t \quad (2.17) \quad \begin{matrix} 23 \\ 24 \end{matrix}$$

- The nodal velocity is obtained from the computed nodal acceleration as:

$$v_i^L = \mathbf{v}_i^k + a_i^k \Delta t \quad (2.18) \quad \begin{matrix} 26 \\ 27 \end{matrix}$$

- Finally, the particle position and its velocity are updated according to:

$$\begin{aligned} \mathbf{x}_p^{t+1} &= \mathbf{x}_p^t + \Delta t \sum_{i=1}^{N_n} v_i^L N_{ip}^t \\ \mathbf{v}_p^{t+1} &= \mathbf{v}_p^t + \Delta t \sum_{i=1}^{N_n} a_i^t N_{ip}^t \end{aligned} \quad (2.19) \quad \begin{matrix} 29 \\ 30 \\ 31 \end{matrix}$$

- At the end of every time step, all the variables on the grid nodes are initialized to zero.

figure 2.4 illustrates the steps involved in a MPM analysis.

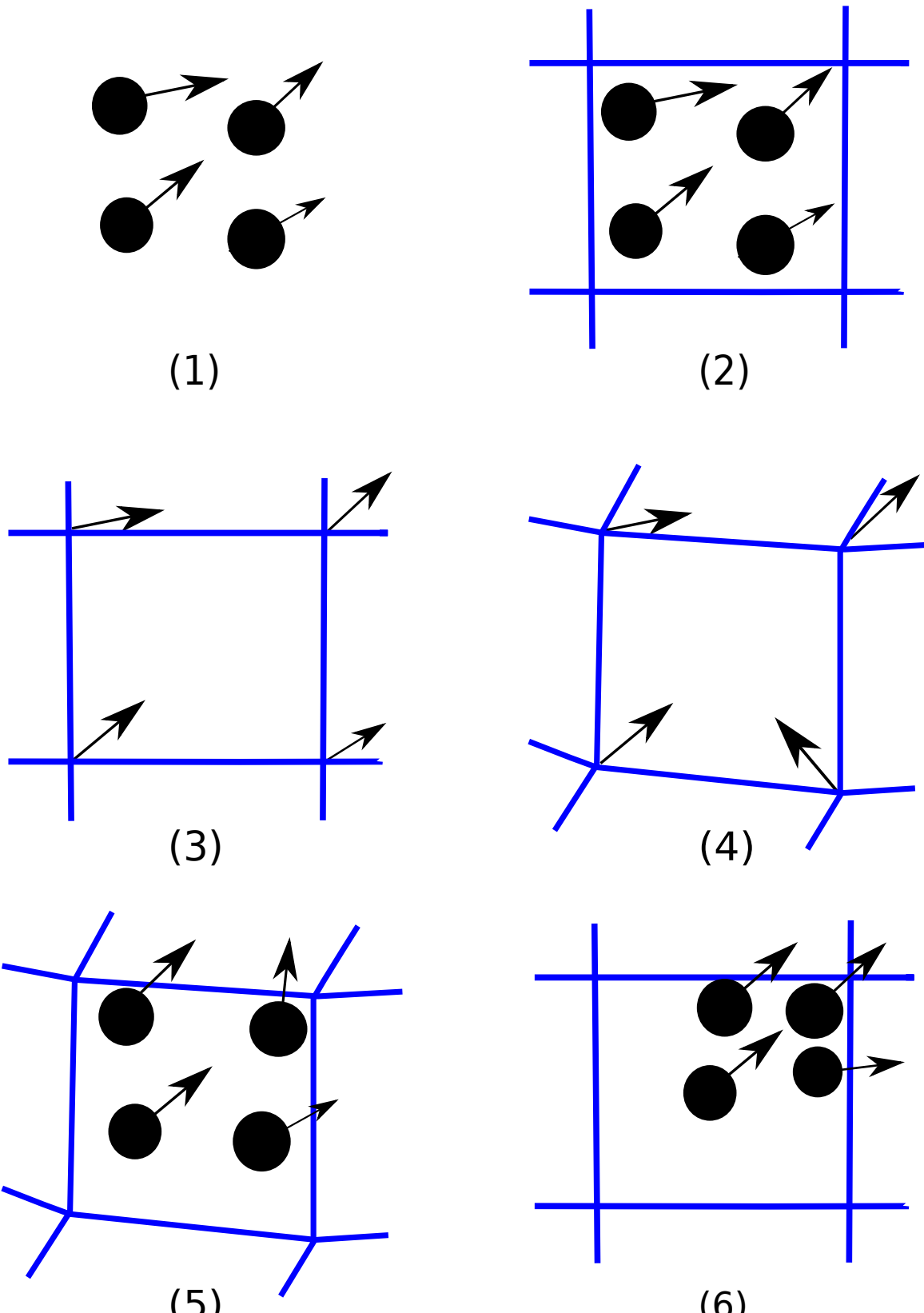


Figure 2.4 Illustration of the steps in the MPM algorithm for particles occupying a single cell in the background grid. (1). A representation of four material points (filled circles), overlaid with the computational grid (solid lines). Arrows represent displacement vectors. (2). The material point state vector (mass, volume, velocity, etc.) is projected to the nodes of the computational grid. (3). The discrete form of the equations of motion is solved on the computational grid, resulting in updated nodal velocities and positions. (4). The updated nodal kinematics are interpolated back to the material points and their state updated. (5). The computational grid is reset to its original configuration and the process repeated. Reproduced after [Bigler et al. \(2006\)](#)

Post processing

34

The final step in any analysis is post-processing. It involves visualization and extraction of the data from the analysis. In mesh-less methods, like the Material Point Method, structures are generally represented as points which represent a discrete region of the body. The MPM facilitates representation of arbitrarily complex geometries and is robust in computing large deformation problems. It has advantages over strictly grid based methods in simulations involving contact between multiple objects (Bardenhagen et al., 2000). The MPM poses a whole new set of visualization problem, it is essential to visualize the general configuration of the body as well as to observe the finer details like development of cracks or separation of chunk of material from the body. The body is discretized into conceptual material points, which carry all the relevant information of the corresponding segment. The unique qualities of the MPM necessitate the need to visualize the particle data in a way that is informative and appropriate. In the MPM, the particle data represents the finite portion of a larger continuum, and the ability to see and interpret the macroscopic structure created by these particles is vital (Bigler et al., 2006). There are two vital aspects in visualizing the MPM data: (1) visualization of the structure represented by material points, and (2) understanding the qualitative trend associated with the material points like mass, velocity or stress. The MPM output data contains both the material point and the grid data, one approach in visualizing the MPM data is by rendering the interpolated particle values on grid nodes using *iso-surfacing* (Lorensen and Cline, 1987) or *volume rendering* (Levoy, 1988) technique. In regions where the material points are sparse, it is necessary that the grid resolution to be sufficiently fine to compensate for the missing features. This results in storing large amount of unnecessary data in regions where sufficient material points are present. Thus, it is advantageous to visualize the MPM data of the material points as particles (Bigler et al., 2006). Particle visualization involves rendering the particles as a sphere or an ellipsoid representing the size and location of the fraction of the continuum (Gumhold, 2003; Krogh et al., 1997; Kuester et al., 2001). Colour mapping of scalar quantities such as mass, velocity, or stress of a material point provide additional qualitative understanding of data.

- ¹ The accuracy of the MPM simulations largely depends on the number of material points
² representing the continuum. The MPM utilizes a grid to compute the deformation of the
³ continuum, hence the size of the cells affects the accuracy of the results. Generally in the MPM,
⁴ the number of particles per cell controls the accuracy of the simulation. Guilkey et al. (2003)
⁵ recommends higher particle density, such as 4 particles per cell, for large deformation problems.
⁶ Very low particle density will result in non-physical opening of cracks in large deformation
⁷ simulations and can be a source for the cell crossing noise. However, higher value of particle
⁸ density affects the computation time.

Draft - v1.0

Wednesday 17th September, 2014 – 02:00

9 Chapter 3

10 Particulate modelling of granular flows

11 3.1 Introduction

12 Granular materials often exhibit different behaviour under different circumstances. Fluidized
13 granular material often resembles a liquid, and reveals surface waves. In certain situations,
14 granular materials behave more like a solid exhibiting plastic deformations. Despite the
15 wide variations in the physical and chemical properties of the grains, the discrete granular
16 structure has a rich generic phenomenology, which motivates us to understand the fundamental
17 behaviour of these materials. A granular material can be considered as a continuous material
18 if it is viewed at a macroscopic scale, ignoring the fact that it is composed of grains. On a
19 macroscopic scale, the behaviour of the granular material could be approximately defined using
20 continuum mechanics. However, On a particle level, the granular materials exhibit complex
21 solid-like and/or fluid like behaviour depending on the way the grains interact with each other.
22 The Analytical and Finite Element models, which consider granular materials as continuum
23 cannot take into account the local geometrical processes that govern the mechanical behaviour
24 of a non-homogeneous soil. The application of continuum models to describe granular flow
25 poses subtle problems for statistical analysis ([Mehta and Barker, 1994](#)). The particle level
26 description of the granular material enriches the macro-scale variables which poorly account
27 for the local rheology of the materials. Numerical models based on the Discrete Element
28 approach proposed by ? are capable of simulating the granular material as a discontinuous
29 system. Although, modern measurement techniques can probe into the local granular variables,
30 like particle position, velocities, contact forces, etc., they have inherent limitations in acquiring
31 those variables. The *discrete-element* approach is a powerful and reliable research tool to study
32 the behaviour granular materials at the grain-scale. This approach involves applying Newton's
33 equation of motion simultaneously to all particles described as rigid solid bodies by considering
34 the contact forces and the external forces acting on the particles. For a given boundary condition,

the collective mechanical response of particles to the external force leads to the relative motion between particles constrained in a dense state and/or by in-elastic collisions in the loose state. ? applied this method to granular geomaterials, and called it the *Distinct Element Method*, to differentiate from the existing *Finite Element method* used in geomechanics. The attribute “distinct” refers to the degrees of freedom of individual particles, but it was later replaced by “discrete” to underline the discrete nature of the system. A similar method called *Discrete Element Method* (DEM) was used at the same time for the simulation of molecular systems with classical schemes that could be directly applied to granular materials. Hence, the acronyms DEM and DEM are used synonymously to describe the methods of simulating granular materials at particle scale. In-spite of the formal analogy (particles and force laws) between granular and molecular systems, the physics is fundamentally different. The interactions between individual grains are governed by unilateral contact laws, and the mechanism of energy dissipation is through friction and inelastic collisions. Moreover, granular materials have a wide variation in their particle shape and size distribution that require appropriate numerical treatments. In the Molecular Dynamics approach, the normal reaction force, which prevents the interpenetration of two grains is proportional to the depth of penetration. Thus, frictional contact between grains can be expressed as a function of the configuration variables, which describe the positions and velocities of the grains ([Radjai and Dubois, 2011](#)). Discrete-Element methods, which describe interactions between grains based on the explicit overlap between the grains are termed as *smooth methods*. Another approach is the *non-smooth approach* ([Jean, 1999](#)), which describes the behaviour of discrete elements using the main features of uni-laterality and Coulomb friction, and by neglecting the finer details such as interpenetration and overlap between grains. The fundamental difference between the non-smooth method and the common DEM or Discrete Element Method (DEM) approach lies in the treatment of small length and time scales involved in the dynamics of granular media. In DEM-type DEM, the particles are treated as rigid bodies but the contacts between particles are assumed to obey the visco-elastic constitutive law. The time-stepping schemes used for the numerical integration of the equations of motion in Discrete Element Method, imply that the contact interactions involve smaller time and length scales. In the CD method, these small scales are neglected and their effects are absorbed into the contact laws. In non-smooth formulation, the particle dynamics is described at a larger scale than the elastic response time and displacement scales ([Jean, 1999; Radjai and Richefeu, 2009](#)).

3.2 Discrete Element Method

- ³ Discrete Element Method computes the equilibrium and the trajectories of a classical multi-body system. The Discrete Element Method is a simple and flexible discrete-element approach, which

5 involves applying Newton's second law of motion to each grain to describe the deformation of
6 the granular assembly.

7

$$m_i \frac{d^2 x_i}{dt^2} = \mathbf{F}_i, (i = 1, \dots, N) \quad (3.1)$$

8 where N is the number of grains in the simulation, m_i is the mass of grain i , x_i is its position, and
9 \mathbf{F}_i is the force exerted on grain. The method consists of calculating the forces \mathbf{F}_i and then solving
10 the ordinary differential in [eq. 3.1](#). In general the system of coupled non-linear differential
11 equations cannot be solved analytically. The approximate numerical solution of these equations,
12 which describes the trajectories of all the particles of the system is called as Discrete Element
13 Method. The idea of Discrete Element Method goes back to Alder and Wainwright who in
14 1957 investigated the physics of hard sphere gases. The name implies that it was first applied to
15 molecular scale problems before being applied to granular materials by [?](#). Discrete Element
16 Method simulations are identical to the real experiments, this involve generation of samples
17 (initial conditions) with N particles and solving the Newton's equation of motion for the system
18 until the properties of the system no longer change with time (equilibration of the system).
19 After equilibration, the actual analysis is performed.

20 The computation of the forces and torques is the central part of the Discrete Element
21 Method simulation. The dynamics of the granular material is governed by Newton's equation of
22 motion which depends on the centre-of-mass coordinates and the Euler angles of the particles i
23 ($i=1, \dots, N$):

24

$$\frac{\partial^2 \vec{r}_i}{\partial t^2} = \frac{1}{m_i} \vec{\mathbf{F}}_i(\vec{r}_j, \vec{v}_j, \vec{\varphi}_j, \vec{\omega}_j)$$

25

$$\frac{\partial^2 \vec{\varphi}_i}{\partial t^2} = \frac{1}{\hat{J}_i} \vec{\mathbf{M}}_i(\vec{r}_j, \vec{v}_j, \vec{\varphi}_j, \vec{\omega}_j), (j = 1, \dots, N)$$

26

27 The force $\vec{\mathbf{F}}_i$ and the torque $\vec{\mathbf{M}}_i$, which act on particle i of mass m_i and the tensorial moment
28 of inertia \hat{J}_i are (sometimes complicated) functions of the particle positions \vec{r}_j , their angular
29 orientations $\vec{\varphi}_j$, and their corresponding velocities \vec{v}_j and $\vec{\omega}_j$. In a two-dimensional system,
30 the angular orientation of a particle is described by a single (scalar) quantity φ_i and the moment
of inertia reduces to a scalar value J_i . The Newton's equation of motion can be written as:

2

$$\frac{\partial^2 \vec{r}_i}{\partial t^2} = \frac{1}{m_i} \vec{\mathbf{F}}_i(\vec{r}_j, \vec{v}_j, \vec{\varphi}_j, \vec{\omega}_j)$$

3

$$\frac{\partial^2 \vec{\varphi}_i}{\partial t^2} = \frac{1}{\hat{J}_i} \vec{\mathbf{M}}_i(\vec{r}_j, \vec{v}_j, \vec{\varphi}_j, \vec{\omega}_j), (j = 1, \dots, N)$$

4

For granular particles in the absence of long range fields, the force $\vec{\mathbf{F}}_i$ and the torque $\vec{\mathbf{M}}_i$ acting upon the particle i are given as sum of the pairwise interaction of particle ‘ i ’ with all other particles of the system:

$$\vec{\mathbf{F}}_i = \sum_{j=1, j \neq i}^N \vec{\mathbf{F}}_{ij}, \quad \vec{\mathbf{M}}_i = \sum_{j=1, j \neq i}^N \vec{\mathbf{M}}_{ij} \quad (3.2)$$

The limitation to pairwise interaction is an abstraction, which is justified if the particles deformation at the contact is trivial. To describe the deformation of granular assemblies one has to take into account the effect of multi-particle interactions. This method is general and can be applied to a wide range of systems. The Discrete Element Method can be used to study the behaviour of grains in rapid flows to static assemblies. The method treats both the conditions in exactly the same way, it is not necessary to divide the system and then treat each condition differently. The simplest model for granular particle is a sphere. In a two-dimensions case, the sphere is reduced to a circular disk. Simulations using spherical particles are numerically very effective since particle collisions can be easily identified and described in a simple way (?).

3.2.1 The Forces

- 2 The force \mathbf{F}_i in eq. 3.1 represents both the grain to grain interaction force, and other external
- 3 forces acting on the system. Therefore, the force \mathbf{F}_i is expressed as:

$$\mathbf{F}_i = \sum_{j \neq 1} \mathbf{F}_{ij} + \mathbf{F}_{ext,i} \quad (3.3)$$

6 where \mathbf{F}_i is the force exerted by grain j on i . The external force $\mathbf{F}_{ext,i}$ is most often the force
7 of gravity, $\mathbf{F}_{ext,i} = m_i \mathbf{g}_i$. The methodology to incorporate any other external forces in the
8 simulation is the same. However, the computation of the interaction forces depends on the
9 numerical method adopted in the study. The methodology used in the present study is described
10 below.

11 Let us consider two grains i and j , in contact (see figure 3.1). The contact force can be
12 decomposed into two components, as the normal (F_n) and the tangential (F_t) components:

$$\mathbf{F}_{ij} = F_n \mathbf{n} + F_t \mathbf{t} \quad (3.4)$$

15 where \mathbf{n} and \mathbf{t} are unit vectors, pointing in the normal and the tangential directions. The
16 procedure adopted to calculate the normal and tangential forces are discussed.

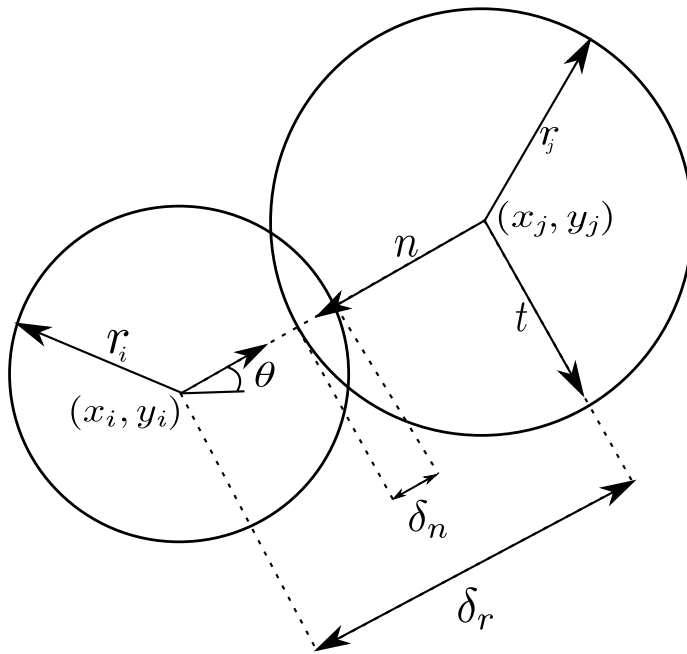


Figure 3.1 Grains i and j in contact, and the separation δ_n is used to calculate the normal force

¹⁷ Normal force

¹⁸ When granular particles collide, part of the kinetic energy is dissipated as heat and the other
¹⁹ part causes deformation of the particle. These deformations generate interaction forces. The
²⁰ grains are considered to be rigid while their contact is assumed to be soft. Thus, the grains do
²¹ not change their shape, instead they overlap. The shapes of the particles are conserved on an
²² average, after many collisions. The overlap at the contact is limited to very small deformations,
²³ which are achieved by defining a repulsive normal force that opposes the overlap. The mutual
²⁴ compression (δ_n) of the particles i and j is defined as:

²⁵

$$\delta_n = |x_i - x_j| - r_i - r_j \quad (3.5)$$

²⁷ where x_i and x_j are the centres of the grains and r_i and r_j are their radii (see Figure 3.1). When
²⁸ $\delta_n > 0$, the two grains are not in contact, and there is no interaction. When $\delta_n < 0$, the two
²⁹ grains overlap, and there is a repulsive normal force that pushes the two grains apart. The
 1 simplest model is to consider the contact as a linear spring with damping. The repulsive force
 2 depends linearly on δ_n , and is controlled by the stiffness of the grain. The energy dissipation
 3 due to the interaction between grains is an intrinsic characteristic of the granular material and
 4 is incorporated by adding a damping force that opposes the relative velocity for the duration of
 5 the contact. The interaction force at the contact is idealized as a simple spring-dashpot system,

with elastic and dissipative constants ([Luding et al., 1994](#)).

$$F_n = \begin{cases} 0, & \delta_n > 0 \\ -k_n \delta_n - \gamma_n \frac{d\delta_n}{dt}, & \delta_n < 0 \end{cases} \quad (3.6)$$

The constant k_n characterises the stiffness of the grain, and must be chosen sufficiently large so that the overlap between the grains remain small. Nevertheless, the solution has an undesirable property of generating an attractive force (?). It arises just before the two particles separate. In this case, we have $d\delta_n/dt > 0$ while δ_n approaches zero. To avoid the attractive force, the force is computed in two stages: a candidate force \hat{F}_n is calculated, and verified whether it is non-negative:

$$\hat{F}_n = -k_n \delta_n - \gamma_n \frac{d\delta_n}{dt}, \quad F_n = \begin{cases} 0, & \hat{F} \leq 0 \\ \hat{F}_n, & \hat{F} > 0 \end{cases} \quad (3.7)$$

For pairwise collisions, the normal force (F_n) represented as $k_n \delta_n + \gamma_n$ causes a decrease in the relative normal velocity of the particles by a factor ε . This factor is the *coefficient of restitution*, and is defined as $\varepsilon \approx g'/g$, where g is the absolute normal relative velocity before the collision and g' corresponds to the post-collision value. The relative velocity, $d\delta_n/dt > 0$, can be obtained by differentiating [eq. 3.5](#). Thus we obtain:

$$\frac{d\delta_n}{dt} = (\mathbf{v}_i - \mathbf{v}_j) \cdot \mathbf{n} \quad (3.8)$$

where $\mathbf{v}_i = dx_i/dt$ is the velocity of grain i and $\mathbf{v}_j = dx_j/dt$ is the velocity of grain j . The numerical integration of [eq. 3.8](#) yields the separation δ_n and permits us to generalise the model and treat the tangential forces as well, as explained in the next section. By integrating Newton's equation of motion it is found that the linear force corresponds to the co-efficient of restitution, which is defined as:

$$\varepsilon = \exp\left(-\frac{\pi \gamma_n}{2m^{eff}} / \sqrt{\frac{Y}{m^{eff}} - \frac{\gamma^2}{2m^{eff}}}\right) \quad (3.9)$$

Tangential force

Granular particles are not perfect spheres, but have a complicated surface texture, therefore at oblique collisions, besides the normal force there is a tangential force too. Even perfectly smooth spheres exert a tangential force due to their bulk viscosity (?). To build a heap of spheres on a flat surface, the particles as well as the surface has to be sufficiently rough, indicating

the dependence of the tangential force on the surface properties of the granular materials. For realistic simulation of granular materials, it is important to consider the tangential force in Discrete Element Method. The tangential force is considered in a similar fashion as the normal force, arising from a spring stretched by the relative motion of the grain. Tangential forces are modelled by considering the relevant relative tangential velocity of the particle surfaces at the point of contact. The point of contact is an approximation, as the description of the normal force assumes a compression δ_n , which implies a contact surface in 3-D or a contact line in 2-D. Assuming a tangential spring of length δ_t exerts an opposing force to the relative tangential displacements (ignoring the effect of relative rolling between the particles), the tangential force can be postulated similar to the normal force (eq. 3.8) as:

$$\frac{d\delta_t}{dt} = (\mathbf{v}_i - \mathbf{v}_i) \cdot \mathbf{t} \quad (3.10)$$

This equation must also be numerically integrated, just like eq. 3.1. The grains are in contact when $\delta_t < 0$, and when $\delta_t = 0$, the grains no longer exert a force on each other. With these assumptions, δ_t can be calculated similar to the normal force. The tangential force is assumed to be governed by Coulomb's friction law.

$$|F_t| \leq \mu F_n \quad (3.11)$$

where F_t is the tangential force and μ is the friction coefficient. It is therefore necessary to constrain the tangential force to remain less than or equal to μF_n . To impose the condition in eq. 3.11, two-stages similar to the normal force computation is adopted. The first step is to evaluate the candidate force, and is then accepted if it obeys the condition in eq. 3.11.

$$\hat{F}_t = -k_t \delta_t - \gamma \frac{d\delta_t}{dt}, \quad F_t = \begin{cases} sgn(F_t), & |\hat{F}| \geq \mu F_n \\ \hat{F}_t, & |\hat{F}| < \mu F_n \end{cases} \quad (3.12)$$

where k_t is the stiffness of the tangential spring and γ is the damping constant. If $|F_t| = \mu F_n$, the contact is sliding, otherwise, it is non-sliding. It can be noted that the normal force (eq. 3.7) and the tangential force (eq. 3.12) are handled in the same way in Discrete Element Method. When the grains slide against each other, they do not retain any memory of their initial position, and hence do not return to its original position. In order to model this behaviour, a limiting value of δ_t is imposed. When the contact slides $\delta_t = \pm \mu F_n / k_t$ is imposed.

In addition to sliding, the grains can roll relative to one another about their centre of mass due to the tangential force acting at their contact surface. In this case, $d\delta_t/dt = 0$. It is important to assume that the grains touch at a single point instead of overlapping, i.e. $\delta_n = 0$. This point

is located at $x_i - r_i \mathbf{n} = x_j + r_j \mathbf{n}$. If we consider that this point belongs to grain i , its velocity is $v_i + r_i(\boldsymbol{\omega} \times \mathbf{n})$. If it belongs to grain j , its velocity is $v_j + r_j(\boldsymbol{\omega} \times \mathbf{n})$. The relative velocity is the difference between these two velocities.

$$\frac{d\delta_t}{dt} = (\mathbf{v}_i - \mathbf{v}_j) \cdot \mathbf{t} - (r_i \boldsymbol{\omega}_i + r_j \boldsymbol{\omega}_j) \times \mathbf{n} \quad (3.13)$$

It should be noted that the eq. 3.13 is only an approximation, as the grains in Molecular Dynamics do not touch at points, but overlap. It is therefore an approximation that produces an error of order $O(\delta_n/r)$ (Radjai and Dubois, 2011). It is assumed that the contact forces are exerted at the point of contact. It implies that the tangential force is accompanied by torque acting on two grains. If the overlap is zero, these torques are:

$$\tau_{ij} = -(a_i \mathbf{n}) \times (F_t \mathbf{t}), \tau_{ji} = -(a_j \mathbf{n}) \times (F_t \mathbf{t}), \quad (3.14)$$

The torques modify the angular velocities of the grains. It is therefore necessary to incorporate the equation for the angular coordinates of the grains in eq. 3.1:

$$I_j \frac{d\boldsymbol{\omega}_i}{dt} = \sum_{j \neq i} \tau_{ij} \quad (3.15)$$

where I_j is the moment of inertia of grain j . The eq. 3.14 is only valid when $\delta_n = 0$. The torque is a vector product of the force and its lever arm. It is assumed that the lever arms have lengths equal to r_i and r_j , which is true only when the grains do not overlap, hence in this case they produce an error of order $O(\delta_n/r)$. It is nevertheless desirable to damp this type of motion (Radjai and Dubois, 2011). The interaction between two solid bodies is much more complex than that is described by the simple linear model. Nevertheless, the linear force law has several advantages. It is simple to implement, and its harmonic behaviour is well understood, which makes it easier to interpret the results. The most common non-linear interaction law is the Hertz law (Hertz, 1882). In certain situations, such as a quasi-static packing, a non-linear law can have significant influence on the acoustic properties (?), and on the global stiffness (?). However, in case of rapid granular flows, the interaction force between the particles has almost no effect on the phenomenon, and a linear law can be used to describe this kind of behaviour (Radjai and Dubois, 2011).

3.2.2 Numerical algorithm and integration scheme

The efficiency of a Discrete Element Method program is mainly determined by its efficiency to compute the interaction forces between particles. If we consider a model system with

pairwise interactions, we have to consider the contribution of the force on particle i due to all its neighbours. If we consider only the interaction between a particle and the nearest image of another particle, then for a system of N particles, we must evaluate $N \times (N - 1)/2$ pair distances. Consider a system of 1000 particles, at every time step all possible pairs of particles have to be considered to compute the interaction forces, hence, $N(N - 1)/2 \approx 500,000$ force computations are required. For short-range particle interactions, the majority of these force evaluations is unnecessary as the corresponding particles are located far apart and do not necessarily touch each other. For a dense system of equally sized particles, the particles can have contacts with not more than 6 particles, this reduces the number of force computation required to $3N \approx 3000$. In the preliminary force computation scheme, at least 166 times more pair interactions are considered than necessary. Therefore, the numerical methods employed in the Discrete Element Method program should try to minimize the computation of interaction forces (?). There are three different methods for the efficient computation of the forces, the *Verlet* algorithm, the *link-cell* algorithm, and a *lattice* algorithm. The *Verlet* algorithm described in Grubmuller et al. (1991) is implemented in the present study.

2
3
4
5
6
7
8
9
10
11
12
13
14
15
16

Verlet list algorithm

The Verlet list algorithm assumes a cut-off value, so that only neighbouring particles that contribute to the energy of a particle i are considered. It is advantageous to exclude the particles that do not interact in the memory expensive energy computation. Verlet (1967) developed a book-keeping technique, commonly referred to as the Verlet list or neighbour list, which is illustrated in 3.2. In this method a second cut-off radius $r_v > r_c$ is introduced, and before we calculate the interactions, a list is made (the Verlet list) of all particles within a radius r_v of the particle i . In the subsequent calculations of the interactions, only those particles in this list will be considered. The idea of the Verlet algorithm is based on a simple property of particle dynamics: neighbourhood relation between particles can only change slowly, i.e. two particles which are close to each other at a given time step will remain as neighbours, at least in the following few time steps. During initialization the neighbourhood relations between the particles, i.e. the distance of all close pairs of particles are computed. Two particles are considered as neighbours if the distance of their surface is smaller than a predefined distance *Verlet distance*:

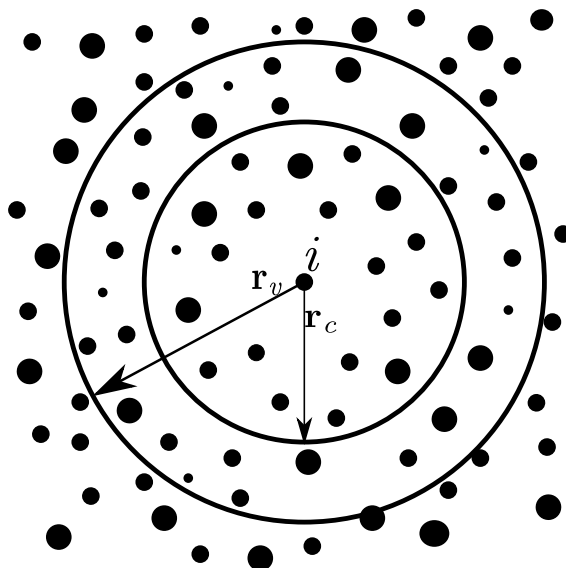


Figure 3.2 The Verlet list: a particle i interacts with those particles with the cut-off radius r_c , the Verlet list contains all the particles within a sphere with radius $r_v > r_c$

$$(|\vec{r}_i - \vec{r}_j| - R_i - R_j) < \text{Verlet distance} \quad (3.16)$$

For each particle there is a *Verlet list* in which the close neighbours are saved. To initialise the Verlet lists efficiently, a grid that covers the simulation area is defined. Its mesh size is larger than the largest particle. For construction of the lists only pairs whose particles reside in the same or adjacent grids are considered. This procedure guarantees the detection of all close pairs

of particles (?). Redundancy in Verlet lists, i.e. if particle i is a neighbour of j , then particle j is a neighbour of i , are avoided by imposing a restriction on the list of particle i contains, such that it contains only neighbours with index $j < i$. For the computation of interaction forces, the Verlet list of particle i is scanned and only pairs which are recorded in one of the Verlet lists are considered. Hence, the Verlet list of each particle i is scanned and the interaction force of i with each entry j in its list is computed. Initially to build the Verlet list, the particles are sorted into a grid of mesh size $dx \times dy$. For each grid there is a list of particles residing in the cell. During the simulation, the neighbourhood relation among the particles change, therefore, the Verlet lists have to be updated. The decision to update a Verlet list depends on how far the particles have travelled since the time when the present list was built. The Verlet list of a particle i must contain at any time all neighbours j with $j < i$. This assures that two particles i and j never touch and are not considered as neighbours, i.e. j is not in the list of i and i is not in the list of j . Hence,

$$|\vec{r}_i - \vec{r}_j| - R_i - R_j > 0 \quad (3.17)$$

The above condition is required for all pairs (i,j) of particles which are *not* known as neighbours. This condition is a criterion to update the Verlet lists (?). Assume at the instant when the Verlet lists are constructed, the surfaces of the particles have the distance $|\vec{r}_i - \vec{r}_j| - R_i - R_j >$ Verlet distance, i.e. they are not classified as neighbours. If the Verlet lists are updated before one of these particles has travelled the distance *verletdistance*/2 since the lists were constructed, they can never collide without being recognized as neighbours first. This is explained in figure 3.3. The impact of optimisation of the Verlet list algorithm has negligible effect on the computation time, as the algorithm is quite efficient already and only consumes a few percent of the total computation time in construction of the Verlet lists. The implementation of the Verlet list algorithm in force computation drastically reduces the computation time in comparison to the linear algorithm. The performance of the Verlet list algorithm is controlled by two crucial parameters: the number of cells N_c , for the construction of the Verlet lists and the Verlet distance r_v (?).

Leap frog or Verlet integration algorithm

Discrete Element Method involves numerically solving Newton's equation of motion eq. 3.1, which is an ordinary differential equation. Choosing an integration algorithm is important, as the forces are not always differentiable in time, and the temporary derivative of the force is discontinuous when the contact splits. It is also very essential to numerically integrate eq. 3.13 with the same precision as eq. 3.1. At first, computational speed seems important. It is usually not very relevant because the fraction of time spent on integrating the equation of motions

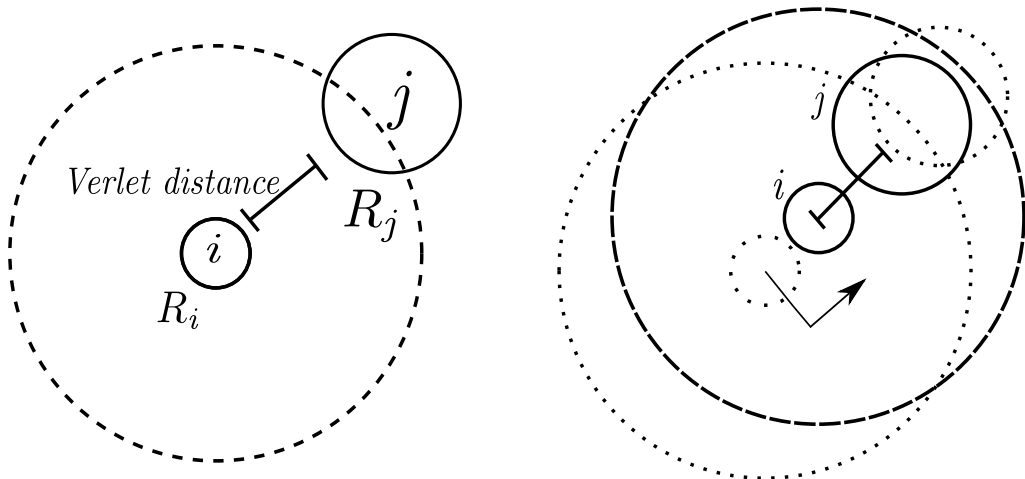


Figure 3.3 Checking the validity of Verlet lists. *Left:* the particles i and j are not recognized as neighbours since the distance of their surface is larger than the Verlet distance. The radius of the dashed circle is $R_i + R_{max} + \text{Verlet distance}$. *Right:* in the most unfortunate case the particles approach each other directly, travelling at the same velocity. As soon as one of the particles has travelled the distance $\text{Verlet distance}/2$ (arrows), the Verlet lists have to be rebuilt. The particles i and j are now recognized as neighbours. Figure redrawn after ?.

(as opposed to computing the interactions) is small. Accuracy for large time steps is more important, because the larger the time step that we can use, the fewer evaluation of the forces are needed per unit of simulation time. Hence, this would suggest that it is advantageous to use a sophisticated algorithm that allows use of larger time step. Algorithms that allow the use of large time steps, achieve this by storing information on increasingly higher-order derivatives of the particle coordinates. Consequently, they tend to require more memory storage. However, the most important aspect to consider is the energy conservation. It is important to distinguish between two kinds of energy conservation: the short time and long time. The sophisticated higher-order algorithms tend to have very good energy conservation at short times. However, they often have undesirable feature that results in drifting of the overall energy for longer times. In contrast, the Verlet style algorithms tend to have only moderate short term energy conservation, but little long-term drift (?). In this case, such algorithms are not useful. They are more complicated to program, and do not yield a more precise solution (?). It might seem important to have an algorithm that accurately predicts the trajectories of all particles for both short and long durations, however no such algorithm exists. In certain cases, two trajectories that are initially very close may diverge exponentially as time progresses. Any integration error, however small it may be, would always diverge the predicted trajectory exponentially from the true trajectory. This phenomenon is called the Lyapunov instability, and it is devastating to the whole idea of Discrete Element Method simulation, but we have good reasons to assume that even this problem need not be serious (?). First of all, one should realize that the aim

17
18
19
20
21
22
23
24
25
26
27
28
29
30
31
32
33
34

of the Discrete Element Method simulation is not to predict precisely what will happen to a system, but to predict the average behaviour of the system that was prepared in an initial state about which we know something (initial position, velocity and energy), but not everything. Hence, Molecular Dynamics technique differs from other methods, which are used to predict the trajectories. However, considerable numerical evidence suggest that the shadow orbits exists, which is a true trajectory of a multi-body system that closely follows the numerical trajectory for a time that is longer in comparison with the time that is required for the Lyapunov instability to develop (?).

Newton's equations of motion are time reversible, and so should be the integration algorithm. The “leapfrog” algorithm or the Verlet integration algorithm is a numerical scheme used to integrate the Newton's equation of motion to calculate the trajectories of particles and was implemented in Discrete Element Method simulation by Verlet (1967). Verlet algorithm is fast and requires less storage memory, it is not particularly accurate for long time steps, and hence, we should expect to compute the forces on all particles rather frequently. Its short-term energy conservation is fair (in versions that use more accurate expression for velocity), but most importantly it exhibits little long-term energy drifts. This is related to the fact that the Verlet algorithm is time reversible and area preserving, however, it does not conserve the total energy of the system exactly (?). Verlet algorithm is simply based on a truncated Taylor expansion of particle co-ordinates.

$$t(t + \Delta t) = rt + \mathbf{v}(t)\Delta t + \frac{f(t)}{2m}\Delta t^2 + \dots \quad (3.18)$$

If we truncate this expansion beyond the term Δt^2 , we obtain the Euler's algorithm, which looks similar to the Verlet Algorithm, but it does not preserve energy and have significant energy drifts. The simplest among the Verlet schemes is the *Leap frog algorithm*, which evaluates the velocities at half-integer time steps and uses these velocities to compute the new positions. The position of each grain is calculated at time $t = 0, \Delta t, 2\Delta t, \dots$, where Δt is the time step. On the other hand, their velocities are calculated at intermediate times, that is, at $t = \Delta t/2, 3\Delta t/2, \dots$. Let the position of a grain at time $t = k\Delta t$ be written as x_k , and its velocity at time $t = \Delta t(k + 1/2)$ be written $\mathbf{v}_{k+1/2}$, and its acceleration at $t = k\Delta t$ be \mathbf{a}_k . Then the following equation is used to advance systematically:

$$\mathbf{v}_{k+1/2} = \mathbf{v}_{k-1/2} + \mathbf{a}_k \Delta t, \quad x_{k+1} = x_k + \mathbf{v}_{k+1/2} \Delta t \quad (3.19)$$

This algorithm determines the new grain position with an error of order $O(\Delta t^4)$. But eq. 3.19 hides a difficulty in the application of this algorithm to granular materials (Radjai and Dubois, 2011). The problem is that the acceleration must be calculated at time $t = k\Delta t$. But the velocities are known at $t = (k - 1/2)\Delta t$, and not at $t = k\Delta t$. One way to get around this problem is to

write:

$$\mathbf{v}_k = \mathbf{v}_{k-1/2} + \mathbf{a}_{k-1}\Delta t / 2 \quad (3.20)$$

The equation uses the acceleration of the preceding time step to estimate the velocity. This approximation does not diminish the order of the algorithm. eq. 3.20 estimates \mathbf{v}_k with an error of order $\mathbf{O}(\Delta t^2)$, which produces an error of the same order in the calculation of the force in eq. 3.19. But this causes only an error of order $\mathbf{O}(\Delta t^3)$ in the velocity and an error of order $\mathbf{O}(\Delta t^4)$ in the position. However, this problem does not exist in energy conservation systems, because the computed forces do not depend on the velocities of the grains. The heaviest computational task is the evaluation of forces and not the integration of equations. The Verlet integration scheme is summarized in eq. 3.21 and figure 3.4. To calculate the forces and acceleration, it requires the positions and velocities at time t:

$$\mathbf{v}(t + \Delta t / 2) = \mathbf{v}(t - \Delta t / 2) + \mathbf{a}(t)\Delta t \quad (22)$$

$$x(t + \Delta t) = x(t) + \mathbf{v}(t + \Delta t / 2)\Delta t \quad (23)$$

$$\mathbf{v}(t) = \mathbf{v}(t - \Delta t / 2) + \mathbf{a}(t - \Delta t)\Delta t / 2 \quad (3.21) \quad (24)$$

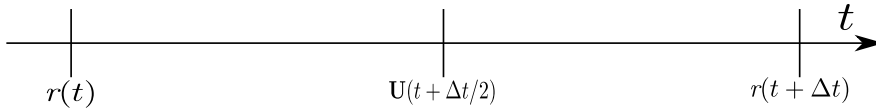


Figure 3.4 Verlet integration scheme

The analysis of the Discrete Element Method formulation reveals that the linear force law gives the model a harmonic character, showing that it is very closely related to simple models widely used in physics and mechanics. The shortest time scales often arise from the oscillations of one or two grains. The integration algorithm must resolve these movements with sufficient precision. Thus, the time steps used must be smaller than these time scales, the most rapid frequency is usually ω_N , the characteristic oscillation frequency of very short waves. This frequency is proportional to ω_0 , which is easier to estimate. Therefore, it is essential to choose a time step $\Delta t \approx \epsilon / \omega_0$, where ϵ is a constant that depends on the integration algorithm. Values such as $\epsilon \approx 0.01$ are often a reasonable choice (?). In the case of rapid granular flows, the time step must be small enough so that the fastest grains move only by a small fraction of their size during one time step. The grains must be stiff enough so that violent collisions do not lead to large overlaps between particles.

4 3.2.3 Boundary conditions

5 In many cases, the dynamic and static properties of a granular system are substantially affected
6 by the interaction of the granular material with the system boundaries, i.e. by the properties of
7 the container or the surface on which the material is present. The effect of boundary conditions
8 on the response of the granular assembly can be noticed in the convective motion of granular
9 material in vibrating containers, the formation of density waves in pipes, the motion of granular
10 material on conveyors, and the clogging of hoppers. In these and many other cases, careful
11 definition of the interaction between the granular material and the contact surface is essential.
12 Of particular importance is the realistic modelling of the wall surface roughness. Unfortunately
13 the mechanical interaction of a granular materials with a rough wall is poorly understood (?).
14 A simple way to define the wall property is to build up the wall from particles, which obey
15 the same rules of interaction as the particles of granular material. By varying the size and
16 position of the wall particles, system boundaries of adjustable roughness can be described.
17 However, the surface roughness that characterizes the frictional properties of the wall has to
18 be arrived iteratively, and may not represent the real conditions. In the present case, a solid
19 wall with corresponding stiffness, damping and frictional characteristics is introduced to model
20 the interaction between particles and the wall. The interaction force is computed in a similar
21 fashion to that of a pair of particles in contact and is divided into the normal and tangential
22 components. The compression of the particle upon collision with the wall is calculated along
23 the normal direction to the wall and the particle contact.

Periodic boundary

1 The effect of a wall on the response of particles is very critical, especially in numerical
2 simulation where the number of particles is relatively fewer in comparison to the experiments.
3 The undesired effect of a wall can be eliminated using periodic boundary conditions, i.e. a
4 periodic extension of the simulation area in one or more dimensions. Any particle leaving the
5 system at one side is reintroduced at the opposite side, and correspondingly the interaction
6 forces between particles at opposite sides of the simulation area are taken into account. In this
7 framework, the simulation domain becomes a unit area containing particles with periodic copies
8 paving the whole system. The periodic boundary conditions extend the system boundaries
9 to infinity, so that the simulation cell simply plays the role of a coordinate system to locate
10 particle positions [3.5](#).

11 The external stresses or displacements are applied on the simulation box by constraining the
12 degrees of freedom of the wall, which are alternatively kept free or fixed depending on whether
13 a stress or a displacement is monitored in a system. With periodic boundary conditions, this role
14

is played by the collective degrees of freedom carried by the coordinate system, whose basis vectors become dynamic variables, and their conjugate stresses are expressed as a state function of the granular configuration (?). In the case of granular systems, there is dissipation of energy during particle interactions. The kinematics, equation of dynamics, and the time-stepping schemes for Discrete Element Method are discussed in detail in Radjai et al. (2011). The periodicity in position implemented in the present study is discussed below.

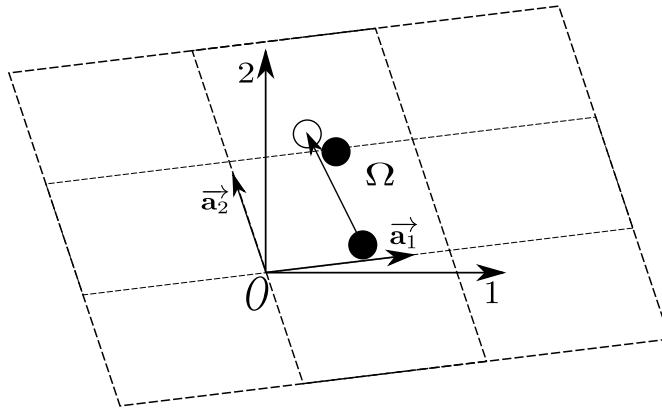


Figure 3.5 A 2D simulation cell ω with its basis vectors in an absolute frame. A particle located at the right boundary interacts with the image of another particle located at the left boundary.

Let us consider a collection of N_p particles with their centres contained in a cell of volume V . The cell can have any shape allowing for a periodic tessellation of space. The simplest shape is a parallelepiped i.e. parallelogram in 2D. The cell and its replicas define a regular lattice characterized by its basis vectors (\vec{a}_1, \vec{a}_2). In the case of a parallelogram, the basis vectors may simply be the two sides of the parallelogram; figure 3.5. The origin O of the simulation cell is a vertex of the cell of coordinates (0, 0) and its replicas are defined by two indices (i_1, i_2) corresponding to a translation of the origin by the vector $i_1 \vec{a}_1 + i_2 \vec{a}_2$. Then, the coordinates $\vec{r}(i')$ of the image i' of a particle $i \in \Omega$ of coordinates $\vec{r}(i')$ are given by:

$$\vec{r}(i') = \vec{r}(i) + \sum_{k=1}^2 i_k \vec{a}_k \quad (3.22)$$

The particles belonging to the cell Ω , characterized by $i_1 = i_2 = 0$, can interact with the particles of the same cell but also with image particles in the neighbouring cells characterized by $i_k \in 1, -1$. There are $3^D - 1$ cells surrounding the simulation cell and they are involved in the search of contact partners for each particle. The distance between two particles i and $j \in \Omega$ is the shortest distance separating i from j or from one of its images j' . As the system evolves in time, a particle i may leave but one of its images i' enters at the same moment. In order to keep all original particles in the cell, the status “original” should be reserved to the particles whose

³ centres belongs to Ω . Hence, whenever a particle i leaves the simulation cell, it becomes an
⁴ image of i' , which then becomes the original. This means that a particle crossing a border of
⁵ the simulation cell, returns to the cell by crossing another border.

⁶ 3.2.4 Particle Assembling Methods

⁷ In order to simulate a granular assembly, it is essential to assign an initial position and velocity
⁸ to all the particles in the system. Particle positions should be chosen to be compatible to the
⁹ structure (granular fabric) we are trying to simulate. In any event, the particles should not
¹⁰ be positioned such that there is an appreciable overlap between particles. In order to achieve
¹¹ the initial position of the particles, various particle-assembling methods can be adopted. The
¹² particle assembling methods can be classified into two broad categories: dynamic methods
¹³ and geometrical approaches. The dynamic approach involves packing of grains using laws of
¹⁴ mechanics and contacts, while in the geometrical method the particles are packed considering
¹⁵ their geometry, i.e. grain size, shape and its position. In general, the packing of particles
¹⁶ can be categorized into two types: crystal/lattice packing, like hexagonal or square pattern of
¹⁷ mono-disperse particles, and random packing with varying density employing mono-disperse
¹⁸ or poly-disperse grains. The crystalline packing arrangements, such as hexagon and square
¹⁹ lattices, are easier to generate, however they have non-trivial effects on the response of the
²⁰ granular system ([Staron et al., 2005](#)). Hexagonal packing is the densest possible arrangement for
²¹ mono-dispersed spherical grains. In 2D, the packing of mono-dispersed circles on a hexagonal
²² lattice yields a packing density of $\eta_h = \frac{1}{6}\pi\sqrt{3} \approx 0.9068$

²³ The rheology of a granular material is controlled by the geometry of the assembly, which
²⁴ includes the particle shape, size distribution, and their arrangement. This prevailing role of
²⁵ geometry sometimes permits to simplify the dynamics in favour of a better description of the
²⁶ geometry and/or higher numerical efficiency ([Radjai and Dubois, 2011](#)). For example, dense
²⁷ granular packing may be efficiently constructed by replacing the equations of dynamics by
²⁸ simple displacement rules satisfying the geometrical constraints. Purely geometrical procedures
²⁹ can be much simpler and numerically faster than dynamic or quasi-static methods. Contrary
³⁰ to dynamic simulation methods, the geometrical methods allow for quick assembling of a
³¹ large number of particles. Such packing may then be used as the initial state for dynamic
³² simulations. The issue of the assembling methods is to construct configurations of particles as
³³ close as possible to a state of mechanical equilibrium with built-in packing properties. This
 can be a target packing density for a given particle size distribution. In the same way, the
 average connectivity of the particles (coordination number) and the anisotropy of the contact
 network are basic geometrical properties. The coordination number represents the mechanical
 response of packing. The homogeneity of the particle assembly in terms of packing fraction

and connectivity is another important property, which depends on the assembling rules. In the present study, the initial grain packing is obtained using ballistic deposition technique.

Ballistic deposition

Initially a random arrangement of particles which do not touch each other is generated (??). The radii of the particles are chosen from the interval of (R_{min}, R_{max}) in such a way that the total mass of all particles from a certain size interval is the same for all sizes, thus ensuring that neither larger nor smaller particles dominate the system. This distribution can be obtained, if the radii are chosen according to the probability distribution:

$$p(R) = \frac{R_{min}R_{max}}{R_{max} - R_{min}} \frac{1}{R^2} \quad (3.23)$$

Random numbers according to the above distribution can be generated from equi-distributed random numbers $z \in [0, 1]$ via the transformation

$$R = \frac{R_{min}R_{max}}{R_{max} - z(R_{max} - R_{min})} \quad (3.24)$$

This transformation is applied to initialise the particle radii and the particles are arranged randomly on a regular lattice. The configuration of particles obtained after this step is presented in ???. In the second step, the particles arranged in a regular lattice are allowed to fall down and are packed using the *random deposition with relaxation method*, a ballistic deposition technique. The geometrical methods help in this way to improve numerical efficiency in the

- 1 preparation phase. For example, gravitational deposition of particles located initially on a
- 2 regular grid can require hours of computation whereas a nearly similar result may be obtained
- 3 by means of a geometrical method in only a few minutes. The drawback is that the resulting
- 4 sample will not be in mechanical equilibrium and no information is available on the contact
- 5 forces. Nevertheless, depending on the relaxation rule, the sample may still be sufficiently close
- 6 to equilibrium to be considered as a good starting point for mechanical simulations. Hence,
- 7 a combined approach of ballistic deposition and Discrete Element Method is adopted in the
- 8 present study to generate mechanically stable samples. The random deposition and relaxation
- 9 method, first proposed by [Vold \(1959\)](#); ? and developed by [Jullien et al. \(1992\)](#) and [Meakin](#)
- 10 [and Jullien \(1985\)](#), is adopted in the present study. The general principle of this method is
- 11 quite simple (see figure 3.6); it consists of placing the particles consecutively on a substrate or
- 12 a layer of already deposited particles. Each particle first touches the substrate or a deposited
- 13 particle, then undergoes a relaxation process (single-particle restructuring) along the steepest
- 14 descent (steepest-descent model) until a more stable position according to a stability criterion

is reached. The construction of the packing proceeds layer by layer from the substrate, hence this deposition model is also known as bottom-to-top restructuring model. The first step is to release a particle from a random position above the substrate. Upon contact with the first deposited particle, the particle rolls following the steepest descent until a new contact is formed with a second particle. In 2D, two contacts are sufficient to balance a particle if its centre of gravity lies between the two contacts. This corresponds to a position of local stable equilibrium. If this criterion is not met, the particle continues to roll and the procedure is iterated until a local stable position is reached. The wall effects are eliminated by adopting periodic boundaries (Sec 3.2.3) in the horizontal direction (perpendicular to that of deposition). figure 3.6 shows a small sample prepared by this method (the grey particles are periodic images of the black ones). In this method, the order of deposited particles is generally random and independent of their sizes. The mechanically stable sample obtained from equilibrating the random deposited and relaxed sample is presented in ??

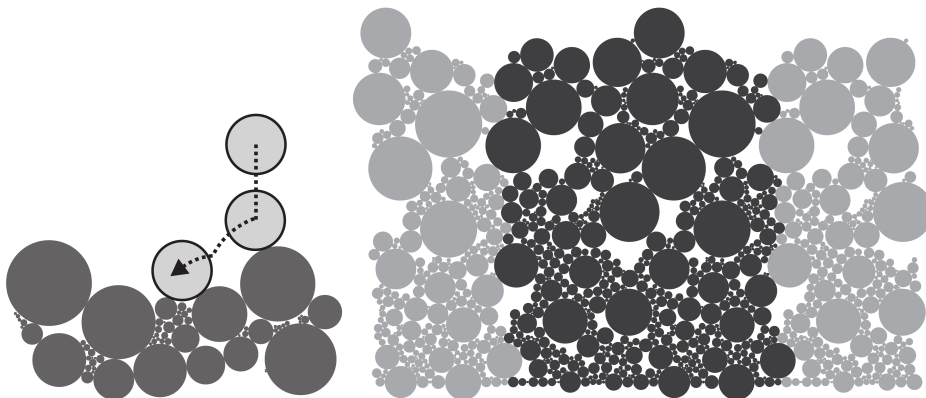


Figure 3.6 (a)*Ballistic deposition*: first contact followed by steepest descent; (b) small-scale periodic sample ([Radjai and Dubois, 2011](#))

Statistical analysis of prepared sample

In order to ensure the homogeneity of the sample prepared using the above technique, a statistical analysis of the sample is performed. Various parameters such as particle size, coordination number, contact normal direction, contact normal force, etc., can be used in the statistical analysis to verify the homogeneity of the prepared sample. Of the various parameters available, the coordination number, i.e. the average number of contacts per particle is chosen to study the homogeneity of the sample, because of its simplicity and its physical significance in representing the density of the sample. With increase in the coordination number, the density of the granular assembly increases. The mechanically stable sample prepared by ballistic deposition technique presented in ?? is used for the statistical analysis. Representative elements

of size $0.02 \text{ m} \times 0.01 \text{ m}$ (highlighted segments in ??) were considered. Each representative element has approximately 40 particles. A histogram is plotted showing the number of particles having a particular coordination number for all the representative elements (??). A normal distribution of the number of particles and the coordination number can be observed from ??.

Most particles are found to have 2 or 3 contacts with its neighbours. The number of particles with higher coordination number, i.e. coordination number greater than 3, is found to increase as we go down the sample. This is attributed to the effect of gravity, which increases linearly as we go down. Representative elements at the top are found to have a shift in their peak towards lower coordination number, as they are less restrained in comparison to their counterparts at the bottom of the sample. Overall, the sample is found to be homogeneous, with representative elements having similar normal distribution of the coordination number. Thus, the prepared sample is a good representation of the actual granular assembly and the simulations based on these samples are found to be more realistic in comparison to crystalline/lattice packing of granular particles.

3.2.5 Voronoi Tessellation

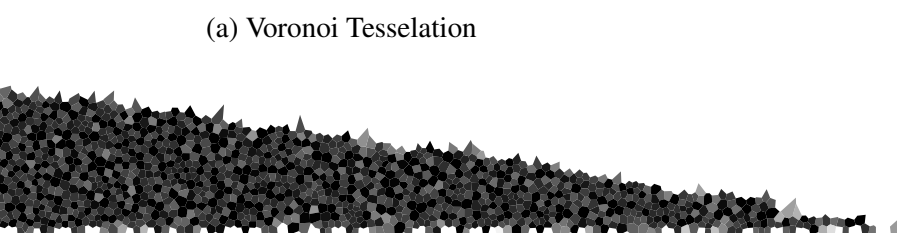
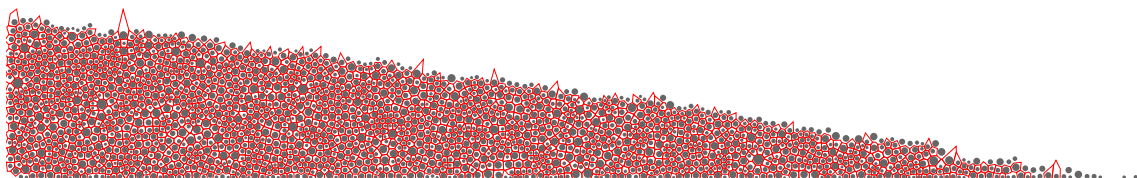


Figure 3.7 Voronoi tessellation to average bulk properties

¹⁵ Chapter 4

¹⁶ Multi-scale modelling of dry granular ¹⁷ flows

¹⁸ 4.1 Introduction

¹⁹ In nature, instabilities of slopes or cliffs are dramatic events involving sudden release of a
²⁰ large mass of soil. However, the prediction of catastrophic events still represents challenge,
²¹ one difficulty being our incomplete understanding of the dynamics of granular flows ([Rondon et al., 2011](#)). Understanding the mechanics is of particular importance for risks assessment.
²² Small scale laboratory experiments are usually unable to properly capture the dynamics of
²³ geophysical events. However, they can be useful to precisely study physical mechanisms, which
²⁴ may play a role in real flows ([Iverson, 1997](#)).

²⁶ Conventionally, granular materials such as soils are modelled as a continuum. On a macroscopic scale, granular materials exhibit many collective phenomena and the use of continuum mechanics to describe the macroscopic behaviour can be justified. However, on a grain scale, the granular materials exhibit complex solid-like and/or fluid-like behaviour depending on how the grains interact with each other. Numerical studies at grain scale allows a precise understanding of the internal flow structure. Recent works on granular materials suggest that a continuum law may be incapable of revealing in-homogeneities at the grain-scale level, such as orientation of force chains, which are purely due to micro-structural effects [Rycroft et al. \(2009\)](#). Discrete Element approaches are capable of simulating the granular material as a discontinuous system allowing one to probe into local variables such as position, velocities, contact forces, etc. The fundamental question is how to model granular materials which exhibit complex phenomenon. It is important to understand the mechanics of granular flows and the ability and limitations of continuum methods in capturing the flow dynamics.

4.2 Granular column collapse

The collapse of a granular column, which mimics the collapse of a cliff, has been extensively studied in the case of dry granular material (Hogg, 2007; Kerswell, 2005; Lajeunesse et al., 2004; Lo et al., 2009; Lube et al., 2005; Staron and Hinch, 2007; Zenit, 2005). The granular column collapse experiment involves filling a rectangular channel of height H_0 and width L_0 with a granular material of mass ‘m’ (see figure 4.1). The granular column is then released *en masse* by quickly removing the gate, thus allowing the granular material to collapse onto the horizontal surface, forming a deposit having a final height H_f and length L_f . Despite the complexity of the intermediate flow dynamics, experimental investigations have shown that the flow evolution, the spreading velocity, the final extent of the deposit, and the energy dissipation can be scaled in a quantitative way independent of the substrate properties, grain size, density,

and shape of the granular material and released mass (Lajeunesse et al., 2005; Lube et al., 2005; Staron and Hinch, 2007). The granular collapse has also been studied using discrete element method, which allows precise measurement of the internal flow structure (Lo et al., 2009; Staron and Hinch, 2006, 2007; Utili et al., 2014). Power laws relating the final run-out and height to the initial aspect ratio of the column were observed. These findings immediately pose the question: are these simple scaling fortuitous, an oversimplification, or in fact indicative of a simple dynamical balance?

Granular flows are conventionally modelled as a frictional dissipation process in continuum mechanics but the lack of influence of inter-particle friction on the energy dissipation and spreading dynamics (Lube et al., 2005) is surprising. However, Kerswell (2005) showed the run-out behaviour has a clear material dependence, which corroborates the conclusion of Lajeunesse et al. (2004) and softens that of Lube et al. (2005). The collapse of a granular column on a horizontal surface is a simple case of granular flow, however a proper model that describes the flow dynamics is still lacking. Simple mathematical models based on conservation of horizontal momentum capture the scaling laws of the final deposit, but fail to describe the initial transition regime. From a theoretical point of view, the spreading has been described using depth averaged equations (Kerswell, 2005; Larrieu et al., 2006). The depth-averaged and Saint-Venant equations struggle to recover the precise dynamic behaviour of the system (Warnett et al., 2013) and only succeeds in predicting the scaling observed for aspect ratio less than one. However, describing larger aspect ratio and capturing the initial stage of the collapse, when the grains experience a rapid change of direction from vertical to horizontal, remain an open challenge,

In the present study, multi-scale numerical modelling, i.e. grain-scale modelling and continuum analyses, of the quasi-two dimensional collapse of granular columns are performed using Discrete Element (DEM) approach and Generalised Interpolation Material Point Method

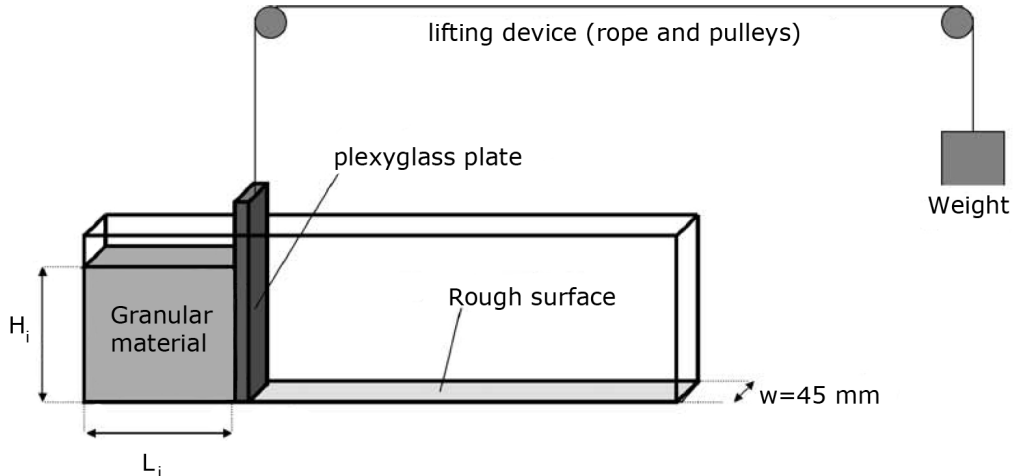


Figure 4.1 Schematic of experimental configuration for 2-D collapse in a rectangular channel, ([Lajeunesse et al., 2004](#))

(GIMPM). GIMPM, a hybrid Eulerian – Lagrangian approach, with Mohr-Coloumb failure criterion is used to describe the continuum behaviour of granular column collapse. While the micro-mechanics of the flow is captured using DEM simulations. Comparing the grain scale behaviour with the continuum simulations highlights the limitations of continuum approaches in modelling the dense granular flows and their ability (or lack thereof) in capturing the complex micro-scale rheology.

4.2.1 Numerical set-up

In this study, numerical simulations of granular columns are analogous to the experimental investigation of column collapse performed by [Lajeunesse et al. \(2004\)](#). The experimental configuration of [Lajeunesse et al. \(2004\)](#) is shown in figure 4.1. Granular material of mass ' M ' was poured into a container to form a rectangular heap of length ' L_0 ', height ' H_0 ' and thickness ' W '. The internal friction angle and the wall friction between the wall and the glass beads measured by [Lajeunesse et al. \(2004\)](#) are listed in table 4.1. The gate was then quickly removed to release the granular mass that spreads in the horizontal channel until it comes to rest. The final run-out distance ' L_f ' and the collapsed height ' H_f ' were measured. The run-out distance and collapse height exhibit a power law relation with the initial aspect ratio ' a ' ($= H_0/L_0$) of the column.

Granular materials when released suddenly on a horizontal surface exhibit transient flow. In this study, the mechanism of flow initiation, spreading dynamics and energy dissipation are studied for varying initial aspect ratios of the granular column. DEM soil grain characteristics match that of the experiment. The particle size distribution (PSD) is one of the most impor-

Table 4.1 Material properties of glass ballotini ([Lajeunesse et al., 2004](#))

Parameter	Value
Mean diameter	1.15 mm
Repose angle	$22 \pm 0.5^\circ$
Avalanche angle	$27.4 \pm 0.5^\circ$
Wall friction angle	$24.8 \pm 0.2^\circ$

tant factors controlling landslide initiation and soil permeability. Cumulative β distribution (described in ??) is used to generate a graded sample with a mean grain diameter of 1.15mm (see figure 4.2b). The DEM sample is composed of ~ 3000 disks with a uniform distribution of diameters by volume fractions in the range $[d_{min}, d_{max}] = 0.92 - 1.38$ mm with polydispersity $r = \frac{d_{max}}{d_{min}} = 1.5$. The granular column is prepared by allowing the randomly placed grains to undergo ballistic deposition with a constant potential head between layers of soil grains. A snapshot of the sample generated is shown in figure 4.2a. A DEM sample with soil grains arranged in a regular hexagonal lattice is also used to study the influence of crystallisation and jamming on the run-out behaviour.

The overlap between grains are determined by the stiffness k_n of the spring in the normal direction. Typically, an average overlap in the range 0.1 to 1.0% is desirable [Zenit \(2005\)](#) and the spring constant is chosen to produce grain overlaps in this range. The stiffness is determined as

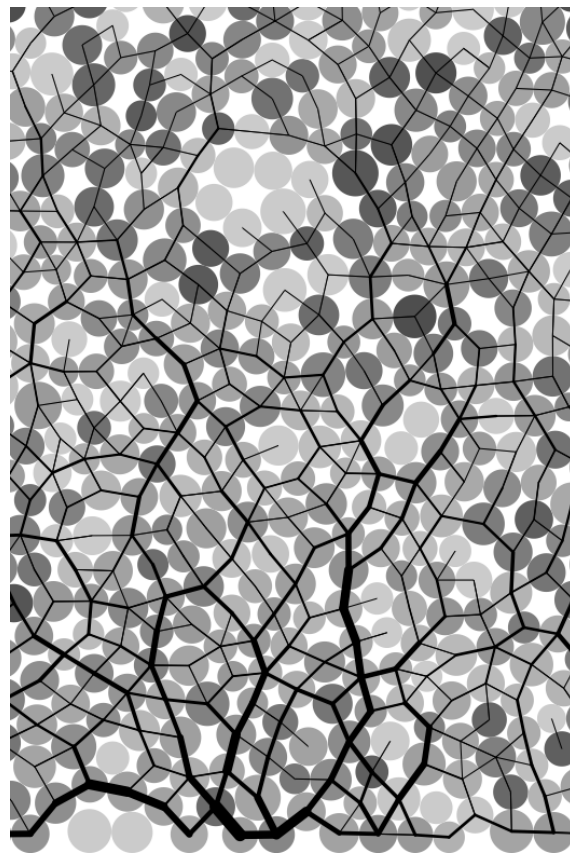
$$k_n = \frac{2\pi G}{(1-\nu)[2\ln(\frac{2r}{A}) - 1]} \quad (4.1)$$

$$A = \left[\frac{2r(1-\nu)f_n}{\pi G} \right]^{\frac{1}{2}}, \quad (4.2)$$

where f_n is the normal contact force; G is the shear modulus; ν is the Poisson's ratio and r is the radius of the grain. A simpler form of stiffness for a spherical grain is defined as

$$k_n = 4ER, \quad (4.3)$$

where E is the Young's modulus of the material and R is the radius of the grain. [Cambou et al. \(2009\)](#) observed that the contact model has negligible influence on the run-out behaviour of rapid granular flows. The granular collapse simulations performed using non-linear Hertz-Mindlin contact model and the linear-elastic contact model showed no significant difference on the granular flow behaviour [Utili et al. \(2014\)](#). Linear-elastic contact model is used in the



(a) DEM sample prepared using ballistic deposition

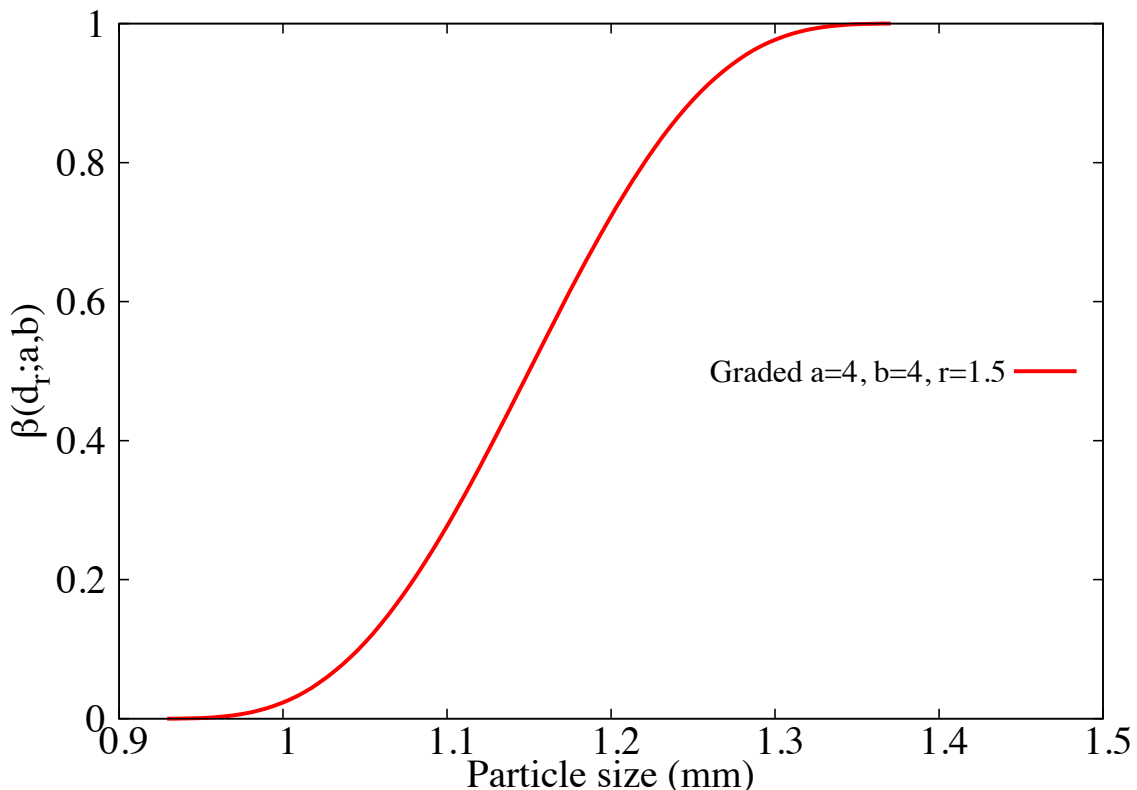
(b) DEM grains generated using the cumulative β distribution

Figure 4.2 DEM sample characteristics

Table 4.2 Micro-mechanical parameters used in DEM simulations

Parameter	Value
Young's modulus of glass bead	$70 \times 10^9 \text{ N m}^{-2}$
Poisson's ratio	0.22 - 0.24
Diameter of glass beads	0.92 to 1.38 mm
Normal and shear stiffness of grains	$1.6 \times 10^8 \text{ N m}^{-1}$
Normal and shear stiffness of wall	$4 \times 10^8 \text{ N m}^{-1}$
Inter-particle friction coefficient, μ	0.53
Wall friction coefficient	0.466
Coefficient of restitution, ϵ	0.755

present study due to its simplicity and lower computation time requirement. The maximum tangential force is limited by the Mohr-Coloumb criterion.

[Staron and Hinch \(2006\)](#) observed that the coefficient of restitution ϵ was dramatically changing the behaviour of the systems for $\epsilon \rightarrow 1$; in particular, this dramatic change is expected to become more important for increasing values of a . On the contrary, for $\epsilon \leq 0.8$, the influence of the coefficient of restitution becomes negligible. In the present study, a value of 0.75 is adopted as the coefficient of restitution, similar values of restitution coefficient was adopted by [Girolami et al. \(2012\)](#); [Zenit \(2005\)](#). The normal damping coefficient C_n is appropriately chosen to achieve the required coefficient of restitution ϵ :

$$C_n = 2\gamma\sqrt{m_{ij}k_n} \quad (4.4)$$

$$\text{where } \gamma = -\frac{\ln(\epsilon)}{\sqrt{\pi^2 + \ln^2(\epsilon)}}, \quad \text{and} \quad m_{ij} = \frac{m_i m_j}{m_i + m_j}. \quad (4.5)$$

The micro-mechanical parameters used in this study are presented in table 4.2. Due to the unsteady nature of the flow, the grains get dispersed on the horizontal plane as discrete bodies start to separate from the main mass, hence the run-out distance is calculated as the position of the farthest grain which has at least one contact with the main mass.

GIMPM with Mohr-Coloumb constitutive model is used to simulate plane strain collapse of granular columns. [Crosta et al. \(2009\)](#) observed that the Mohr-Coloumb with non-associate flow rule is able to capture granular collapse dynamics and models the strong vertical motion components, but it does not suffer the limitations of typical shallow water equation methods. In order to understand the ability and limitations of continuum approaches in capturing the local rheology, it is important to scale the grain scale properties, such as inter-particle friction and stiffness, to the continuum scale (macroscopic friction and Young's modulus). [Crosta et al. \(2009\)](#) observed that the friction angle plays a significant role on the run-out behaviour. In

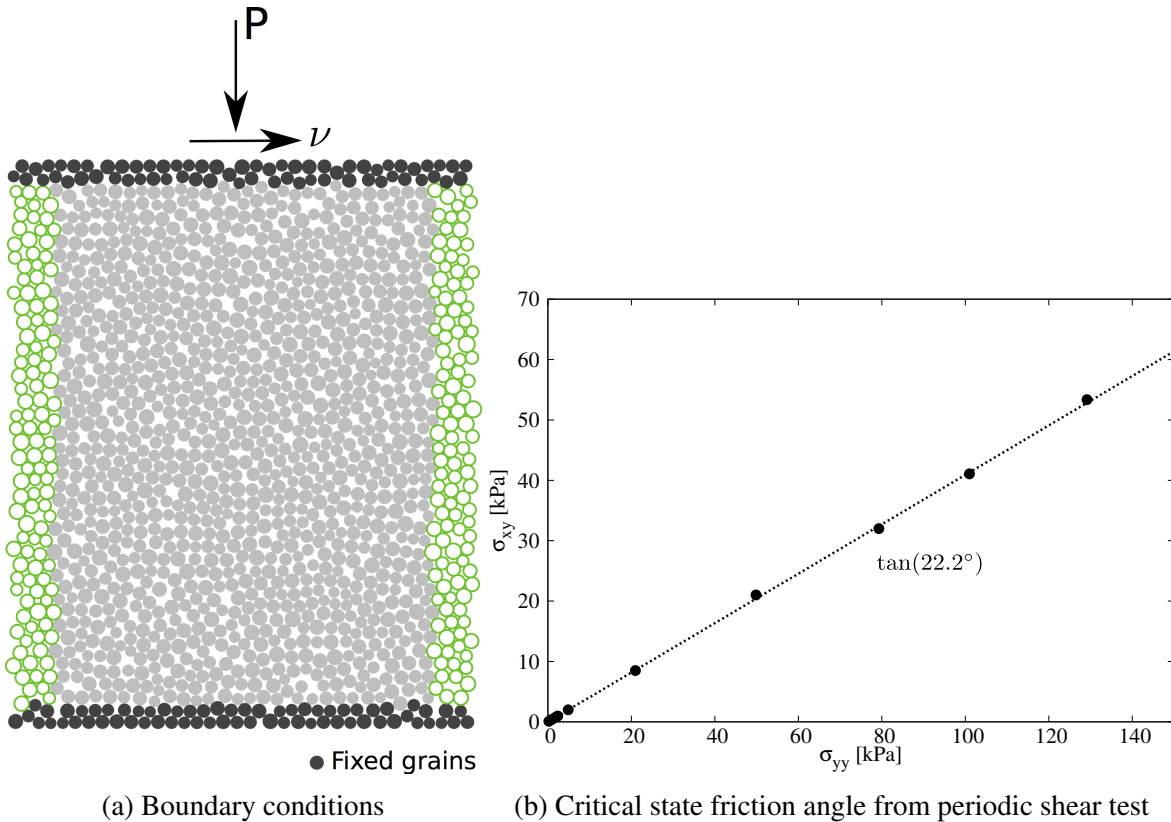


Figure 4.3 Periodic shear test

MPM simulations, the granular flow is assumed to be in critical state and the critical state friction angle is used in the Mohr-Coloumb model. In order to obtain the critical state friction angle of the granular sample, a shear test is performed using 1078 DEM grains. A bi-periodic boundary condition is adopted on the sides of the sample (see figure 4.3a). Two layers of fixed grains (shown in black) is placed at the top and the bottom of the shear sample. A normal pressure ‘P’ and a horizontal velocity v is applied to the fixed grains at the top of the shear sample. The normal effective stress is varied in the sample and the average shear stress of the sample is measured. The sample was sheared until critical state was reached. The slope of shear stress versus normal effective stress gives the critical state friction angle. A critical state friction angle of 22.2° is obtained. The macroscopic friction angle is in the range observed by Estrada et al. (2008); Mitchell and Soga (2005). The Young’s modulus of the granular assembly is obtained as the initial slope of the stress-strain plot of a uni-axial compression of a granular column using DEM.

Guilkey et al. (2003) suggests using at least four material points per cell for large deformation problems. In the present study, 16 material points per cell is adopted. If the mesh is too fine and the number of particles is too large, the particle size $2l/p$ decreases, and the GIMPM

Table 4.3 Parameters used in continuum simulations

Parameter	Value
Material point spacing	0.575 mm
Number of material points per cell	16
Young's Modulus, E	1.98×10^6 Pa
Poisson's ratio, ν	0.22 to 0.24
Friction angle, ϕ	$23.2 \pm 0.2^\circ$
Dilatancy angle, Φ	0°
Density, ρ	1800 kg m^{-3}
Wall friction	0.466
Time step increment	1.0×10^{-6} s

interpolation function tends to approach the original MPM function, as shown by ?. Hence GIMPM loses the merit that it reduces the numerical noise due to material points crossing the background mesh. In addition, the probability of particles crossing the background mesh increases with decrease in mesh size, hence, more noise can be produced Abe et al. (2013). The effect of number of material points per cell on the run-out behaviour is discussed in section 4.3.5. Each material point represents one-fourth of a DEM soil grain. The parameters used for the continuum analyses are presented in table 4.3.

4.2.2 Deposit morphology

MPM and DEM simulations of granular column collapse are performed by varying the initial aspect ratio of the column. The normalized final run-out distance, $\Delta L = (L_f - L_0)/L_0$, as a function of the initial aspect ratio 'a' of the column is presented in figure 4.4. Similar to the experimental behaviour a power law relation between the run-out and the initial aspect ratio of the column is observed. Two distinct flow regimes can be seen: (a) for 'a' < 1.7 a linear relation between the spread and aspect ratio can be observed, and (b) for 'a' > 1.7 a power-law relationship exists. In the present study, the following scaling law for the run-out (using DEM) is observed:

$$\frac{L_f - L_0}{L_0} \approx \begin{cases} 1.67a, & a \lesssim 2.3 \\ 2.5a^{2/3}, & a \gtrsim 2.3 \end{cases} \quad (4.6)$$

Both, MPM and DEM simulations are able to capture the linear relationship for 'a' < 1.7, and the simulation results agree with the experimental investigation Lajeunesse et al. (2005). This shows that a simple frictional dissipation model is able to capture the flow dynamics for

columns with smaller aspect ratio. For ‘a’ < 1.7, the normalised run-out distance predicted using DEM simulations are very close to the run-out observed in the experiments. DEM simulations with hexagonal packing shows shorter run-out distances in comparison to randomly packed sample. This difference in the run-out behaviour might be due to the crystallisation and jamming effects in hexagonal packing. The small difference in the final run-out between DEM and experimental results can be attributed to the variation in the packing of grains. Also, the experimental data corresponds to granular column collapse in a rectangular channel, the collapse is not a pure two-dimensional collapse as in the case of numerical simulations.

Significant difference in the final run-out between MPM, which is based on a simple frictional model for dissipation of potential energy, and DEM simulations for ‘a’ > 1.7 indicates a change in the mechanism of energy dissipation for columns with large aspect ratios (‘a’ > 1.7). [Staron and Hinch \(2005\)](#) observed that a constant frictional dissipation model cannot describe a power-law relation observed at large aspect ratio. A transition in the run-out behaviour at an aspect ratio of 1.7 indicates a change in flow dynamics. Similar behaviour in the run-out distance was observed by [Bandara \(2013\)](#) for columns with large the aspect ratio ≥ 2 .

The longer run-out distance in MPM simulations at large aspect ratios might be influenced by the amount of material mobilised during the collapse. In tall columns, the entire column participates in the flow, in contrast to short columns where the collapse is due to avalanching of flanks, [Lajeunesse et al. \(2004\)](#). It is possible that MPM simulations collapses more resulting in longer run-out distance. Figure 4.5 shows the normalized final height as a function of the initial aspect ratio of the column. Similar to the run-out behaviour, the normalised-height also shows two distinct regimes. The scaling of final height of the column with the initial aspect ratio of the column can be written as

$$\frac{H_f}{L_i} \propto \begin{cases} a, & a \lesssim 0.7 \\ a^{2/3}, & a \gtrsim 0.7 \end{cases} \quad (4.7)$$

The final height predicted by both DEM and MPM simulations match the experimental data for columns with smaller aspect ratio (‘a’ ≤ 0.7). Linear relationship between the final height and the aspect ratio indicates that only a part of the granular column is mobilised during the collapse. For tall columns, both approaches predict similar normalised height. However, the normalised height observed in MPM is higher than in DEM simulations, which is in contrast to the idea of increase in the amount of material mobilised during the collapse in MPM simulations resulting in longer run-out distance. Hence, the longer run-out observed in MPM simulations is due a change in the flow dynamics at higher aspect ratios, which is not captured in MPM simulations. The final height of a column is controlled by the amount of static region in the

23 granular column collapse, while the run-out distance is essentially a function of the flowing
 24 mass. Hence, it is essential to compare the evolution of flow and the internal flow structure in
 25 DEM and MPM simulations.

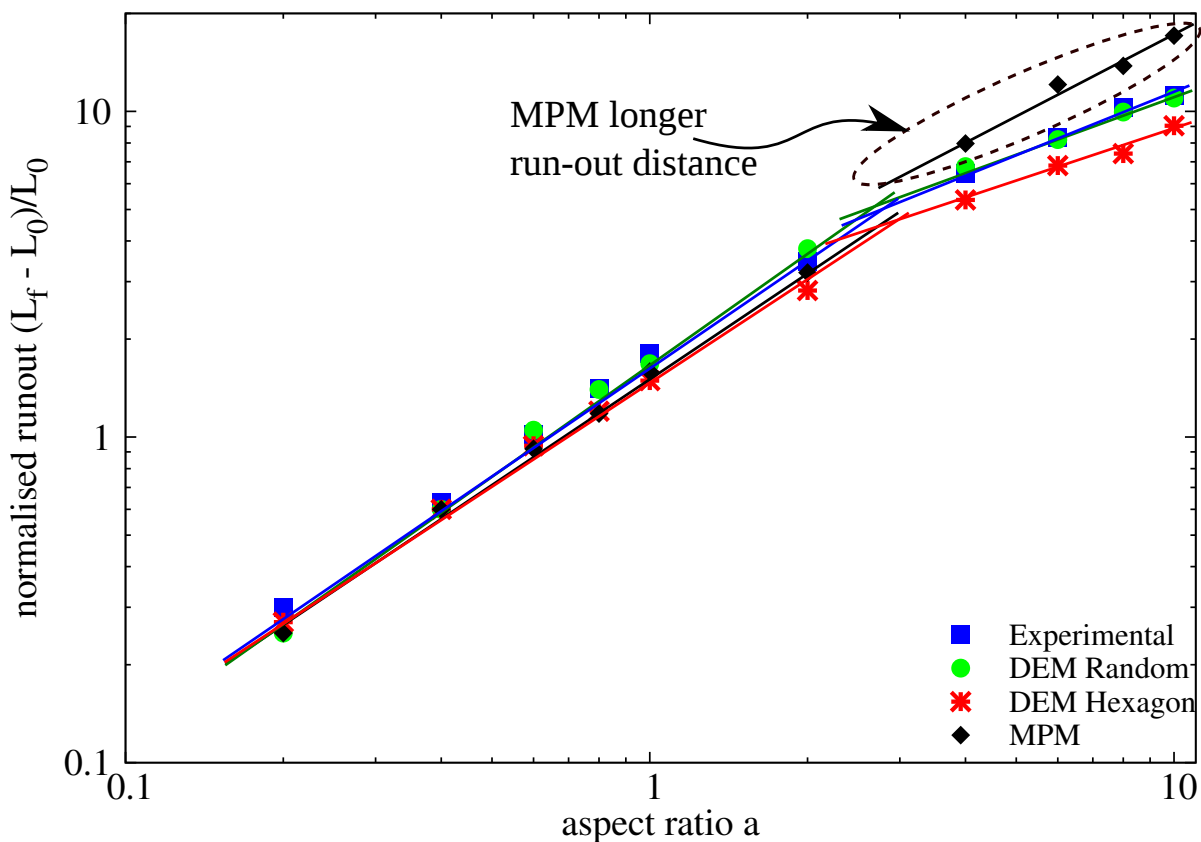


Figure 4.4 Normalised final run-out distance for columns with different initial aspect ratio

26 4.2.3 Flow evolution and internal flow structure

27 The normalised run-out and height as a function of the aspect ratio indicates that, for a given
 28 granular material and substrate properties, the flow dynamics and the final deposit morphology
 29 are independent of the volume of granular material released, but depend only on the geometry
 30 of the column. A power law relationship is observed between the run-out distance and the
 31 initial aspect ratio of the column. A transition in the run-out behaviour at an aspect ratio of 2.3
 32 indicates a change in the flow dynamics.

33 For smaller aspect columns ('a' < 2.3), the flow is initiated by a failure at the edge of the
 34 pile along a well-defined fracture surface. The granular mass fails through avalanching of
 35 flanks producing a truncated cone-like deposit ('a' < 0.7) or conical deposit ('a' > 0.7). The

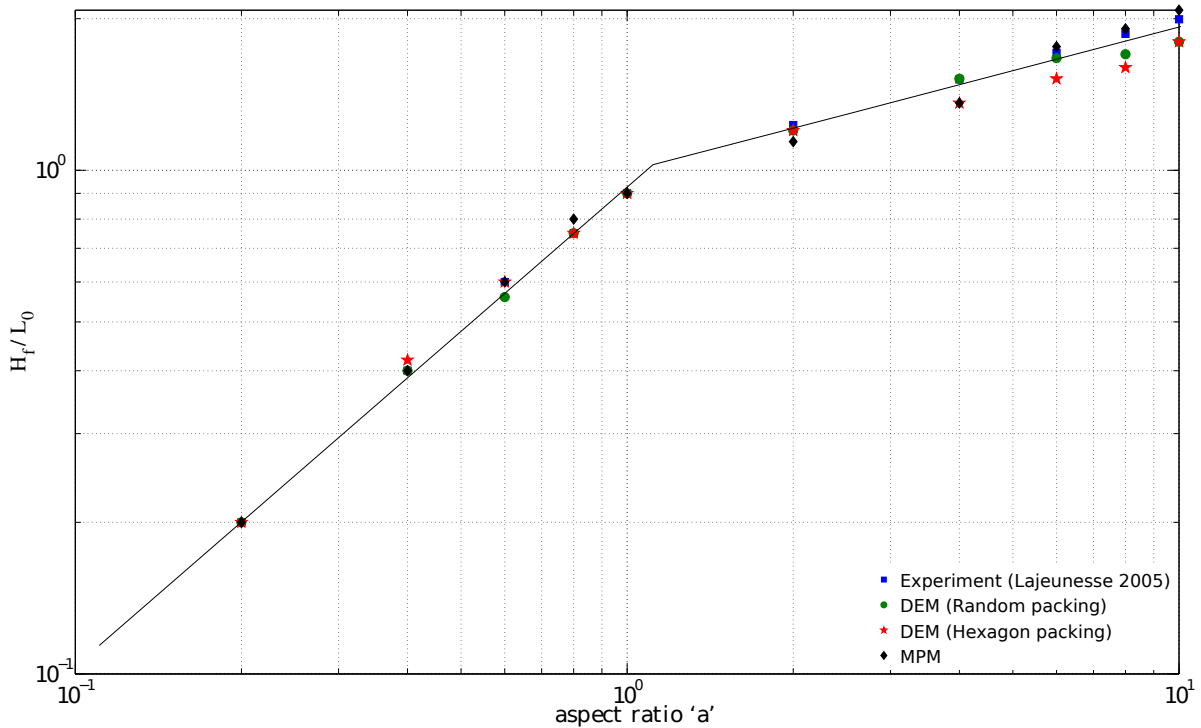


Figure 4.5 Normalised final collapse height for columns with different initial aspect ratio

- 36 grains located above the failure surface move “*en masse*” leaving a static region underneath the
failure surface.

Dimensional analysis of granular column collapse reveals an intrinsic time defined as $\sqrt{H_i/g}$. This intrinsic time is a transient time of order τ_c , at which the flow is fully developed, i.e., the potential energy available at the initiation of collapse is now fully converted to kinetic energy. Numerical simulation of the velocity profile of a granular column ($'a'=0.4$) at critical time τ_c is presented in figure 4.6. At critical time, the velocity field depends only on the position of the grain along the sliding mass. The maximum velocity is observed at the front of the flowing mass corresponding to that of a plug flow in horizontal direction. Particulate and continuum simulations show similar run-out distance at the critical time. Both approaches show similar quantity of material destabilised above the failure surface. However, the crystalline arrangement of soil grains in a hexagonal packing results in a different flow mechanics, which also shows the effect of jamming at the flow front. The continuum nature of MPM results in a slightly different geometry of the material destabilised above the failure surface in comparison to DEM simulations. The velocity profile is similar to a steady granular surface flow observed by Lajeunesse et al. (2004).

For columns with lower initial aspect ratios, the run-out distance is proportional to the mass flowing above the failure surface. The spreading results from a Coulomb-like failure of the edges

and implies no free fall of the column. [Daerr and Douady \(1999\)](#) also observed active Coulomb yielding in transient granular surface flows. In this case, the effective friction properties of the flow can be simply predicted from the shape of the final deposit. The amount of mass mobilized during the collapse is significantly affected by the angle of the failure surface. Figure 4.6 shows that both numerical techniques predict a distinct failure surface when the flow is fully developed at critical time τ_c . The angle of the failure surface is found to be about 55° . The failure surface begins from the toe of the column and protrudes inwards at an angle of 50 to 55° . The formation of the “truncated conical deposit” or “conical deposit” depends only on the initial length of the column, as the angle of the failure surface is found to be independent of the aspect ratio. The failure angle is consistent with the interpretation in terms of *active Coulomb failure* ([Lajeunesse et al., 2004](#)), which leads to a predicted failure angle $\theta_y = 45^\circ + \delta/2$, where δ is the internal friction angle of the granular material. In the present study, the friction angle of the glass beads is 22° , which leads to $\theta_y = 45^\circ + 22^\circ/2 = 56^\circ$, which is in good agreement with the numerical simulations and experimental observations by [Lajeunesse et al. \(2004\)](#). The fracture angle has a direct effect on the transition between the truncated cone and the conical deposit occurring at an aspect ratio of 0.7 . [Schaefer \(1990\)](#) observed the onset of instabilities in a narrow wedges of 56 to 65° for Cambridge-type constitutive models that describes granular flows, which is in-line with the failure angle observed in the present study.

The final profile of the granular column with an initial aspect ratio of 0.4 is shown in

[figure 4.7](#). Both MPM and DEM show similar run-out behaviour. The continuum approach is able to capture the flow dynamics of short columns, wher the failure mechanism is active Coulomb failure. In dense hexagonal packing, the failure surface is steep due to crystallisation effect. The variation in the angle of the failure surface causes a difference in the amount of material destabilised, and in turn in the run-out distance. This crystallisation phenomenon is found to have a significant influence on the final deposit of the granular column. [Lacaze and Kerswell \(2009\)](#) observed that poly-disperse grains have lesser tendency to crystallize especially in the case of tall columns.

For tall columns ($'a' > 2.3$), the flow is still initiated by a well defined failure surface as can be seen in [figure 4.8](#). However, in this case the initial granular column is much higher than the top of the failure surface. Due to gravity most of the grains in the column experience free-fall consuming the column along their way. When they reach the vicinity of the failure surface, the flow gets deviated along the horizontal direction releasing a huge amount of kinetic energy gained during the free fall. For larger aspect ratio ($a > 0.7$), the resulting static region is a cone, the final height of the cone, i.e, H_f lies above the summit of the failure surface. Hence, a different evolution is observed from that of the axis-symmetric geometry ([Lube et al., 2005](#)), where the final height coincides with the summit of the failure surface forming a truncated

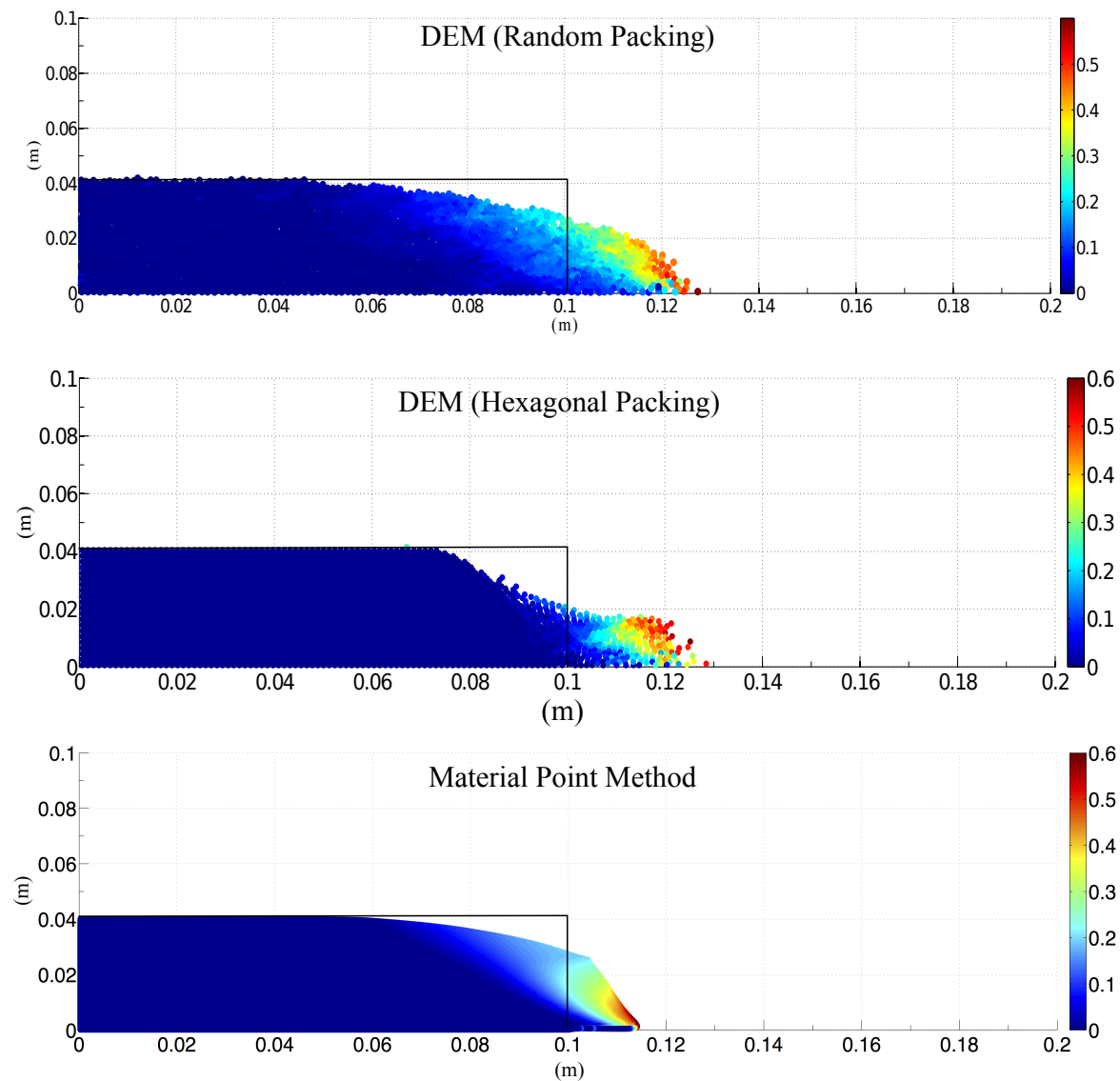


Figure 4.6 Velocity profile of a granular column collapse ($a' = 0.4$ & $t = \tau_c$)

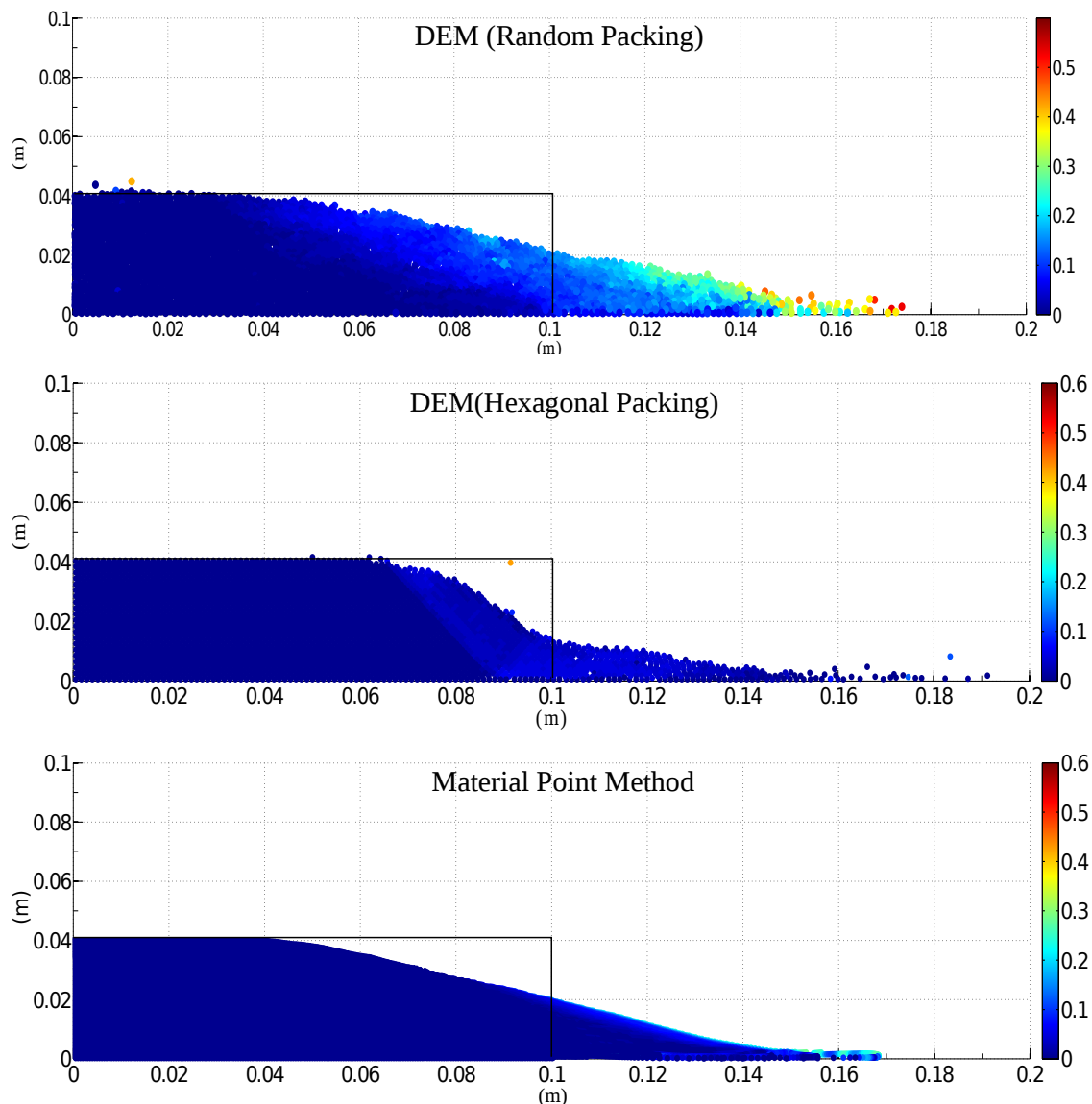


Figure 4.7 Velocity profile of a granular column collapse ($a' = 0.4$ & $t = 3 \times \tau_c$)

¹⁸ conical deposit. [Lajeunesse et al. \(2004\)](#) observed that the variation in the deposit morphology
¹⁹ between the axis-symmetric case and the rectangular collapse to be a geometrical effect rather
²⁰ than as an experimental artefact.

²¹ An initial failure surface starting from the toe end of the column at an angle of about 55°
²² can be observed at the critical time τ_c . As the collapse of the granular collapse progresses,
²³ successive failure planes parallel to the initial failure surface are formed and shear failure occurs
²⁴ along these planes. The presence of several shear bands in the final profile of the collapsed
²⁵ granular column confirms this hypothesis. Crystallisation in hexagonal packing has a significant
²⁶ effect on the run-out distance by forming series of parallel shear bands. However, the Material
²⁷ Point Method fails to capture the formation of shear bands during the collapse. This observation
²⁸ throws light on the mechanics of propagation of shear bands in massive landslides such as
²⁹ the Storegga submarine landslide. The flow behaviour becomes similar to that of columns
³⁰ with lower aspect ratio as the flow starts descending along the failure plane. The final profile
³¹ of the collapsed granular column with an initial aspect ratio of 6 is presented in Figure 4.9.

¹ For tall columns, the dissipation process is more complex due to the free-fall dynamics. The
² vertical acceleration of the grains induces a non-trivial mass distribution in the flow while
³ spreading. This mass distribution plays a dominant role in the power-law scaling law obeyed
⁴ by the run-out ([Staron and Hinch, 2006](#)).

⁵ Regardless of the experimental configuration and the initial aspect ratio of the columns, the
⁶ flow is initiated by a well-defined rupture surface, above which the material slides down leaving
⁷ a static region underneath the failure plane. Depending on the aspect ratio of the column, two
⁸ asymptotic behaviours are observed. For smaller aspect ratios, the flow is dominated by friction
⁹ where as large aspect ratio columns are influenced by the pressure gradient.

¹⁰ To study the influence of aspect ratio on the flow dynamics of granular columns, the flow
¹¹ front $L(t)$ and the maximum height of column $H(t)$ are tracked. The evolution of scaled height
¹² (H_f/L_0) and the run-out distance $(L_f - L_0)/L_0$ with time for granular columns with an initial
¹³ aspect ratio of 0.4 and 6 are presented in figure 4.10. Three distinct regions can be observed
¹⁴ in the flow evolution of granular column collapse regardless of the initial aspect ratio of the
¹⁵ column. An initial transient acceleration phase is observed for a time $0.8\tau_c$. This phase is
¹⁶ followed by a heap movement of granular materials at the foot with a constant spreading
¹⁷ velocity V for about $2\tau_c$. When time ‘ t ’ > τ_c , the velocity varies linearly with depth in the
¹⁸ flowing layer and decreases exponentially with depth near the static layer. This velocity profile
¹⁹ is similar to those observed in steady granular surface flows ([Lajeunesse et al., 2004](#)). Most of
²⁰ the run-out happens during this phase. The final phase involves deceleration of the flow front
²¹ and the flow comes to rest after $0.6\tau_c$. The spreading of the granular column ceases after a time
²² in the order of about $3\tau_c$, however some motion still persists along the free surface behind the

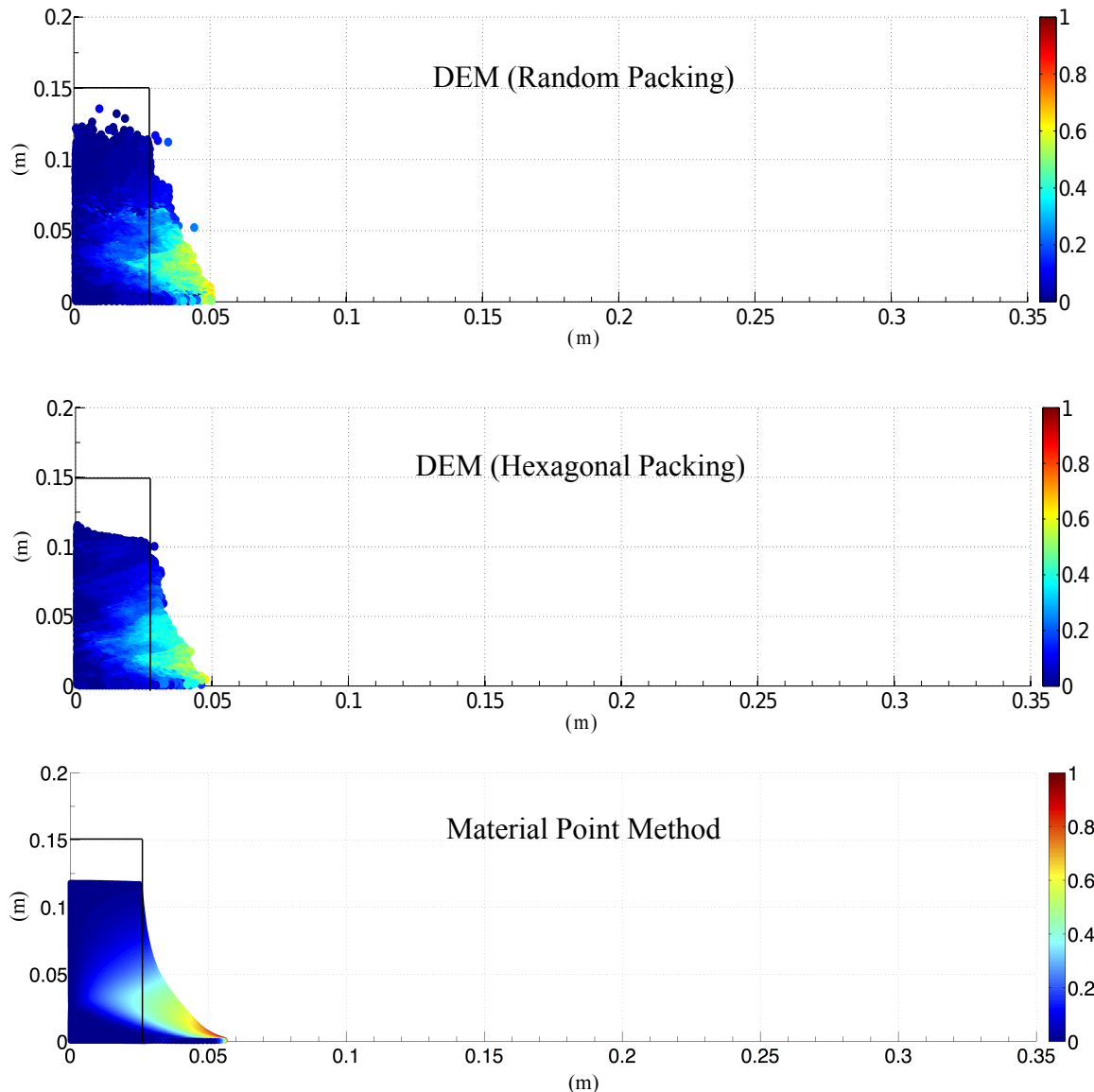


Figure 4.8 Velocity profile of a granular column collapse ($a' = 6$ & $t = \tau_c$)

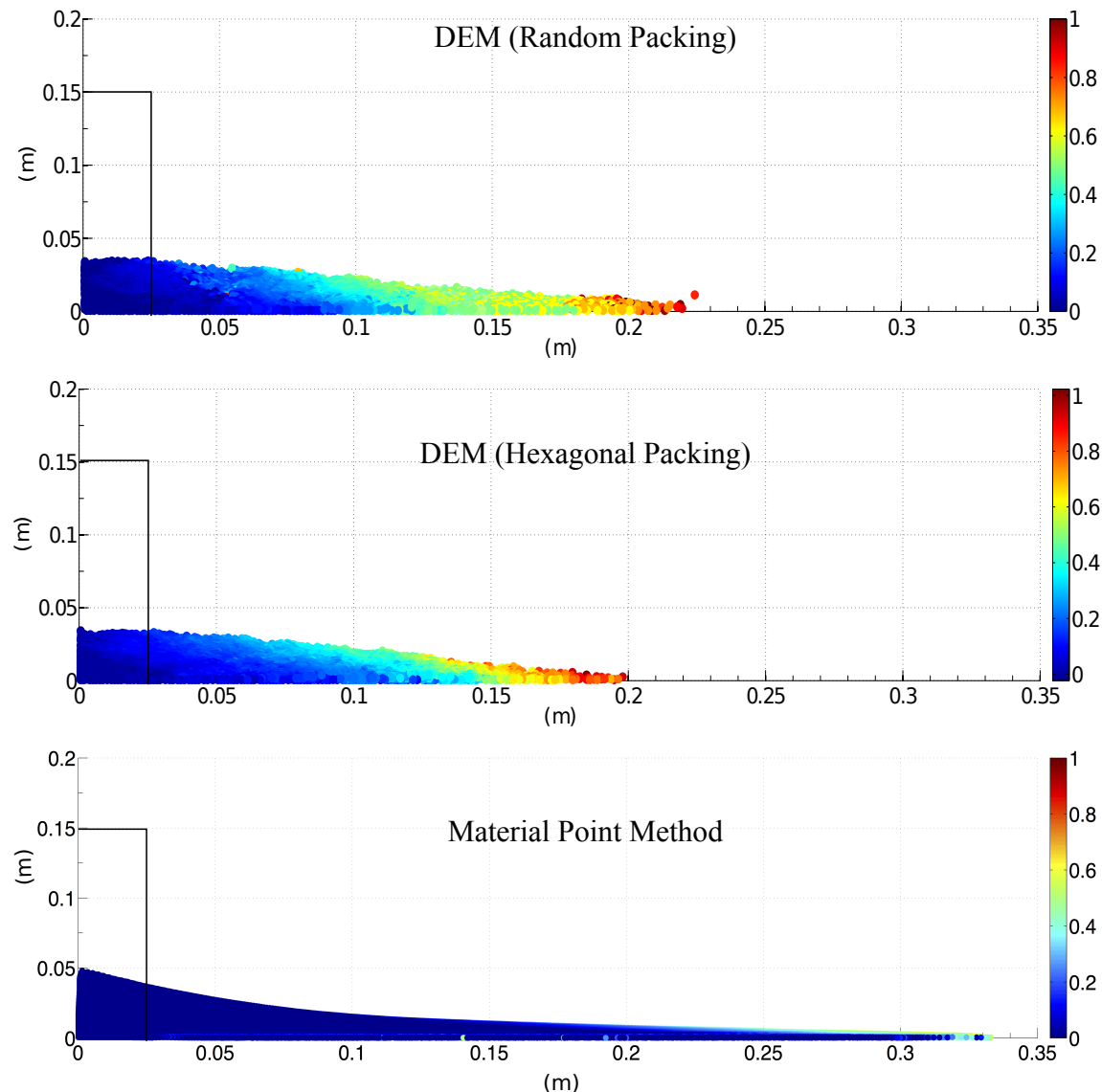


Figure 4.9 Velocity profile of a granular column collapse ($a' = 6$ & $t = 3 \times \tau_c$)

²³ flow front for a much longer time due to internal rearrangement, the duration of which can last
²⁴ up to $t \approx 6\tau_c$.

²⁵ For smaller aspect ratios, the critical time is evaluated as the point of intersection of
²⁶ the scaled run-out and height. The critical time predicted for both hexagonal and random
²⁷ packing of grains matches the experimental observations. However, the Material Point Method
²⁸ overestimates the critical time by a factor of 1.25, which means that it takes longer for the
²⁹ flow to be fully mobilized. However, the actual run-out duration is short and the granular
³⁰ materials comes to rest abruptly at about $t = 3\tau_c$. For columns with larger aspect ratios, the
³¹ continuum and particulate approaches simulate similar flow evolution behaviour for times
³² up to $3\tau_c$, beyond which particulate simulations stabilise and come to rest, while the flow
³³ continues to evolve in MPM simulations resulting in larger run-outs than expected. The flow
³⁴ tends to come to rest at time $t = 6\tau_c$. The three phases in a granular flow can be distinctly
¹ observed in the flow evolution plot for a granular column with initial aspect ratio of 6 (see
² Figure figure 4.10b). For larger aspect ratios, the flow evolution behaviour observed in the
³ case of random packing matches the experimental observation by Lajeunesse et al. (2004).
⁴ Hexagonal packing predicts longer time for the flow to evolve, which can be attributed to the
⁵ increase in the internal resistance due to crystallisation of grains. MPM overestimates the
⁶ critical time by 50%, however has the same value of run-out as the particulate simulations, at
⁷ time $t = 3\tau_c$, beyond which the material continues to flow until it ceases at $6\tau_c$. In order to
⁸ understand the flow dynamics in the case of Material Point Method it is important to study the
⁹ effect of different parameters on the deposit morphology.

¹⁰ 4.2.4 Energy dissipation mechanism

¹¹ The time evolution of the flow exhibited three distinct stages during the collapse of a granular
¹² column. Studying the energy dissipation mechanism provides useful insight into the flow
¹³ dynamics. shows the time evolution of potential energy (E_p) and kinetic energy (E_k) normalized
¹⁴ by the initial potential energy E_o .

$$\begin{aligned} \text{¹⁵} \quad E_p &= \sum_{p=1}^{N_p} m_p g h_p \\ \end{aligned} \tag{4.8}$$

$$\begin{aligned} \text{¹⁶} \quad E_{ki} &= \frac{1}{2} \sum_{p=1}^{N_p} m_p v_p^2 \\ \text{¹⁷} \end{aligned} \tag{4.9}$$

¹⁸ where N_p is the total number of particles, m_p is the mass of a particle ‘ p ’, h_p is the height and
¹⁹ v_p is the velocity of the particle ‘ p ’. It can be observed from the figure that the initial potential
²⁰ energy stored in the particle is converted to kinetic energy which is dissipated as the granular

4.2 Granular column collapse

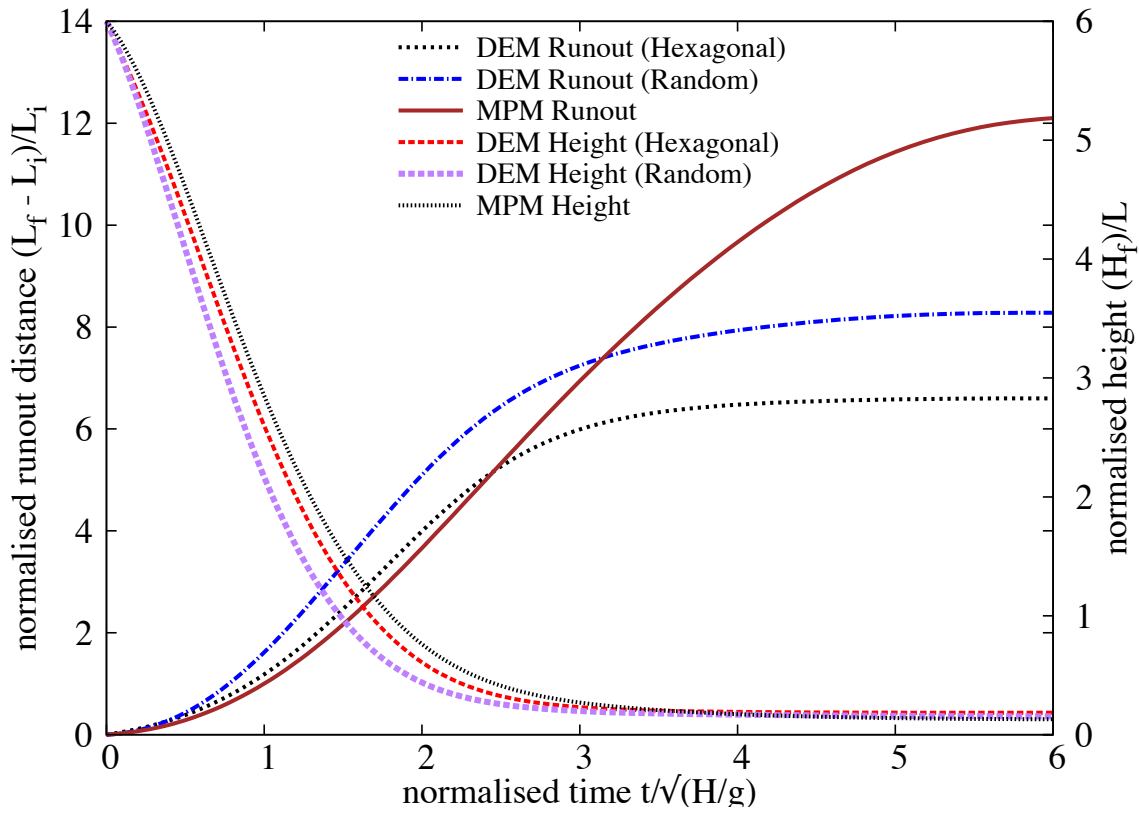
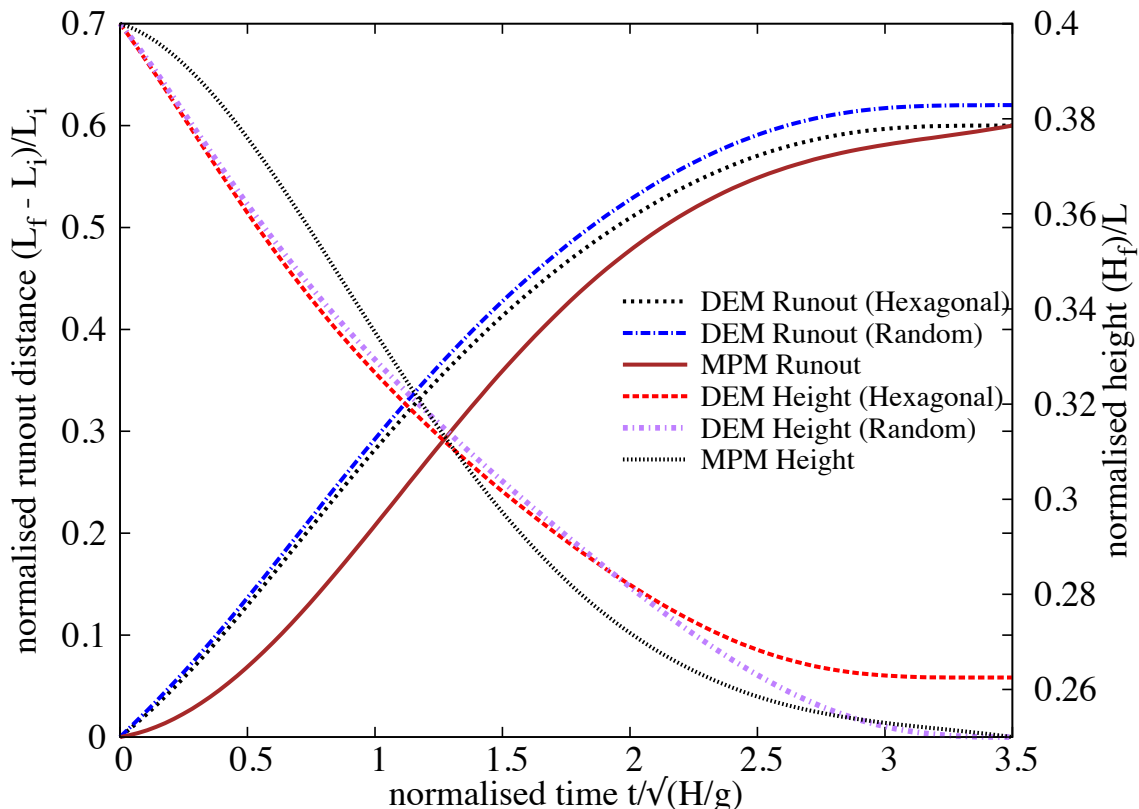


Figure 4.10 Flow evolution of granular column collapse

material flows down. Three successive stages can be identified in the granular column collapse. In the initial acceleration stage ($t < 0.8\tau_c$), the initial potential energy stored in the grains is converted into vertical motion. In the second stage, the grains undergo collisions with the bottom plane and/or with neighbouring grains, and the stored potential energy is converted into horizontal motion. In the third stage, the grains eventually leave the base area of the column and flow sideways. As the process involves collective dynamics of all the particles, it is difficult to predict the exact trajectory of a grain, however, the overall dynamics can be explained. To explain the dissipation of energy during the collapse, [Staron et al. \(2005\)](#) assumed that the total initial potential energy stored in the system is completely dissipated through friction over the entire run-out distance as:

$$\mu m_0 g \times (L_f - L_i) = m_0 g H_o \quad (4.10)$$

where μ is the friction coefficient. The model predicts well the flow dynamics for columns with larger aspect ratios, as most of the initial potential energy is dissipated during the collapse involving the entire column. However, for columns with smaller aspect ratios, only a portion of the mass above the failure surface is involved in the flow. Hence, the energy dissipation should involve only the grains lying above the failure surface. A mathematical model, which considers the grains lying above the failure surface, will be derived to predict the flow dynamics of the granular column collapse for different aspect ratios.

4.2.5 Role of initial grain properties

[Lube et al. \(2005\)](#) observed that the run-out distance scales with the initial aspect ratio of the column, independent of the material properties. The run-out evolution after the initial transition regime is a frictional dissipation process, and the lack of influence of material properties on the run-out behaviour is inconsistent with continuum modelling of granular flow behaviour. [Balmforth and Kerswell \(2005\)](#) observed that the material properties has almost no influence on the exponent of the normalised run-out as a function of the initial aspect ratio. The numerical constant of proportionality, however, showed clear material dependence. This corroborates the conclusions of [Lajeunesse et al. \(2004\)](#) and softens that of [Lube et al. \(2005\)](#). [Daerr and Douady \(1999\)](#) observed the strong influence of initial packing density and the internal structure on the behaviour of granular flows.

It should be noted that the collapse experiment is highly transient and no clear stationary regime was observed. On the contrary, the acceleration and the deceleration phases cover nearly the whole duration of the spreading. This makes the analysis of the structure of the flow and its relation with other characteristic of the system uneasy. Considering this, we were able

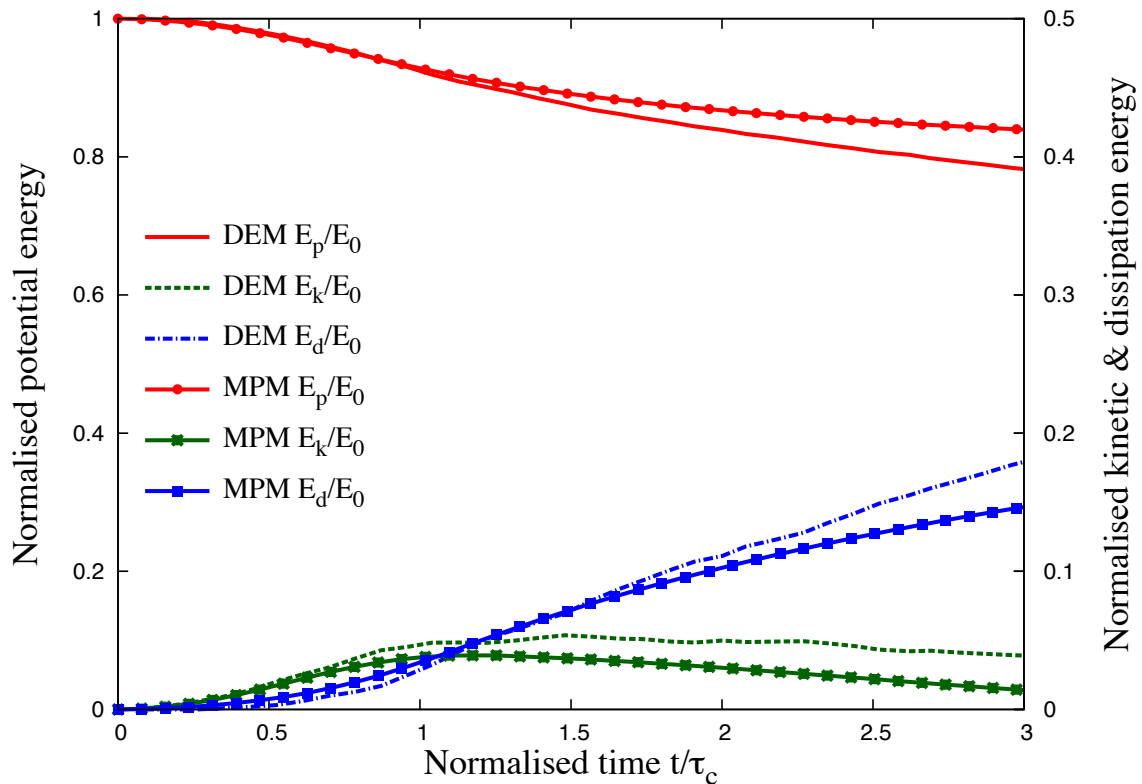
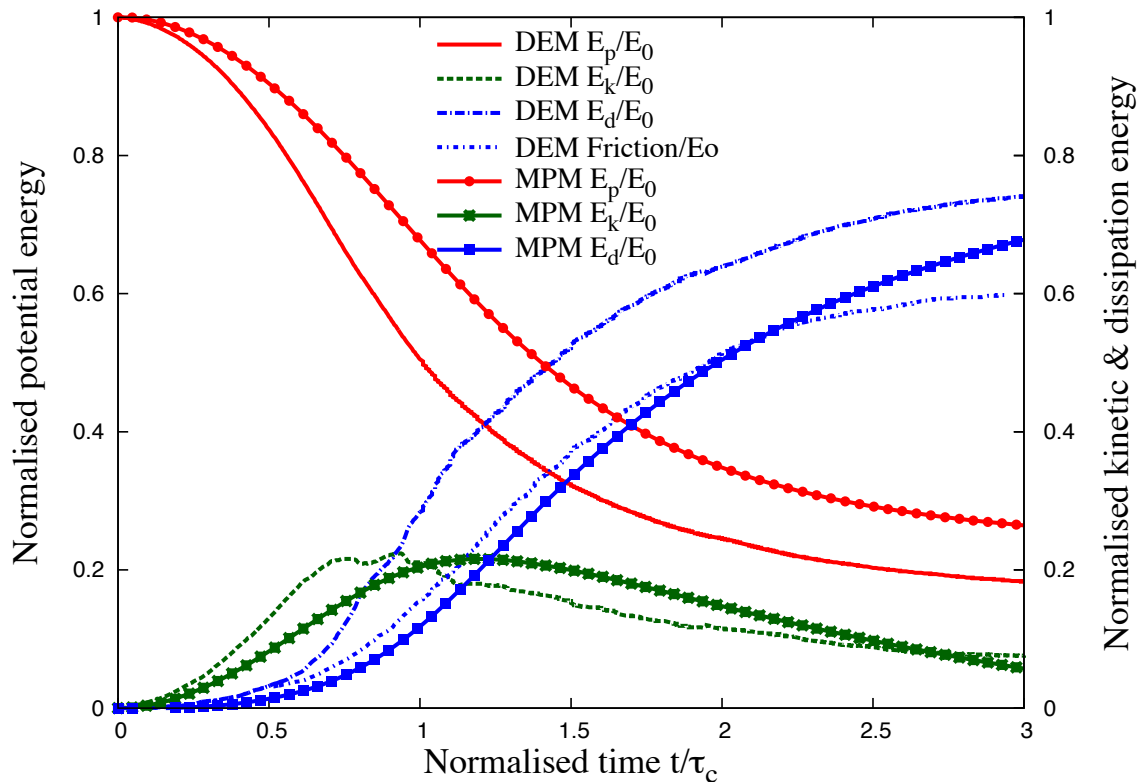
(a) Energy evolution of a column with ' a' = 0.4(b) Energy evolution of a column with ' a' = 6

Figure 4.11 Energy evolution of granular column collapse

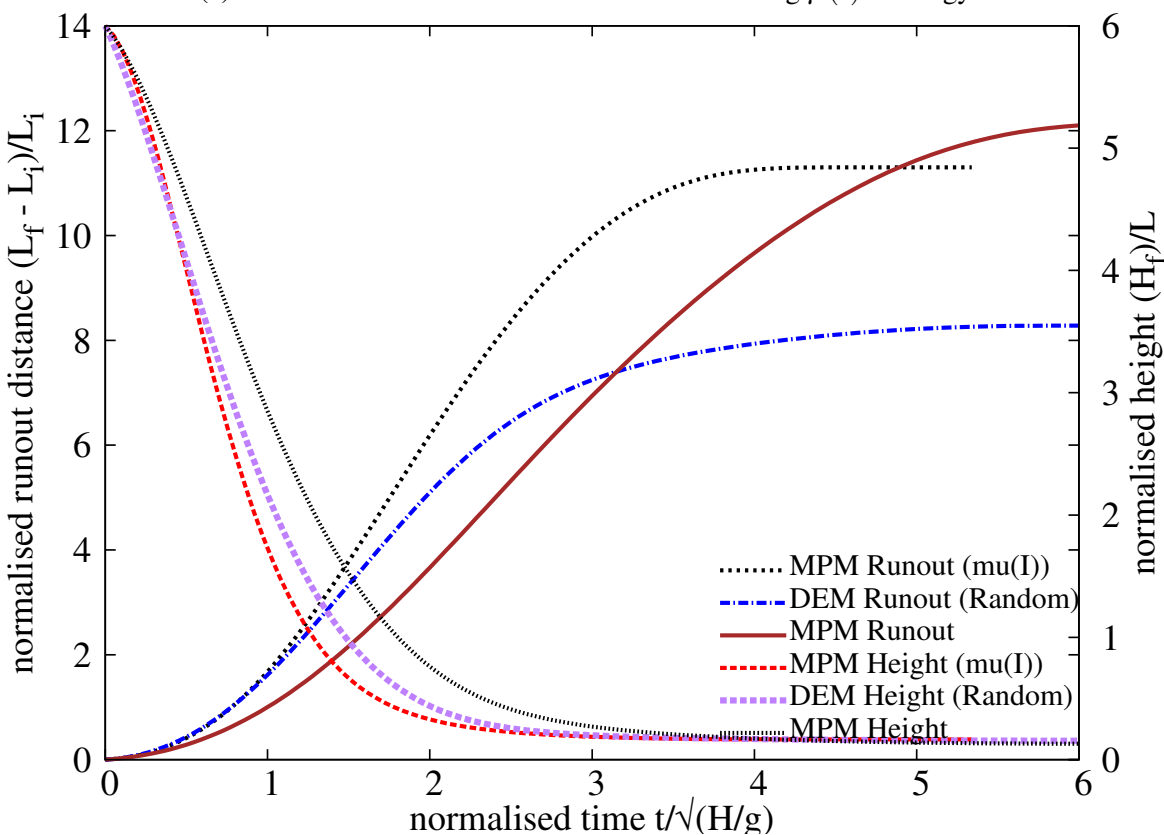
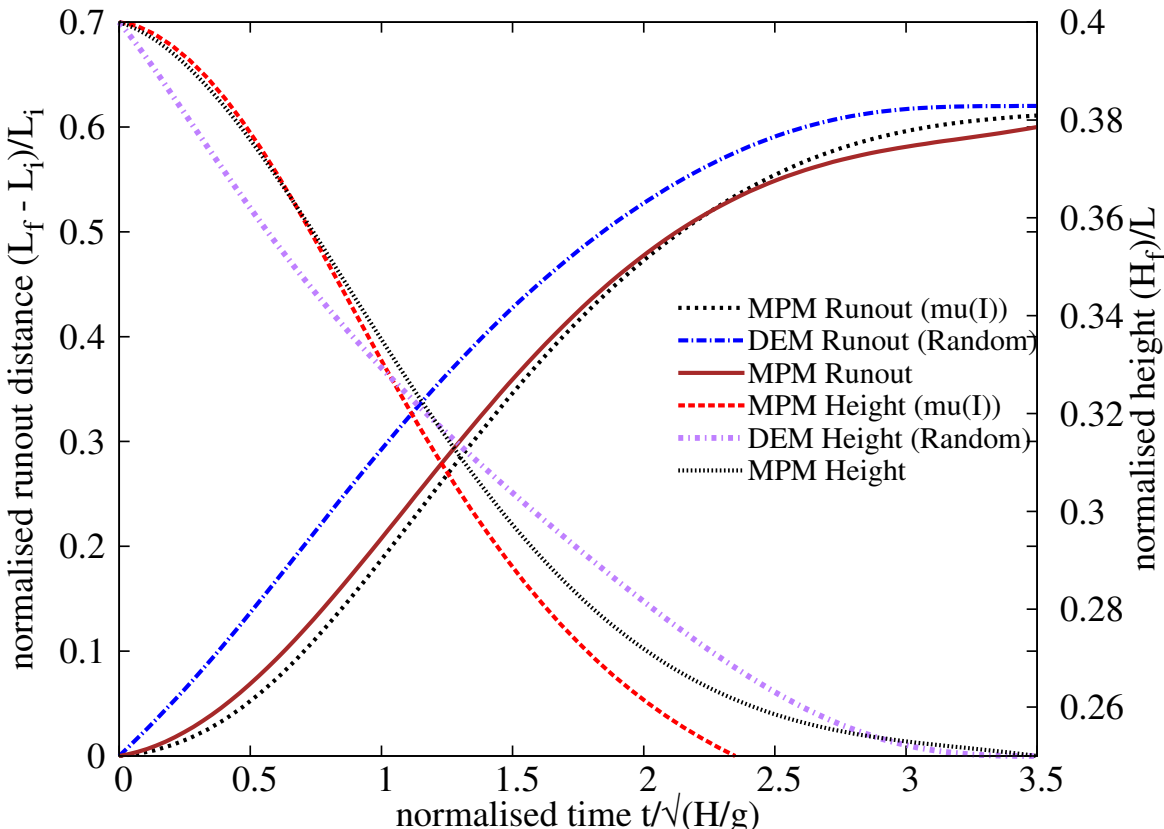


Figure 4.12 Flow evolution of granular column collapse using $\mu(I)$ rheology

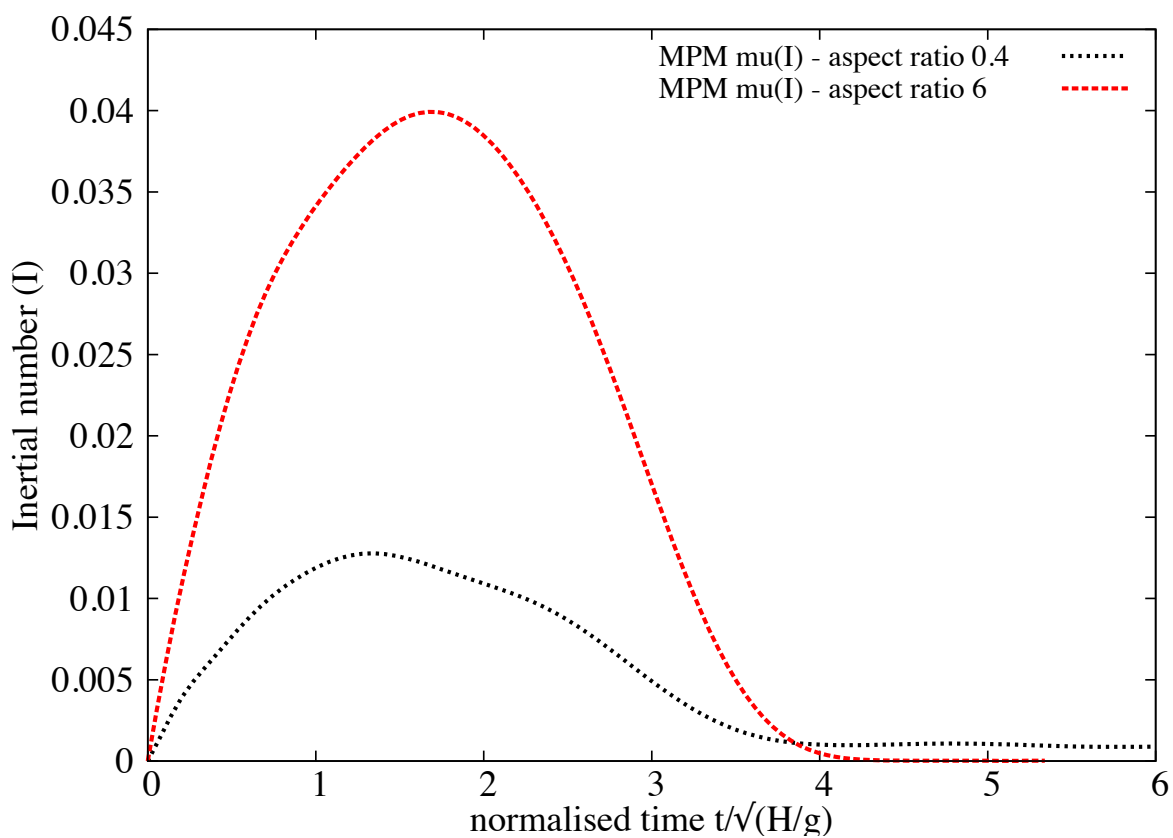


Figure 4.13 Evolution of inertial number with time for columns with ' a' = 0.4 and ' a' = 6

2 to show nevertheless how the initial condition was dominating the behaviour of the spreading
3 through the mass distribution induced in the flow. This means that the knowledge of the final
4 run-out is not a sufficient characterization of the deposit: one also needs to know how mass
5 is distributed to understand the dynamics and the dissipation process. This is expected to
6 be true in natural contexts as well as in experiments. While the inter-grain friction μ does
7 not affect the early vertical dynamics, nor the power-law dependence, it controls the effective
8 frictional properties of the flow, and its internal structure. It is interesting to note that the details
9 of the structure of the flow do not influence the final run-out dependence, and thus seem to
10 play a marginal role in the overall behaviour of the spreading. This could explain why simple
11 shallow-water model with basic rheology but where the free-fall dynamics was accounted for
12 could reproduce the run-out scalings.

13 At this stage, it appears that the collapse experiment for large aspect ratios mixes two very
14 different dynamics: while the second stage consists of a “conventional” horizontal granular
15 flows, the first stage implies a large vertical acceleration. It shows how the initial condition can
16 influence the overall behaviour of a granular system, and suggests that triggering mechanisms
17 play a crucial role in the case of natural flows. This stresses the necessity of accounting for
18 vertical acceleration in continuum models in the perspective of producing realistic prediction
19 of the behaviour of granular flows.

20 The numerical constants of proportionality, however, show clear material dependence. This
21 corroborates the conclusion of [Balmforth and Kerswell \(2005\)](#); [Lajeunesse et al. \(2004\)](#) and
22 softens that of [Lube et al. \(2005\)](#).

23 **4.3 Slopes subjected to impact loading**

24 Transient granular flows occur very often in nature. Well-known examples are rockfalls, debris
25 flows, and aerial and submarine avalanches. They form a major element of landscape reshape
and their high destructive potential is a substantial factor of risk. Natural granular flows may be
triggered as a result of different processes such as gradual degradation, induced by weathering
or chemical reactions, liquefaction and external forces such as earthquakes.

Granular flows have been studied in laboratory experiments in different geometries such as
tilted piles leading to slope failure and surface avalanches ([Iverson, 1997](#); ?) or by considering
vertical columns of grains collapsing and spreading under their own weight ([Lajeunesse et al.,](#)
[2004, 2005](#)). The dynamics observed in the experiments is often nontrivial in the sense that
the final configurations after the dissipation of the whole kinetic energy can not be readily
predicted by means of simple laws based on the Mohr-Coulomb nature of the material. For

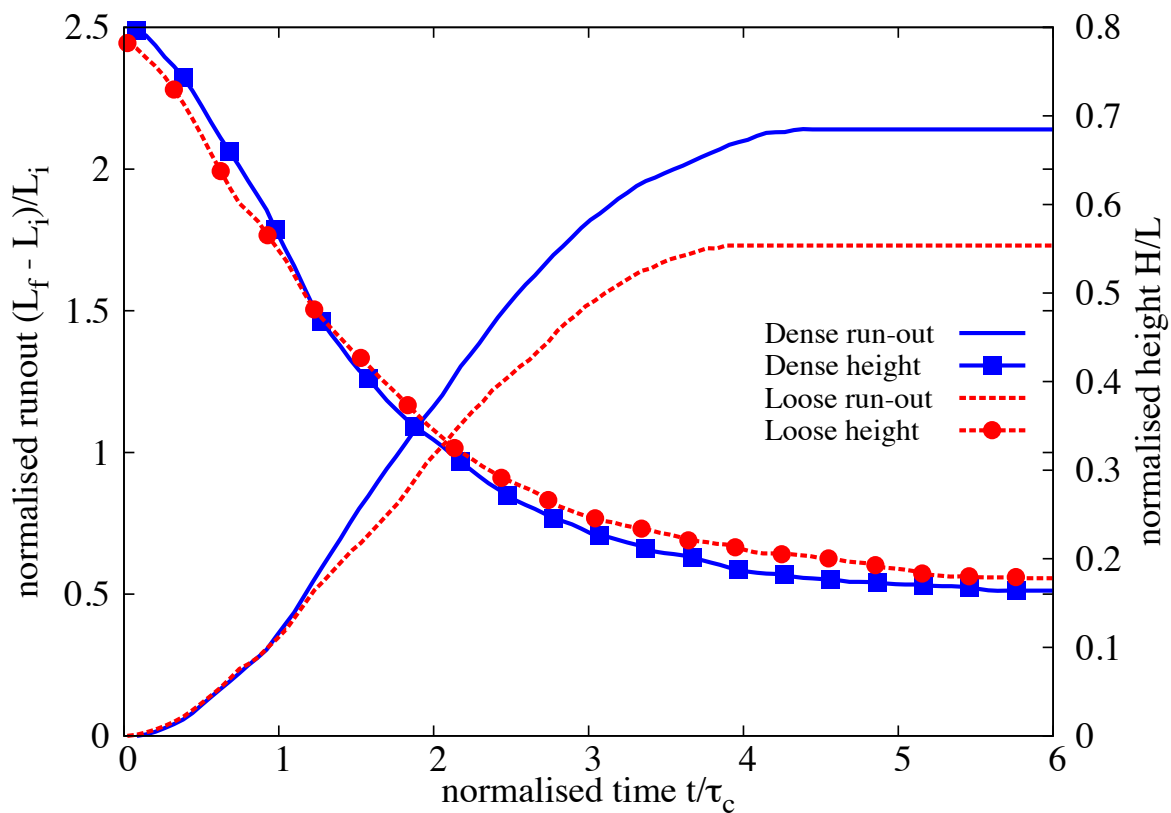
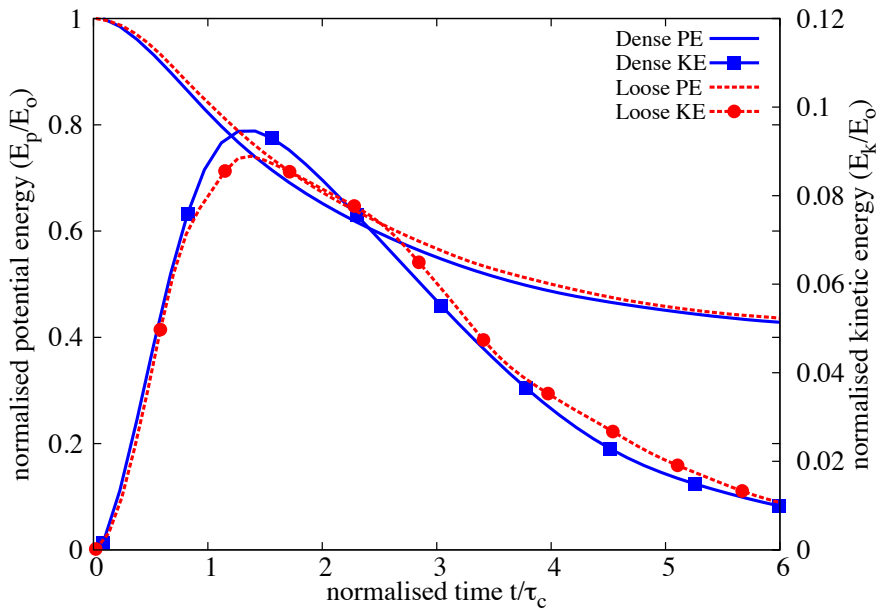
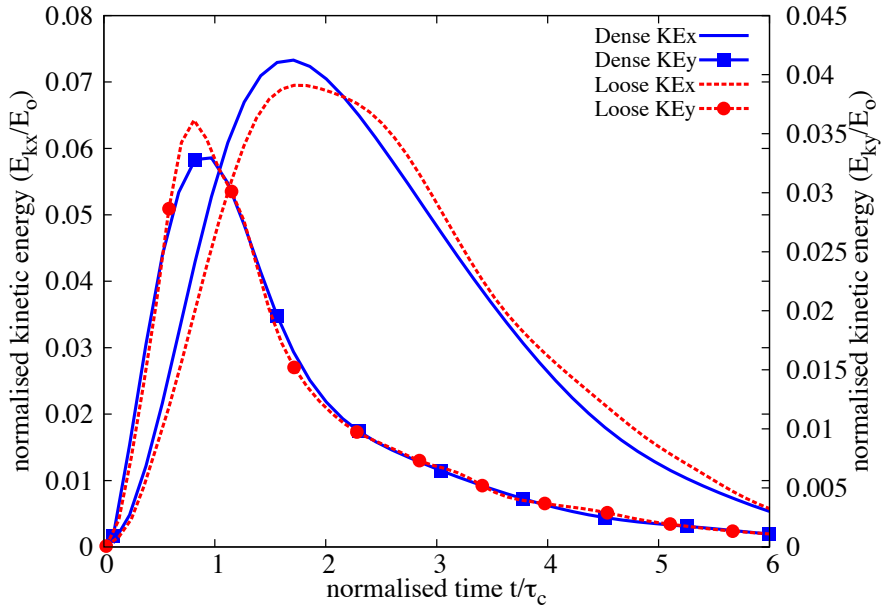


Figure 4.14 Effect of density on run-out evolution ' a' = 0.8

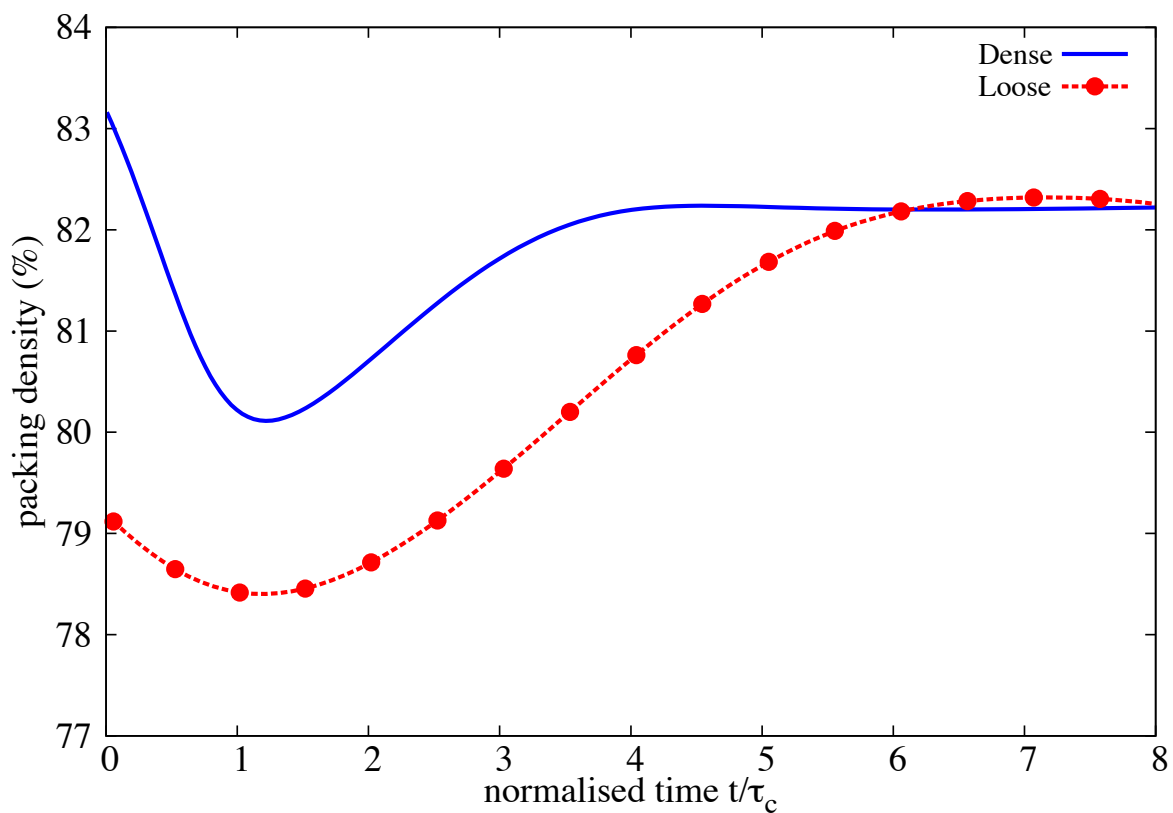


(a) Evolution of potential and kinetic energy



(b) Effect of kinetic energy

Figure 4.15 Effect of density on energy evolution $a = 0.8$

Figure 4.16 Evolution of local packing density ' a' = 0.8

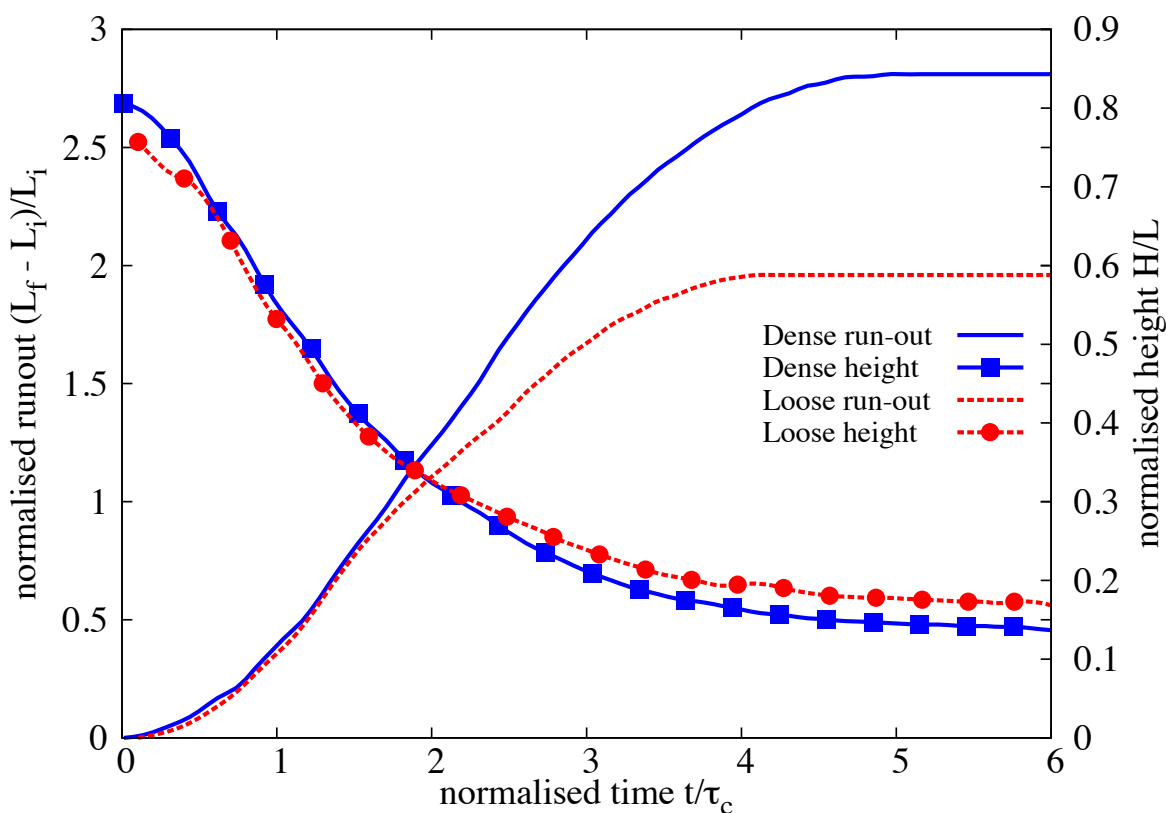


Figure 4.17 Effect of density on run-out evolution ' a' = 0.8 (poly-dispersity ' r ' = 6)

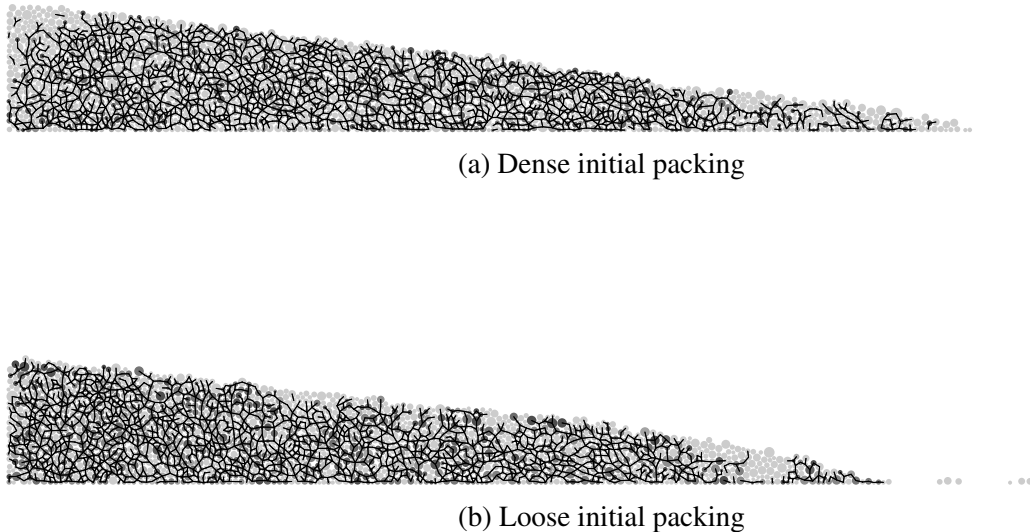
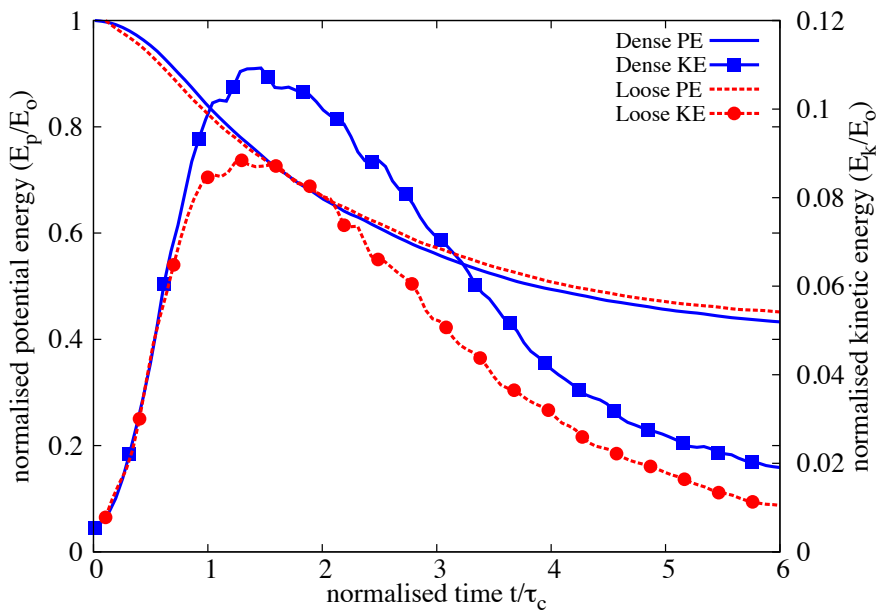


Figure 4.18 Snapshots of granular column collapse $t = 6\tau_c$

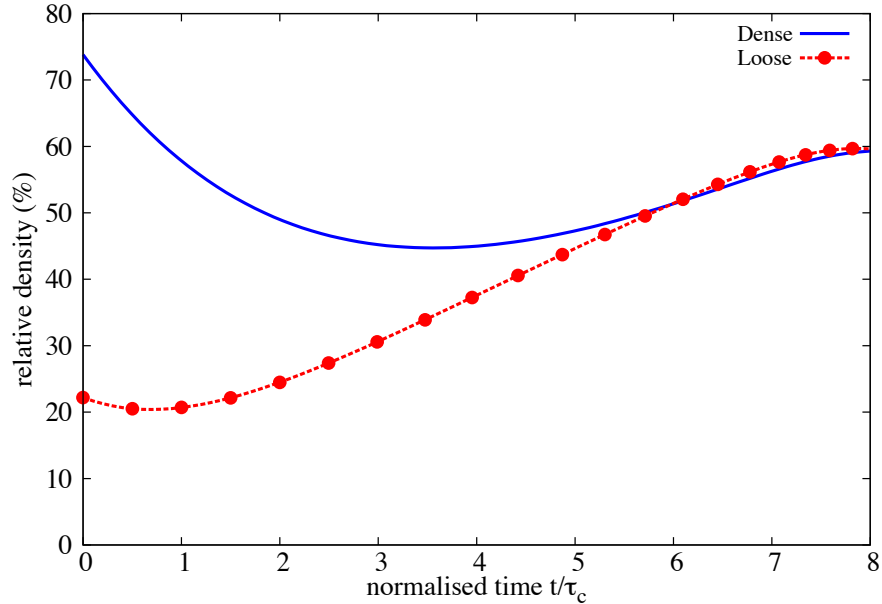
example, in collapsing columns, the run-out distance is found to obey a power-law dependence upon the initial aspect ratio of the column.

The observed nontrivial transient dynamics is often correctly reproduced by the DEM, which provides a powerful tool for the grain-scale analysis of the trigger and its subsequent dynamics (Staron and Lajeunesse, 2009; Staron et al., 2005). However, even in simplified geometries such as those investigated in the experiments, the DEM suffers from a serious short-coming in the number of particles that can be simulated in a reasonable time. This is a critical issue when more complex geometries or long-time granular processes are considered, or when particle size distributions are broad. For this reason, most numerical studies are performed in 2D or simple particles shapes and size distributions are considered.

It is also obvious that classical modelling strategies based on the finite element method (FEM) cannot be used for the simulation of very large deformations. In various application of FEM, this problem is treated by means of technical tools such as re-meshing. Such methods are, however, not robust and lead to round-off errors and mesh-sensitivity. In contrast, the so-called Material Point Method (MPM) is an alternative approach for continuum problems that allows for indefinitely large deformations without re-meshing ?. In this method, the material points carry the information on state variables and a background fixed grid is used to solve the governing equations. The information between the material points and the grid is exchanged via suitable shape functions. The MPM has been applied with success to a number of solid



(a) Evolution of potential and kinetic energy

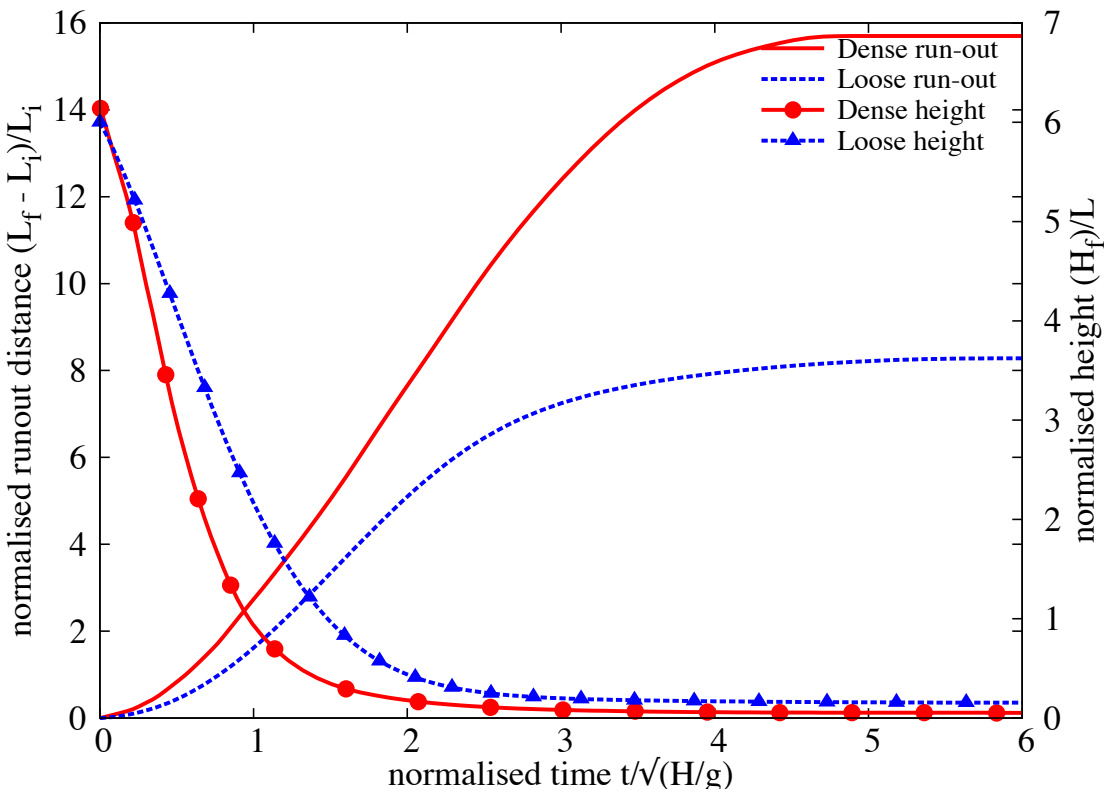


(b) Evolution of packing density

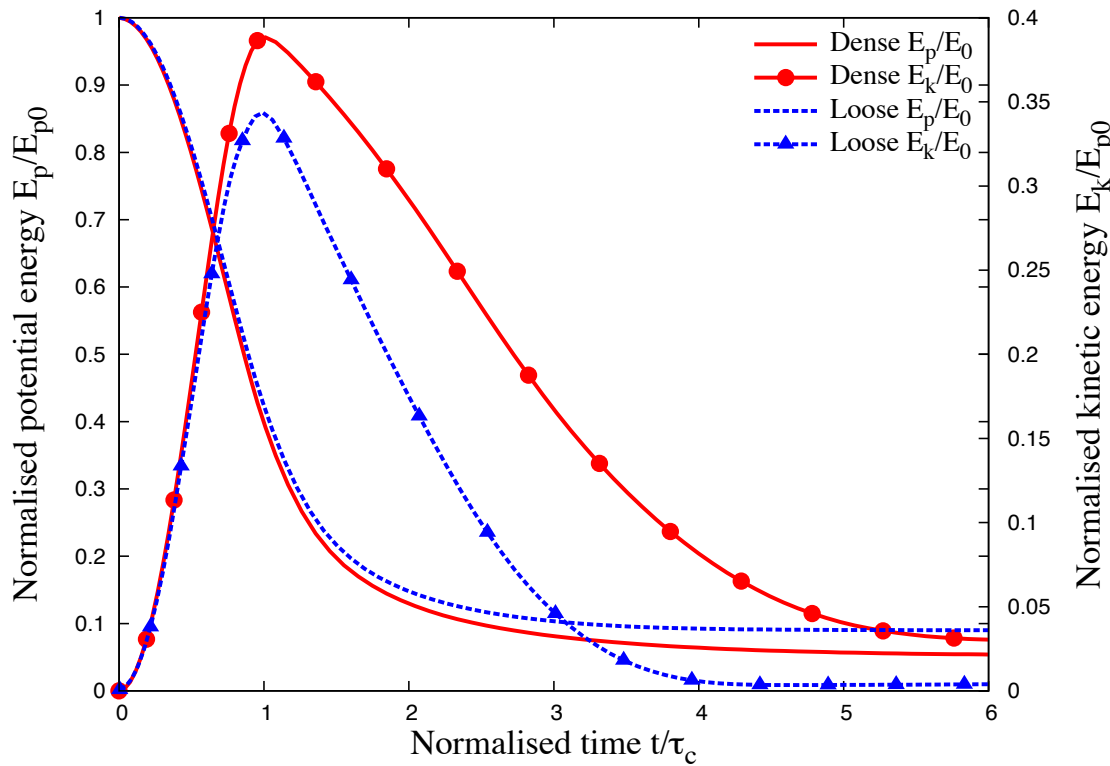
Figure 4.19 Effect of density on energy and packing fraction evolution ' a' = 0.8 (poly-dispersity ' r ' = 6)

4.3 Slopes subjected to impact loading

101



(a) Effect of density on run-out evolution



(b) Effect of density on energy evolution

Figure 4.20 Effect of density on run-out behaviour and energy evolution ' a' = 0.6

mechanics problems and its theoretical foundations have recently been investigated by several authors.

In this paper, we are concerned with the ability of the MPM, as a continuum approach, to reproduce the evolution of a granular pile under its own weight or when destabilized by energy input. In particular, a central issue is whether power-law dependence of the run-out distance and time with respect to the initial geometry or energy can be reproduced by a simple prescription of the Mohr-Coulomb plastic behaviour within a MPM code. We therefore perform extensive simulations by varying continuously different input parameters and compare the data with those obtained from DEM simulations of the same system. We compare in detail the evolution of the profile of the pile and its total kinetic energy between the two methods and for different initial states. As we shall see, the MPM can successfully simulate the transient evolution with a single input parameter, namely the internal angle of friction. This opens the way to the simulation of geological-scale flows on complex topographies.

4.3.1 Numerical procedures

The numerical samples are composed of ~ 13000 disks with a uniform distribution of diameters by volume fractions in the range $[d_{min}, d_{max}]$ with $d_{max} = 1.5d_{min}$. The mean particle diameter and mass are $d \simeq 0.0025$ m and $m \simeq 0.0123$ kg, respectively. The particles are first poured uniformly into a rectangular box of given width and then the right-hand side wall is shifted further to the right to allow the particles to spread. A half-pile is obtained when all particles come to rest; see ???. This procedure leads to a mean packing fraction $\simeq 0.83$.

Table 4.4 DEM simulation of simple shear test (?)

Parameter	Value
Mean grain diameter	≈ 2.455 mm
Grain diameter $[d_{min} : d_{max}]$	[2.0, 3.0] mm
Friction coefficient	0.4
Grain density	2600kg m^{-3}
Restitution coefficient	0
Number of grains	1174

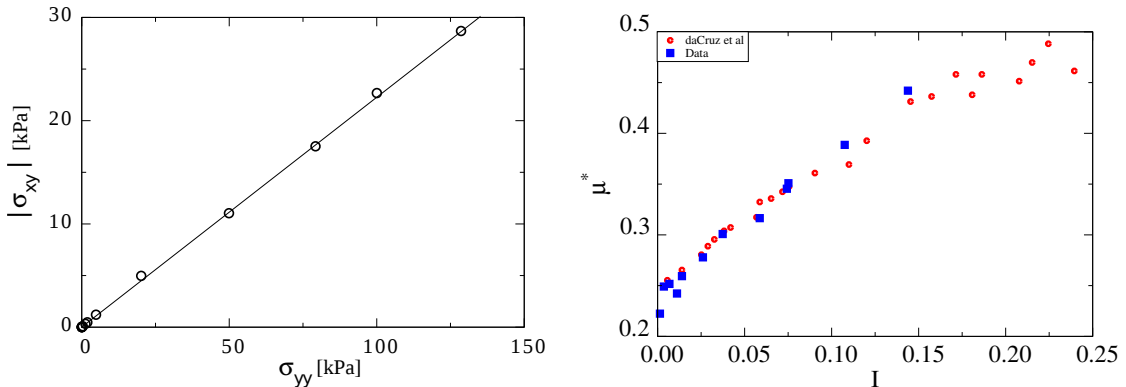
The initial static pile is set into motion by applying a constant horizontal gradient $v_{0x}(y) = k(y_{max} - y)$ with $k > 0$. Such a configuration mimics the energy transfer mechanism of a horizontal quake along the bottom of the pile. We are interested in the evolution of the geometry of the pile and its total kinetic energy as a function of the initial input energy E_0 . The run-out distance R_f is the distance of the rightmost particles from the left wall when the pile

¹⁹ comes to rest. It will be normalized by the initial extension R_0 of the pile, as in the experiments
²⁰ of collapsing columns. The total run-out duration t_f is the time that the pile takes to reach its
²¹ final run-out distance R_f .

²² The initial static pile is set into motion by applying a horizontal velocity $v_{0x}(y)$ to all
²³ particles during a short interval of time. Different velocity fields were tested: 1) The same
²⁴ velocity $v_{0x}(y) = v_0$ applied to all particles, 2) The same velocity $v_{0x}(y) = v_0$ applied to a
¹ column of particles next to the left wall, 3) a constant velocity gradient $v_{0x}(y) = k(y_{max} - y)$
² with $k > 0$. The first two pushing modes mimic the case of a pile impacted from the left
³ by a moving mass (tsunami, debris...) whereas the last mode represents energy transfer by
⁴ horizontal quake of the bottom line. We will compare briefly below the effect of different
⁵ pushing modes, but later we will mainly explore the third mode. We are interested in the
⁶ evolution of the geometry of the pile and its total kinetic energy as a function of the initial
⁷ energy input E_0 . The run-out distance R_f is the distance of the rightmost particles from the left
⁸ wall when the pile comes to rest. It will be normalized by the initial extension R_0 of the pile,
⁹ as in the experiments of collapsing columns. The total run-out duration t_f is the time that the pile
¹⁰ takes to reach its final run-out distance R_f .

For grain scale simulations, classical DEM and Contact Dynamics approach is used. A
¹¹ detailed description of the Contact Dynamics method can be found in [Jean \(1999\)](#); [Radjai](#)
¹² and [Dubois \(2011\)](#); [Radjai and Richefeu \(2009\)](#); ?. This method is based on implicit time
¹³ integration of the equations of motion and a nonsmooth formulation of mutual exclusion and
¹⁴ dry friction between particles. The CD method requires no elastic repulsive potential and no
¹⁵ smoothing of the Coulomb friction law for the determination of forces. For this reason, the
¹⁶ simulations can be performed with large time steps compared to discrete element simulations.
¹⁷ The unknown variables are particle velocities and contact forces, which are calculated at each
¹⁸ time step by taking into account the conservation of momenta and the constraints due to mutual
¹⁹ exclusion between particles and the Coulomb friction. We use an iterative research algorithm
²⁰ based on a nonlinear Gauss-Seidel scheme. The only contact parameters within the CD method
²¹ are the friction coefficient μ_s , the normal restitution coefficient e_n and the tangential restitution
²² coefficient e_t between particles. We will investigate the effect of these parameters on the
²³ evolution of kinetic energy and the profile of the pile.

The natural units of our system are the mean particle diameter d , mean particle mass m
²⁵ and gravity g . For this reason, in the following we normalize the lengths by d , the times by
²⁶ $(d/g)^{1/2}$, the velocities by $(gd)^{1/2}$ and the energies by mgd .



(a) Evaluating the critical state friction angle from periodic shear test. (b) Evolution of Inertial number with friction μ

Figure 4.21 Periodic shear test using CD (?).

4.3.2 Evolution of pile geometry and run-out

In this section, we consider the spreading process following the initial energy input into the pile. Fig. ?? shows several snapshots of the pile for an initial input energy $E_0 = 61$ (in dimensionless units). The pile is sheared from the bottom to the top, thus leaving a cavity in the vicinity of the left wall. The cavity is partially filled while the pile continues to spread to the right.

In this section, we consider the spreading process following the initial energy input into the pile. Fig. ?? shows several snapshots of the pile for each pushing mode and for the same initial energy $E_0 = 61$ (in dimensionless units). In mode 1, where the same velocity is imparted to all particles, the whole pile moves away from the left wall over a short distance and then it spreads out and declines in slope. The spreading continues farther until the slope nearly declines to zero. In mode 2, where the velocity is applied to a column of particles next to the left wall, the particles belonging to the column are literally expelled from the pile. They fall back farther way on the pile after a ballistic travel above the pile. At the same time, the right side of the pile slightly spreads away while the left side is filled by the particles rolling down into the gap left by the column. In mode 3, the pile is sheared from the bottom to the top, leaving thus a cavity in the vicinity of the left wall. The cavity is partially filled while the pile continues to spread.

All pushing modes involve a transient with a sharp change of the geometry of the pile followed by continuous spreading to the right. In mode 2, most of the energy is carried away by the ejected particles. In mode 1, the pile has a rigid-body velocity component and moves away from the left wall, but shows an efficient energy transfer leading to a long run-out distance. The transient is more energy consuming in mode 3 compared to mode 1. For this reason, the run-out distance in mode 3 is long but shorter than in mode 1. In the following, we analyze in more detail the evolution of the pile in mode 3, which mimics a horizontal quake from the bottom

and, despite the creation of a cavity, remains always in contact with the left wall irrespective of the input energy.

Figure 4.4 shows the normalized run-out distance $(R_f - R_0)/R_0$ and total run-out time t_f as a function of the input energy E_0 . We observe two regimes both characterized by a power-law run-out distance and time as a function of E_0 . In the first regime, corresponding to the range of low input energies $E_0 < 40 \text{ mgd}$, the run-out distance varies as $R_f \propto (E_0)^\alpha$ with $\alpha \simeq 0.61 \pm 0.04$ over nearly one decade while the duration keeps a constant value $t_f \simeq 60 (d/g)^{0.5}$ irrespective of the value of E_0 ! The error on the value of the exponent represents the confidence interval of linear fits on the logarithmic scale. An average run-out speed can be defined from the ratio $v_s = (R_f - R_0)/t_f$. According to the data, we have $v_s \propto (E_0)^{0.61 \pm 0.04}$. Since the initial average velocity varies as $v_0 \propto (E_0)^{0.5}$, this difference between the values of the exponents suggests that the mobilized mass during run-out declines when the input energy is increased. As we shall see below, the constant run-out time reflects also the collapse of the particles into the cavity left behind the pile.

In the second regime, corresponding to the range of high input energies $E_0 > 40 \text{ mgd}$, the run-out distance varies as $R_f \propto (E_0)^{\alpha'}$ over one decade with $\alpha' \simeq 0.77 \pm 0.03$ while the duration increases as $t_f \propto (E_0)^{\beta'}$ with $\beta' \simeq 0.21 \pm 0.04$. Hence, in this regime the average run-out speed varies as $v_s \propto (E_0)^{0.56 \pm 0.07}$. This exponent is close to the value 0.5 in $v_0 \propto (E_0)^{0.5}$, and hence, within the confidence interval of the exponents, in the second regime we may assume $\beta' \simeq \alpha' - 0.5$ and $v_s \propto v_0$.

It is worth noting that a similar power-law dependence of the run-out distance and time were found in the case of collapsing columns of grains with respect to the initial aspect ratio Topin et al. (2012). In the column geometry, the particles spread away owing to the kinetic energy acquired during gravitational collapse of the column. Topin et al. found that the run-out distance varies as a power law of the available peak kinetic energy at the end of the free-fall stage with an exponent $\simeq 0.5$. This value is below those obtained here for both regimes. This is, however, physically plausible since the distribution of particle kinetic energies at the end of the collapse is more chaotic than in our simulations where the energy is supplied from the very beginning in a well-defined shear mode. As pointed out by Staron et al. (2005), the distribution of kinetic energies is an essential factor for the run-out distance.

4.3.3 Decay of kinetic energy

The non-trivial evolution of the pile geometry in two regimes suggests that the energy supplied to the pile is not simply dissipated by shear and friction with the bottom plane. We also need to split the kinetic energy into its different components (x , y and rotation) of the velocity field. The input energy is in the x component, but due to both the creation of a cavity next to the left

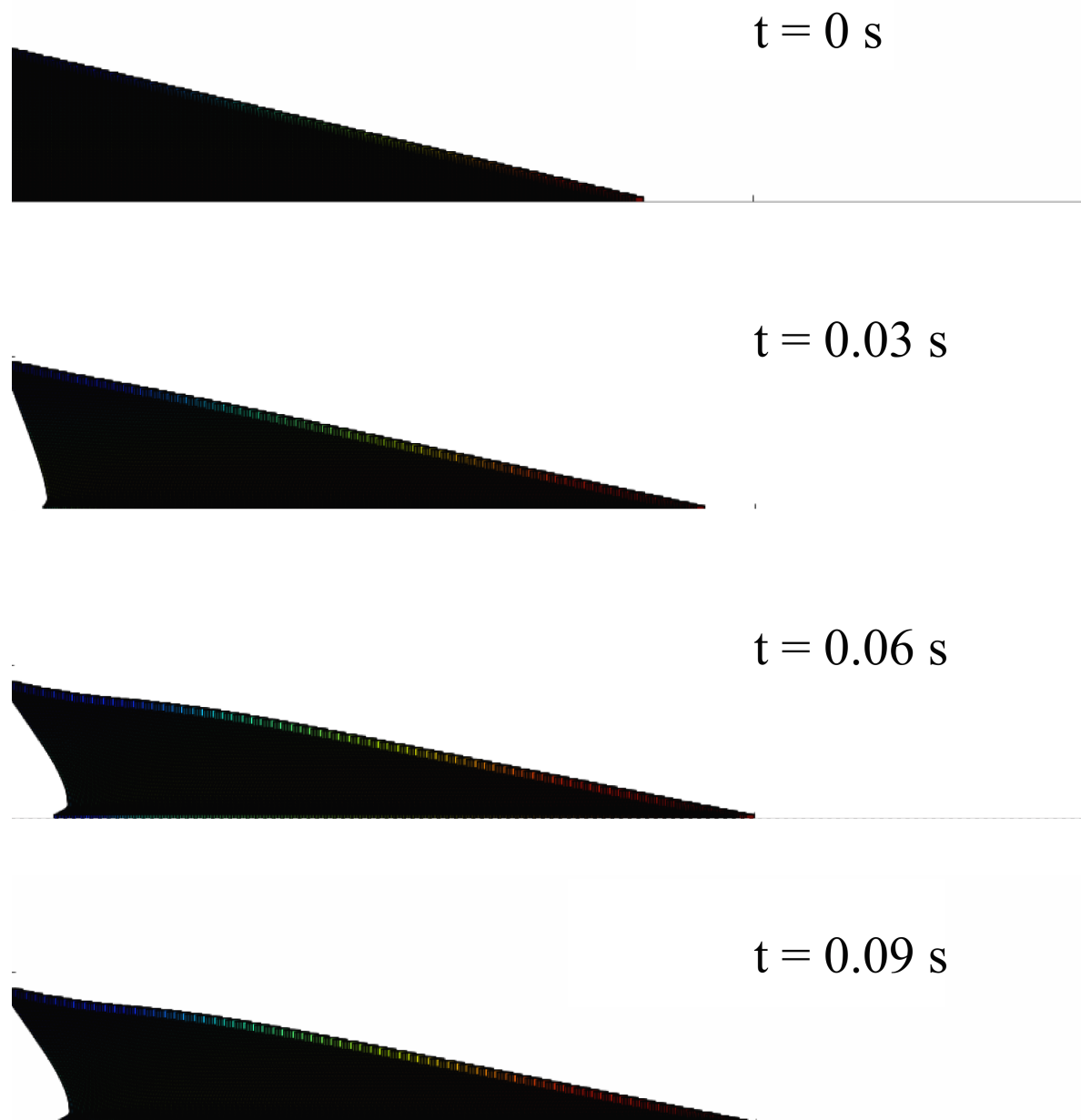


Figure 4.22 Snapshots of MPM simulations of the evolution of granular pile subjected to a gradient impact energy.

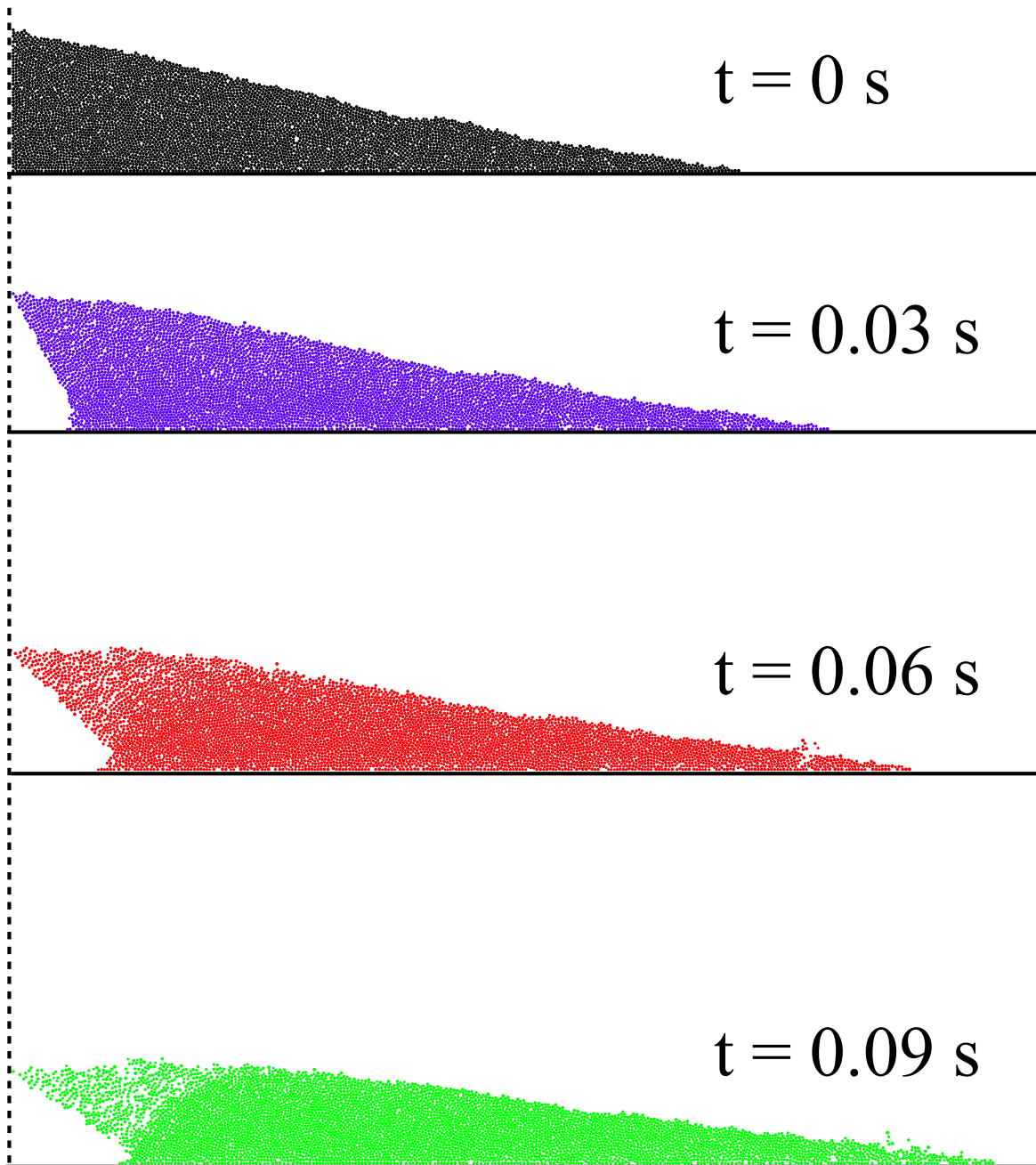


Figure 4.23 Snapshots of CD simulations of the evolution of granular pile subjected to a gradient impact energy (?).

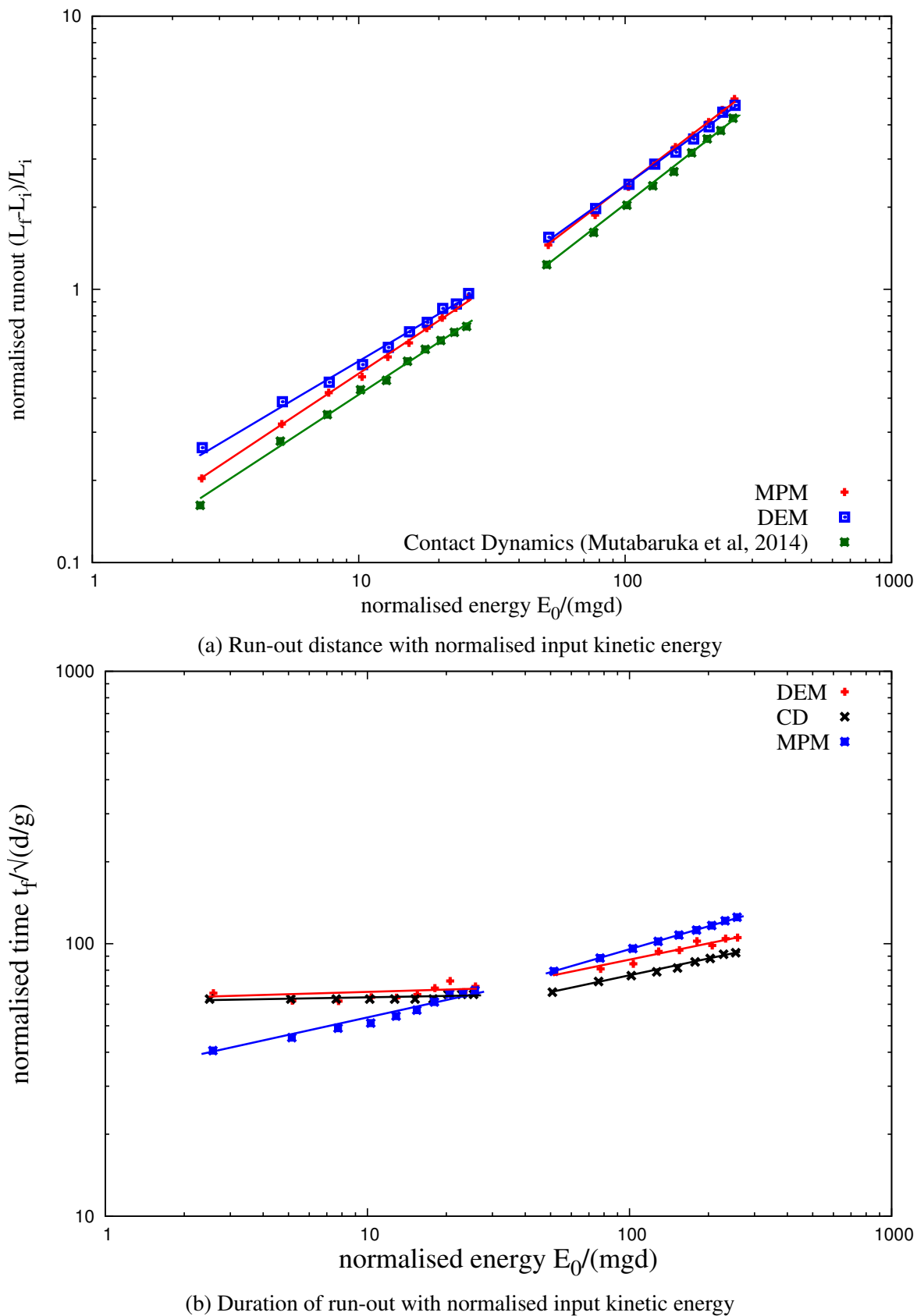


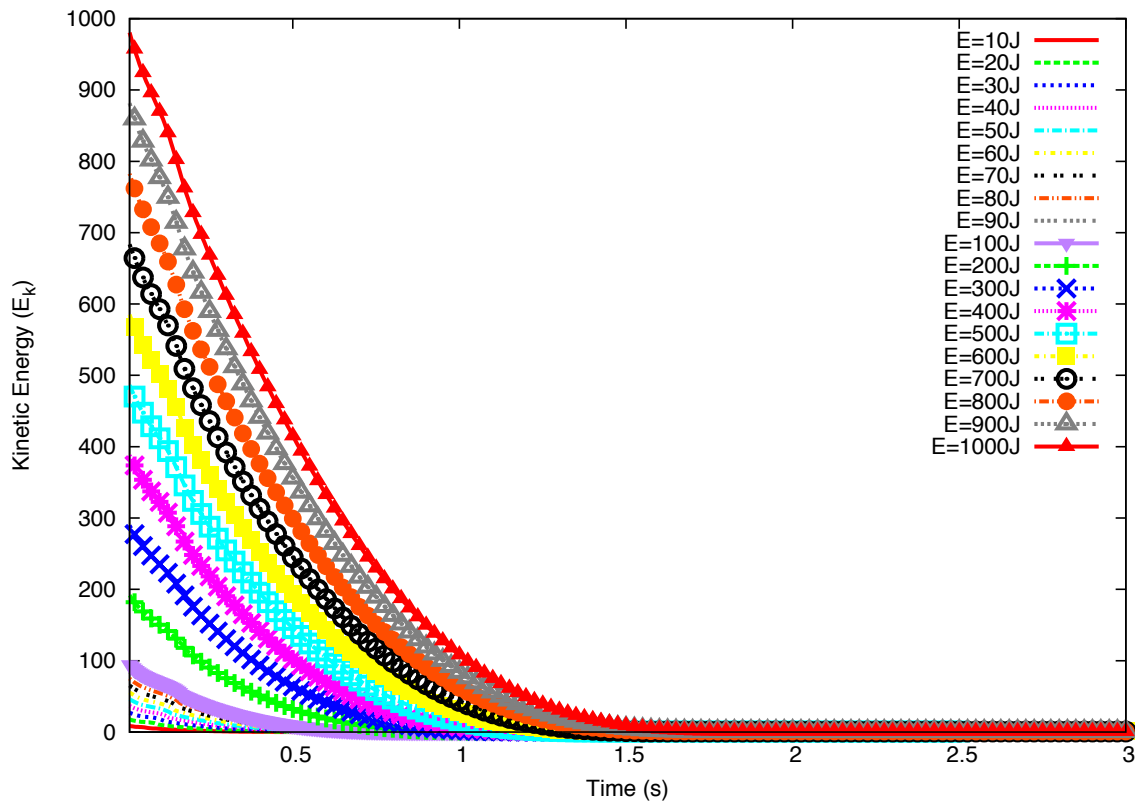
Figure 4.24 Run-out behaviour of a pile subjected a gradient impact energy

wall and the rolling of the particles down the free surface of the pile and between particles, a fraction of the energy is first transferred to the y component of the velocity field and dissipated during the transient. In this section, we analyse these features in order to arrive in a picture consistent with the evolution of the pile shape.

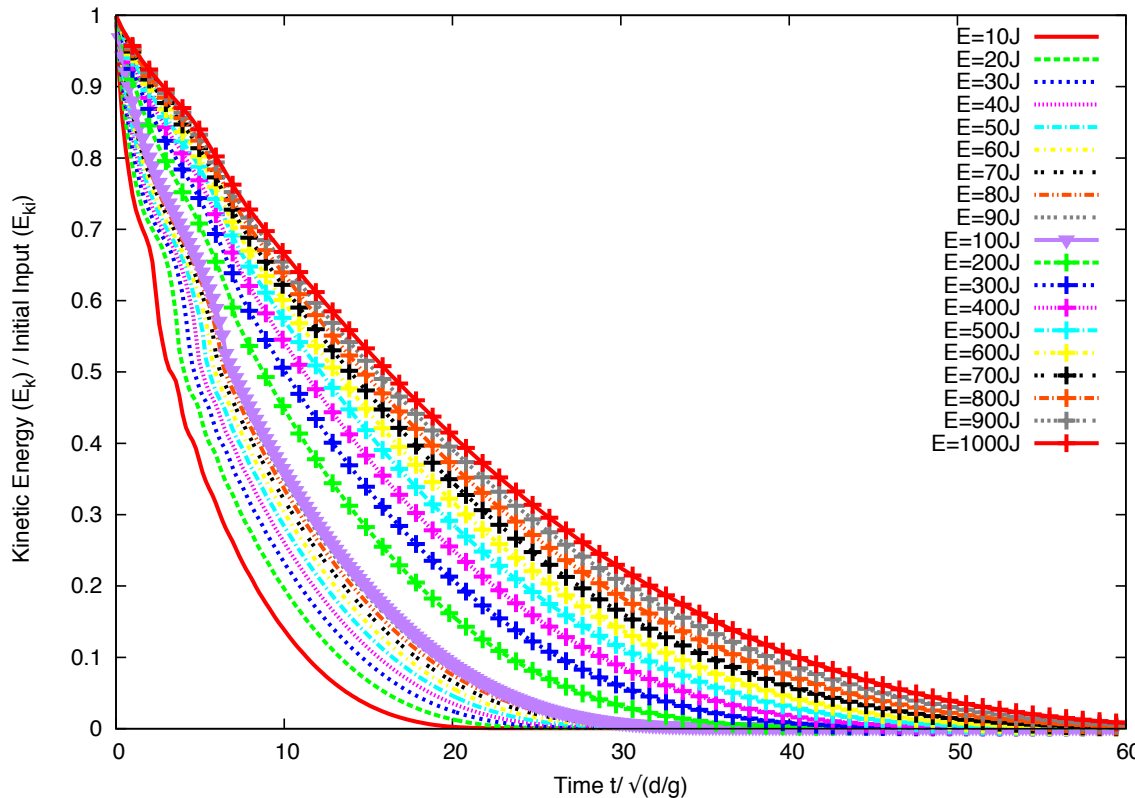
The decay of the total kinetic energy E is displayed in ??(a) for values of the input energy E_0 . We observe an initial fast drop of E followed by a regular fall-off until the end of the run-out. This regular fall-off occurs clearly with two different functional forms, thus revealing two stages in the evolution of the pile. ??(b) shows the same plots normalized by E_0 . We see that all plots corresponding to the first regime (low energies) collapse nearly on to a single time evolution. This is consistent with the fact that, as previously shown, in this regime the run-out time t_f is independent of the input energy. In contrast, the plots corresponding to the second regime (high energies) collapse only at the beginning of run-out, i.e. for $t < t_1 \simeq 7.5 (d/g)^{0.5}$.

?? displays the evolution of kinetic energy in the translational (E_x and E_y) and rotational (E_θ) degrees of freedom of the particles. E_x decays as the total energy, but E_y and E_θ increase and pass through a peak before decaying rapidly to a negligibly small level. The transient is best observed for E_y , which has significant values only for $t < t_1$. This energy represents the proportion of kinetic energy transferred to the y component of the velocity field due to the destabilization of the pile and collapse of particles in the cavity behind the pile. We note that the lower E_0 , the higher the peak value of E_y/E_0 . This means that, at low values of the input energy a larger fraction of input energy E_0 is consumed in the destabilization process whereas at a high level of input energy, most of it is dissipated in the spreading phase. For this reason, the total duration t_1 of this destabilization transient is nearly the same in both regimes and its value is controlled by the gravity rather than the input energy. The height of the pile being of the order of 80 d , the total free-fall time for a particle located at this height is $\simeq 12 (d/g)^{0.5}$, which is of the same order as t_1 . As to the rotational energy, its contribution both to the transient stage and spreading appears to be negligible.

To analyze the second phase in the second regime, we now consider only the kinetic energy E'_{x0} available at the end of the transient. This energy is responsible for most of the run-out and hence it is expected to control the run-out distance and time. Fig. ??(a) shows the evolution of E_x normalized by E'_{x0} as a function of time. The plots have seemingly the same aspect but they show different decay times. A decay time τ can be defined as the time required for E_x to decline by a factor 1/2. Fig. ??(b) shows the same data in which the time t' elapsed since t_1 is normalized by τ . Interestingly, now all the data nicely collapse on the same curve. We checked that this curve can not be fitted by simple functional forms such as variants of exponential decay. This means that the spreading of the pile is not a self-similar process in agreement with the fact that the energy fades away in a finite time t'_f .



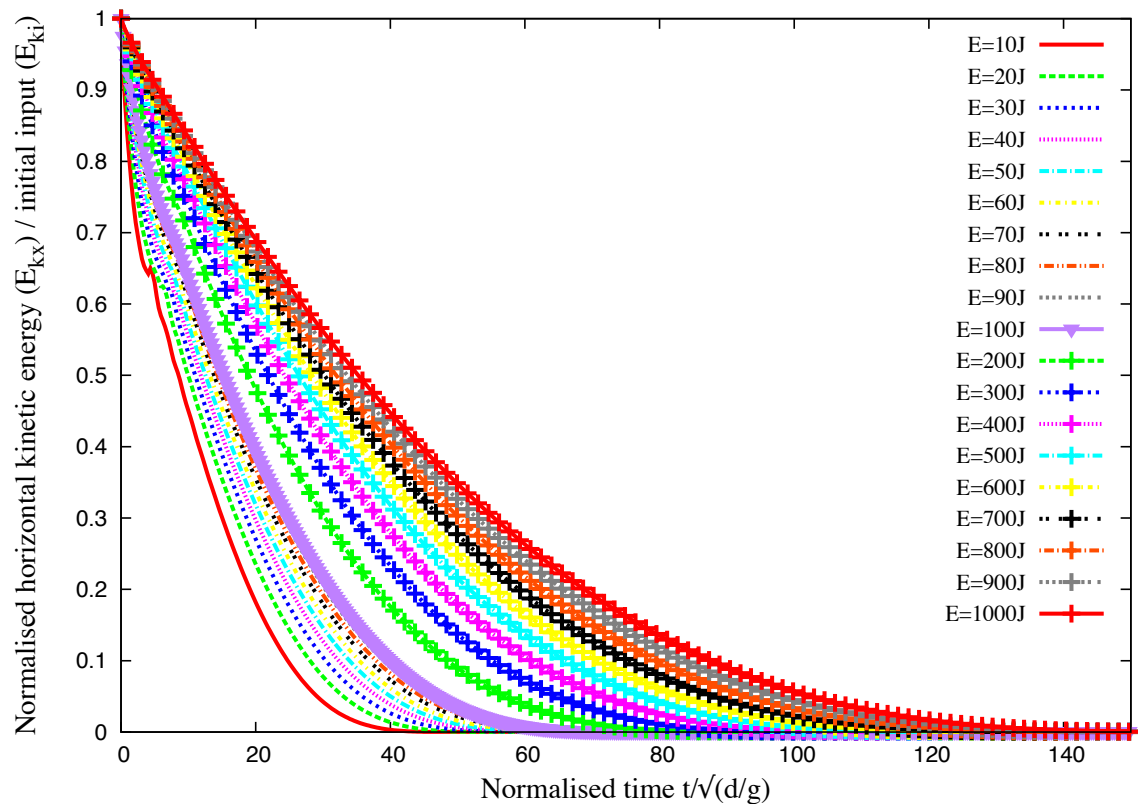
(a) Evolution of total kinetic energy with time



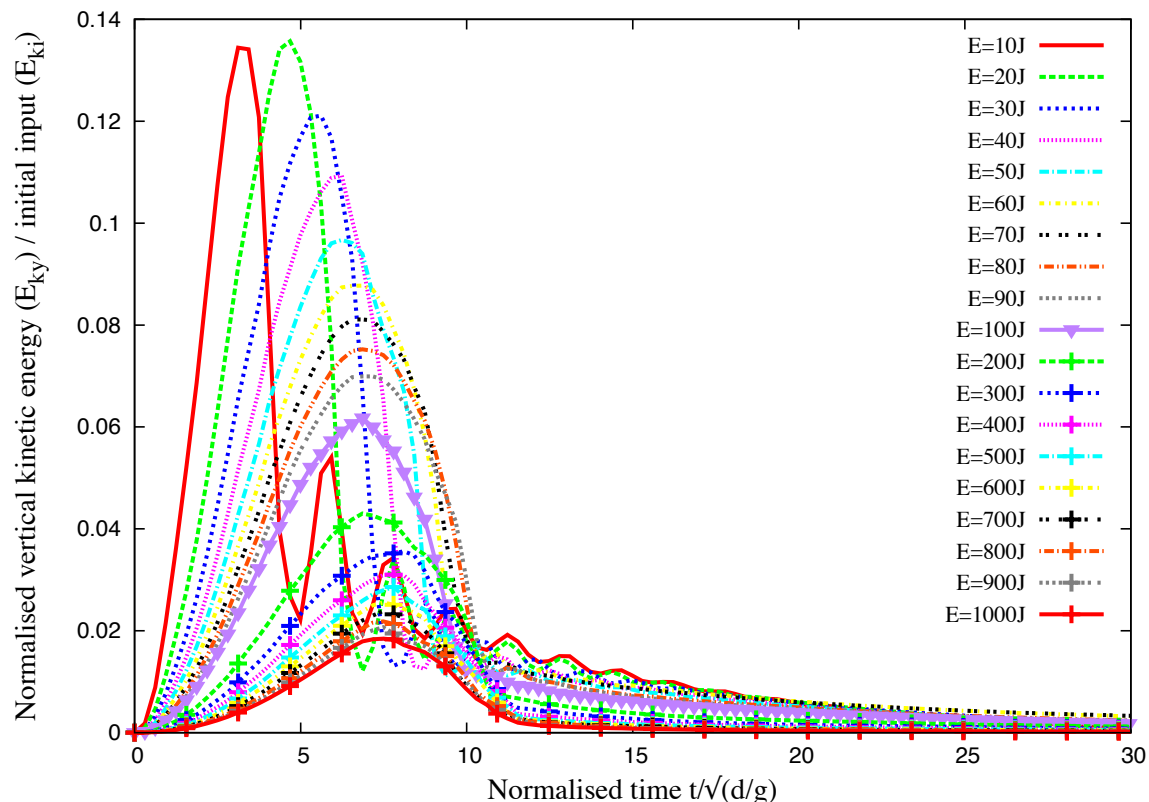
(b) Evolution of normalised kinetic energy with normalised time

Figure 4.25 Evolution of kinetic energy with time

4.3 Slopes subjected to impact loading



(a) Evolution of normalised horizontal kinetic energy with time



(b) Evolution of normalised vertical kinetic energy with time

Figure 4.26 Evolution of vertical and horizontal kinetic energy with time

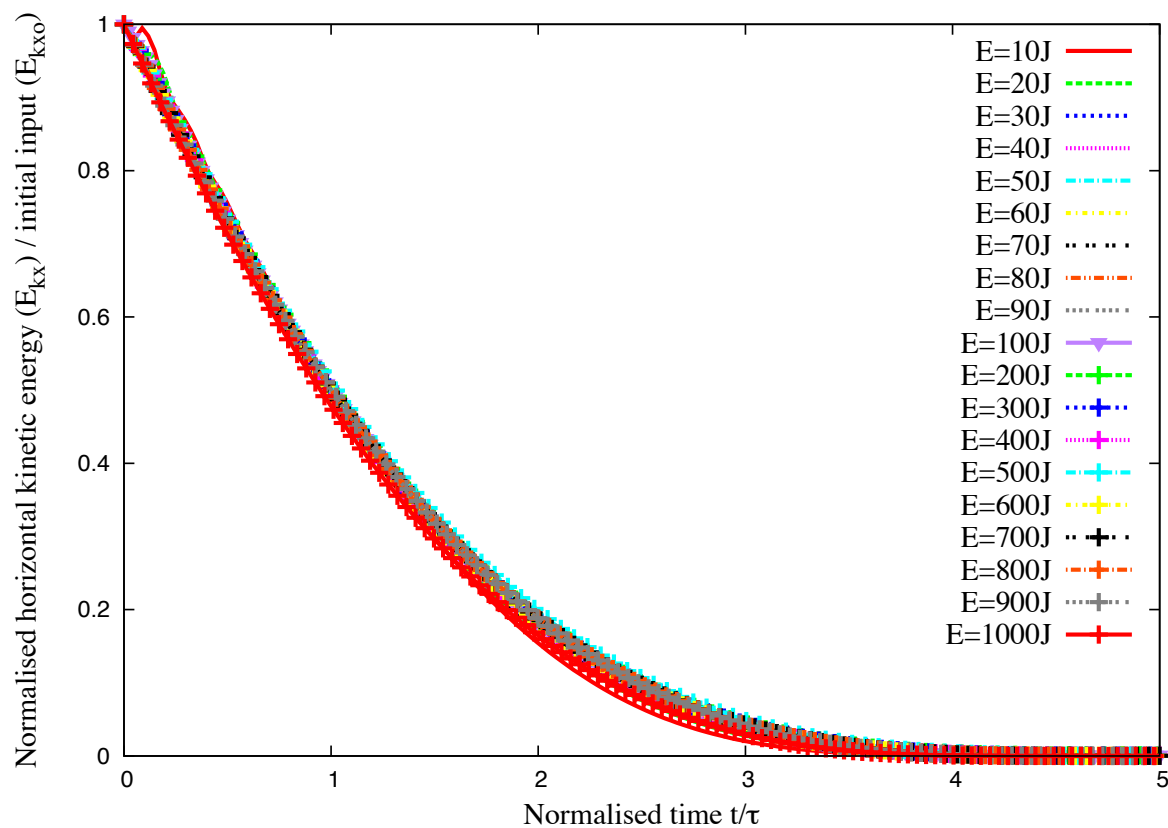


Figure 4.27 Evolution of kinetic energy in the x component of the velocity field normalized by the available kinetic energy at the end of the transient as a function of normalized time.

18 The scaling of the data with the decay time τ suggests also that the run-out time t'_f since the
 19 beginning of the second phase might be a simple function of τ . Figure 4.27 shows both t'_f and
 20 τ as a function of E'_{x0} , where we observe a power law for both times over nearly one decade.
 21 The run-out time $t'_f \propto (E'_{x0})^{\beta'}$ has the same exponent $\beta' \simeq 0.21 \pm 0.03$ as t_f as a function of E_0
 22 (see Fig. 4.4). For the decay time we have $\tau \propto (E'_{x0})^{\beta''}$ with $\beta'' \simeq 0.28 \pm 0.03$. The relation
 23 between the two times can thus be expressed as

$$24 \quad t'_f = k \tau (E'_{x0})^{\beta'' - \beta'}, \quad (4.11)$$

25 where $k \simeq 5 \pm 0.4$ and $\beta'' - \beta' \simeq -0.05 \pm 0.06$. This value is small enough to be neglected
 26 within the confidence interval of our data. It is therefore plausible to assume that the run-out
 27 time is a multiple of the decay time and the spreading process is controlled by a single time.
 28 We however note that a weak dependence on the energy E'_{x0} is consistent with the fact that the
 29 whole available energy at the beginning of the second phase is not dissipated in the spreading
 30 process (calculated from the position of the tip of the pile) since the pile keeps deforming by
 31 the movements of the particles at the free surface even when the tip comes to rest. This can
 32 explain the small difference between the two exponents as observed here.

1 4.3.4 Effect of friction

2 The run-out distance and time and the dissipation of kinetic energy are controlled by the input
 3 energy and collective dynamics of the whole pile, as it was analyzed in the previous sections.
 4 But they are expected to depend also on the friction. We performed a series of simulations with
 5 different values of base friction. The results are shown in Fig. ?? for the profiles of the pile and
 6 evolution of the kinetic energy in time. We see no difference in the results for different values
 7 of $e_n = e_t$. This is a consequence of the fact that, even at large input energies, the pile remains
 8 in a dense state so that multiple collisions inside the pile occur at small time scales compared
 9 to the deformation time. When the restitution coefficients are increased, more collisions occur
 10 during a longer time interval but the overall energy dissipation rate by collisions remains the
 11 same. This effect is a seminal example of collective effects which erase the influence of local
 12 parameters at the macroscopic scale. In contrast with the restitution coefficients, however, the
 13 effect of the friction coefficient is quite important for the run-out, as observed in Fig. ?? for
 14 both the energy decay and geometrical profile of the pile. Both the run-out distance and decay
 15 time decrease as the friction coefficient is increased. This effect is much more pronounced at
 16 low values of the friction coefficient. The run-out time, for example, is reduced by a factor 4 as
 μ_s is increased from 0.1 to 0.4 while the run-out times and profiles do not change much for
 $\mu_s = 0.7$. This “saturation effect” was evidenced in a systematic way in simple shear tests and

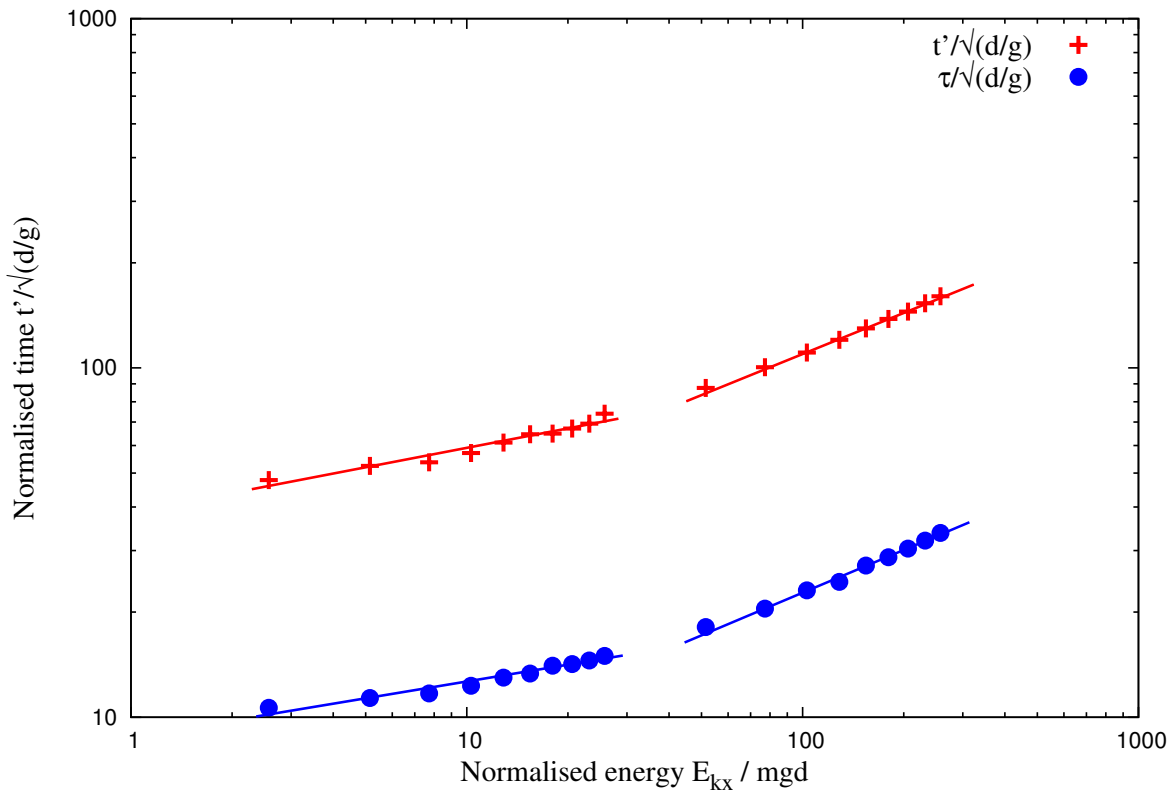
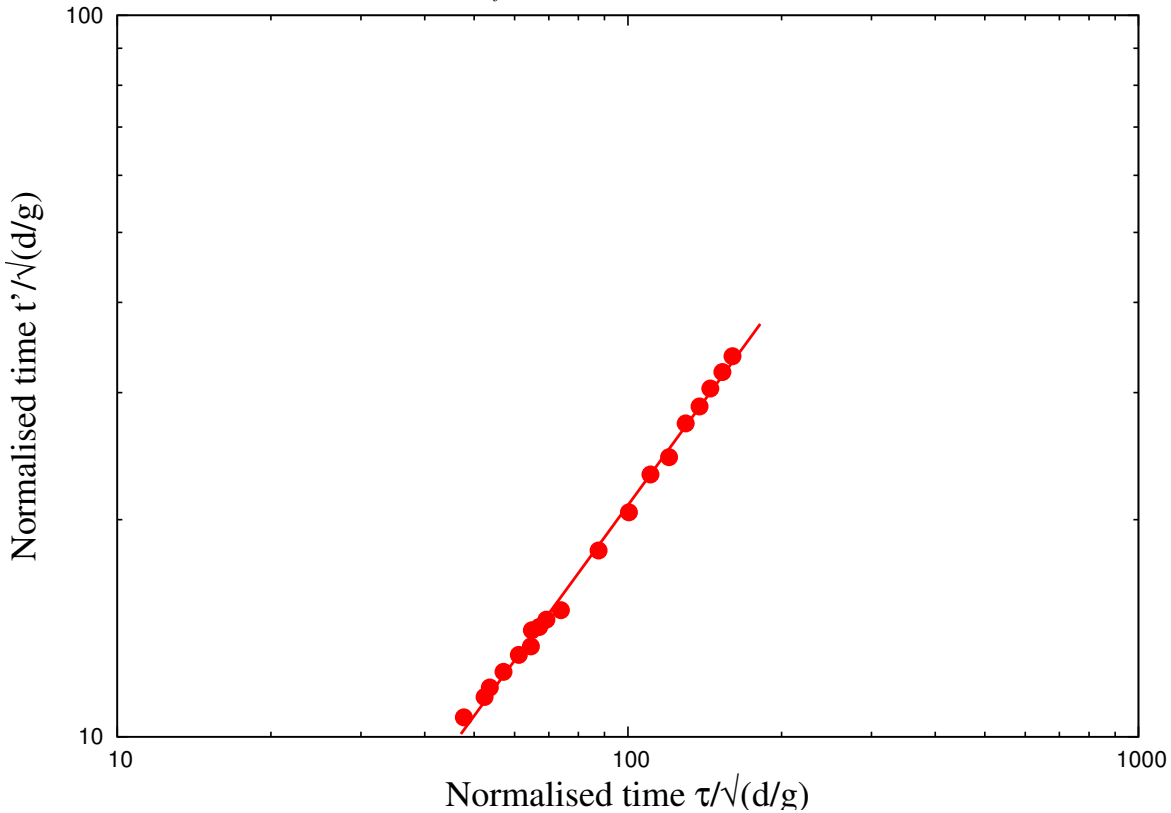
(a) Power law evolution of t'_f and τ as a function of kinetic energy E_{kx0} .(b) Linear relationship between decay time and run-out time after the transient as a function of the normalized kinetic energy E_{kx0} .

Figure 4.28 Decay time and run-out time as a function of the normalised kinetic energy E_{kx0} .

explained by the observation that the dissipation rate may reach a saturation point where the dilation of the granular material and rolling of the particles change in response to the increase of the friction coefficient [Estrada et al. \(2008\)](#).

17

18

19

20

Mode of dissipation

21

The choice of this geometry was motivated by our main goal to focus on the effect of an input energy on the consecutive dynamics of a granular material. For the range of input energies investigated in this pushing test by means of contact dynamics simulations, we observed a
1 power-law dependence of the run-out distance and time with non-trivial exponents. This is
2 a central result of this work as it reveals that the power-law behaviour is a generic feature of
3 granular dynamics. The values of the exponents are not simple functions of the geometry.

22

23

24

4 We also evidenced two regimes with different values of the exponents: a low-energy
5 regime and a high-energy regime. The first regime reflects mainly the destabilization of the
6 pile by the quake with a run-out time independent of the input energy whereas the second
7 regime is governed by the spreading dynamics induced by the higher value of the input energy.
8 We showed that the evolution of the pile in this high-energy regime can be described by a
9 characteristic decay time and the energy available at the end of the first stage where the pile is
10 destabilized by the quake.

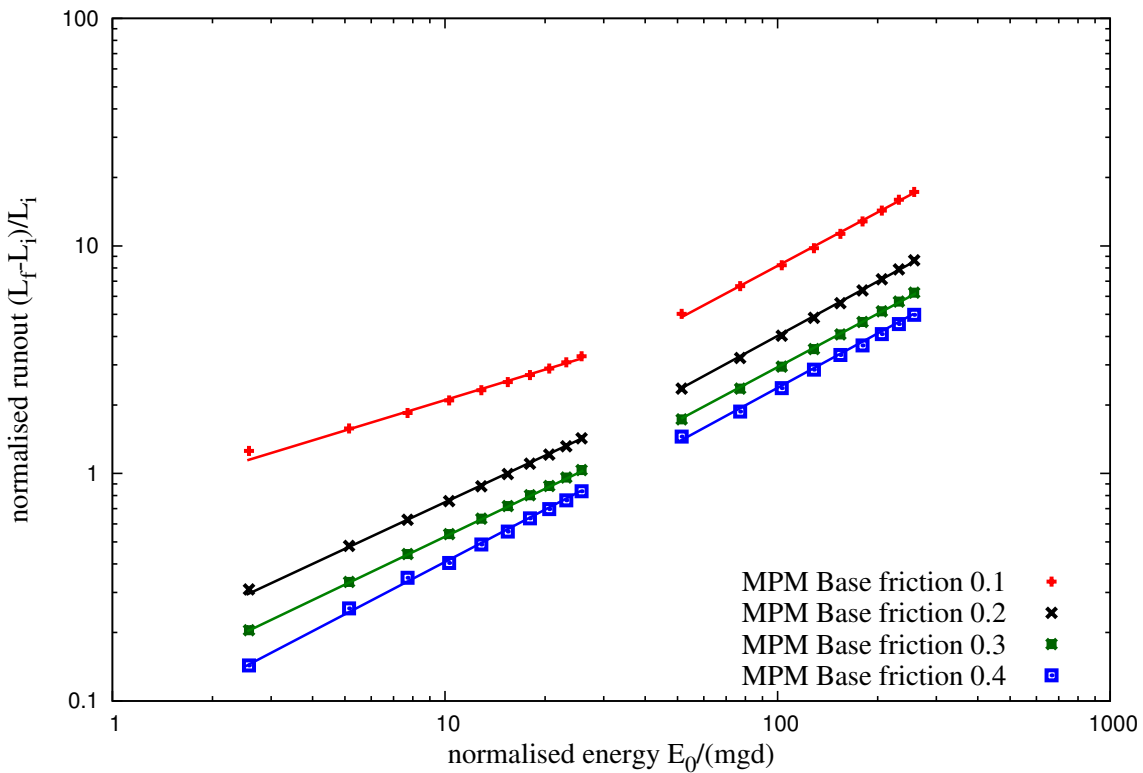
11 This work may be pursued along two directions: 1) experimental realization of a similar
12 setup with different modes of energy injection and 2) investigating the effect of various particle
13 shapes or the presence of an ambient fluid. Although numerical simulations are generally
14 reliable with realistic results found in the past studies of steady flows, we believe that the
15 transients are more sensitive situations than steady states and the experiments are necessary
16 for checking the validation of the results suggested by the simulations. Provided a convenient
17 method is used for supplying kinetic energy homogeneously into a pile, our configuration is
18 also interesting for the investigation of the behavior of a pile immersed in a viscous fluid.

19 4.3.5 Effect of material points

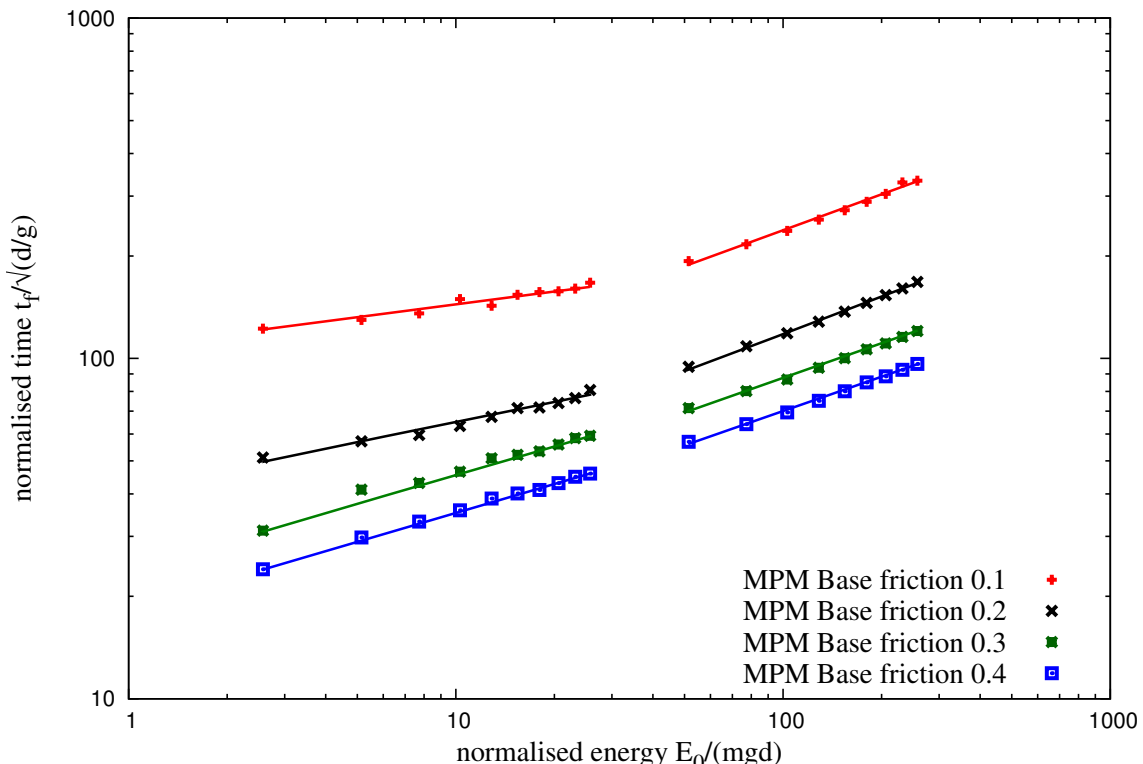
20 4.3.6 Comparison with granular column collapse

21 4.4 Summary

22 Multi-scale simulation of granular column collapse was performed to understand the ability and
23 limitations of continuum models to capture the micro-mechanics of dense granular flows. The



(a) Effect of friction on the run-out distance



(b) Effect of friction on the duration of run-out.

Figure 4.29 Effect of friction on the run-out behaviour

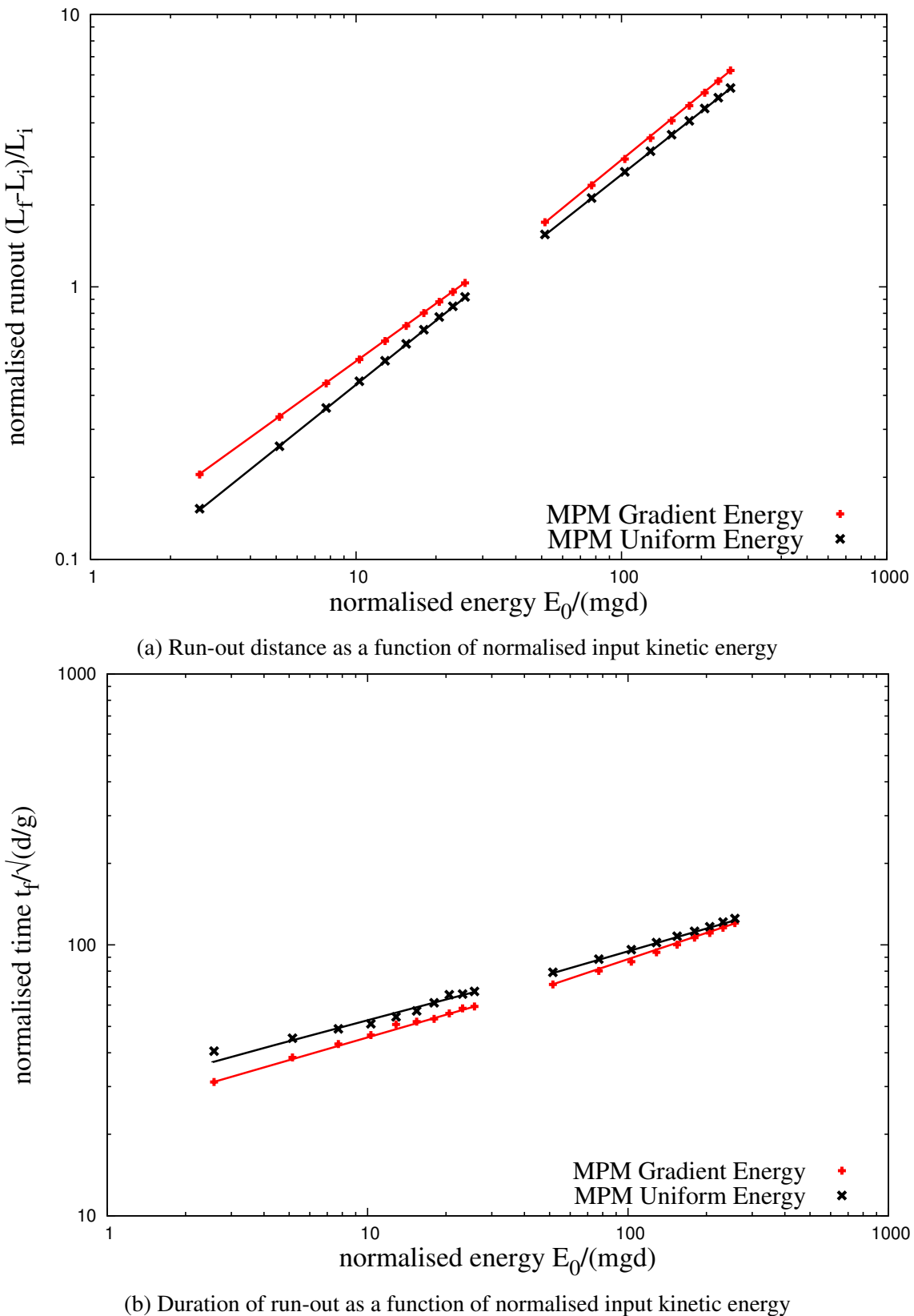


Figure 4.30 Effect of input velocity distribution on the run-out behaviour

$t = 0 \text{ s}$



$t = 0.03 \text{ s}$



$t = 0.06 \text{ s}$



$t = 0.09 \text{ s}$



Figure 4.31 Snapshots of MPM simulations of the evolution of granular pile subjected to a gradient impact energy $E_0 = 61 \text{ mgd}$.

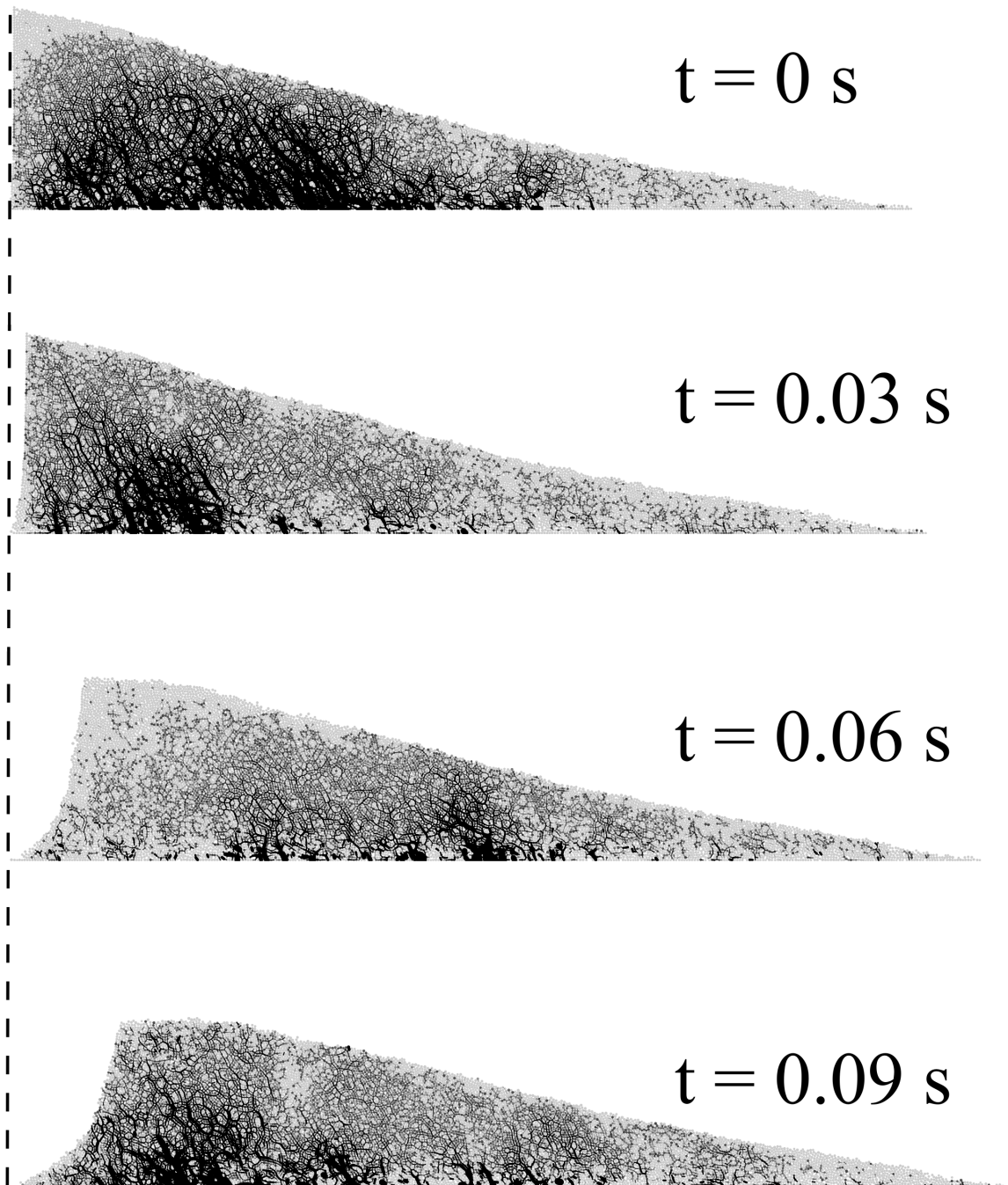


Figure 4.32 Snapshots of DEM simulations of the evolution of granular pile subjected to a gradient impact energy $E_0 = 61 \text{ mgd}$.

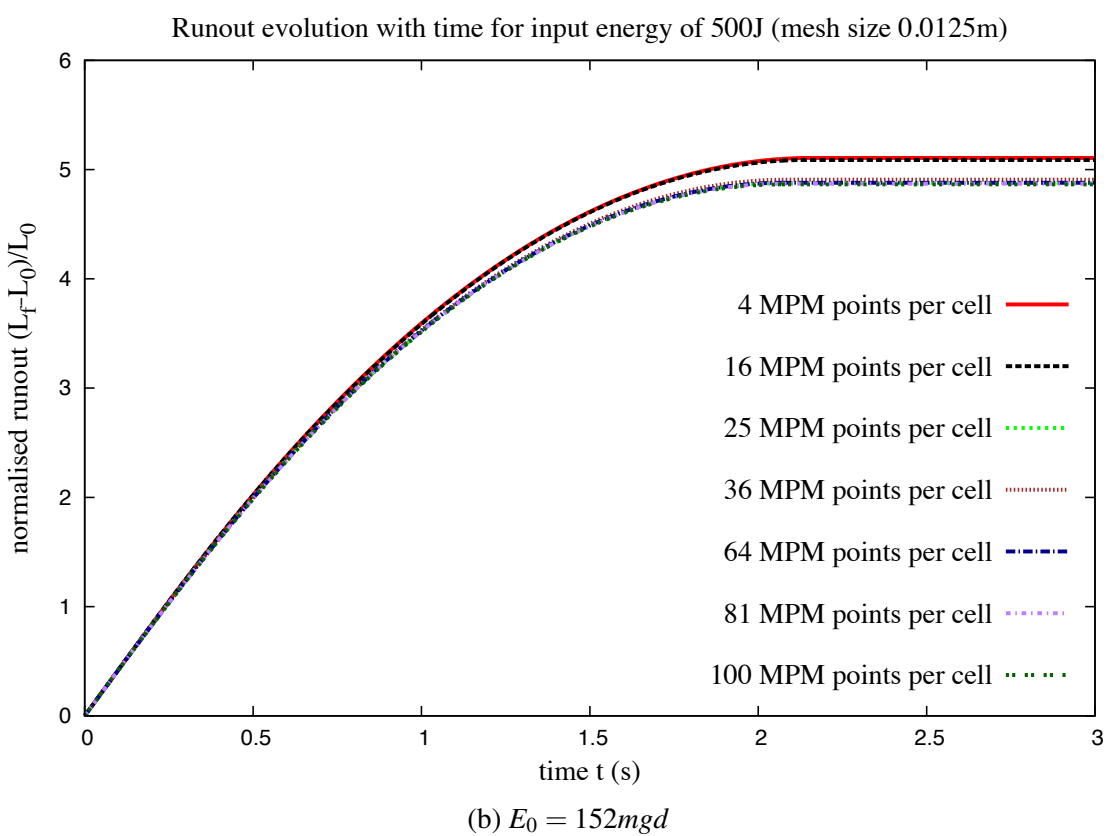
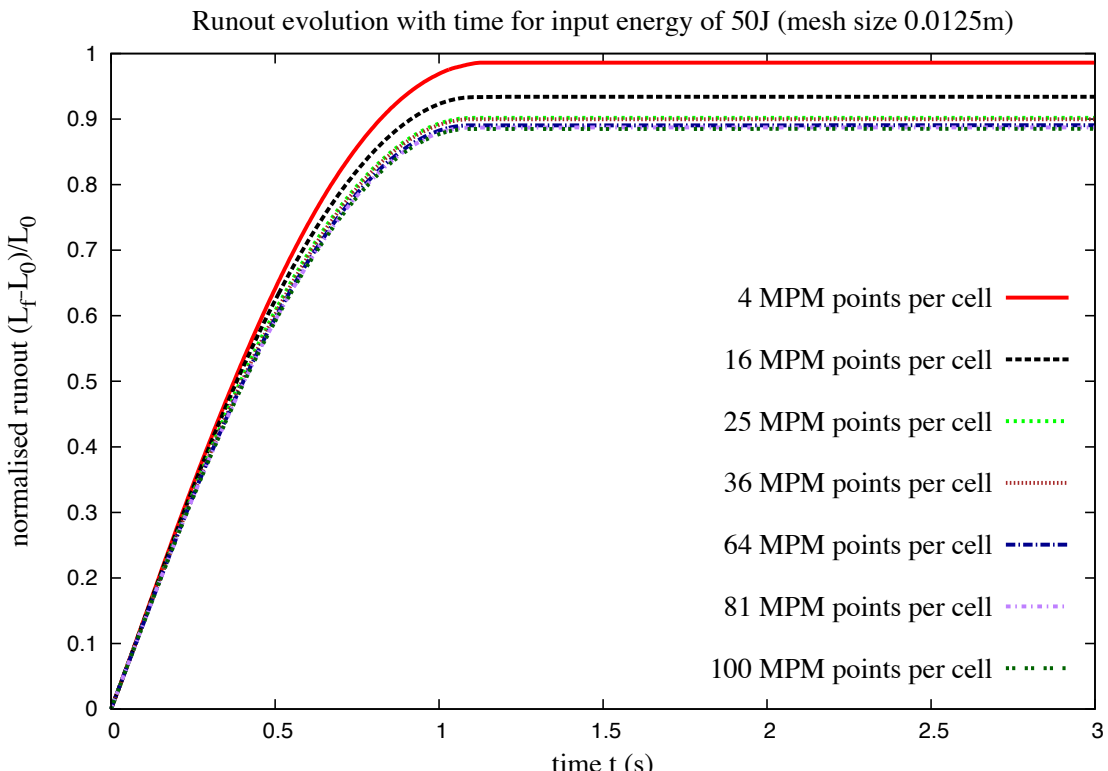


Figure 4.33 Evolution of run-out with time for varying material points per cell.

4.4 Summary

121

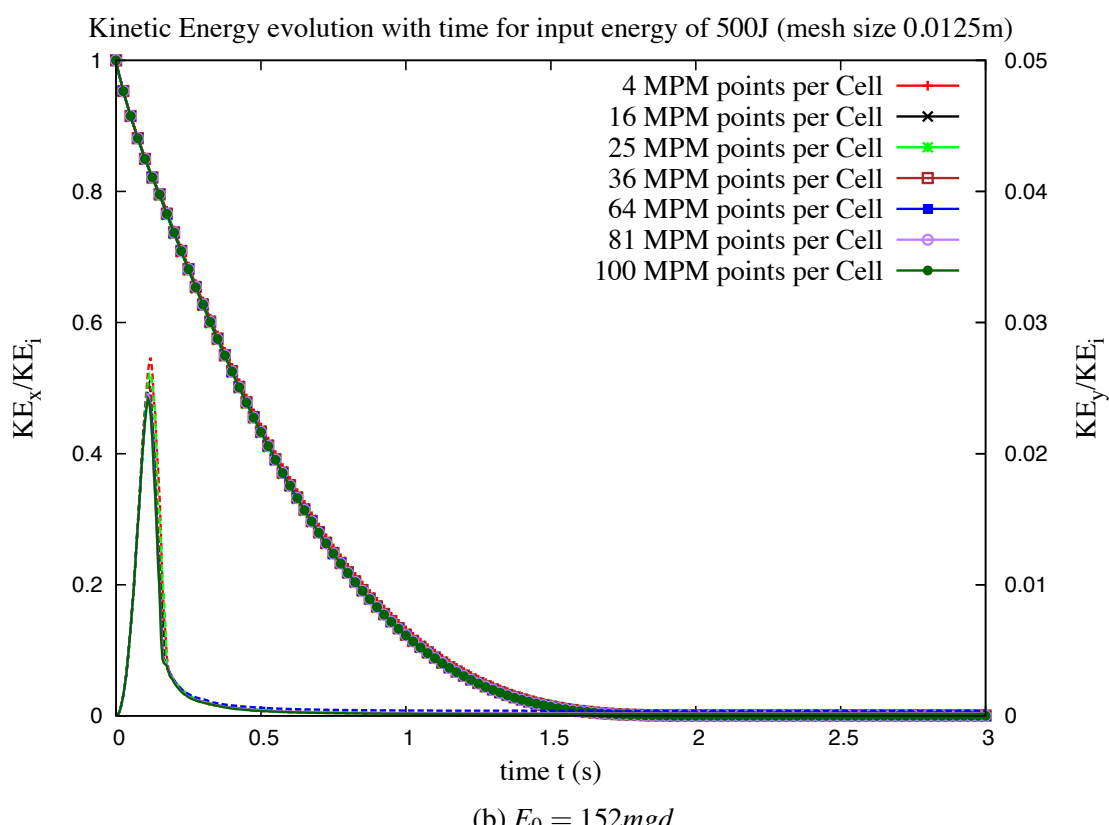
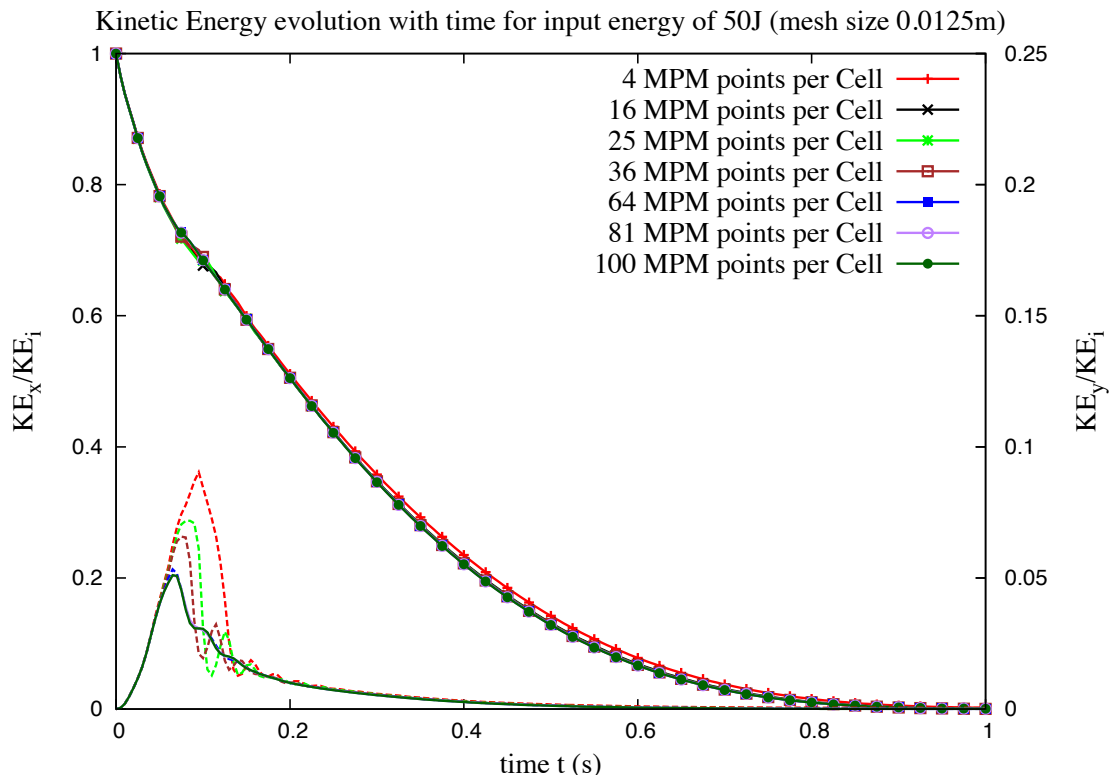


Figure 4.34 Evolution of kinetic with time for varying material points per cell

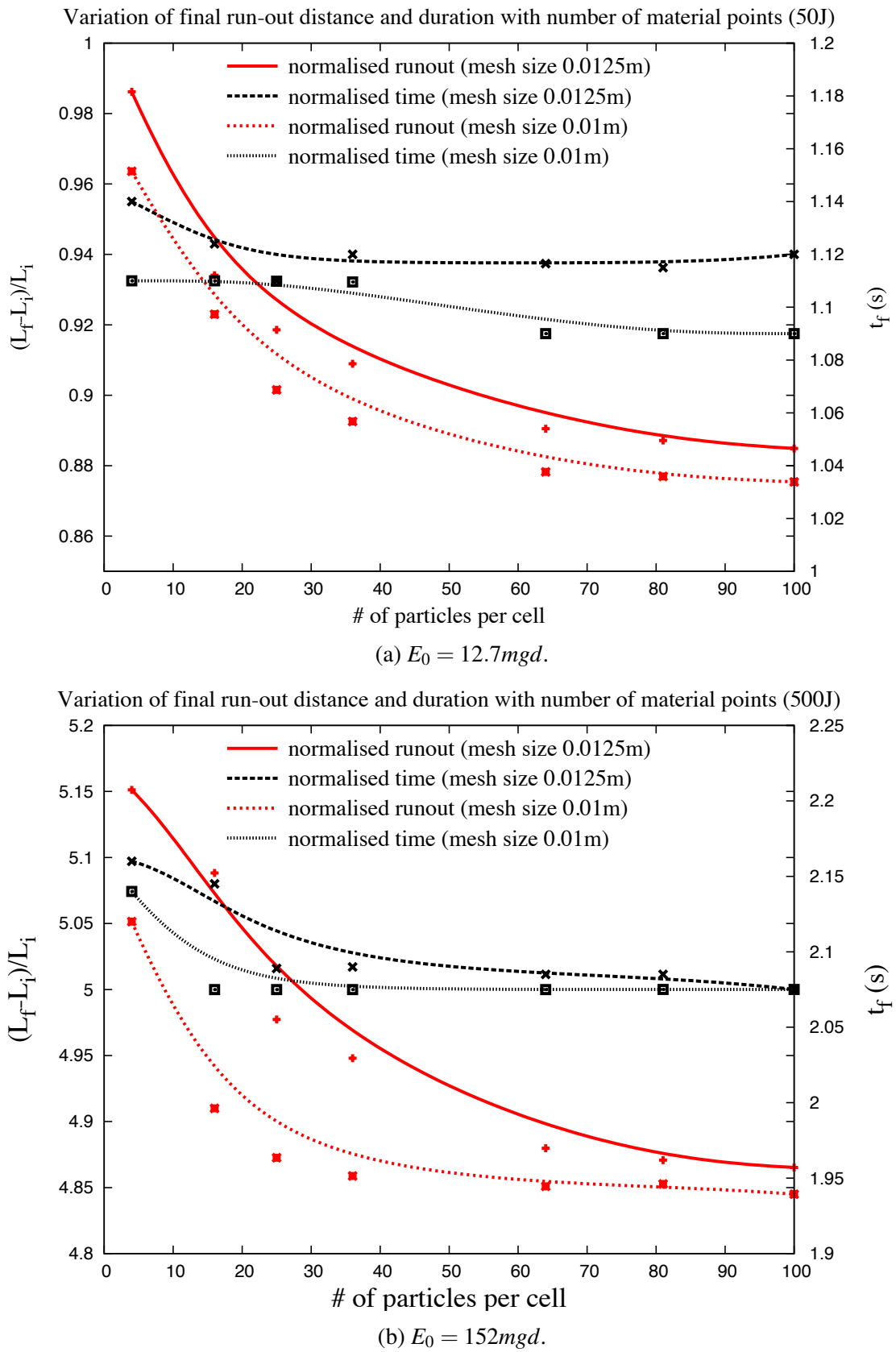


Figure 4.35 Evolution of run-out and duration of flow for varying material points per cell.

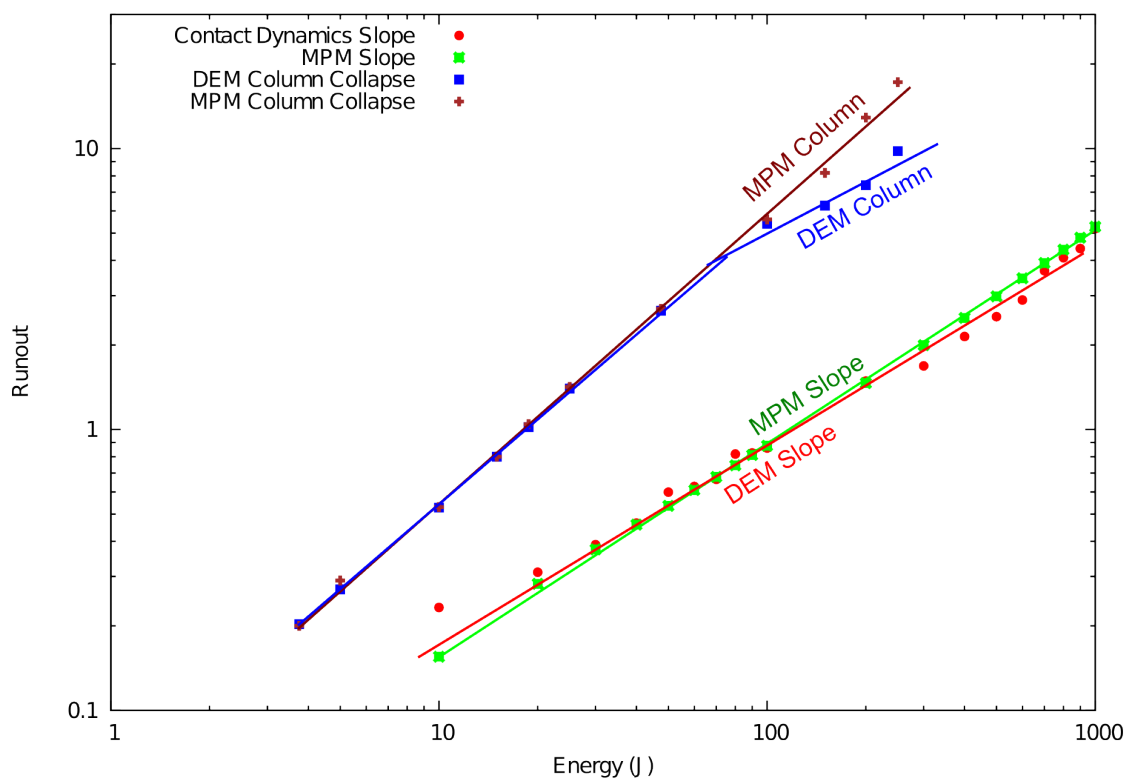


Figure 4.36 Comparison of column collapse with slope subjected to impact loading.

²⁴ run-out behaviour predicted by both continuum and DEM simulations matches for columns
²⁵ with small aspect ratios, where the dissipation is predominantly frictional. However, MPM
²⁶ predicts larger run-out distances for columns with higher aspect ratios. Energy evolution
²⁷ studies using DEM simulations reveal that the run-out behaviour is independent of frictional
²⁸ properties of the granular material and collision predominates the initial free-fall regime. The
²⁹ lack of a collisional energy dissipation mechanism in MPM results in over prediction of run-out
³⁰ distances.

³¹ Chapter 5

³² Numerical modelling of fluid–grain ³³ interactions

5.1 Fluid simulation using lattice Boltzmann method

Grain–fluid systems can be found in many scientific and engineering applications, such as suspensions, fluidised beds, sediment transport, and geo-mechanical problems. In general, the fundamental physical phenomena in these systems are not well understood mainly due to the intricate complexity of grain–fluid interactions and the lack of powerful analysis tools ([Han et al., 2007a](#)). In addition to the interaction among soil grains, the motion of soil grains is mainly driven by gravity and the hydrodynamic force exerted by the fluid. The fluid flow pattern can be significantly affected by the presence of soil grains and this often results in a turbulent flow. Hence, the development of an effective numerical framework for modelling both the fluid flow patterns and the grain–fluid interactions is very challenging.

Development of a numerical framework depends crucially on the size of the soil grains relative to the domain/mesh size ([Feng et al., 2007](#)). Traditionally, the Navier-Stokes equation is solved by a grid-based Computational Fluid Dynamics (CFD) method, such as the Finite Volume Method, FVM, ([Capecelatro and Desjardins, 2013](#)) or a mesh-free technique such as

- ¹ Smooth Particle Hydrodynamics (SPH) ([Sun et al., 2013](#)). The grid size in FVM or the smooth
- ² length in SPH for discretisation of the Navier-Stokes equation is at least an order of magnitude
- ³ larger than the grain diameter ([Xiong et al., 2014](#)).

- ⁴ In situations where the average domain concentration phase is far from dilute, the com-
- ⁵ putational effort is mostly devoted to the grain dynamics. The hydrodynamic forces on the
- ⁶ soil grains are applied based on an empirical relation using the domain-averaged local poros-
- ⁷ ity of the soil grains in the grid. As a result, developing a fast fluid hydrodynamics solver

is unimportant for dense flows. However, most geo-mechanical problems involve complex interactions between the solid and the fluid phase. This requires accurate modelling of the fluid flow pattern. Additionally, geophysical problems, such as submarine landslides and debris flow have a relatively large simulation domain, which requires parallel computation. Implementing traditional grid-based CFD methods face great challenges on multi-processor systems (Xiong et al., 2014). Although mesh-free approaches are free from the problem of parallel scalability, its modelling accuracy and speed are relatively low when compared to grid-based CFD methods. Therefore, an accurate, fast and a highly scalable scheme is required to model fluid - grain systems in geo-mechanics.

The Navier-Stokes equation describes the motion of a non-turbulent Newtonian fluid. The equation is obtained by applying Newton's second law to the fluid motion, together with an assumption that the fluid stress is the sum of the viscous term, proportional to the gradient of the velocity, and the pressure term. Conventional CFD methods compute pertinent flow fields, such as velocity u and pressure p , by numerically solving the Navier-Stokes equation in space x and time t . Alternatively, the transport equation or the Boltzmann equation, which deals with a single particle distribution function $f(x, \xi, t)$ in phase space (x, ξ) and time t , can be used to solve various problems in fluid dynamics.

The Lattice Boltzmann Method (LBM) (Chen and Doolen, 1998; Han et al., 2007b; He and Luo, 1997a,b; Mei et al., 2000; Zhou et al., 2012) is an alternative approach to the classical Navier-Stokes solvers for fluid flows. LBM works on an equidistant grid of cells, called lattice cells, which interact only with their direct neighbours. In LBM, the discretisation of continuum equations is based on microscopic models and mesoscopic continuum theories. LBM is a special discretising scheme of the Boltzmann equation where the particle distribution functions (mass fractions) collide and propagate on a regular grid. The important aspect, however, is the *discretisation of the velocity*, which means that the particle velocities are restricted to a predefined set of orientations.

The theoretical premises of the LB equation are that (1) hydrodynamics is insensitive to the details of microscopic physics, and (2) hydrodynamics can be preserved so long as the conservation laws and associated symmetries are respected in the microscopic and mesoscopic level. Therefore, the computational advantages of LBM are achieved by drastically reducing the particle velocity space ξ to only a very few discrete points without seriously degrading the hydrodynamics (Mei et al., 2000). This is possible because LBM rigorously preserves the hydrodynamic moments of the distribution function, such as mass density and momentum fluxes, and the necessary symmetries (He and Luo, 1997a,b). LBM has evolved as a comprehensive fluid solver and its theoretical aspects link well with the conventional central finite difference scheme (Cook et al., 2004).

4 5.1.1 Formulation

5 LBM is a ‘micro-particle’ based numerical time-stepping procedure for the solution of incom-
 6 pressible fluid flows. Consider a 2D incompressible fluid flow with density ρ and kinematic
 7 viscosity ν , in a rectangular domain D . The fluid domain is divided into rectangular grids or
 8 lattices, with the same grid length ‘ h ’ in both x - and y -directions (see figure 5.1).

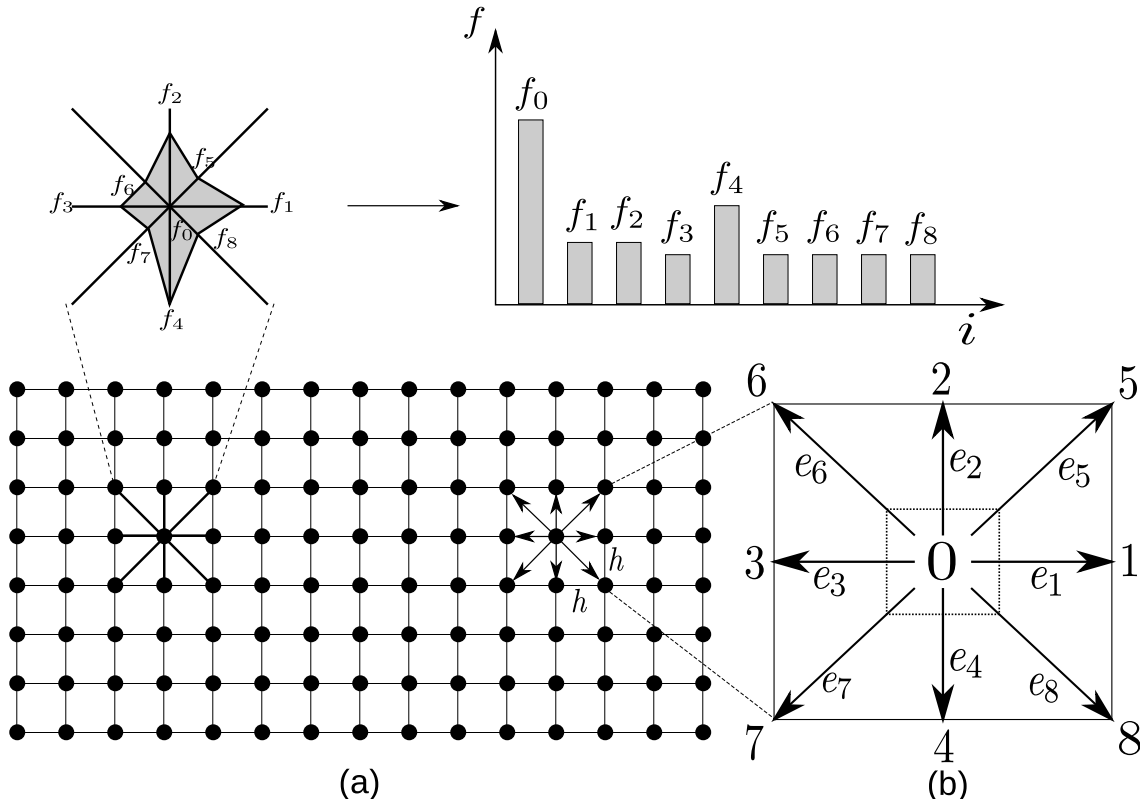


Figure 5.1 The Lattice Boltzmann discretisation and D2Q9 scheme: (a) a standard LB lattice and histogram views of the discrete single particle distribution function/direction-specific densities f_i ; (b) D2Q9 model.

9 These lattices are usually classified in the literature using the $D\alpha Q\beta$ -notation, where α
 10 denotes the space dimensionality and β is the number of discrete velocities (but also including
 11 the possibility of having particles at rest) within the momentum discretisation. The most
 12 common lattices are the $D2Q9$ and the $D3Q19$ -models, see He et al. (1997). The present study
 13 focuses on two-dimensional problems, hence the $D2Q9$ momentum discretisation is adopted.

14 LBM discretises the Boltzmann equation in space to a finite number of possible particle
 15 spatial positions, microscopic momenta, and time. Particle positions are confined to the
 16 lattice nodes. The fluid particles at each node are allowed to move to their eight intermediate
 neighbours with eight different velocities $e_i (i = 1, \dots, 8)$. A particle can remain at its own node,

which is equivalent to moving with zero velocity e_o . The particle mass is uniform, hence these microscopic velocities and momentum are always effectively equivalent (Han et al., 2007b). Referring to the numbering system shown in figure 5.1, the nine discrete velocity vectors are defined as

$$\begin{cases} e_0 = (0, 0); \\ e_1 = C(1, 0); e_2 = C(0, 1); e_3 = C(-1, 0); e_4 = C(0, -1); \\ e_5 = C(1, 1); e_6 = C(-1, 1); e_7 = C(-1, -1); e_8 = C(1, -1), \end{cases} \quad (5.1)$$

where C is the lattice speed that is defined as $C = h/\Delta t$, and Δt is the discrete time step. The primary variables in LB formulation are called the *fluid density distribution functions*, f_i , each representing the probable amount of fluid particles moving with the velocity e_i along the direction i at each node. The macroscopic variables are defined as functions of the particle distribution function (see figure 5.1)

$$\begin{cases} \rho = \sum_{i=0}^{\beta-1} f_i & \text{(macroscopic fluid density)} \\ \text{and} \\ \overrightarrow{u} = \frac{1}{\rho} \sum_{i=0}^{\beta-1} f_i \overrightarrow{e}_i & \text{(macroscopic velocity)}, \end{cases} \quad (5.2)$$

where $i \in [0, \beta - 1]$ is an index spanning the discretised momentum space. There are nine fluid density distribution functions, $f_i (i = 0, \dots, 8)$, associated with each node in the *D2Q9* model. The evolution of the density distribution function at each time step for every lattice point is governed by

$$f_i(\mathbf{x} + \mathbf{e}_i \Delta t, t + \Delta t) = f_i(\mathbf{x}, t) - \frac{1}{\tau} [f_i(\mathbf{x}, t) - f_i^{eq}(\mathbf{x}, t)] \quad (i = 0, \dots, 8), \quad (5.3)$$

where for any grid node \mathbf{x} , $\mathbf{x} + \mathbf{e}_i \Delta t$ is its nearest node along the direction i . τ is a non-dimensional relaxation time parameter, which is related to the fluid viscosity; and f_i^{eq} is termed as the equilibrium distribution function that is defined as

$$\begin{cases} f_0^{eq} = w_0 \rho (1 - \frac{3}{2C^2} \mathbf{v} \cdot \mathbf{v}) \\ \text{and} \\ f_i^{eq} = w_i \rho (1 + \frac{3}{C^2} \mathbf{e}_i \cdot \mathbf{v} \frac{9}{2C^2} (\mathbf{e}_i \cdot \mathbf{v})^2 - \frac{3}{2C^2} \mathbf{v} \cdot \mathbf{v}) \quad (i = 0, \dots, 8), \end{cases} \quad (5.4)$$

5.1 Fluid simulation using lattice Boltzmann method

129

in which, w_i represents the fixed weighting values:

$$w_0 = \frac{4}{9}, \quad w_{1,2,3,4} = \frac{1}{9}, \quad \text{and} \quad w_{5,6,7,8} = \frac{1}{36}. \quad (5.5) \quad 26$$

The right-hand side of eq. 5.3 is often denoted as $f_i(\mathbf{x}, t_+)$ and termed the post collision distribution. LBM ensures conservation of total mass and total momentum of the fluid particles at each lattice node (see eq. 5.3). The lattice Boltzmann modelling consists of two phases: *collision* and *streaming*. The collision phase computed in the right-hand side of eq. 5.3 involves

- 1 only those variables that are associated with each node \mathbf{x} , and therefore is a local operation.
- 2 The streaming phase then explicitly propagates the updated distribution functions at each node
- 3 to its neighbours $\mathbf{x} + e_i \Delta t$, where no computations are required and only data exchange between
- 4 neighbouring nodes are necessary. These features, together with the explicit time-stepping
- 5 nature and the use of a regular grid, make LB computationally efficient, simple to implement
- 6 and easy to parallelise (Han et al., 2007b).

- 7 The streaming step involves the translation of the distribution functions to their neighbouring
- 8 sites according to the respective discrete velocity directions, as illustrated in figure 5.2 in
- 9 the D2Q9 model. The collision step, (see figure 5.3) consists of re-distribution the local
- 10 discretised Maxwellian equilibrium functions in such a way that local mass and momentum are
- 11 invariants. In incompressible flows, the energy conservation is equivalent to the momentum
- 12 conservation (He et al., 1997).

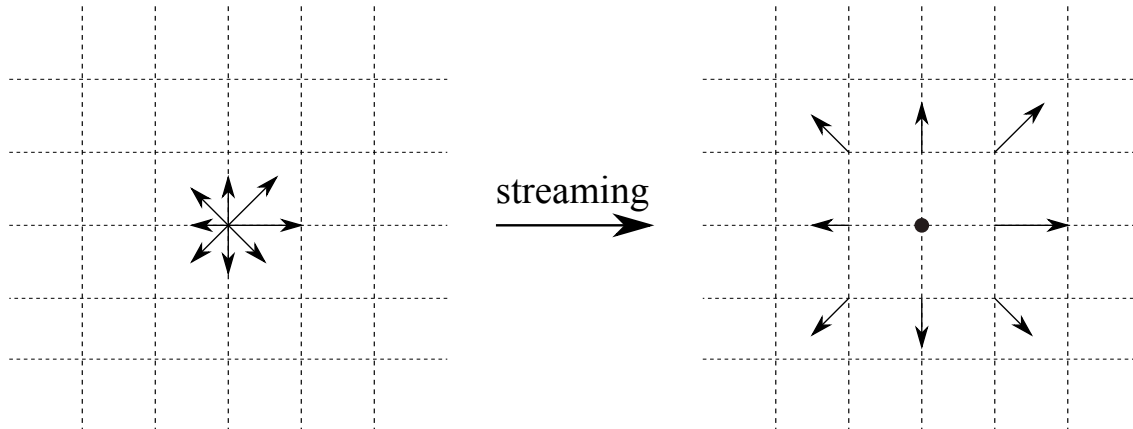


Figure 5.2 Illustration of the streaming process on a D2Q9 lattice. The magnitude of the distribution functions remains unchanged, but they move to a neighbouring node according to their direction.

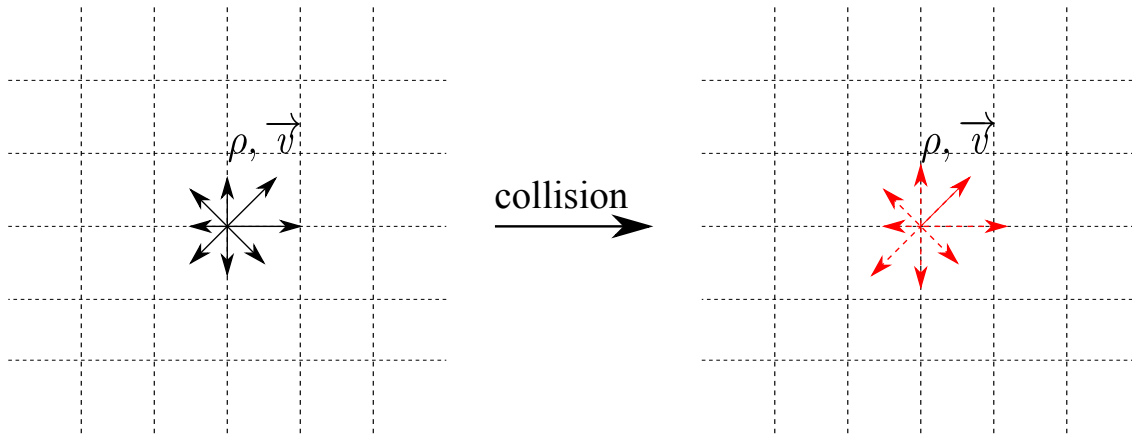


Figure 5.3 Illustration of the collision process on a $D2Q9$ lattice. The local density ρ and velocity v are conserved, but the distribution functions change according to the relaxation to local Maxwellian rule.

₁₃ The standard macroscopic fluid variables, such as density ρ and velocity v , can be recovered
₁₄ from the distribution functions as

₁₅

$$\rho = \sum_{i=0}^8 f_i, \quad \text{and} \quad \rho \mathbf{v} = \sum_{i=0}^8 f_i e_i. \quad (5.6)$$

₁₆ The fluid pressure field ‘ p ’ is determined by the equation of state

₁₇

$$p = C_s^2 \rho, \quad (5.7)$$

₁₈ where C_s is termed the fluid speed of sound and is related to the lattice speed C as

₁₉

$$C_s = C/\sqrt{3}. \quad (5.8)$$

₂₀ The kinematic viscosity of the fluid ν is implicitly determined by the model parameters h ,
₂₁ Δt and τ as

₂₂

$$\nu = \frac{1}{3}(\tau - \frac{1}{2}) \frac{h^2}{\Delta t} = \frac{1}{3}(\tau - \frac{1}{2}) Ch, \quad (5.9)$$

₂₃ which indicates that these three parameters are related to each other and have to be appropriately
₂₄ selected to represent the correct fluid viscosity. An additional constraint to the parameter
₂₅ selection is the lattice speed C , which must be sufficiently large in comparison to the maximum
₂₆ fluid velocity v_{max} , to ensure accuracy of the solution. The ‘computational’ Mach number, M_a ,
defined as

₁

$$M_a = \frac{v_{max}}{C}. \quad (5.10) \quad ₂$$

Theoretically, for an accurate solution, the Mach number is required to be $<< 1$. In practice, M_a should be at least smaller than 0.1 (He et al., 1997). From a computational point of view, it is more convenient to choose h and τ as two independent parameters and Δt as the derived parameter

$$\Delta t = (\tau - \frac{1}{2}) \frac{h^2}{3v}. \quad (5.11)$$

It can be observed that τ has to be greater than 0.5 (He et al., 1997). Since there is no a priori estimation available to determine appropriate values of h and τ , for a given fluid flow problem and a known fluid viscosity v , a *trial and error* approach is employed to ensure a smaller *Mach Number*. This is similar to choosing an appropriate Finite Element mesh size, without using automatic adaptive mesh techniques.

5.1.2 Lattice Boltzmann - Multi-Relaxation Time (LBM-MRT)

The Lattice Boltzmann Bhatnagar-Gross-Krook (LGBK) method is capable of simulating various hydrodynamics, such as multiphase flows and suspensions in fluid (Succi, 2001; Succi et al., 1989). However, LBM suffers from numerical instability when the dimensionless relaxation time τ is close to 0.5. The Lattice Boltzmann Method – Multi-Relaxation Time (LBM-MRT) overcomes the deficiencies of linearised single relaxation LBM-BGK approach, such as the fixed Prandtl number ($Pr=v/\kappa$), where the thermal conductivity ‘ κ ’ is unity (Liu et al., 2003). LBM-MRT offers better numerical stability and has more degrees of freedom. In LBM-MRT the advection is mapped onto the momentum space by a linear transformation and the flux is finished within the velocity space (Du et al., 2006).

The lattice Boltzmann equation with multiple relaxation time approximation is written as

$$f_\alpha(\mathbf{x} + \mathbf{e}_i \Delta_t, t + \Delta_t) - f_\alpha(\mathbf{x}, t) = -\mathbf{S}_{\alpha i}(f_i(\mathbf{x}, t) - f_i^{eq}(\mathbf{x}, t)), \quad (5.12)$$

where \mathbf{S} is the collision matrix. The nine eigen values of \mathbf{S} are all between 0 and 2 so as to maintain linear stability and separation of scales. This ensures that the relaxation times of non-conserved quantities are much faster than the hydrodynamic time scales. The LGBK model is a special case in which the nine relaxation times are all equal and the collision matrix $\mathbf{S} = \frac{1}{\tau} \mathbf{I}$, where \mathbf{I} is the identity matrix. The evolutionary progress involves two steps, advection and flux:

$$f_\alpha^+(\mathbf{x}, t) - f_\alpha(\mathbf{x}, t) = -\mathbf{S}_{\alpha i}(f_i(\mathbf{x}, t) - f_i^{eq}(\mathbf{x}, t)) \quad (5.13)$$

$$f_\alpha(\mathbf{x} + e_\alpha \Delta_t, t + \Delta_t) = f_\alpha^+(\mathbf{x}, t). \quad (5.14)$$

¹⁵ The advection (eq. 5.13) can be mapped to the momentum space by multiplying with a
¹⁶ transformation matrix \mathbf{M} . The evolutionary equation of LBM–MRT is written as

$$\mathbf{f}(\mathbf{x} + \mathbf{e}_i \Delta_t, t + \Delta_t) - \mathbf{f}(\mathbf{x}, t) = -\mathbf{M}^{-1} \hat{\mathbf{S}}(\hat{\mathbf{f}}(\mathbf{x}, t) - \hat{\mathbf{f}}^{eq}(\mathbf{x}, t)), \quad (5.15)$$

¹⁸ where \mathbf{M} is the transformation matrix mapping a vector \mathbf{f} in the discrete velocity space $\mathbb{V} = \mathbb{R}^b$
¹⁹ to a vector $\hat{\mathbf{f}}$ in the moment space $\mathbb{V} = \mathbb{R}^b$.

$$\hat{\mathbf{f}} = \mathbf{M}\mathbf{f}, \quad (5.16)$$

$$\mathbf{f}(\mathbf{x}, t) = [f_0(\mathbf{x}, t), f_1(\mathbf{x}, t), \dots, f_8(\mathbf{x}, t)]^T. \quad (5.17)$$

²³ The collision matrix $\hat{\mathbf{S}} = \mathbf{M}\mathbf{S}\mathbf{M}^{-1}$ in moment space is a diagonal matrix:

$$\hat{\mathbf{S}} = \text{diag}[s_1, s_2, s_3, \dots, s_9].$$

²⁵ The transformation matrix \mathbf{M} can be constructed via Gram-Schmidt orthogonalisation procedure.
²⁶ The general form of the transformation matrix \mathbf{M} can be written as

$$\mathbf{M} = [|p\rangle, |e\rangle, |e^2\rangle, |u_x\rangle, |q_x\rangle, |u_y\rangle, |q_y\rangle, |p_{xx}\rangle, |p_{xy}\rangle]^T, \quad (5.18)$$

²⁸ whose elements are,

$$|p\rangle = |e_\alpha|^0 \quad (5.19a)$$

$$|e\rangle_\alpha = Qe_\alpha^2 - b_2 \quad (5.19b)$$

$$|e^2\rangle_\alpha = a_1(Qe_\alpha^4 - b_6) + a_2(Qe_\alpha^4 - b_6) \quad (5.19c) \quad 1$$

$$|u_x\rangle_\alpha = e_{\alpha,x} \quad (5.19d) \quad 2$$

$$|q_x\rangle_\alpha = (b_1 e_\alpha^2 - b_3) e_{\alpha,x} \quad (5.19e) \quad 3$$

$$|u_y\rangle_\alpha = e_{\alpha,y} \quad (5.19f) \quad 4$$

$$|q_y\rangle_\alpha = (b_1 e_\alpha^2 - b_3) e_{\alpha,y} \quad (5.19g) \quad 5$$

$$|p_{xx}\rangle_\alpha = d e_{\alpha,x}^2 - e_\alpha^2 \quad (5.19h) \quad 6$$

$$|p_{xy}\rangle_\alpha = e_{\alpha,x} e_{\alpha,y}, \quad (5.19i) \quad 7$$

where $d = 2$ and $Q = 9$, $b_1 = \sum_{\alpha=1}^Q e_{\alpha,x}^2$, $b_2 = \sum_{\alpha=1}^Q e_\alpha^2$, $b_3 = \sum_{\alpha=1}^Q e_\alpha^2 e_{\alpha,x}^4$, $a_1 = ||e^2||^2$, and
 $a_2 = \sum_{\alpha=0}^{Q-1} (Qc_\alpha^2 - b_2) \times (Qc_\alpha^4 - b_6)$. 9
10

Explicitly, the transformation matrix can be written as

$$\mathbf{M} = \begin{bmatrix} 1 & 1 & 1 & 1 & 1 & 1 & 1 & 1 & 1 \\ -4 & -1 & -1 & -1 & -1 & 2 & 2 & 2 & 2 \\ 4 & -2 & -2 & -2 & -2 & 1 & 1 & 1 & 1 \\ 0 & 1 & 0 & -1 & 0 & 1 & -1 & -1 & 1 \\ 0 & -2 & 0 & 2 & 0 & 1 & -1 & -1 & 1 \\ 0 & 0 & 1 & 0 & -1 & 1 & 1 & -1 & -1 \\ 0 & 0 & -2 & 0 & 2 & 1 & 1 & -1 & -1 \\ 0 & 1 & -1 & 1 & -1 & 0 & 0 & 0 & 0 \\ 0 & 0 & 0 & 0 & 0 & 1 & 1 & 1 & 1 \end{bmatrix}. \quad (5.20)$$

11

12

13

¹ The corresponding equilibrium distribution functions in moment space $\widehat{\mathbf{f}}^{eq}$ is given as

$$\widehat{\mathbf{f}}^{eq} = [\rho_0, e^{eq}, e^{2eq}, u_x, q_x^{eq}, q_y^{eq}, p_{xx}^{eq}, p_{xy}^{eq}]^T, \quad (5.21)$$

² where

$$e^{eq} = \frac{1}{4}\alpha_2 p + \frac{1}{6}\gamma_2(u_x^2 + y_y^2) \quad (5.22a)$$

$$e^{2eq} = \frac{1}{4}\alpha_3 p + \frac{1}{6}\gamma_4(u_x^2 + y_y^2) \quad (5.22b)$$

$$q_x^{eq} = \frac{1}{2}c_1 u_x \quad (5.22c)$$

$$q_y^{eq} = \frac{1}{2}c_2 u_y \quad (5.22d)$$

$$p_{xx}^{eq} = \frac{3}{2}\gamma_1(u_x^2 - u_y^2) \quad (5.22e)$$

$$p_{xy}^{eq} = \frac{3}{2}\gamma_3(u_x u_y). \quad (5.22f)$$

³ To get the correct hydrodynamic equation, the values of the co-efficients are chosen as $\alpha_2 = 24$,
⁴ $\alpha_3 = -36$, $c_1 = c_2 = -2$, $\gamma_1 = \gamma_3 = 2/3$, $\gamma_2 = 18$ and $\gamma_4 = -18$. The values of the elements in
⁵ the collision matrix are: $s_8 = s_9 = \tau$ and $s_1 = s_4 = s_6 = 1.0$ and the others vary between 1.0
⁶ and 2.0 for linear stability. Through the Chapman-Enskog expansion (Du et al., 2006), the
⁷ incompressible Navier-Stokes equation can be recovered and the viscosity is given as

$$\nu = c_s^2 \Delta t (\tau - 0.5). \quad (5.23)$$

16

¹⁷ **5.1.3 Boundary conditions**

¹⁸ Boundary conditions (BC) form an important part of any numerical technique. In many cases,
¹⁹ the boundary conditions can strongly influence the accuracy of the algorithm. Velocity and
²⁰ pressure are not the primary variables in LBM, hence the standard pressure, velocity, and
²¹ mixed boundary conditions cannot be imposed directly. Alternative conditions in terms of the
²² distribution functions are adopted to describe the boundary conditions.

²³ **Periodic boundary condition**

²⁴ The simplest type of boundary condition is the periodic boundary. In this case, the domain is
²⁵ folded along the direction of the periodic boundary pair. For boundary nodes, the neighbouring
²⁶ nodes are on the opposite boundary, using the normal referencing of neighbours (see figure 5.1a).
²⁷ From the perspective of submarine landslide modelling, the periodic boundary conditions are
²⁸ useful for preliminary analysis, as they imply a higher degree of symmetry of the fluid domain.
 Further information on the periodic boundary condition can be found in Aidun et al. (1998). ¹

No-slip boundary condition ²

The most commonly adopted BC in the lattice Boltzmann approach is the no-slip BC, especially
³ the simple bounce-back rule, which is quite elegant and surprisingly accurate. The basic idea is
⁴ that the incoming distribution functions at a wall node are reflected back to the original fluid
⁵ nodes, but with the direction rotated by π radians. The bounce-back boundary condition is one
⁶ of the benefits of LBM, as it is trivial to implement and it allows one to effortlessly introduce
⁷ obstacles into the fluid domain. However, the boundary conditions have been proven to be only
⁸ first-order accurate in time and space (Pan et al., 2006). A straightforward improvement is to
⁹ consider the wall-fluid interface to be situated halfway between the wall and the fluid lattice
¹⁰ nodes (Ziegler, 1993). It involves defining the *solid* nodes as those lying within the stationary
¹¹ wall regions, and the *fluid* nodes otherwise. Then, if i is the direction between a fluid node n_1
¹² and a solid node n_2 , the bounce-back rule requires that the incoming fluid particle from n_1 to
¹³ n_2 be reflected back along the direction it came from, i.e., ¹⁴

$$f_{-i}(\mathbf{x}, t + \Delta t) = f_i(\mathbf{x}, t_+), \quad (5.24) \quad 15$$

where $-i$ denotes the opposite direction of i . The bounce back rule is illustrated in figure 5.4.
¹⁶ This simple rule ensures that no tangential velocity exists along the fluid-wall interface, thereby
¹⁷ a non-slip condition is imposed, and can be extended to any shapes or objects in a fluid flow (Han
¹⁸ et al., 2007a; Zou and He, 1997). The slip boundary conditions have similar treatment to the
¹⁹

5.1 Fluid simulation using lattice Boltzmann method

135

non-slip condition, except that the distribution functions are reflected in the boundary instead of bounce-back ([Succi, 2001](#)). 20
21

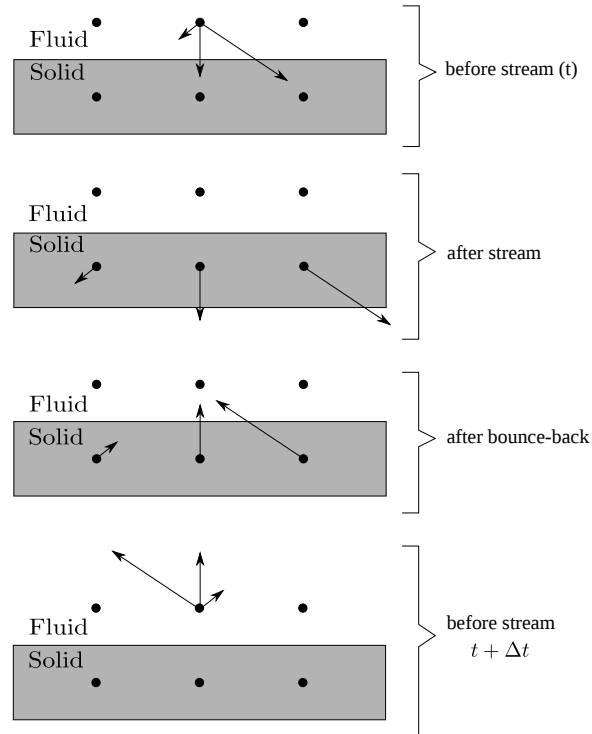


Figure 5.4 Half-way bounce back algorithm for the *D2Q9* model adopted after [Sukop and Thorne \(2006\)](#).

Pressure and velocity boundary condition

22

- ¹ The pressure (Dirichlet) boundary condition can be imposed in lattice Boltzmann by specifying
² a fluid density at the pressure boundary ([Zou and He, 1997](#)). To impose a pressure boundary
³ along the y-direction (for example, consider the left hand side inlet boundary in figure 5.5), a
⁴ density $\rho = \rho_{in}$ is specified from which the velocity is computed. The vertical component of
⁵ the velocity on the boundary is set as zero, $u_y = 0$. After streaming, f_2, f_3, f_4, f_6 , and f_7 are
⁶ known, u_x and f_1, f_5, f_8 are to be determined from [eq. 5.2](#) as

$$f_1 + f_5 + f_8 = \rho_{in} - (f_0 + f_2 + f_3 + f_4 + f_6 + f_7) \quad (5.25)$$

$$f_1 + f_5 + f_8 = \rho_{in} u_x + (f_3 + f_6 + f_7) \quad (5.26)$$

$$f_5 - f_8 = f_2 - f_4 + f_6 - f_7, \quad (5.27)$$

¹¹ Consistency of equations (5.25) and (5.26) gives

$$\text{12} \quad u_x = 1 - \frac{[f_0 + f_2 + f_4 + 2 * (f_3 + f_6 + f_7)]}{\rho_{in}}. \quad (5.28)$$

¹³ The bounce-back rule for the non-equilibrium part of the particle distribution normal to the
¹⁴ inlet is used to find $f_1 - f_1^{eq} = f_3 - f_3^{eq}$. The values of f_5 and f_8 can be obtained from f_1 :

$$\begin{aligned} \text{15} \quad f_1 &= f_3 + \frac{2}{3}\rho_{in}u_x \\ \text{16} \quad f_5 &= f_7 - \frac{1}{2}(f_2 - f_4) + \frac{1}{6}\rho_{in}u_x \\ \text{17} \quad f_8 &= f_6 + \frac{1}{2}(f_2 - f_4) + \frac{1}{6}\rho_{in}u_x. \end{aligned} \quad (5.29)$$

The corner node at inlet needs some special treatment. Considering the bottom node at inlet
as an example, after streaming, f_3, f_4, f_7 are known; ρ is defined, and $u_x = u_y = 0$. The particle
distribution functions f_1, f_2, f_5, f_6 , and f_8 are to be determined. The bounce-back rule for the
non-equilibrium part of the particle distribution normal to the inlet and the boundary is used to
find

$$f_1 = f_3 + (f_1^{eq} - f_3^{eq}) = f_3 \quad (5.30)$$

$$f_2 = f_4 + (f_1^{eq} - f_3^{eq}) = f_4. \quad (5.31)$$

Using these we can compute

$$f_5 = f_7 \quad (5.32)$$

$$f_6 = f_8 = \frac{1}{2}[\rho_{in} - (f_1 + f_2 + f_3 + f_4 + f_5 + f_6 + f_7 + f_8)]. \quad (5.33)$$

Similar procedure can be applied to the top inlet node and the outlet nodes. Von Neumann
boundary conditions constrain the flux at the boundaries. A velocity vector $u = [u_0 \ v_0]^T$ is
specified, from which the density and pressure are computed based on the domain. The velocity
boundary condition can be specified in a similar way (Zou and He, 1997). The pressure
and velocity boundary conditions contribute additional equation(s) to determine the unknown
distribution functions. In the case of velocity boundary, the boundary condition equation is
sufficient to determine the unknown distribution functions in the D2Q9 model, however the
pressure boundary conditions require additional constitutive laws to determine the unknown
distribution functions.

Table 5.1 LBM parameters used in simulating laminar flow through a circular pipe.

Parameter	Value
Density ρ	1000 kg m ⁻³
Relaxation parameter τ	0.51
Kinematic viscosity	1×10^{-6} m ² s ⁻¹
Grid resolution ‘h’	1 ⁻² m
Number of steps	50,000
Error in predicting horizontal velocity	0.009 %

5.2 Validation of the lattice Boltzmann method

To verify the incompressible LBM model implemented in the above section, numerical simulation of a transient development of steady state Poiseuille flow in a straight channel is performed. At $t = 0$, the LBM water particles ($\rho = 1000\text{kg/m}^3$) are simulated to flow through a channel of width ‘H’ (= 0.4 m) and simulation length ‘L’ (2.5H) under constant body force. Periodic boundary conditions are applied at either end of the channel and the pressure gradient is set to zero, which simulates the condition of a continuous flow of fluid in a closed circular pipe. The length ‘L’ has no effect on the simulation as no streamwise variation is detected in the solution. The parameters adopted in LBM simulation are presented in table 5.1. Sufficient time is allowed for the flow to travel beyond the required development length so that the flow is laminar (Durst et al., 2005). The development length X_D required for a flow to be fully laminar is

$$X_D/H = [(0.619)^{1.6} + (0.0567R_e)^{1.6}]^{1/1.6}, \quad (5.34)$$

where R_e is the Reynolds number. The velocity profile at steady state is presented in figure 5.5. A maximum horizontal velocity of 0.037863 m s⁻¹ is observed along the center-line of the channel. The maximum horizontal velocity is compared with the closed-form based on the Haygen-Poiseuille flow equation for no-slip boundary condition (Willis et al., 2008)

$$U_x = \frac{\Delta P}{2\mu L} \left[\frac{H^2}{4} - y^2 \right], \quad (5.35)$$

where v_x is the horizontal velocity (m/s); ΔP is the pressure gradient, μ dynamic viscosity of the fluid. LBM predicts the maximum horizontal velocity within an error of 0.009 %.

In order to further validate the accuracy of the lattice Boltzmann code, the transient development of the Poiseuille’s flow is compared with the CFD simulation performed using ANSYS Fluent. Finite Volume Method is a common CFD technique, which involves solving

the governing partial differential equation (Navier-Stokes) over the discretised control volume. This guarantees the conservation of fluxes over a particular control volume. The finite volume equations yield governing equations of the form

$$\frac{\partial}{\partial t} \iiint Q dV + \iint F dA = 0, \quad (5.36)$$

where Q is the vector of conserved variables, F is the vector of fluxes in the Navier-Stokes equation, V is the volume of control volume element, and A is the surface area of the control volume element.

A 2D rectangular plane of length 1 m and height 0.04 m is discretised into 400 cells

of size 1^{-2} m (see figure 5.6). A constant velocity is applied at the inlet. Water ($\rho = 2$ 998.2 kg/m³, viscosity ' η' = 1×10^{-3} Ns/m²) is allowed to flow through the channel and it develops into a fully laminar flow. The least squares approach was adopted to solve the gradient, and a maximum of 100 iteration steps were carried out until the solution converged.

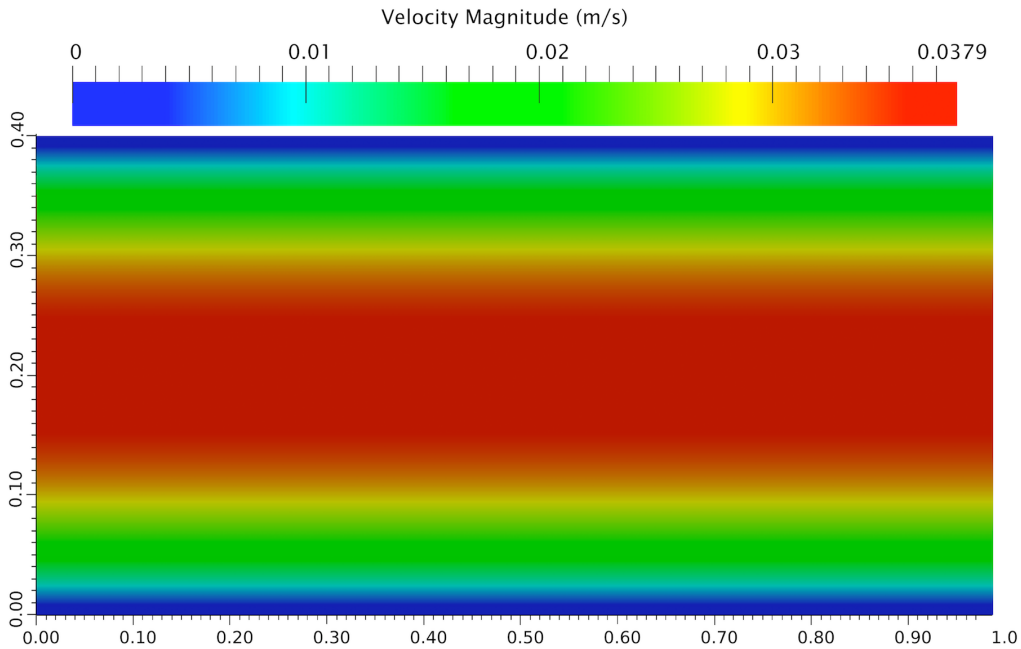


Figure 5.5 Velocity profile: LBM Simulation of a laminar flow through a channel.

The velocity profile obtained from the CFD simulation at cross-section ‘L/4’ is shown in figure 5.7. Figure 5.8 compares the development of computed velocity profiles with the analytical solution. At normalised time $t = 1$, the flow approaches steady state. It can be observed that LBM has excellent agreement with CFD and the analytical solution at various stages of flow evolution.

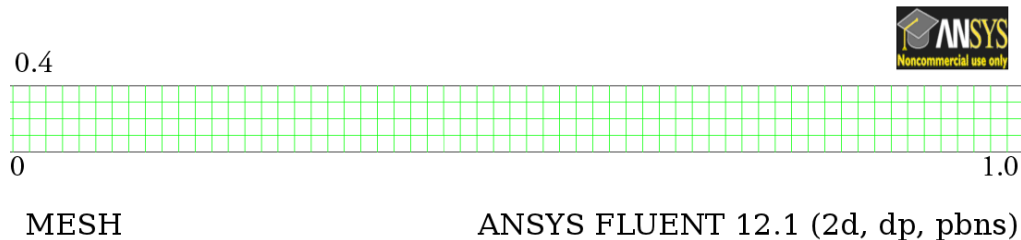


Figure 5.6 Finite Volume mesh used in the CFD analysis of laminar flow through a channel.

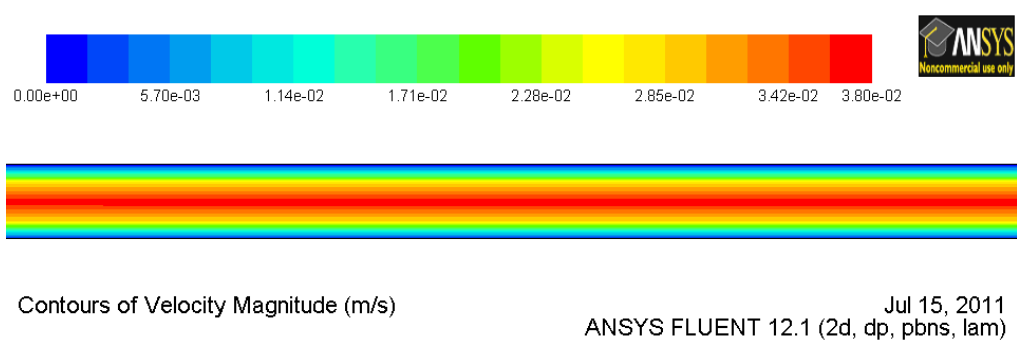


Figure 5.7 Velocity profile: CFD analysis of laminar flow through a channel.

10 In order to study the capability of the lattice Boltzmann technique to simulate fluid–solid
 11 interaction, LB simulation of a fluid flow around a rectangular obstacle is compared with
 12 the CFD technique. A solid wall of height ‘H/2’ is placed at length ‘L/4’ in the channel.
 13 Bounce-back algorithm is employed to model the fluid-wall interaction in LBM. In the CFD
 14 model, the control volume is discretised into 10,000 cells. A constant velocity is applied in the
 15 inlet and the horizontal velocity profile is recorded. Both, CFD and LBM simulations were
 16 performed to study the influence of a solid wall on the fluid flow behaviour.

17 The horizontal velocity profile obtained after 50,000 LBM iterations is presented in fig-
 18 ure 5.9. LBM is able to capture the velocity shedding around the edges of the wall. The velocity
 19 profile obtained from the CFD analysis is presented in figure 5.10. The horizontal velocity
 20 profile at ‘L/4’ at $t = 1$ is shown in figure 5.11. The maximum horizontal velocity from the
 21 CFD analysis is 0.3% higher in comparison with the LBM simulation. The discrepancy in
 22 the horizontal velocity profile (figure 5.11) can be attributed to the relaxation parameter used
 23 in the LBM, which is obtained by a trial and error procedure. The velocity profile obtained
 24 from the LBM simulation compares qualitatively with the FE analysis performed by [Zhong and](#)
 25 [Olson \(1991\)](#). Thus, it can be concluded that the lattice Boltzmann method is a suitable form of
 26 numerical representation of the Navier-Stokes equation to model fluid – solid interactions.

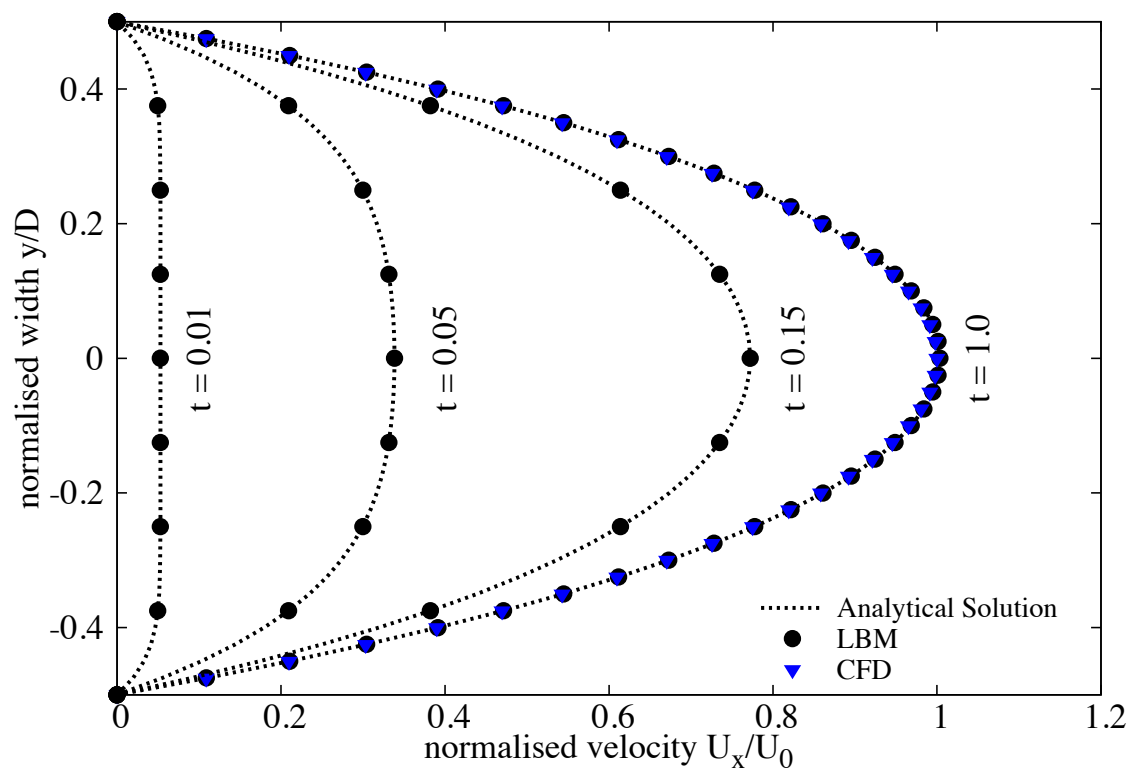


Figure 5.8 Development of the Poiseuille velocity profile in time: comparison between LBM simulation, CFD simulation and the analytical solution. Time is made dimensionless by H/U_0 .

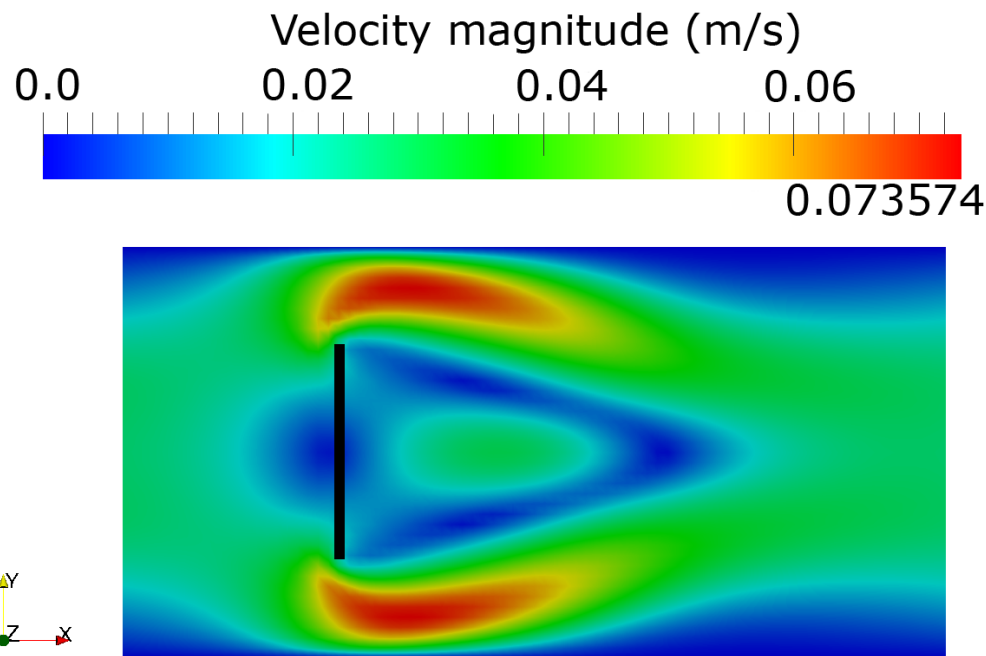


Figure 5.9 LBM simulation of velocity profile for a laminar flow through a pipe with an obstacle at L/4.

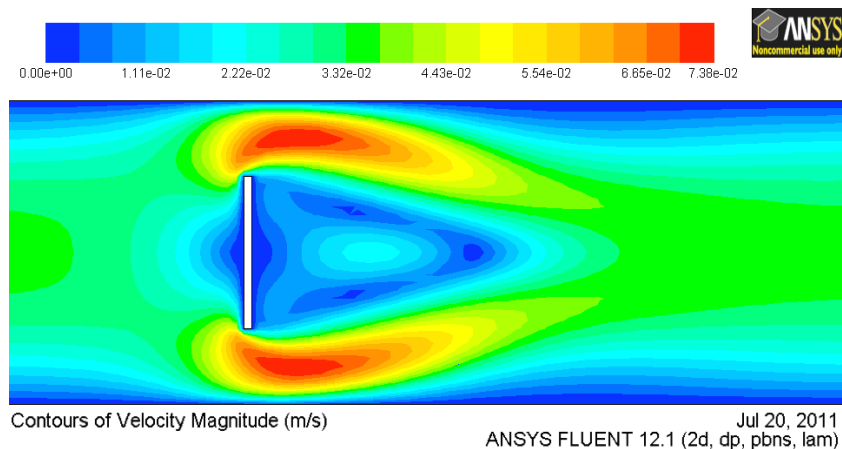


Figure 5.10 CFD simulation of velocity contour for a laminar flow through a pipe with an obstacle at L/4.

5.3 Turbulence in lattice Boltzmann method

The above formulation of lattice Boltzmann has been successfully applied to many fluid flow problems, however it is restricted to flows with low Reynolds number. Modelling fluids with low viscosity like water and air remains a challenge, necessitating very small values of h , and/or τ very close to 0.5 (He et al., 1997). The standard lattice Boltzmann can deal with laminar

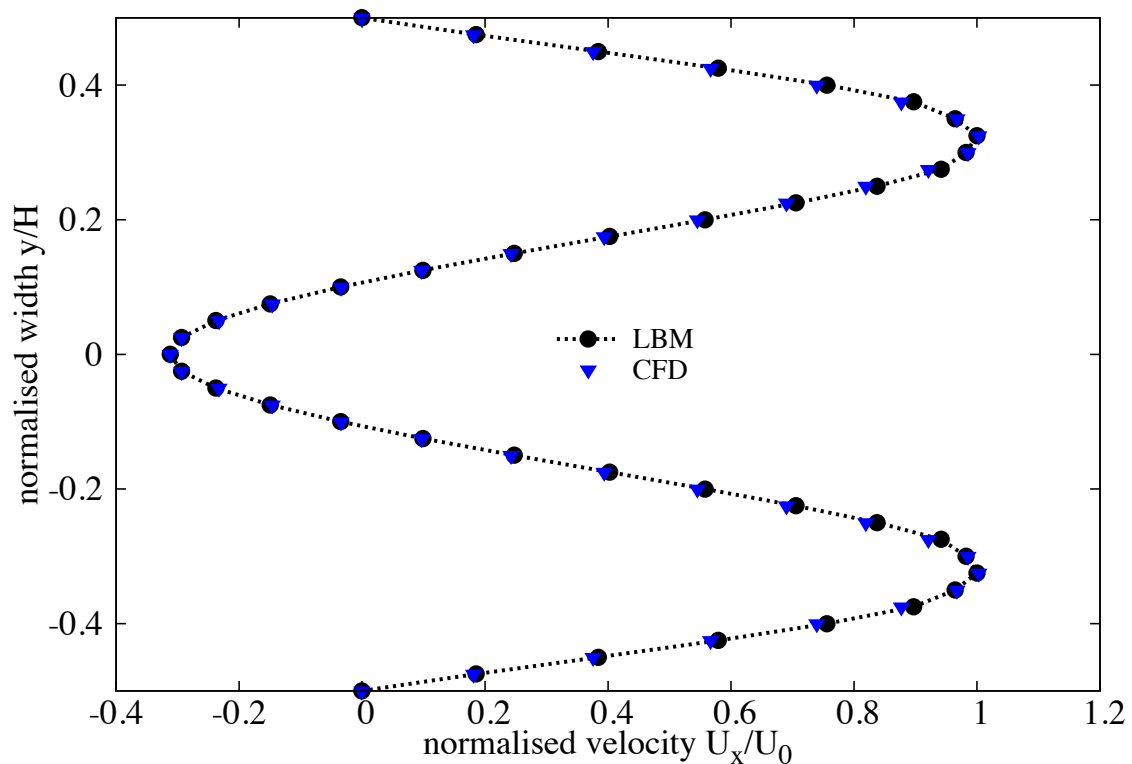


Figure 5.11 LBM and CFD simulation of a flow around an obstacle.

5.3 Turbulence in lattice Boltzmann method

143

³² flows, while practical problems with small kinematic viscosity are often associated with flows
¹ having large Reynolds numbers, i.e. flows which are unsteady or turbulent in nature. The
² turbulent flows are characterised by the occurrence of eddies with multiple scales in space, time
³ and energy.

⁴ The large eddy simulation (LES) is the most widely adopted approach to solve turbulent
⁵ flow problems. It directly solves the large scale eddies, which carry the predominant portion of
⁶ the energy, and the smaller eddies are modelled using a sub-grid approach. The separation of
⁷ scales is achieved by filtering of the Navier-Stokes equations, from which the resolved scales
⁸ are directly obtained. The unresolved scales are modelled by a one-parameter Smagorinski
⁹ sub-grid methodology, which assumes that the Reynolds stress tensor is dependent only on the
¹⁰ local strain rate ([Smagorinsky, 1963](#)). It involves parametrising the turbulent energy dissipation
¹¹ in the flows, where the larger eddies extract energy from the mean flow and ultimately transfer
¹² some of it to the smaller eddies which, in turn, pass the energy to even smaller eddies, and so
¹³ on up to the smallest scales. At the smallest scale, the eddies convert the kinetic energy into the
¹⁴ internal energy of the fluid. At this scale, the viscous friction dominates the flow ([Frisch and](#)
¹⁵ [Kolmogorov, 1995](#)).

¹⁶ In the Smargonisky model, the turbulent viscosity ν is related to the strain rate S_{ij} and a
¹⁷ filtered length scale ‘h’ as follows

$$\text{¹⁸} \quad S_{ij} = \frac{1}{2}(\partial_i u_j + \partial_j u_i) \quad (5.37)$$

$$\text{¹⁹} \quad \nu_t = (S_c h)^2 \bar{S} \quad (5.38)$$

$$\text{²⁰} \quad \bar{S} = \sqrt{\sum_{i,j} \tilde{S}_{i,j} \tilde{S}_{i,j}}, \quad (5.39)$$

²² where S_c is the Smagorinski constant, which is close to 0.03 ([Yu et al., 2005](#)). The effect of the
²³ unresolved scale motion is taken into account by introducing an effective collision relaxation
²⁴ time scale τ_t , so that the total relaxation time τ_* is written as

$$\text{²⁵} \quad \tau_* = \tau + \tau_t, \quad (5.40) \quad \text{¹$$

²⁶ where τ and τ_t are respectively the standard relaxation times corresponding to the true fluid
²⁷ viscosity ν and the turbulence viscosity ν_t , defined by a sub-grid turbulence model. The new
²⁸

viscosity ν_* corresponding to τ_* is defined as

$$\nu_* = \nu + \nu_t \quad 5$$

$$= \frac{1}{3}(\tau_* - \frac{1}{2})C^2\Delta t = \frac{1}{3}(\tau + \tau_t - \frac{1}{2})C^2\Delta t \quad 6$$

$$\nu_t = \frac{1}{3}\tau_t C^2\Delta t. \quad 7$$

$$8$$

The Smagorinski model is easy to implement and the lattice Boltzmann formulation remains unchanged, except for the use of a new turbulence-related viscosity τ_* . The component s_1 of the collision matrix becomes $s_1 = \frac{1}{\tau + \tau_t}$.

The effectiveness of LBM-LES model in simulating unsteady flows is verified by modelling the Kármán vortex street. In fluid dynamics, a Kármán vortex street is a repeating pattern of vortices caused by unsteady separation of fluid flow around circular obstacles. A vortex street will only be observed above a limiting value of Reynolds number of 90. The Reynolds number is computed based on the cylinder diameter ‘D’ and the mean flow velocity U of the parabolic inflow profile:

$$Re = \frac{UD}{\nu}. \quad 12$$

13

14

15

16

17

LBM particles are simulated to flow through a 2D rectangular channel with an aspect ratio ‘L/H’ of 2.5. A cylinder of diameter ‘d’ = 0.27H is placed at H/2. The pressure gradient at the inlet and the outlet is varied to create flows with different mean velocities. Numerical simulations of vortex shedding behind a circular obstacle are carried out for three different fluid flow regimes (Reynolds number of 55, 75, and 112). The fully developed fluid flows for different Reynolds numbers are shown in figure 5.12. It can be observed from figure 5.12 that the von Kármán vortex street can only be observed at high a Reynolds number of 112 ($Re > 90$), which shows the ability of the LBM turbulence model to capture instabilities in fluid flow.

One important quantity taken into account in the present analysis is the Strouhal number St ,

19

20

21

22

23

24

25

26

27

1

2

3

4

5

6

7

8

9

10

11

12

13

14

15

16

17

18

19

20

21

22

23

24

25

26

27

1

2

3

4

5

6

7

8

9

10

11

12

13

14

15

16

17

18

19

20

21

22

23

24

25

26

27

1

2

3

4

5

6

7

8

9

10

11

12

13

14

15

16

17

18

19

20

21

22

23

24

25

26

27

$$St = \frac{fD}{U_{max}}. \quad 5.44$$

1

2

3

4

5

6

7

8

9

10

11

12

13

14

15

16

17

18

19

20

21

22

23

24

25

26

27

1

2

3

4

5

6

7

8

9

10

11

12

13

14

15

16

17

18

19

20

21

22

23

24

25

26

27

1

2

3

4

5

6

7

8

9

10

11

12

13

14

15

16

17

18

19

20

21

22

23

24

25

26

27

1

2

3

4

5

6

7

8

9

10

11

12

13

14

15

16

17

18

19

20

21

22

23

24

25

26

27

1

2

3

4

5

6

7

8

9

10

11

12

13

14

15

16

17

18

19

20

21

22

23

24

25

26

27

1

2

3

4

5

6

7

8

9

10

11

12

13

14

15

16

17

18

19

20

21

22

23

24

25

26

27

1

2

3

4

5

6

7

8

9

10

11

12

1

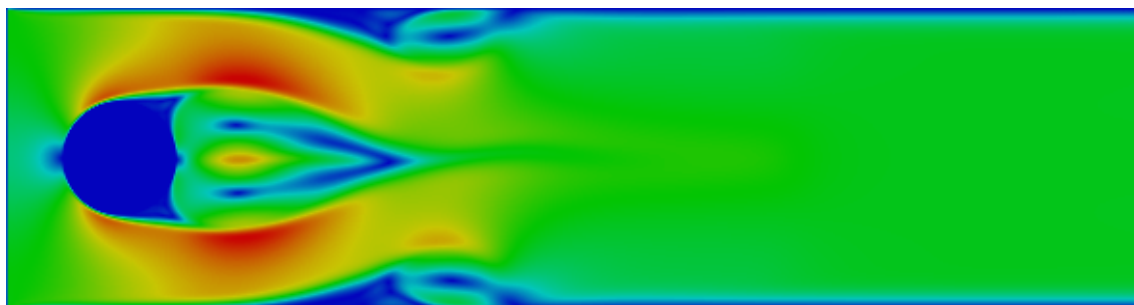
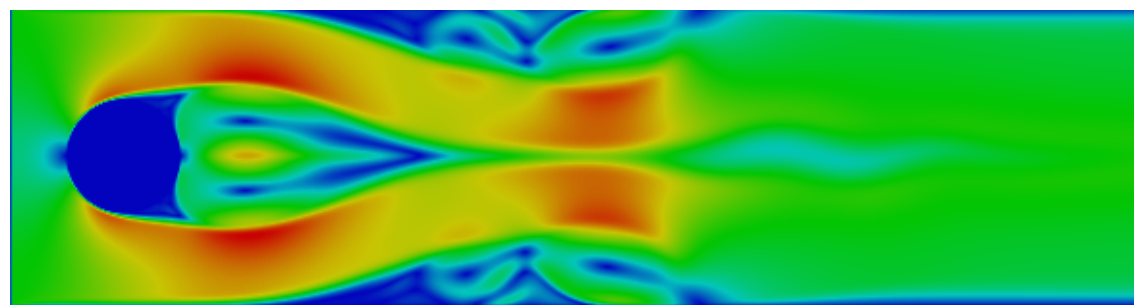
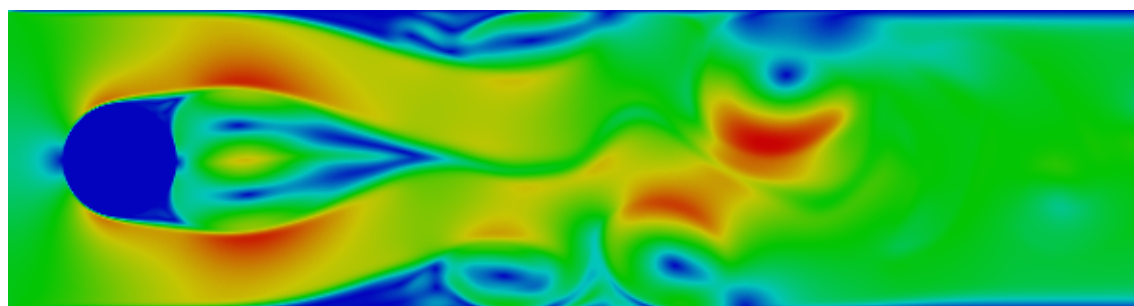
(a) $\text{Re} = 55$ (b) $\text{Re} = 75$ (c) $\text{Re} = 112$

Figure 5.12 Kármán vortex street

Table 5.2 Computed Strouhal number for fluid flows with different Reynolds number

Reynolds number	Strouhal number	
	LBM	FVM
55	0.117	0.117
75	0.128	0.129
112	0.141	0.141

* FVM results are from [Breuer et al. \(2000\)](#)

5.4 Coupled LBM and DEM for fluid-grain interactions

Modelling fluid–grain interactions in submarine landslides requires the ability to simulate the interactions at the dynamic fluid – solid boundaries. In principle, the conventional FE and FVM based approaches for solving the Navier-Stokes equations with moving boundaries and/or structural interaction ([Bathe and Zhang, 2004](#)) can be applied to particle fluid interaction problems. The common feature of these approaches is to model the interaction between the fluid and the solid to a high degree of accuracy. However, the main computational challenge is the need to continuously generate new geometrically adapted meshes to circumvent severe mesh distortion, which is computationally very intensive ([Han et al., 2007b](#)).

The lattice Boltzmann approach has the advantage of accommodating large particle sizes and the interaction between the fluid and the moving grains can be modelled through relatively simple fluid - grain interface treatments. Further, employing DEM to account for the grain/grain interaction naturally leads to a combined LB – DEM solution procedure. The Eulerian nature of the lattice Boltzmann formulation, together with the common explicit time step scheme of both LBM and DEM makes this coupling strategy an efficient numerical procedure for the simulation of fluid – grain systems.

LBM – DEM technique is a powerful predictive tool for gaining insights into many fundamental physical phenomena in fluid-solid systems. Such a coupled methodology was first proposed by ([Cook et al., 2004](#)) for simulating fluid-grain systems dominated by fluid-grain and grain-grain interactions. To capture the actual physical behaviour of the fluid-grain system, it is essential to model the boundary condition between the fluid and the grain as a non-slip boundary condition, i.e. the fluid velocity near the grain should be similar to the velocity of the grain boundary. The soil grains in the fluid domain are represented by lattice nodes. The discrete nature of the lattice will result in stepwise representations of the surfaces, which are otherwise circular, this is neither accurate nor smooth, unless sufficiently small lattice spacing is adopted.

6 Modified bounce back rule

7 To accommodate the movement of solid particles in the commonly adopted bounce-back rule
 8 (see section 5.1.3), Ladd (1994) modified the ‘no-slip’ rule for a given boundary link i to be

$$9 \quad f_i(\mathbf{x}, t + \Delta t) = f_i(\mathbf{x}, t_+) - \alpha_i e_i \cdot v_b \quad (\alpha_i = 6w_i \rho / C_s^2), \quad (5.45)$$

10 where $f_i(\mathbf{x}, t_+)$ is the post collision distribution at the fluid or solid boundary node \mathbf{x} , and v_b is
 11 the velocity at the nominal boundary point at the middle of the boundary link i

$$12 \quad \mathbf{v}_b = \mathbf{v}_c + \boldsymbol{\omega} \times (\mathbf{x} + e_i \Delta t / 2 - \mathbf{x}_c), \quad (5.46)$$

13 in which v_c and $\boldsymbol{\omega}$ are the translational and angular velocities at the mass centre of the solid
 14 particle, respectively. \mathbf{x}_c and $\mathbf{x} + e_i \Delta t / 2$ are the coordinates of the centre and the nominal
 15 boundary point, respectively. The impact force on the soil grain from the link is defined as

$$16 \quad \mathbf{F}_i = 2[f_i(\mathbf{x}, t_+) - \alpha_i e_i \cdot v_b] / \Delta t. \quad (5.47)$$

17 The corresponding torque \mathbf{T}_i , produced by the force with respect to the centre of the particle is
 18 computed as

$$19 \quad \mathbf{T}_i = \mathbf{r}_c \times \mathbf{F}_i (\mathbf{r}_c = \mathbf{x} + \mathbf{e}_i \Delta t / 2 - \mathbf{x}_c). \quad (5.48)$$

20 Then the total hydrodynamic force and torque exerted on the particle can be calculated by
 21 summing up the forces and torques from all the related boundary links:

$$22 \quad \begin{aligned} \mathbf{F} &= \sum_i \mathbf{F}_i \\ \mathbf{T} &= \sum_i \mathbf{T}_i. \end{aligned} \quad (5.49)$$

23 Ladd and Verberg (2001) described a methodology that minimises the oscillations resulting
 24 from soil grains crossing lattices at a very high speed. The methodology involves combining
 25 several extensions for the fluid simulation like the treatment of moving curved boundaries with
 26 the scheme of Yu et al. (2003) and a fluid/grain force interaction method with the momentum
 27 exchange method of Ladd and Verberg (2001). The simulation of the moving curved grain
 28 surfaces results in the intersection of links between two nodes at arbitrary distances (Iglberger
 et al., 2008). These distance values are referred to as delta values:

$$2 \quad \delta = \frac{\text{Distance between fluid node and soil surface}}{\text{Distance between fluid node and soil node}} \in [0, 1]. \quad (5.50)$$

For each pair of a fluid and grain node, a delta value has to be calculated. Delta values of zero are not possible as the nodes on the surface are considered as solid nodes. The algorithm for computation of the δ value is presented in [Iglberger et al. \(2008\)](#). Figure 5.13 shows the three possible situations for delta values between 0 and 1. The fluid particles in LBM are always considered to be moving at the rate of one lattice per time step ($\delta\mathbf{x}/\delta t$), for delta values smaller than 0.5. For δ values larger than 0.5, the fluid particles would come to rest at an intermediate node \mathbf{x}_i . In order to calculate the reflected distribution function in node \mathbf{x}_f , an interpolation scheme has to be applied. The linear interpolation scheme of [Yu et al. \(2003\)](#) is used in the present study, which uses a single equation, irrespective of the value of δ being smaller or larger than 0.5, to the reflected distribution function that is computed as

$$\begin{aligned} f_{\bar{\alpha}}(\mathbf{x}_f, t + \delta t) = & \frac{1}{1 + \delta} \cdot [(1 - \delta) \cdot f_{\alpha}(\mathbf{x}_f, t + \delta t) + \delta \cdot f_{\alpha}(\mathbf{x}_b, t + \delta t) \\ & + \delta \cdot f_{\bar{\alpha}}(\mathbf{x}_{f2}, t + \delta t) - 2w_a \rho_w \frac{3}{c^2} e_a \cdot \mathbf{u}_w], \end{aligned} \quad (5.51)$$

where w_{α} is the weighting factor, ρ_w is the fluid density in node \mathbf{x}_f , and \mathbf{u}_w is the velocity at the bounce-back wall. In order to couple the fluid-grain interaction, the LBM approach is extended by adopting a force integration scheme, to calculate the fluid force acting on the grain surface, and the momentum exchanged method described earlier. The physical force acting on grain agglomerates is calculated as the sum over all fluid/grain node pairs, resulting in

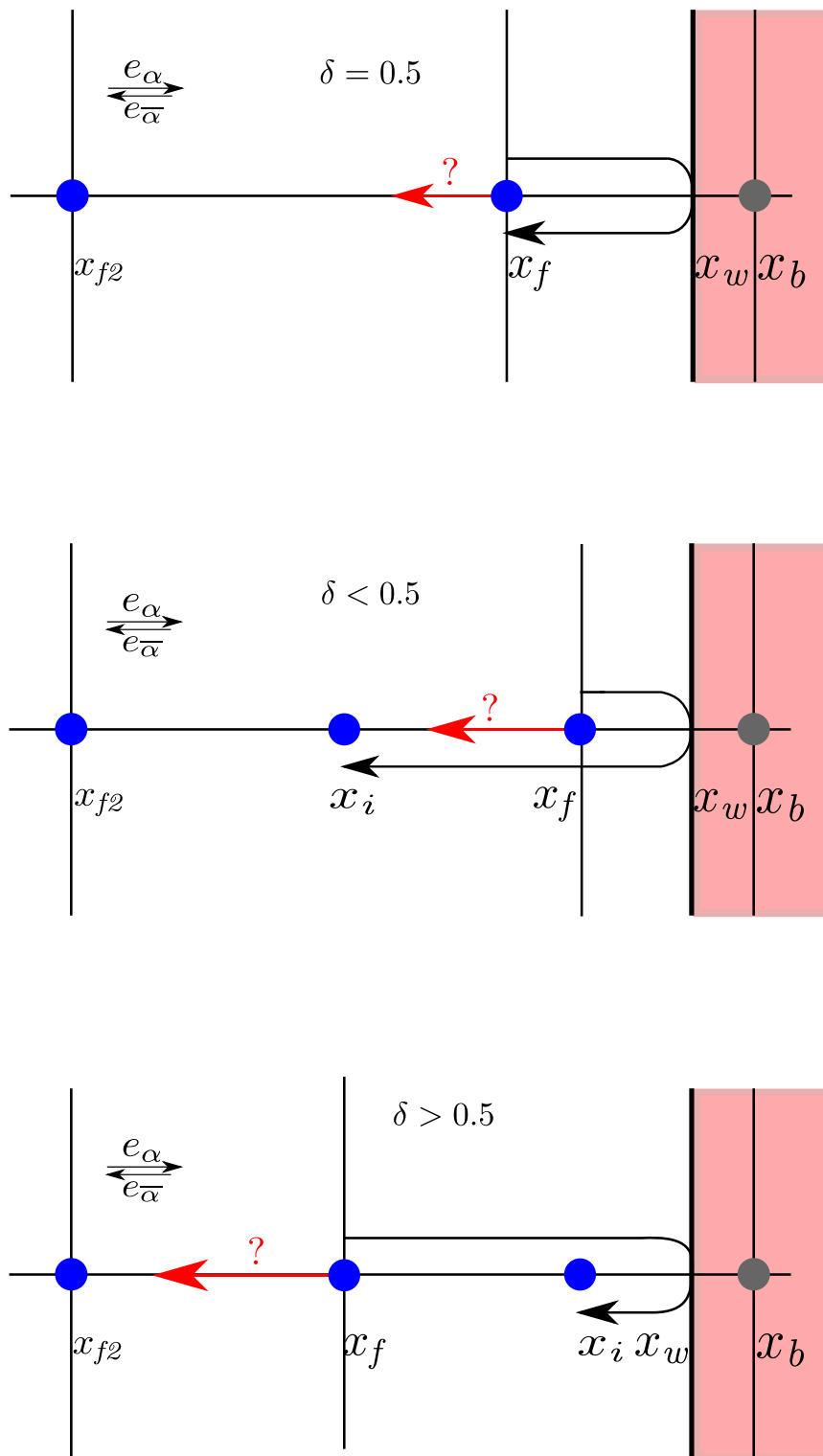
$$F = \sum_{\mathbf{x}_b} \sum_{\alpha=1}^{19} \mathbf{e}_{\alpha} [f_{\alpha}(\mathbf{x}_b, t) + f_{\bar{\alpha}}(\mathbf{x}_f, t)] \delta\mathbf{x}/\delta t. \quad (5.52)$$

After the force calculations, the coupled rigid body physics can be simulated in order to move the grains / grain-agglomerates according to the applied forces. The total hydrodynamic forces and torque exerted on a grain can be computed as ([Cook et al., 2004](#); [Noble and Torczynski, 1998](#))

$$\mathbf{F}_f = Ch \left[\sum_n \left(\beta_n \sum_i f_i^m e_i \right) \right] \quad (5.53)$$

$$\mathbf{T}_f = Ch \left[\sum_n (\mathbf{x}_n - \mathbf{x}_c) \times \left(\beta_n \sum_i f_i^m e_i \right) \right]. \quad (5.54)$$

The summation is over all lattice nodes covered by the soil grain, and \mathbf{x}_n represents the coordinate of the lattice node n .

Figure 5.13 Bounce back boundaries for different values of δ

When grains are not in direct contact among themselves, but are driven by the fluid flow

31

and body force, i.e. gravity, their motion can be determined by Newton's equation of motion

$$m\mathbf{a} = \mathbf{F}_f + m\mathbf{g} \quad (5.55)$$

$$J\ddot{\theta} = \mathbf{T}_f, \quad (5.56)$$

where m and J are respectively the mass and the moment of inertia of a grain, $\ddot{\theta}$ is the angular acceleration, \mathbf{g} is the gravitational acceleration, \mathbf{F}_f and \mathbf{T}_f are respectively the hydrodynamic forces and torque. The equation can be solved numerically by an explicit numerical integration, such as the central difference scheme.

The interaction between the soil grains, and the soil grains with the walls are modelled using the DEM technique. To solve the coupled DEM–LBM formulation, the hydrodynamic force exerted on soil grains and the static buoyancy force are considered by reducing the gravitational acceleration to $(1 - \rho/\rho_s)\mathbf{g}$, where ρ_s is the density of the grains. When taking into account all forces acting on an element, the dynamic equations of DEM can be expressed as

$$m\mathbf{a} + c\mathbf{v} = \mathbf{F}_c + \mathbf{F}_f + m\mathbf{g}, \quad (5.57)$$

where \mathbf{F}_c denotes the total contact forces from other elements and/or the walls, and c is a damping coefficient. The term $c\mathbf{v}$ represents a viscous force that accounts for the effect of all possible dissipation forces in the system including energy lost during the collision between grains. Considering a linear contact model

$$\mathbf{F}_c = k_n\delta, \quad (5.58)$$

where k_n is the normal stiffness and δ is the overlap, the critical time step associated with the explicit integration is determined as (He et al., 1997)

$$\Delta t_{cr} = 2(\sqrt{1 + \xi^2} - \xi)/\omega, \quad (5.59)$$

where $\omega = \sqrt{k_n/m}$ is the local contact natural frequency and $\xi = c/2m\omega$ is the critical damping ratio. The actual time step used for the integration of the Discrete Element equations is

$$\Delta t_D = \lambda \Delta t_{cr}. \quad (5.60)$$

The time step factor λ is chosen to be around 0.1 to ensure both stability and accuracy (He et al., 1997).

When combining the Discrete Element modelling of the grain interactions with the LB formulation, an issue arises. There are now two time steps: Δt for the fluid flow and Δt_D for the particles. Since Δt_D is normally smaller than Δt , Δt_D is slightly reduced to a new value Δt_s so that Δt and Δt_s have an integer ratio n_s

$$\Delta t_s = \frac{\Delta t}{n_s} \quad (n_s = [\Delta t / \Delta t_D] + 1). \quad (5.61)$$

This results in a sub-cycling time integration for the Discrete Element part. At every step of the fluid computation, n_s sub-steps of integration are performed for the Discrete Element Method (5.57) using the time step Δt_s . The hydrodynamic force \mathbf{F}_f is unchanged during the sub-cycling.

5.4.1 Draft, kiss and tumbling: Sedimentation of two grains

In multiphase flows, fundamental mechanisms of fluid – grain and grain – grain interactions are very important for accurately predicting the flow behaviours. The sedimentation of two circular grains in a viscous fluid serves as the simplest problem to study these two types of interactions, and many experimental and numerical studies have been carried out to investigate this behaviour (Komiwas et al., 2005; Wang et al., 2014). Fortes (1987) observed experimentally that in the sedimentation of two grains under gravity in a Newtonian fluid, the two grains would undergo the draft, kiss and tumbling (DKT) phenomenon.

The *draft*: grain 2 is first placed within the hydrodynamic drag above grain 1. As the hydrodynamic drag of grain 1 is a depression zone, grain 2 is attracted inside. The *kiss*: grain 2 increases its vertical velocity until it touches grain 1. The horizontal velocity of grain 1 increases and its vertical velocity decreases below that of grain 2. *Tumbling*: grain 2 having the same horizontal velocity and higher vertical velocity than grain 1, overtakes grain 1.

LBM-DEM simulation of two grains under gravity in a viscous Newtonian fluid reproduces

the draft, kiss and tumble effect (see figure 5.14). They are in agreement with the experimental description of the DKT effect. For better understanding of the DKT effect, the time history of three distances between the grains (normalised to the diameter of the grain D) are tracked i.e., the difference in the transverse coordinates δ_x/D and longitudinal coordinates δ_y/D of the two grain centres, and the gap between the two surfaces $\delta = \sqrt{\delta_x^2 + \delta_y^2} - 1$ (see figure 5.15c).

As shown in figure 5.14, grain 1 trails grain 2. As grain 2 approaches the depression zone, corresponding to negative fluid pressure behind grain 1, the velocity of the trailing grain increases as the grains approach closer, this is in agreement with the experimental description of the draft. Grain 2 increases its vertical velocity more than grain 1 until it touches grain 1. The kiss happens at a normalised time $(t / \sqrt{(D/g)}) = 25$. At this stage, the gap δ between the

11 grains is zero, but the actual gap is about one lattice spacing for the LBM collision model. After
12 this time, the vertical velocity of grain 1 decreases and its horizontal velocity increases as the
13 grains tumble. At this stage, the grains still remain in contact, i.e., the gap remains unchanged
14 $\delta = 0$. Subsequently, the two grains separate and move away from each other. Figure 5.15b
15 shows that the terminal velocities of the two grains are in good agreement with the terminal
16 velocity of a single grain found by an independent simulation and calculated using the empirical
17 Schiller and Nauman formula ([Komiwas et al., 2005](#)).

18 **5.5 GP-GPU Implementation**

19 Graphics Processing Unit (GPU) is a massively multi-threaded architecture that is widely
20 used for graphical and now non-graphical computations. Today's GPUs are general purpose
21 processors with support for an accessible programming interface. The main advantage of GPUs
22 is their ability to perform significantly more floating point operations (FLOPs) per unit time
23 than a CPU. General Purpose computations on GPUs (GPGPUs) often achieve speedups of
24 orders of magnitude in comparison with optimised CPU implementations.

25 A GPU consists of several *Streaming Multiprocessors* (SMs). Each SM contains 32 CUDA
26 processors. Each CUDA processor has a fully pipelined integer arithmetic logic unit (ALU)
27 and a floating point unit (FPU). The FPU complies with the IEEE 754-2008 industry standard
28 for floating-point arithmetic, capable of double precision computations. The SM schedules
29 work in groups of 32 threads called warps. Each SM features two warp schedulers and two
30 instruction dispatch units, allowing two warps to be issued and executed concurrently. Each
31 thread has access to both L1 and L2 caches, which improves the performance for programs
32 with random memory access.

33 The occupancy rate of the SPs, i.e. the ratio between the number of threads run and the
34 maximum number of executable threads, is an important aspect to take into consideration for
the optimisation of a CUDA kernel. Even though a block may only be run on a single SM, it is
possible to execute several blocks concurrently on the same SM. Hence, tuning the execution
grid layout allows one to increase the occupancy rate. Nevertheless, reaching the maximum
occupancy is usually not possible, as the threads executed in parallel on one SM have to share
the available registers ([Obrecht and Kuznik, 2011](#)).
1
2
3
4
5

6 Many-core processors are promising platforms for intrinsically parallel algorithms such as
7 the lattice Boltzmann method. Since the global memory for GPU devices shows high latency
8 and LBM is data intensive, the memory access pattern is an important issue for achieving good
9 performances. Whenever possible, global memory loads and stores should be coalescent and
aligned, but the propagation phase in LBM can lead to frequent misaligned memory accesses.
10

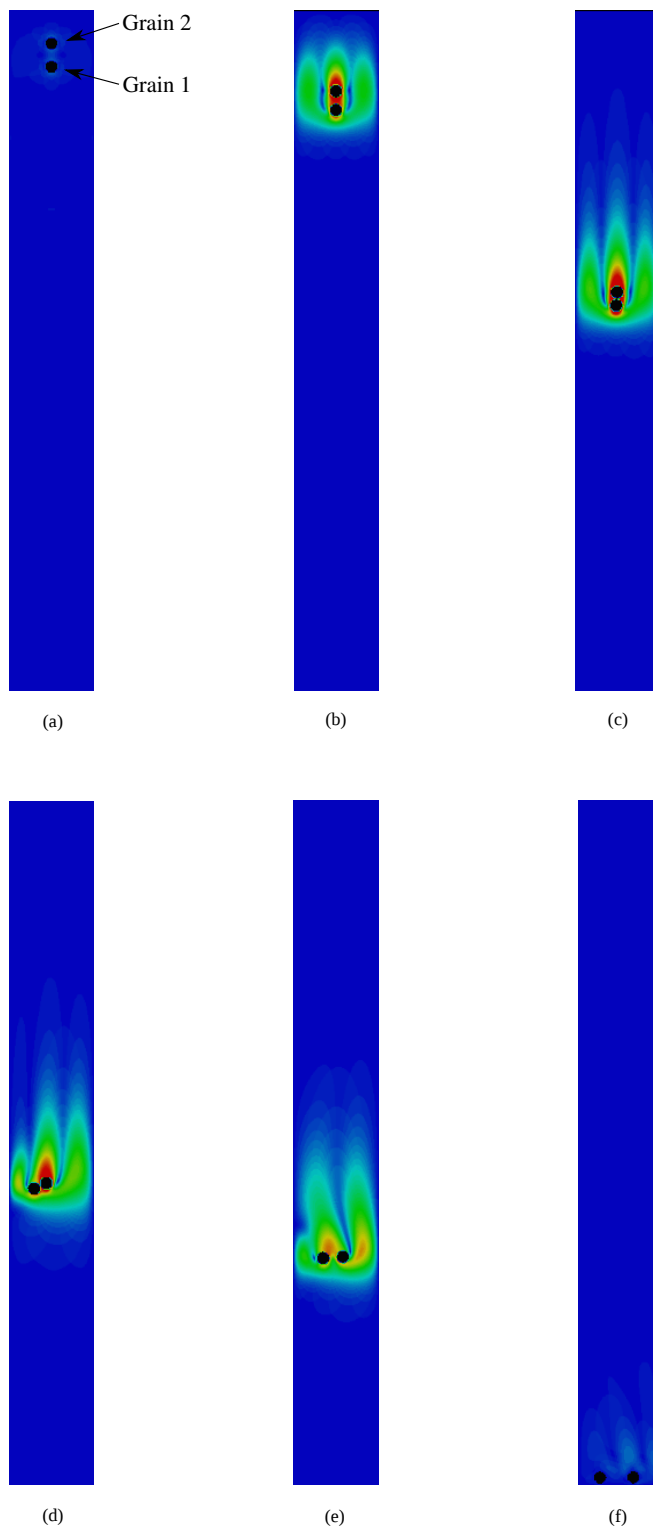


Figure 5.14 Time series of draft, kiss and tumble of two grains during sedimentation in a viscous fluid.

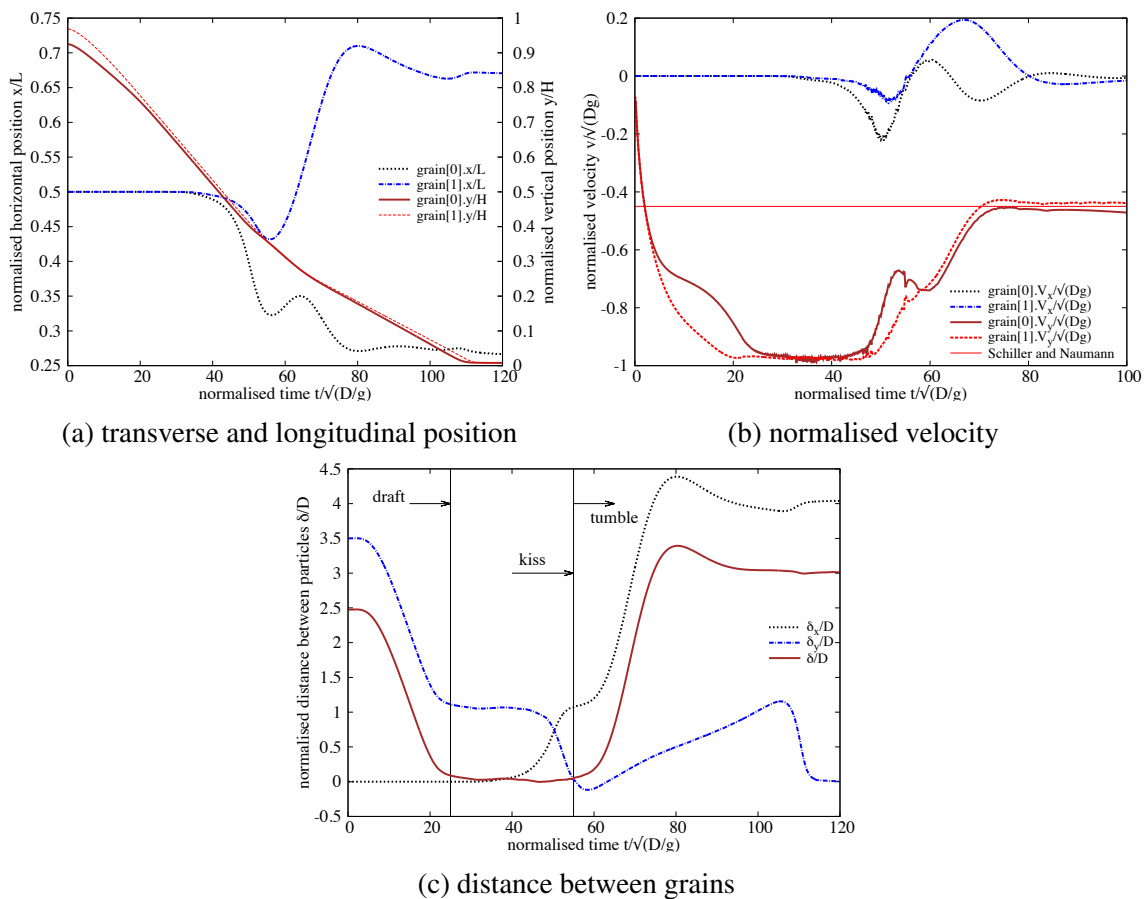


Figure 5.15 Time history of two circular grains during sedimentation.

Also, the data transfer between the host and the device is very expensive. In the present study,
the LBM implementation follows carefully chosen data transfer schemes in global memory.

There are three ways to accelerate GPGPU applications: (a) Using ‘drop-in’ libraries,
(b) using directives by exposing parallelism, and (c) using dedicated GPGPU programming
languages. OpenACC (Open Accelerators) is an open GPU directives programming standard
for parallel computing on heterogeneous CPU/GPU systems. Unlike conventional GPU pro-
gramming languages, such as CUDA, OpenACC uses directives to specify parallel regions in
the code and performance tuning works on exposing parallelism. OpenACC targets a host-
directed execution model where the sequential code runs on a conventional processor and
computationally intensive parallel pieces of code (kernels) run on an accelerator such as a GPU
(see figure 5.16).

The original GPGPU LBM – DEM code was implemented in C using OpenACC API v1.0,
which was released in November 2011. The current implementation in C++ uses OpenACC API
v2.0a ([OpenACC-Members, 2013](#)) and has two compute constructs, the kernels construct and
the parallel construct. LBM – DEM implementation predominantly uses the OpenACC gang and
vector parallelism. The LBM – DEM code runs sequential and computationally less intensive
functions on the CPU, OpenMP multi-threading is used when possible. Computationally
intensive functions are converted to a target accelerator specific GPU parallel code. Schematics
of a heterogeneous CPU/GPU system is shown in figure 5.16.

OpenACC offers kernel and parallel constructs to parallelise algorithms on CUDA kernels.
The loop nests in a kernel construct are converted by the compiler into parallel kernels that
run efficiently on a GPU. There are three steps to this process. The first is to identify the
loops that can be executed in parallel. The second is to map that abstract loop parallelism
onto a concrete hardware parallelism. In OpenACC terms, gang parallelism maps to grid-level
parallelism (equivalent to a CUDA blockIdx), and vector parallelism maps to thread-level
parallelism (equivalent to a CUDA threadIdx). The compiler normally maps a single loop
1 across multiple levels of parallelism using strip-mining. Finally, in step three the compiler
2 generates and optimizes the actual code to implement the selected parallelism mapping.

3 An OpenACC parallel construct creates a number of parallel threads that immediately begin
4 executing the body of the parallel construct redundantly. When a thread reaches a work-sharing
5 loop, that thread will execute some subset of the loop iterations, depending on the scheduling
6 policy as specified by the program or at the runtime. The code generation and optimization
7 for a parallel construct is essentially the same as for the kernel construct. A key difference
8 is that unlike a kernel construct, the entire parallel construct becomes a single target parallel
9 operation, aka a single CUDA kernel. Both constructs allow for automatic vectorization within
10 the loops ([Wolfe, 2012](#)).

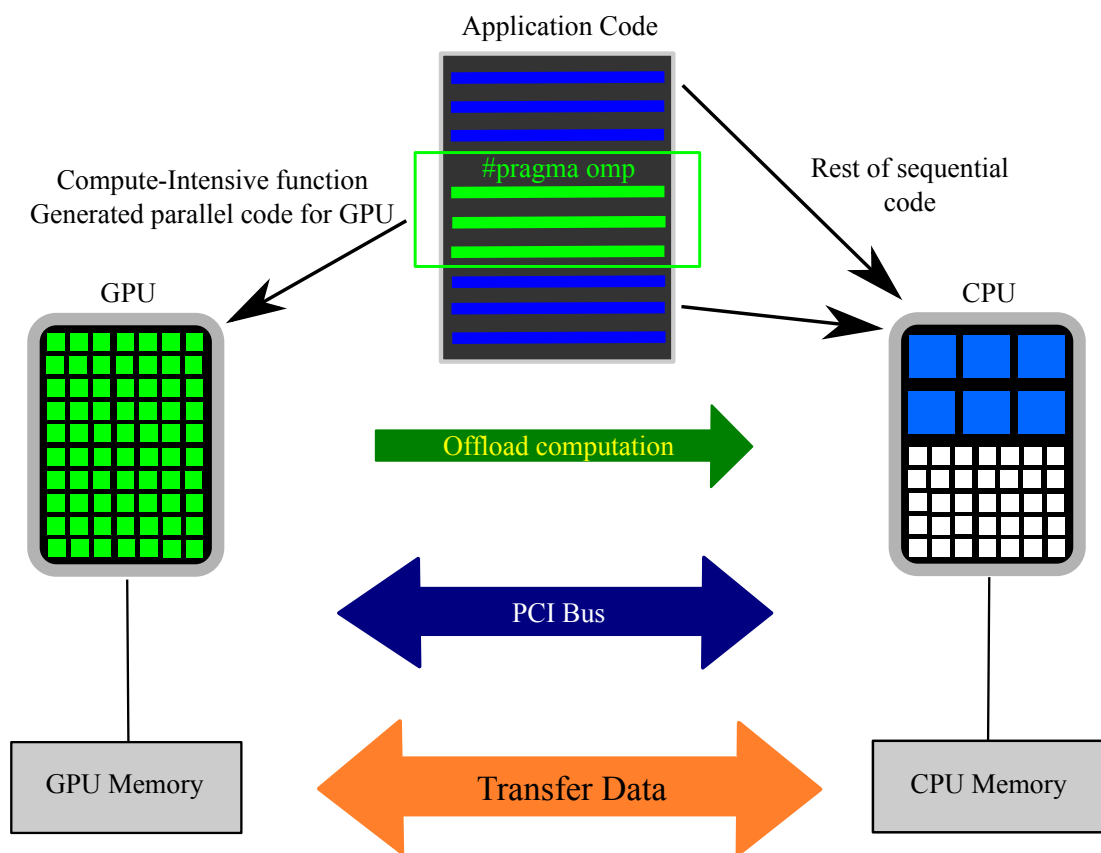


Figure 5.16 Schematics of a heterogeneous CPU/GPU system.

11 An excerpt from the LBM-DEM code showing the OpenACC GPU implementation of
 12 the hydrodynamic force computation is presented in Listing 5.1. The kernels loop construct
 13 tells the compiler to map the body of the following loop into an accelerator kernel. The GPU
 14 implementation uses a two-dimensional grid splitting the iterations across both the vector and
 15 gang modes. The kernel is mapped to a vector mode mapped (aligned with CUDA threadidx% x)
 16 with a vector length (thread block size) of 128. The kernel is also mapped to gang parallelism,
 17 aligned to CUDA blockidx% x , to avoid partition camping by mapping the stride-1 loop to
 18 the x dimension. The compiler strip-mines the loop into chunks of 256 iterations, mapping
 19 the 256 iterations of a chunk in vector mode across the threads of a CUDA thread block,
 20 and maps the $n/256$ chunks in gang mode across the thread blocks of the CUDA grid. The
 21 consecutive iterations (i and $i+1$), which refer to contiguous array elements ($f_{hf}[i]$ and $f_{hf}[i+1]$),
 22 are mapped to adjacent CUDA threads in the same thread block, to optimize for coalesced
 23 memory accesses.

Listing 5.1 OpenACC GPU implementation of the hydrodynamic force computation.

```

24 1 //OpenACC Kernels copy data between the host and the device
  2 #pragma acc kernels
  3 copyout(fhf1 [0: nbgrains ], f hf2 [0: nbgrains ], f hf3 [0: nbgrains ])
  4 copyin(obst [0:][0:], g [0: nbgrains ], ey [0:], f [0:][0:][0:], ex [0:])
  5 //Create individual threads for each DEM grain
  6 #pragma acc parallel for
  7 for ( i=0; i<nbgrains ;i++) {
  8   // Reset hydrodynamic forces to zero at the start of time step
  9   f hf1 [ i]=f hf2 [ i]=f hf3 [ i ]=0. ;
 10   // Iterate through all lattice nodes
 11   for ( y=0; y<ly;y++) {
 12     for ( x=0; x<lx;x++) {
 13       if (obst [x ][y]==i) {
 14         // generate code to execute the iterations in parallel with
 15         // no synchronization
 16         #pragma acc for independent
 17         for ( iLB=1; iLB<Q; iLB++) {
 18           next_x=x+ex[iLB];
 19           next_y=y+ey[iLB];
 20           if (iLB<=half) halfq=half ;
 21           else halfq= -half;
```

```

22     if (obst[next_x][next_y]!=i) {
23         fnx=(f[x][y][iLB+halfq]+f[next_x][next_y][iLB])*ex[iLB+halfq];
24         fny=(f[x][y][iLB+halfq]+f[next_x][next_y][iLB])*ey[iLB+halfq];
25         fhf1[i]=fhf1[i]+fnx;
26         fhf2[i]=fhf2[i]+fny;
27         fhf3[i]=fhf3[i]-fnx*(y-(g[i].x2-wall_bottom_y)/dx)
28             +fny*(x-(g[i].x1-wall_left_x)/dx);
29     }
30 }
31 }
32 }
33 }
34 }
```

Memory transaction optimisation is more important than computation optimisation. Registers do not give rise to any specific problem apart from their limited amount. Global memory, being the only one accessible by both the CPU and the GPU, is the critical path as it suffers from high latency. However, this latency is mostly hidden by the scheduler which stalls inactive warps until data are available. For data intensive LBM, this aspect is generally the limiting factor ([Obrecht and Kuznik, 2011](#)). To optimise the global memory transactions, the memory access is coalesced and aligned, as explained above. The memory transactions between the host and the target through a PCI bus are kept to a minimum.

A two-dimensional fluid – grain system, which consists of 7.2 million LBM nodes and 2500 DEM grains is used to demonstrate the ability of the GPGPU LBM – DEM code. The wall time required to compute 100 iterations of the given LBM – DEM problem is compared for executions running on a single CPU thread, multi-threaded CPU (using OpenMP) and the GPGPU implementations (see table 5.3). The speed-up of parallel implementations are measured against the single CPU thread execution time. OpenMP parallelised multi-threaded CPU execution running on 12 cores achieved a speed-up of 13.5x in comparison to a serial implementation. GPGPU implementation using OpenACC delivered an impressive 126x speed-up in comparison to a single thread CPU execution and about 10 times quicker than a CPU parallel code. In other words, a simulation that would have ordinarily taken 126 days to compute, could now be finished in a day using a GPU.

Scalability is an important criterion when developing high-performance computing codes. Scalability in GPUs is measured in terms of SM utilisation. It is important to distribute sufficient work to all SMs such that on every cycle the warp scheduler has at least one warp eligible to issue instructions. In general, sufficient warps on each SM should be available to

Table 5.3 GPU vs CPU parallelisation

Execution	Computational Time (s)	Speedup
CPU 1 OpenMP thread	2016	–
CPU 2 OpenMP threads	1035	1.5 x
CPU 4 OpenMP threads	660	3.0 x
CPU 12 OpenMP threads	150	13.5 x
GPU OpenACC	16	126.0 x

Wall time for 100 iteration for 7.2 Million LBM nodes and 2500 DEM grains.

* CPU OpenMP threads - 6 core Intel Xeon @ 3.3GHz

† GPU threads - GeForce GTX 580 - 512 CUDA cores

5 hide instruction and memory latency and to provide a variety of instruction types to fill the
6 execution pipeline. Figure 5.17 shows the scalability of GP-GPU implementation as the LBM
7 domain size is increased from 500,000 to 9 million nodes. With increase in LBM nodes the
8 computation time increases linearly with a slope of about 2, which shows that the LBM-DEM
9 implementation algorithm scales with the domain size.

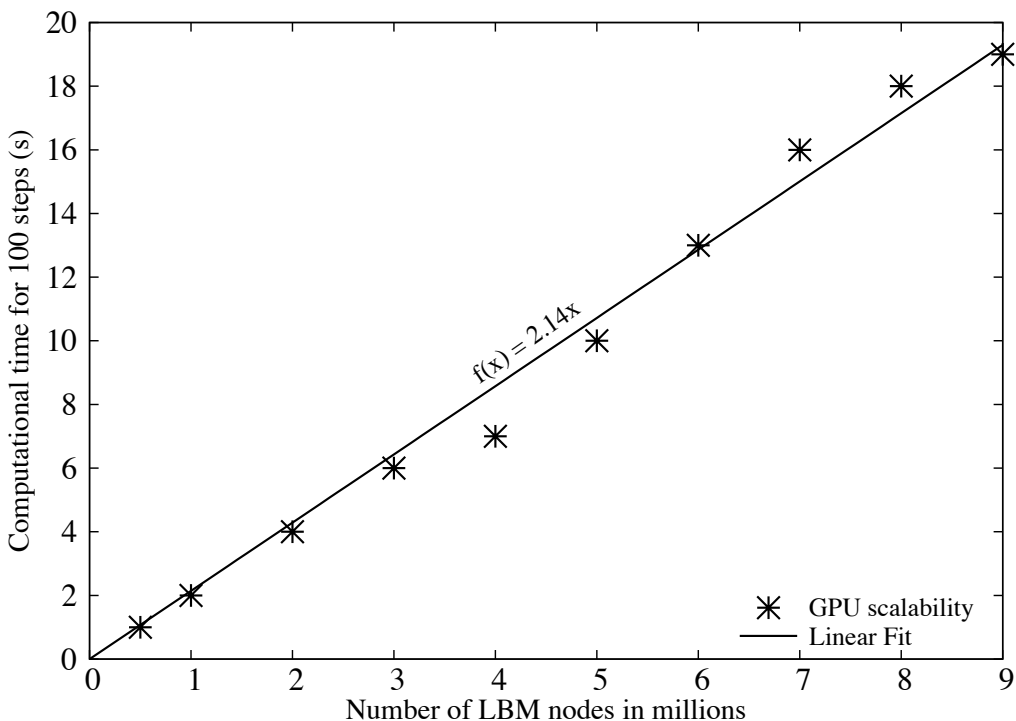


Figure 5.17 GPU scalability with increase in LBM nodes

10 A two-dimensional coupled LBM-DEM technique is developed to understand the local
11 rheology of granular flows in fluid. The coupled LBM-DEM technique offers the possibility to

12 capture the intricate microscale effects such as the hydrodynamic instabilities. The Smagorinsky
13 turbulence model is implement in LBM to capture the unsteady flow dynamics in underwater
14 granular avalanches. The GPGPU implementation of the coupled LBM – DEM technique
15 offers the capability to model large scale fluid – grain systems, which are otherwise impossible
1 to model using conventional computation techniques. Efficient data transfer mechanisms that
2 achieves coalesced global memory ensures that the GPGPU implementation scales linearly
3 with the domain size.

⁴ Chapter 6

⁵ Underwater granular flows

⁶ 6.1 Submarine granular flows down incline plane

⁷ The flow of dense granular material is a common phenomenon in engineering predictions, such
⁸ as avalanches, landslides, and debris-flow modelling. Despite the huge amount of research
⁹ that has gone into describing the behaviour of granular flows, a constitutive equation that
¹⁰ describes the overall behaviour of a flowing granular material is still lacking. The initiation and
¹¹ propagation of submarine granular flows depend mainly on the slope, density, and quantity of
¹² the material destabilised. Although certain macroscopic models are able to capture the simple
¹³ mechanical behaviours, the complex physical mechanisms that occur at the grain scale, such as
¹⁴ hydrodynamic instabilities, the formation of clusters, collapse, and transport, have largely been
¹⁵ ignored ([Topin et al., 2011](#)). The momentum transfer between the discrete and the continuous
¹⁶ phases significantly affects the dynamics of the flow ([Peker and Helvacı, 2007](#)). Grain-scale
¹⁷ description of the granular material enriches the macro-scale variables, which poorly account
¹⁸ for the local rheology of the materials. In order to describe the mechanism of saturated and/or
¹⁹ immersed granular flows, it is important to consider both the dynamics of the solid phase and
²⁰ the role of the ambient fluid ([Denlinger and Iverson, 2001](#)). In particular, when the solid phase
²¹ reaches a high volume fraction, it is important to consider the strong heterogeneity arising from
²² the contact forces between the grains, the drag interactions which counteract the movement
²³ of the grains, and the hydrodynamic forces that reduce the weight of the solids inducing a
²⁴ transition from dense compacted to a dense suspended flow ([Meruane et al., 2010](#)). The case of
²⁵ the collapse in presence of an interstitial fluid has been less studied. In this paper, we study the
²⁶ submarine granular flows in the inclined configuration. We study the effect of permeability,
²⁷ density and slope angle on the run-out evolution.

²⁸ In this study, a 2D poly-disperse system ($d_{max}/d_{min} = 1.8$) of circular discs in fluid was
²⁹ used to understand the behaviour of granular flows on inclined planes (see Figure [6.1](#)). The soil

30 column was modelled using 1000 discs of density 2650 kg m^{-3} and a contact friction angle of
 31 26° . The collapse of the column was simulated inside a fluid with a density of 1000 kg m^{-3} and
 32 a kinematic viscosity of $1 \times 10^{-6} \text{ m}^2 \text{ s}^{-1}$. The choice of a 2D geometry has the advantage of
 1 cheaper computational effort than a 3D case, making it feasible to simulate very large systems.
 2 A granular column of aspect ratio ‘a’ of 0.8 was used. A hydrodynamic radius $r = 0.9R$ was
 3 adopted during the LBM computations. Dry analyses were also performed to study the effect
 4 of hydrodynamic forces on the run-out distance.

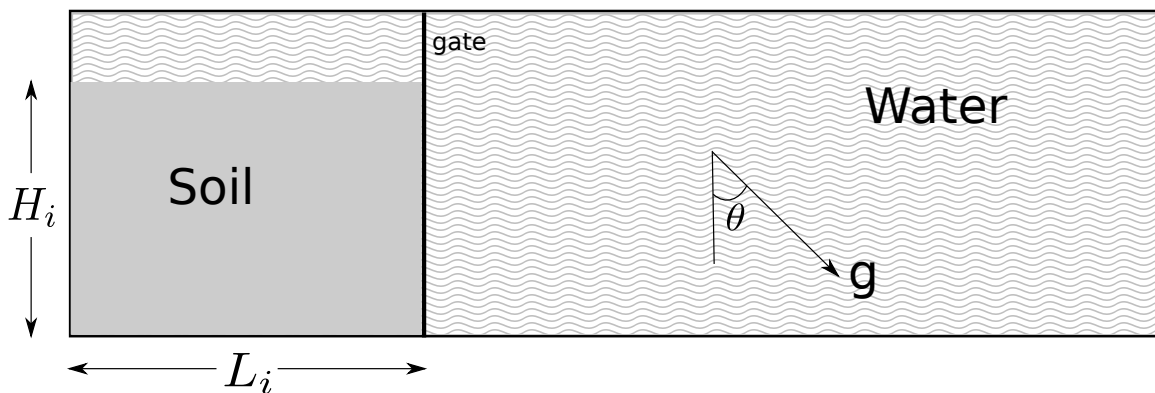


Figure 6.1 Underwater granular collapse set-up

6.1.1 Effect of initial density

The morphology of the granular deposits in fluid is shown to be mainly controlled by the initial volume fraction of the granular mass and not by the aspect ratio of the column (Pailha et al., 2008; Rondon et al., 2011). In order to understand the influence of the initial packing density on the run-out behaviour, a dense sand column (initial packing density, $\Phi = 83\%$) and a loose sand column ($\Phi = 79\%$) were used. The granular columns collapse and flow down slopes of varying inclinations (2.5° , 5° and 7.5°).

The evolution of run-out distances for a dense sand column with time in dry and submerged conditions for varying slope inclinations are presented in figure 6.2. The run-out distance is longer in submerged condition than the dry condition for a flow on a horizontal surface. However, with increase in the slope angle the run-out in the fluid decreases.

Dense granular columns in fluid take a longer time to collapse and flow, due to the development of large negative pore-pressure, as the dense granular material dilates during the initial phase of the flow. The morphology of dense granular flows down slopes of varying inclinations at the critical time ($t = \tau_c = \sqrt{H/g}$, when the flow is fully mobilised) are shown in figure 6.4.

It can be seen that the viscous drag on the dense column tend to predominate over the influence of hydroplaning on the run-out behaviour. This influence can be observed in the

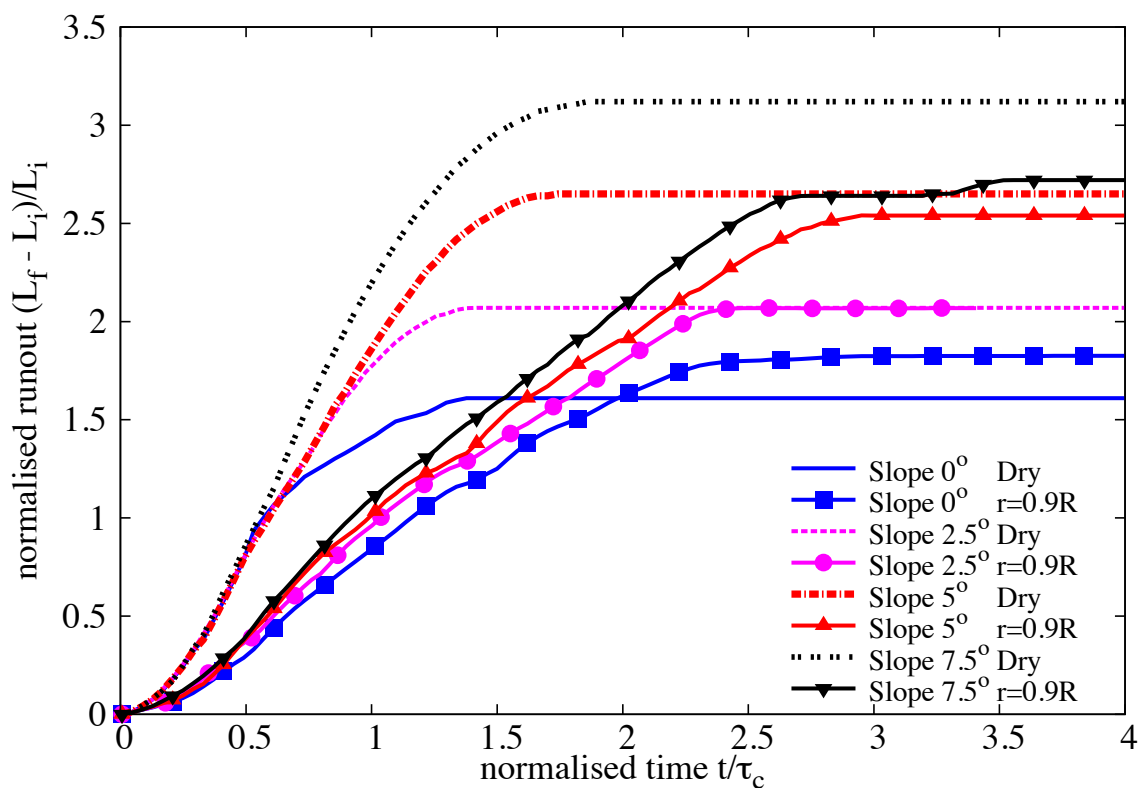


Figure 6.2 Evolution of run-out with time (dense)

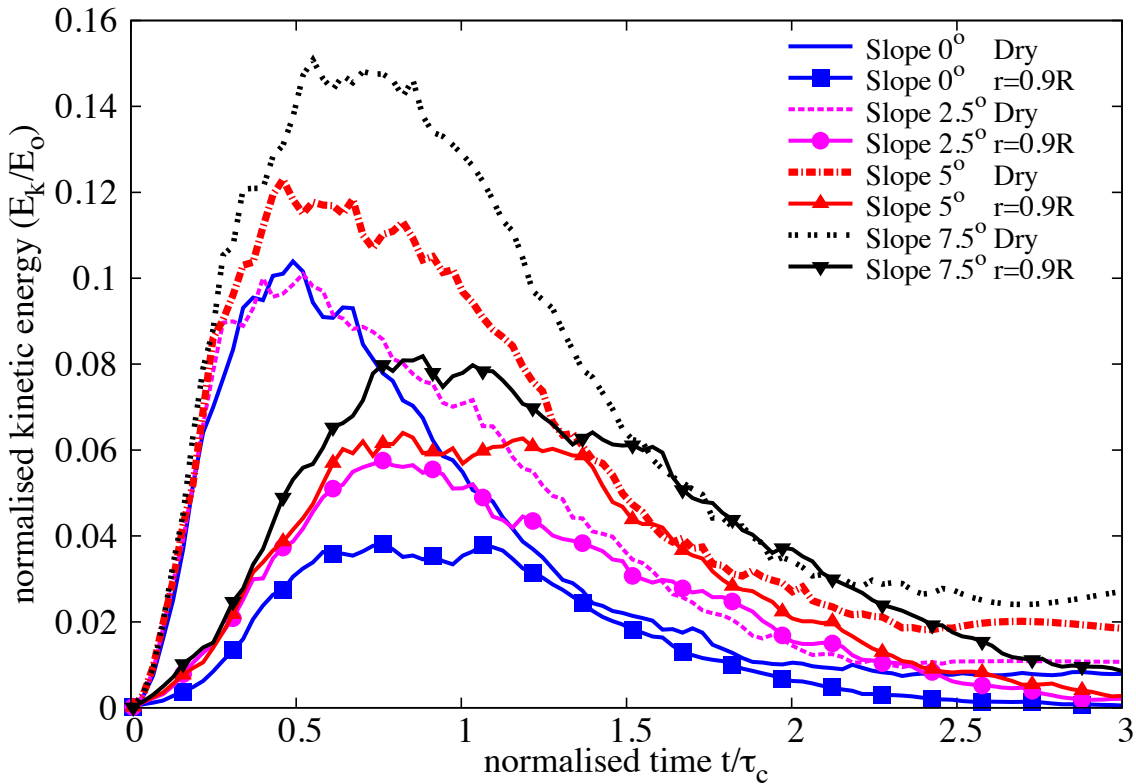
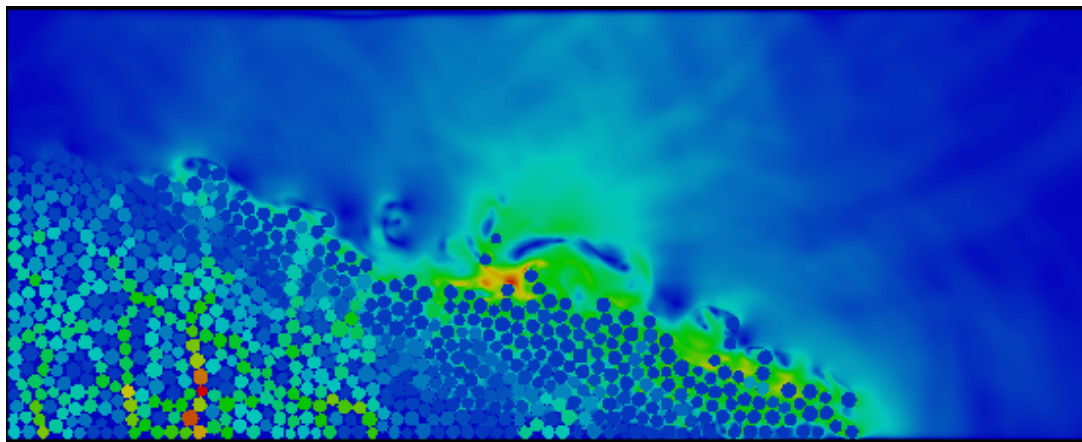


Figure 6.3 Evolution of Kinetic Energy with time (dense case)

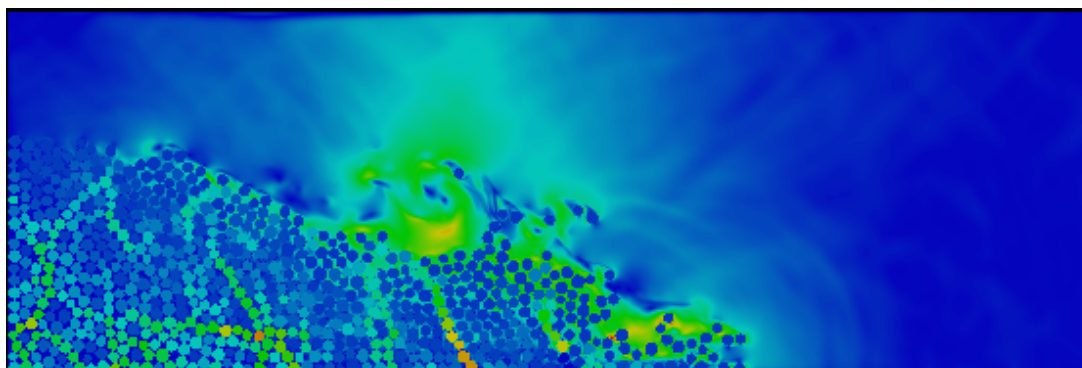
smaller peak kinetic energy for granular column in fluid compared to it's dry counterpart (see Figure 6.3). With increase in slope angle, the volume of material that dilates increases. This results in large negative pore pressures and more viscous drag on the granular material. Hence, the difference in the run-out between the dry and the submerged condition, for a dense granular assembly, increases with increase in the slope angle.

In contrast to the dense granular columns, the loose granular columns (relative density $I_D = 30\%$) show longer run-out distance in immersed conditions (see Figure 6.5). The run-out distance in fluid increases with increase in the slope angle compared to the dry cases. Loose granular material tends to entrain more water at the base of the flow front, creating a lubricating surface, which causes longer run-out distance (see Figure 6.6). The hydroplaning effect causes an increase in the velocity the loose condition in comparison with the dense condition (see Figure 6.7).

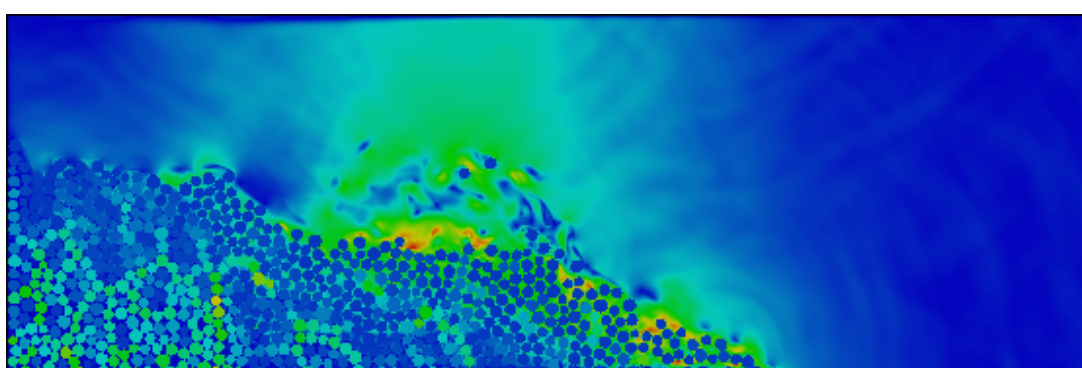
The evolution of packing density (see Figure 6.8) shows that dense and the loose conditions reach similar packing density. This indicates that the dense granular column dilates more and is susceptible to higher viscous drag forces. Whereas in the loose condition, a positive



(a) Slope 2.5



(b) Slope 5.0



(c) Slope 7.5

Figure 6.4 Flow morphology at critical time for different slope angles (dense)

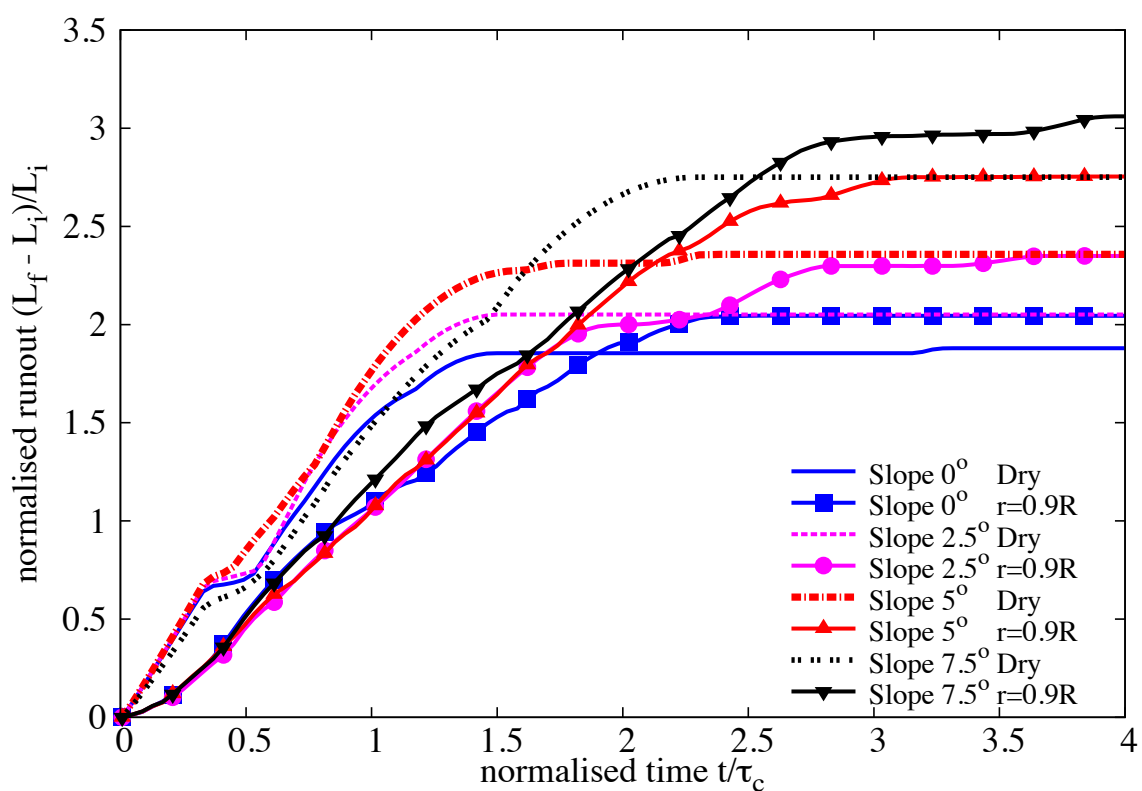
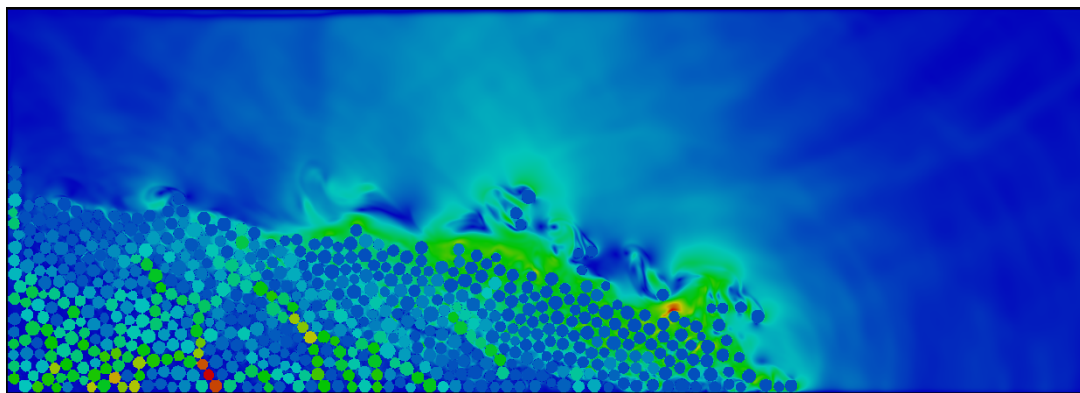
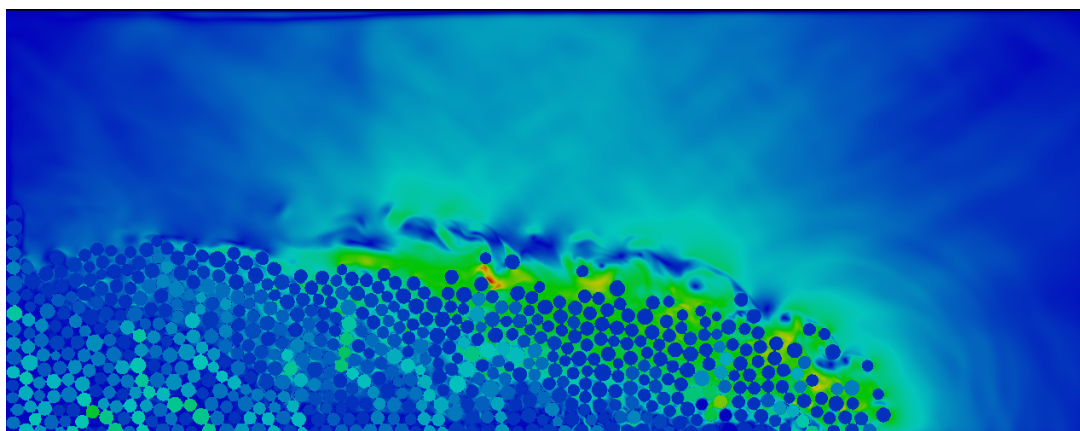


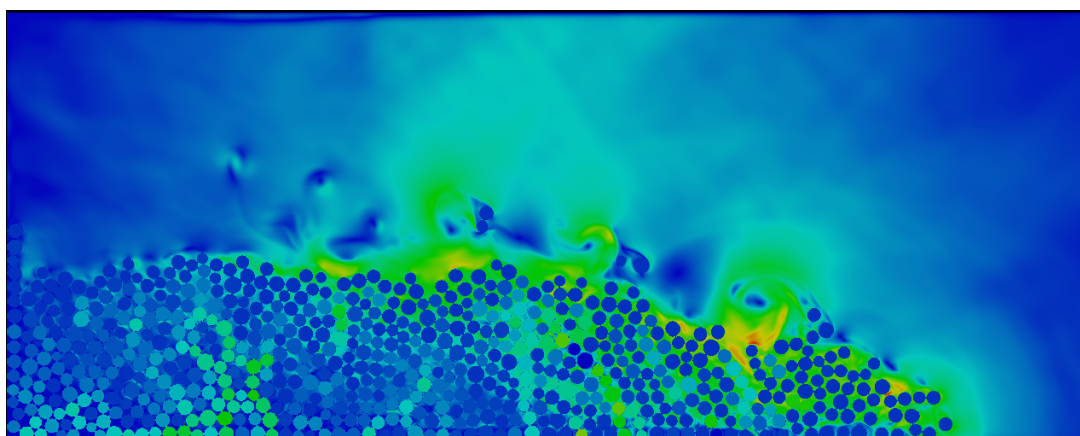
Figure 6.5 Evolution of run-out with time (loose)

6.1 Submarine granular flows down incline plane**167**

(a) Slope 2.5



(b) Slope 5.0



(c) Slope 7.5

Figure 6.6 Flow morphology at critical time for different slope angles (loose)

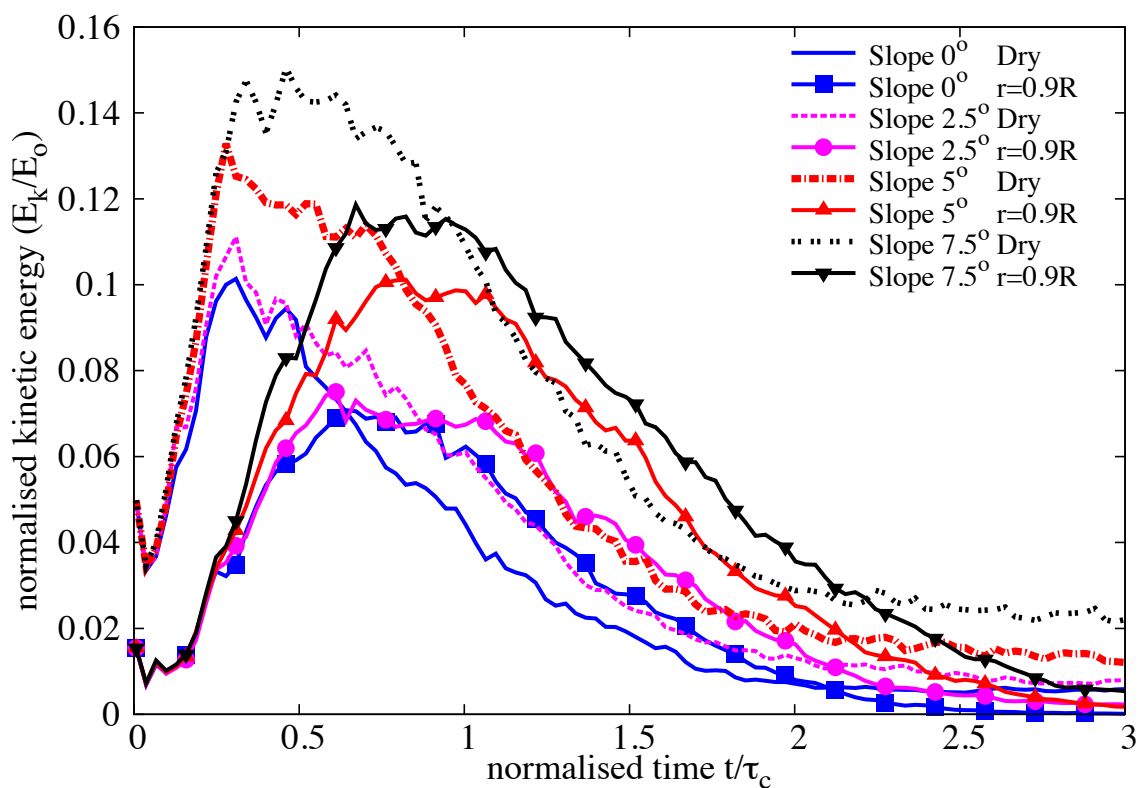


Figure 6.7 Evolution of Kinetic Energy with time (loose)

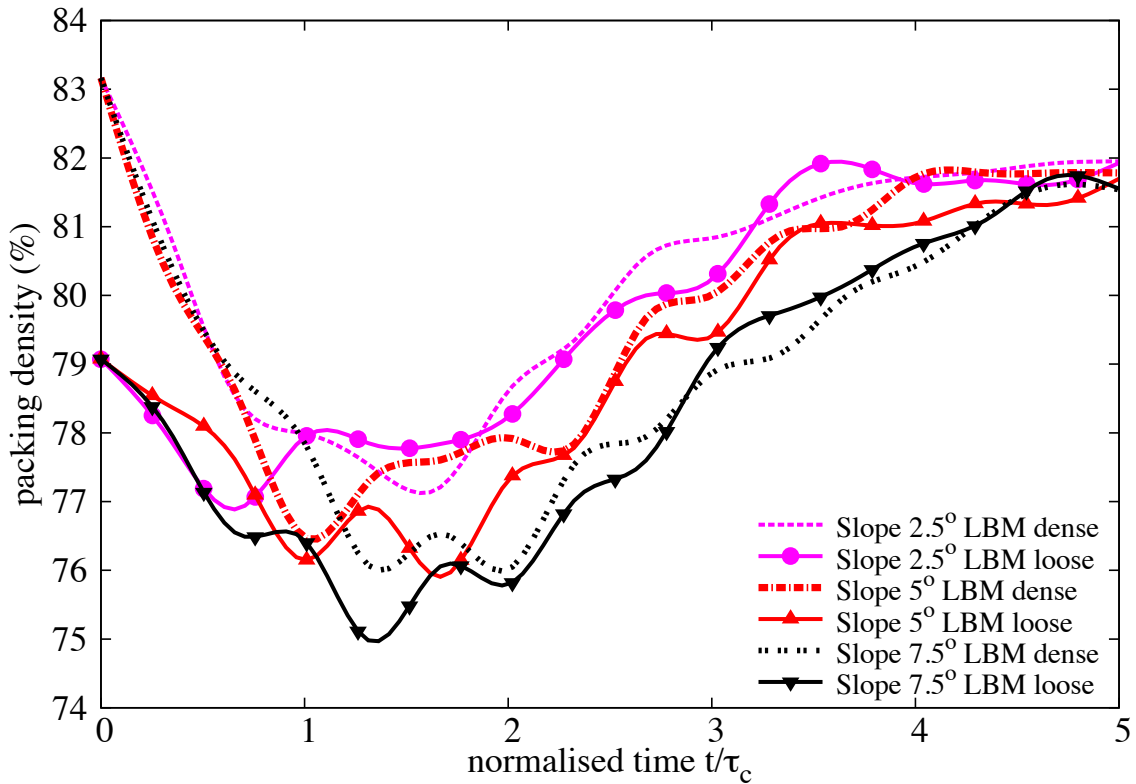


Figure 6.8 Evolution of packing density with time

6 pore-pressure is observed at the base of the flow, indicating entrainment of water at the base,
7 i.e. hydroplaning resulting in longer run-out distance.

8 6.1.2 Effect of permeability

9 In DEM, the grain – grain interaction is described based on the overlap between the grains at the
10 contact surface. In a 3D granular assembly, the pore spaces between grains are interconnected.
11 Whereas in a 2-D assembly, the grains are in contact with each other that result in a non-
12 interconnected pore-fluid space. This causes a no flow condition in a 2-D case. In order to
13 overcome this difficulty, a reduction in radius is assumed only during the LBM computation
14 phase (fluid and fluid – solid interaction). The reduction in radius allows interconnected pore
15 space through which the surrounding fluid can flow. This technique has no effect on the grain –
16 grain interactions computed using DEM. See Kumar et al. (2012) for more details about the
17 relationship between reduction in radius and permeability of the granular assembly.

18 For a slope angle of 5°, the hydrodynamic radius of the loosely packed grains was varied
19 from $r = 0.7R$ (high permeability), 0.75R, 0.8R, 0.85R to 0.9R (low permeability). The run-
20 out distance is found to increase with decrease in the permeability of the granular assembly

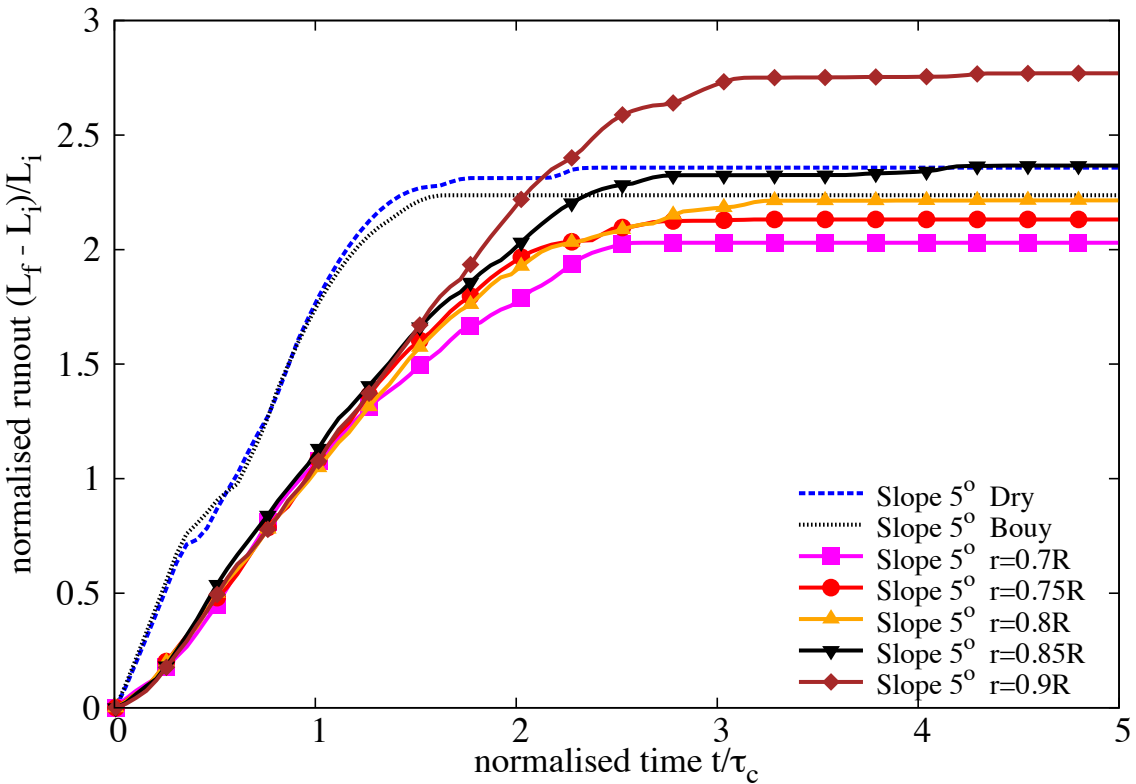


Figure 6.9 Evolution of run-out with time for different permeability (loose slope 5°)

(see Figure 6.9). The run-out distance for high permeable conditions ($r = 0.7R - 0.8R$) were lower than their dry counterparts. Although, decrease in permeability resulted in an increase in the run-out distance, no significant change in the run-out behaviour was observed for a hydrodynamic radius of up to 0.8R.

With further decrease in permeability ($r = 0.85R$ and $0.9R$), the run-out distance in the fluid was greater than the run-out observed in the dry condition. At very low permeability ($r = 0.9R$), granular material started to entrain more water at the base, which causes a reduction in the effective stress accompanied by a lubrication effect on the flowing granular media. This can be seen as a significant increase in the peak kinetic energy and the duration of the peak energy, in comparison with dry and high permeable conditions (see Figure 6.11).

The permeability of the granular column did not have an influence on the evolution of height during the flow. However, dry granular column tends to collapse more than the immersed granular column (see Figure 6.10).

Positive pore-pressure generation at the base of the flow was observed for low permeable conditions. Inspection of the local packing density showed entrainment of water at the base of the flow, which can also be observed by the steep decrease in the packing density (see Fig-

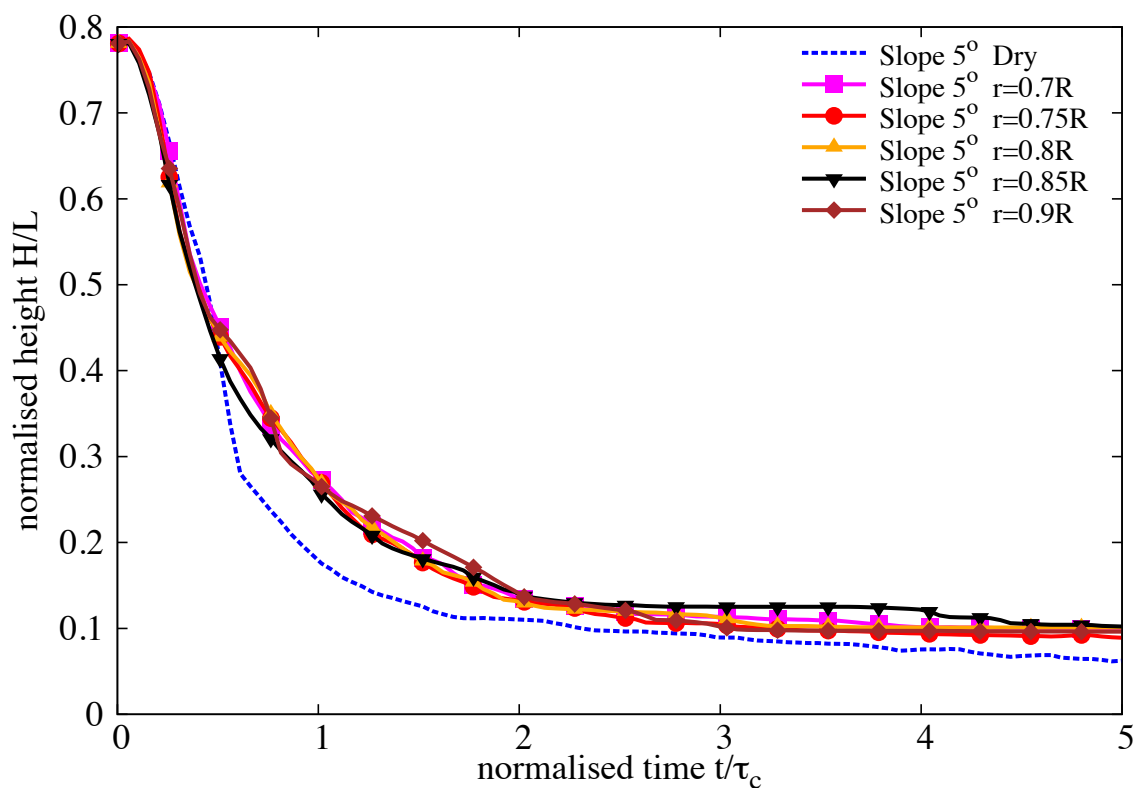


Figure 6.10 Evolution of height with time for different permeability (loose slope 5°)

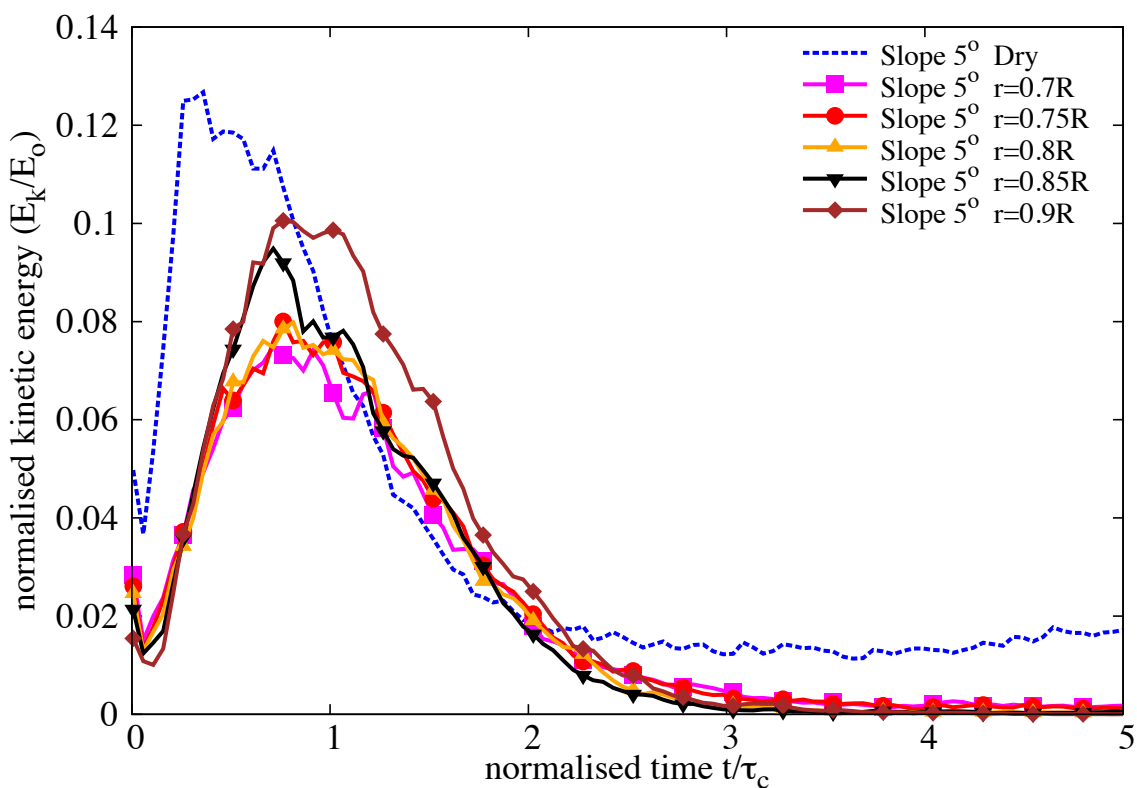


Figure 6.11 Evolution of Kinetic Energy with time for different permeability (loose slope 5°)

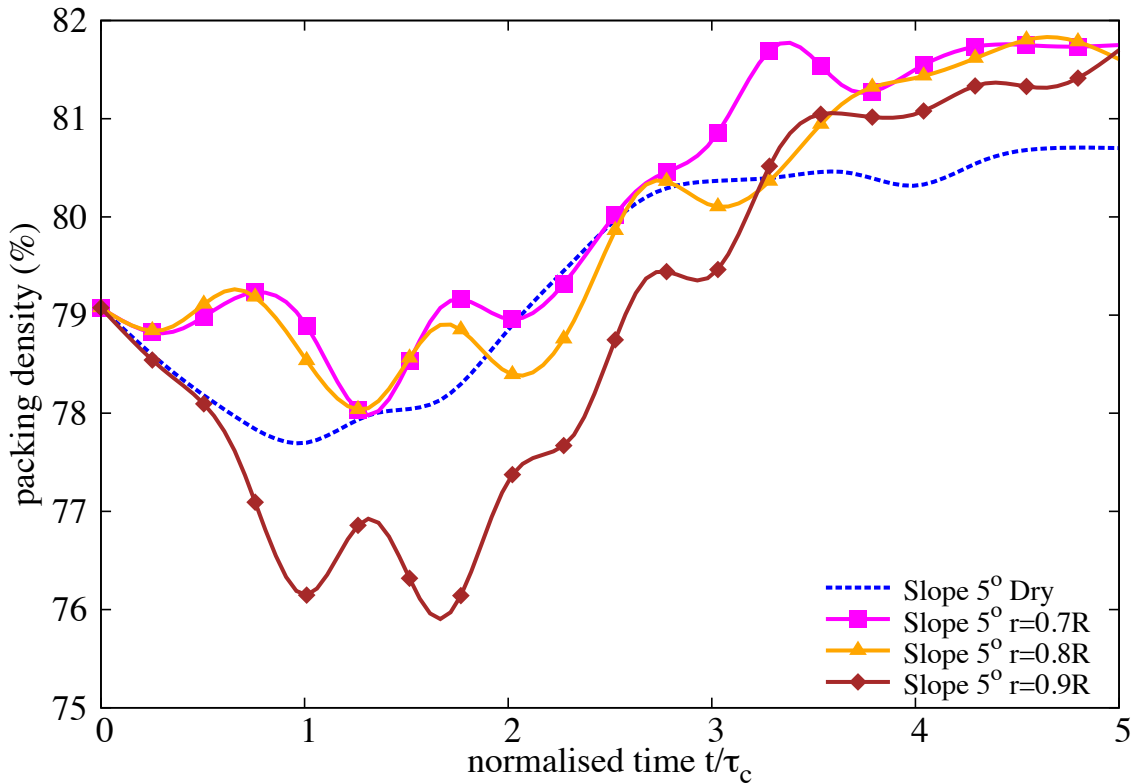


Figure 6.12 Evolution of packing density with time for different permeability (loose slope 5°)

ure 6.12) for the very low permeability condition ($r = 0.9R$). At the end of the flow ($t \geq 3 \times \tau_c$), the excess pore-pressure dissipates and the granular material, irrespective of their permeability, reaches almost the same packing density.

6.1.3 Summary

Two-dimensional LB-DEM simulations were performed to understand the behaviour of submarine granular flows. Unlike dry granular collapse, the run-out behaviour in fluid is dictated by the initial volume fraction. Granular columns with loose packing tend to flow longer in comparison to dense columns, due to entrainment of water at the base resulting in lubrication. The loose column when it starts flowing expands and ejects liquid, leading to a partial fluidization of the material. However, with increase in the slope angle, the run-out in fluid is influenced by the viscous drag on the granular materials. The run-out distance in fluid increases with decrease in permeability. More research work is required to characterise the flow behaviour of granular materials, especially in submerged conditions.

Draft - v1.0

Wednesday 17th September, 2014 – 02:00

Chapter 7

14

Conclusions and future work

15

7.1 Introduction

16

The Multi-scale modelling of granular flows involves simulating the granular materials in discrete and continuum scales. In the present study, a C++ code has been developed to model the granular materials as discrete-elements using the Discrete Element Method technique. The Material Point Method code, developed in the University of Cambridge, has been adopted to study the flow of granular materials as a continuum. Multi-scale analyses of the collapse of the granular columns with different aspect ratios were performed using continuum and particle-scale approaches. In the present study, the solid-fluid interactions in the Discrete Element approach is modelled by coupling the Lattice Boltzmann Method, a Newtonian fluid solver, with the Discrete Element Method technique. This chapter presents an overview of the future research along with the proposed research schedule. This chapter also presents an outline of the final thesis and the proposed papers based on this research work.

17

18

19

20

21

22

23

24

25

26

27

7.2 Outline of future research

28

This research work involves the following stages: (1) understanding the limits of the continuum and the discrete-element approaches in modelling the granular flow, and investigating the influence of various microscopic parameters on the macroscopic flow behaviour, (2) understanding the differences in the mechanism of the granular flows in dry and submerged conditions, and (3) Modelling the granular flow behaviour using the $\mu(I)$ rheology for dry and submerged flow conditions.

29

30

31

32

33

34

7.2.1 Multi-scale simulations of granular flows

35

1 The continuum and discrete-element simulations of the dry and the submerged granular flows
2 will be performed to understand the differences in their flow mechanism. Multi-scale analyses of
3 granular flows enable us to understand the limitations of the continuum approach in modelling
4 large deformation granular flow problems, and help us to identify the micro-scale parameters
5 responsible for the complex macroscopic behaviour. Multi-scale modelling of the collapse
6 of a granular columns on a horizontal surface have been performed. Continuum simulations
7 accurately predict the granular flow behaviour for columns with smaller aspect ratios, however
8 they fail to capture the dynamics of the flow for columns with larger aspect ratios.

9 In order to understand the difference in the flow dynamics with increasing aspect ratios,
10 further analyses will be performed to study the mechanism of energy dissipation in the particle
11 scale, i.e. the evolution of kinetic energy and potential energy with time. A simple mathematical
12 relationship based on the initial potential energy of the grains lying above the failure surface
13 is being developed to describe the flow dynamics of the granular column collapse problem
with different aspect ratios. The relationship will enable us to understand the variation in the
flow dynamics in the continuum and the particle-scale. The continuum description of granular
column collapse showed non-physical behaviour near the foot of the column, further analyses
will be carried out to understand the effect of interface properties on the run-out distance.
Further details on the continuum modelling of granular flow are presented in the next section.
Micro-scale parameters influencing the flow dynamics will be identified and the influence of
these parameters on the deposit morphology will be investigated. Multi-scale analysis of large
deformation flow problem such as flow of dry granular materials down an inclined flume will
be performed. This analysis will provide an insight on the limits of the continuum approach
in modelling large deformation problems, which involve large shear-rates. The results from
the analysis will be compared with the experimental results of Denlinger and Iverson (2001)
on miniature flume experiments. The influence of parameters, such as particle size, density,
packing and dilatancy, on the flow dynamics will be explored. These studies will be useful in
describing the granular flow behaviour using the $\mu(I)$ rheology.

1
2
3
4
5
6
7
8
9
10
11
12
13
14

15 In order to understand the differences in the mechanism between the dry and the submerged
16 granular flows, multi-scale analysis of granular flows in fluid will be performed. In particle-scale
17 approach, the Discrete Element Method technique coupled with Lattice Boltzmann approach
18 will be adopted to study the collapse of granular columns in fluids. Dynamic fluid-coupling
19 in the Material Point Method will be developed to study the behaviour of granular flows in
20 fluids. The numerical simulations will be verified with the experimental results of Cassar
21 et al. (2005) on immersed granular flows. The effect of packing density of granular material,
22 frictional parameters and the viscosity of the fluid on the flow dynamics and the phase-transition

behaviour will also be investigated. The influence of the fluid viscosity on the flow behaviour
 will also be investigated. The variation in the flow dynamic and the deposit morphology for dry
 and submerged granular flows will also be analysed. The parameters that cause a change in the
 flow dynamic between the dry and the submerged flow conditions will be used in extending the
 $\mu(I)$ rheology for submerged granular flows.

23
24
25
26
27

7.2.2 Developments in Material Point Method

28
29
30
31
32
33
34
35

The present MPM code is capable of solving the granular flow problems using the Mohr-
 Coulomb constitutive model. It is also capable of solving seepage problems with static
 fluid-solid interface. In the present study, the Material Point Method will be extended to
 solve 3D problems and it will be implemented into a standard framework, similar to the Finite
 Element framework developed in the University of Cambridge. Constitutive models such as
 Nor-Sand and $\mu(I)$ rheology will be implemented to model the dense granular flows. Modified
 Nor-Sand constitutive model ([Robert, 2010](#)) implemented in the present study will be validated

- 1 by performing element testing and the results will be verified with the results of ?.
- 2 The current MPM code is capable of simulating only small deformation problems, however special attention
- 3 is required in modelling large deformation problems, especially those involving two-phase
- 4 systems. Objective stress rate such as Jaumann stress rate has been implemented to study large
- 5 deformation problems. The dynamic re-meshing technique ([Shin, 2010](#)) will be implemented
- 6 to efficiently solve large deformation problems. The dynamic meshing approach is useful for
- 7 problems involving motion of a finite size body in unbounded domains, in which the extent of
- 8 material run-out and the deformation is unknown a priori. The approach involves searching for
- 9 cells that only contain material points, thereby avoiding unnecessary storage and computation.

1
2
3
4
5
6
7
8
9
10
11
12
13

The present fluid coupling algorithm in the MPM involves only static boundaries, and conserves the equation of momentum for fluid particles by introducing additional particles in a cell, when the number of particles decreases. A dynamic solid-fluid interface modelling in the Material Point Method will be developed. The approach involves the following steps: identification of the soil particles along the boundary of the current soil domain, obtaining the nodal numbers for the edges of each soil particle and definition of a new boundary (see Figure 7.1). The shape of the boundary is approximated by equivalent rectangular grids, similar to the coupling technique adopted in the discrete-element approach. The procedure is repeated until the entire boundary is defined. This process is repeated for each time step to simulate the dynamic boundary behaviour which is common in the case of granular flows in a fluid.

4
5
6
7
8
9
10
11
12
13

The MPM code will be extended to include the phase-transition behaviour in a continuum domain for partially fluidized granular flows ([Aranson and Tsimring, 2001, 2002; Volfson et al., 2003](#)). The theory is based on the hydrodynamics of the flow, coupled with an order parameter

14
15
16

equation, which describes the transition between the flowing and the static components of the granular system. The order parameter is defined as a fraction of static contacts among all contacts between particles. The shear stresses in a partially fluidized granular matter is assumed to have two components: the dynamic part that is proportional to the shear strain rate and the strain-independent or the static part. The ratio of these two parts is a function of the order parameter. The relative magnitude of the static shear stress is controlled by the order parameter which varies from 0 in the liquid phase to 1 in the solid phase.

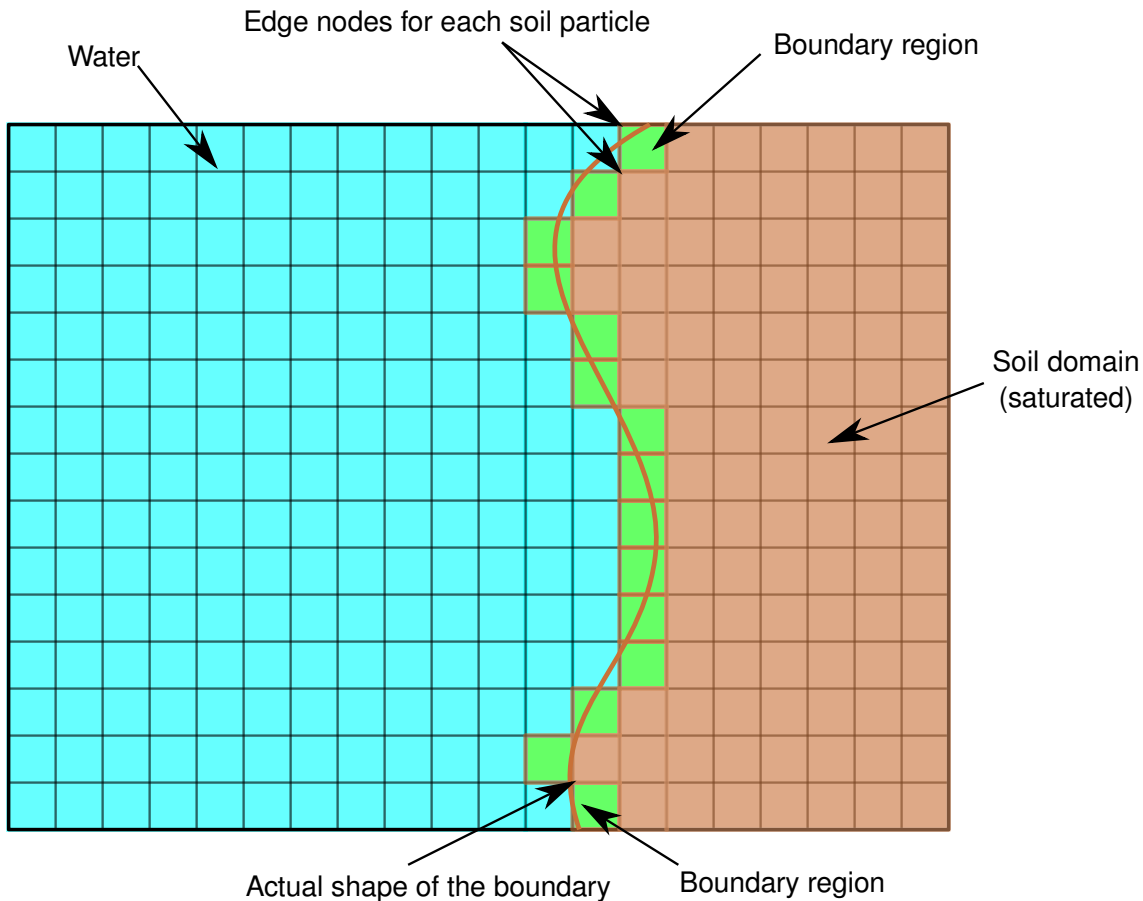


Figure 7.1 Identification of dynamic solid-fluid boundary

7.2.3 The I rheology

The $\mu(I)$ rheology is capable of describing the behaviour of dense granular flows. However, it considers the yield strength as an adjustable rheological property, which contradicts the basic understanding that the strength evolves as the debris-flow motion progresses. Also, the $\mu(I)$ rheology uses the Mohr-Coulomb constitutive model to describe the yielding of granular materials. In the present study, the evolution of soil strength with time will be considered using

models based on critical state framework. Nor-Sand constitutive model will be implemented in
1 the present study to describe the plastic flow of granular materials. The $\mu(I)$ rheology will be
2 extended to describe the behaviour of granular flows in fluids. In the case of dense granular
3 flows, the parameter I is described as the ratio between the time taken for a particle to fall
4 into the hole, t_{micro} , and the meantime, t_{mean} , which is inversely related to the shear rate. If the
5 velocity of the ambient fluid is low, then the time taken by the particle to fall into a hole, is then
6 controlled by the viscosity of the ambient fluid (Pouliquen et al., 2005). The $\mu(I)$ rheology
7 will be modified to include the effect of fluid viscosity to model granular flows in fluids based
8 on the parameters identified to control the flow dynamics.

9 7.2.4 Homogenization of granular flows

10 Granular materials are composed of grains in contact, and are therefore discontinuous and
11 heterogeneous. The macroscopic material properties of these materials are linked to the fabric of
12 the medium. It is interesting to define the behaviour of granular materials at the macroscopic
13 scale from characteristics defined at the local scale. This approach has been widely developed
14 for heterogeneous continuum and is known as the homogenization method. This kind of
15 approach is different from the phenomenological one, in which the constitutive model is
16 derived from the general laws of thermodynamics. These phenomenological models introduce
17 some material parameters whose values are obtained from the simulations performed on
18 representative volume element. The main objective of the homogenization method is to obtain
19 a constitutive relation at the scale of a representative volume element, based on the information
20 on the material behaviour at the micro-scale and the micro-structure. For granular media, the
21 micro-scale is generally the grain scale. The scale of the representative volume element is of
22 several orders of magnitude higher. The homogenization process is based on three relations,
23 a localization operator, a local constitutive law and an averaging operator, see Chapter 6. An
24 intrinsic difficulty in the case of granular materials arises from the fact that the variables at
25 the micro-scale and the macro-scale are of different nature. At the micro-scale the material
26 behaviour is described using vectorial variables such as contact forces, grain displacement and
27 grain rotation, whereas the macroscopic behaviour law uses tensorial variables (stress tensor,
28 strain tensor). The micro-polar plasticity constitutive formulation (Suiker et al., 2001) that is
29 directly related to micro-scale properties, such as contact stiffness, particle density, particle
30 radius and its micro-structure will be extended to large scale deformation problems which
31 involves loss or gain of contacts between grains. Discrete Element Method simulations provide
32 useful insight on the role of contact forces at micro-scale. The macroscopic stress is related
33 to microscopic contact forces using the virtual work theorem. The microscopic kinematic
34 variables usually considered are the displacement of the centre of mass of the particle and the

³⁵ ration of the particle. The local phenomena occurring at the micro-scale during the deformation of granular material are complex. Different approaches have been proposed in the literature to establish the link between particle-level displacements and macro-scale deformations. The micro-behaviour is converted into a macroscopic model through the conservation of internal work. The local constitutive law gives the value of contact forces and the average over the sample provides the value of the stress tensor.

1
2
3
4
5

References

- Abe, K., Soga, K., and Bandara, S. (2013). Material Point Method for Coupled Hydromechanical Problems. *Journal of Geotechnical and Geoenvironmental Engineering*, page 04013033. 7
8
9
- Aidun, C., Lu, Y., and Ding, E. (1998). Direct analysis of particulate suspensions with inertia using the discrete Boltzmann equation. *Journal of Fluid Mechanics*, 373(-1):287–311. 10
11
- Aranson, I. S. and Tsimring, L. S. (2001). Continuum description of avalanches in granular media. *Physical Review E - Statistical, Nonlinear, and Soft Matter Physics*, 64(2 I):203011–203014. 12
13
14
- Aranson, I. S. and Tsimring, L. S. (2002). Continuum theory of partially fluidized granular flows. *Physical Review E*, 65(6):061303. 15
16
- Bagnold, R. (1954). Experiments on a gravity-free dispersion of large solid spheres in a Newtonian fluid under shear. *Proceedings of the Royal Society of London. Series A. Mathematical and Physical Sciences*, 225(1160):49. 17
18
19
- Balmforth, N. J. and Kerswell, R. R. (2005). Granular collapse in two dimensions. *Journal of Fluid Mechanics*, 538:399–428. 20
21
- Bandara, S. (2013). *Material Point Method to simulate Large Deformation Problems in Fluid-saturated Granular Medium*. PhD thesis, University of Cambridge. 22
23
- Bardenhagen, S. and Kober, E. (2004). The generalized interpolation material point method. *Computer Modeling in Engineering and Sciences*, 5(6):477–496. 24
25
- Bardenhagen, S. G., Brackbill, J. U., and Sulsky, D. (2000). The material-point method for granular materials. *Computer Methods in Applied Mechanics and Engineering*, 187(3-4):529–541. 26
27
28
- Bareschino, P., Lirer, L., Marzocchella, A., Petrosino, P., and Salatino, P. (2008). Self-fluidization of subaerial rapid granular flows. *Powder Technology*, 182(3):323–333. 29
30
- Bathe, K. and Zhang, H. (2004). Finite element developments for general fluid flows with structural interactions. *International Journal for Numerical Methods in Engineering*, 60(1):213–232. 31
32
33
- Bigler, J., Guilkey, J., Gribble, C., Hansen, C., and Parker, S. (2006). A case study: Visualizing material point method data. *Proceedings of Euro Vis 2006*, pages 299–306. 34
35

Breuer, M., Bernsdorf, J., Zeiser, T., and Durst, F. (2000). Accurate computations of the laminar flow past a square cylinder based on two different methods: lattice-Boltzmann and finite-volume. *Journal of Heat and Fluid Flow*, 21(2):186–196.

36
37
38

¹ Cambou, B., Jean, M., and Radjaï, F. (2009). *Micromechanics of granular materials*. Wiley-
² ISTE.

³ Campbell, C. (1986). The effect of microstructure development on the collisional stress tensor
⁴ in a granular flow. *Acta Mechanica*, 63(1):61–72.

⁵ Campbell, C. and Brennan, C. (1985). Computer simulation of granular shear flows. *Journal
6 of Fluid Mechanics*, 151:167–88.

⁷ Campbell, C. S. (1990). Rapid Granular Flows. *Annual Review of Fluid Mechanics*, 22(1):57–
⁸ 90.

⁹ Campbell, C. S. (2002). Granular shear flows at the elastic limit. *Journal of Fluid Mechanics*,
¹⁰ 465:261–291.

¹¹ Campbell, C. S. (2006). Granular material flows - An overview. *Powder Technology*,
¹² 162(3):208–229.

¹³ Capecelatro, J. and Desjardins, O. (2013). An Euler–Lagrange strategy for simulating particle-
¹⁴ laden flows. *Journal of Computational Physics*, 238(0):1–31.

¹⁵ Cassar, C., Nicolas, M., and Pouliquen, O. (2005). Submarine granular flows down inclined
¹⁶ planes. *Physics of Fluids*, 17(10):103301–11.

¹⁷ Chen, S. and Doolen, G. G. D. (1998). Lattice Boltzmann method for fluid flows. *Annual
18 review of fluid mechanics*, 30(1):329–364.

¹⁹ Chen, Z. and Brannon, R. (2002). An evaluation of the material point method. *Sandia National
20 Laboratories (SAND2002-0482)*.

²¹ Choi, J. (2005). *Transport-limited aggregation and dense granular flow*. PhD thesis.

²² Cook, B., Noble, D., and Williams, J. (2004). A direct simulation method for particle-fluid
²³ systems. *Engineering Computations*, 21(2/3/4):151–168.

²⁴ Coulomb, C. A. (1776). *Essai sur une application des règles de maximis & minimis {à}
25 quelques problèmes de statique, relatifs à l'architecture*. De l’Imprimerie Royale.

²⁶ Crosta, G. B., Imposimato, S., and Roddeman, D. (2009). Numerical modeling of 2-D granular
²⁷ step collapse on erodible and nonerodible surface. *J. Geophys. Res.*, 114(F3):F03020.

²⁸ Da Cruz, F., Emam, S., Prochnow, M., Roux, J. N., and Chevoir, F. (2005). Rheophysics of
²⁹ dense granular materials: Discrete simulation of plane shear flows. *Physical Review E -
30 Statistical, Nonlinear, and Soft Matter Physics*, 72(2):1–17.

³¹ Daerr, A. and Douady, S. (1999). Two types of avalanche behaviour in granular media. *Nature*,
³² 399(6733):241–243.

- ³³ Daniel, R. C., Poloski, A. P., and Eduardo Saez, A. (2007). A continuum constitutive model for cohesionless granular flows. *Chemical Engineering Science*, 62(5):1343–1350.
- ³⁴ Denlinger, R. and Iverson, R. (2001). Flow of variably fluidized granular masses across three-dimensional terrain, ii: Numerical predictions and experimental tests. *J. Geophys. Res.*, 106(B1):553–566.
- Du, R., Shi, B., and Chen, X. (2006). Multi-relaxation-time lattice Boltzmann model for incompressible flow. *Physics Letters A*, 359(6):564–572.
- Durst, F., Ray, S., Unsal, B., and Bayoumi, O. (2005). The development lengths of laminar pipe and channel flows. *Journal of fluids engineering*, 127:1154.
- Estrada, N., Taboada, A., and Radjai, F. (2008). Shear strength and force transmission in granular media with rolling resistance. *Physical Review E*, 78(2):021301.
- Feng, Y. T., Han, K., and Owen, D. R. J. (2007). Coupled lattice Boltzmann method and discrete element modelling of particle transport in turbulent fluid flows: Computational issues. *International Journal for Numerical Methods in Engineering*, 72(9):1111–1134.
- Forterre, Y. and Pouliquen, O. (2008). Flows of Dense Granular Media. *Annual Review of Fluid Mechanics*, 40(1):1–24.
- Fortes, A. (1987). Nonlinear mechanics of fluidization of beds of spherical particles. *Journal of Fluid Mechanics*.
- Frisch, U. and Kolmogorov, A. (1995). *Turbulence: the legacy of AN Kolmogorov*. Cambridge University Press.
- Girolami, L., Hergault, V., Vinay, G., and Wachs, A. (2012). A three-dimensional discrete-grain model for the simulation of dam-break rectangular collapses: comparison between numerical results and experiments. *Granular Matter*, pages 1–12.
- Goldhirsch, I. (2003). Rapid granular flows. *Annual Review of Fluid Mechanics*, 35:267–293.
- Grubmüller, H., Heller, H., Windemuth, A., and Schulten, K. (1991). Generalized verlet algorithm for efficient molecular dynamics simulations with long-range interactions. *Molecular simulations*, 6:121–142.
- Guilkey, J., Harman, T., Xia, A., Kashiwa, B., and McMurtry, P. (2003). An Eulerian-Lagrangian approach for large deformation fluid structure interaction problems, Part 1: algorithm development. *Advances in Fluid Mechanics*, 36:143–156.
- Gumhold, S. (2003). Splatting illuminated ellipsoids with depth correction. volume 2003, pages 245–252.
- Han, K., Feng, Y., and Owen, D. (2007a). Coupled lattice Boltzmann and discrete element modelling of fluid–particle interaction problems. *Computers & Structures*, 85(11-14):1080–1088.
- Han, S., Zhu, P., and Lin, Z. (2007b). Two-dimensional interpolation-supplemented and Taylor-series expansion-based lattice Boltzmann method and its application. . . . in *Nonlinear Science and Numerical Simulation*, 12(7):1162–1171.

- ¹ Harlow, F. H. (1964). The particle-in-cell computing method for fluid dynamics. *Computer Methods in Physics*, 3:319–343.
- ³ He, X. and Luo, L. L.-S. (1997a). Theory of the lattice Boltzmann method: From the Boltzmann equation to the lattice Boltzmann equation. *Physical Review E*, 56(6):6811.
- ⁵ He, X. and Luo, L.-S. (1997b). A priori derivation of the lattice Boltzmann equation. *Physical Review E*, 55(6):R6333–R6336.
- ⁷ He, X., Zou, Q., Luo, L. S., and Dembo, M. (1997). Analytic solutions of simple flows and analysis of nonslip boundary conditions for the lattice Boltzmann BGK model. *Journal of Statistical Physics*, 87(1):115–136.
- ¹⁰ Hertz, H. (1882). Über die Berührungen fester elastischer Körper. *Journal für die Reinen und Angewandte Mathematik*, 92:156–171.
- ¹² Hogg, A. J. (2007). Two-dimensional granular slumps down slopes. *Physics of Fluids*, 19(9):9.
- ¹³ Hutter, K., Koch, T., Pluuss, C., and Savage, S. (1995). The dynamics of avalanches of granular materials from initiation to runout. Part II. Experiments. *Acta Mechanica*, 109(1):127–165.
- ¹⁵ Hutter, K., Wang, Y., and Pudasaini, S. P. (2005). The Savage–Hutter Avalanche Model: How Far Can It be Pushed? *Philosophical Transactions: Mathematical, Physical and Engineering Sciences*, 363(1832):1507–1528.
- ¹⁸ Iddir, H. and Arastoopour, H. (2005). Modeling of multitype particle flow using the kinetic theory approach. *AICHE Journal*, 51(6):1620–1632.
- ²⁰ Igelberger, K., Thurey, N., and Rude, U. (2008). Simulation of moving particles in 3D with the Lattice Boltzmann method. *Computers & Mathematics with Applications*, 55(7):1461–1468.
- ²² Iverson, R. (2003). The debris-flow rheology myth. pages 303–314.
- ²³ Iverson, R. M. (1997). The physics of debris flows. *Rev. Geophys.*, 35(3):245–296.
- ²⁴ Jaeger, H., Nagel, S., and Behringer, R. (1996). Granular solids, liquids, and gases. *Reviews of Modern Physics*, 68(4):1259–1273.
- ²⁶ Jean, M. (1999). The non-smooth contact dynamics method. *Computer Methods in Applied Mechanics and Engineering*, 177(3-4):235–257.
- ²⁸ Jenkins, J. T. and Savage, S. B. (1983). A theory for the rapid flow of identical, smooth, nearly elastic, spherical particles. *Journal of Fluid Mechanics*, 130:187–202.
- ³⁰ Johnson, A. (1965). *A model for debris flow*. PhD thesis.
- ³¹ Jop, P., Forterre, Y., and Pouliquen, O. (2006). A constitutive law for dense granular flows. *Nature*, 441(7094):727–730.
- ³³ Josserand, C., Lagree, P. Y., and Lhuillier, D. (2004). Stationary shear flows of dense granular materials: A tentative continuum modelling. *European Physical Journal E*, 14(2):127–135.

- ³⁵ Jullien, R., Meakin, P., and Pavlovitch, A. (1992). Random packings of spheres built with sequential models. *Journal of Applied Physics*, 25:4103. 1
- Kamrin, K. (2008). *Stochastic and deterministic models for dense granular flow*. PhD thesis. 2
- Kamrin, K. (2010). Nonlinear elasto-plastic model for dense granular flow. *International Journal of Plasticity*, 26(2):167–188. 3
- 4
- Kamrin, K., Rycroft, C. H., and Bazant, M. Z. (2007). The stochastic flow rule: a multi-scale model for granular plasticity. *Modelling and Simulation in Materials Science and Engineering*, 15(4):S449–S464. 5
- 6
- 7
- Kerswell, R. (2005). Dam break with Coulomb friction: A model for granular slumping? *Physics of Fluids*, 17:057101. 8
- 9
- Komiwes, V., Mege, P., Meimon, Y., and Herrmann, H. (2005). Simulation of granular flow in a fluid applied to sedimentation. *Granular Matter*, 8(1):41–54. 10
- 11
- Krogh, M., Painter, J., and Hansen, C. (1997). Parallel sphere rendering. *Parallel Computing*, 23(7):961–974. 12
- 13
- Kuester, F., Bruckschen, R., Hamann, B., and Joy, K. (2001). Visualization of particle traces in virtual environments. pages 151–157. 14
- 15
- Kumar, K., Soga, K., and Delenne, J.-Y. (2012). *Discrete Element Modelling of Particulate Media*. Special Publication. Royal Society of Chemistry, Cambridge. 16
- 17
- Lacaze, L. and Kerswell, R. R. (2009). Axisymmetric Granular Collapse: A Transient 3D Flow Test of Viscoplasticity. *Physical Review Letters*, 102(10):108305. 18
- 19
- Lacaze, L., Phillips, J. C., and Kerswell, R. R. (2008). Planar collapse of a granular column: Experiments and discrete element simulations. *Physics of Fluids*, 20(6). 20
- 21
- Ladd, A. J. (1994). Numerical simulations of particulate suspensions via a discretized Boltzmann equation. Part 1. Theoretical foundation. *Journal of Fluid Mechanics*, 271:285–309. 22
- 23
- Ladd, A. J. C. and Verberg, R. (2001). Lattice-Boltzmann Simulations of Particle-Fluid Suspensions. *Journal of Statistical Physics*, 104(5):1191–1251. 24
- 25
- Lajeunesse, E., Mangeney-Castelnau, A., and Vilotte, J. P. (2004). Spreading of a granular mass on a horizontal plane. *Physics of Fluids*, 16(7):2371. 26
- 27
- Lajeunesse, E., Monnier, J. B., and Homsy, G. M. (2005). Granular slumping on a horizontal surface. *Physics of Fluids*, 17(10). 28
- 29
- Larrieu, E., Staron, L., and Hinch, E. J. (2006). Raining into shallow water as a description of the collapse of a column of grains. *Journal of Fluid Mechanics*, 554:259–270. 30
- 31
- Lemiale, V., Muhlhaus, H. B., Meriaux, C., Moresi, L., and Hodkinson, L. (2011). Rate effects in dense granular materials: Linear stability analysis and the fall of granular columns. *International Journal for Numerical and Analytical Methods in Geomechanics*, 35(2):293–308. 32
- 33
- 34
- 35

- Levoy, M. (1988). Display of surfaces from volume data. *Computer Graphics and Applications*, 1 IEEE, 8(3):29–37.
- Li, S. and Liu, W. (2002). Meshfree and particle methods and their applications. *Applied Mechanics Reviews*, 55:1.
- Liu, S. H., Sun, D. A., and Wang, Y. (2003). Numerical study of soil collapse behavior by discrete element modelling. *Computers and Geotechnics*, 30(Compindex):399–408.
- Lo, C. Y., Bolton, M., and Cheng, Y. P. (2009). Discrete element simulation of granular column collapse. In *AIP Conf. Proc. Powders and Grains 2009*, volume 1145 of *6th International Conference on Micromechanics of Granular Media, Powders and Grains 2009*, pages 627–630.
- Lorensen, W. and Cline, H. (1987). Marching cubes: A high resolution 3D surface construction algorithm. *ACM Siggraph Computer Graphics*, 21(4):163–169.
- Lube, G., Huppert, H. E., Sparks, R. S. J., and Freundt, A. (2005). Collapses of two-dimensional granular columns. *Physical Review E - Statistical, Nonlinear, and Soft Matter Physics*, 72(4):1–10.
- Luding, S., Clément, E., and Blumen, A. (1994). Anomalous energy dissipation in molecular-dynamics simulations of grains: The "detachment" effect. *Physical Review* ..., 50:4113.
- Mangeney, A., Roche, O., and Hungr, O. (2010). Erosion and mobility in granular collapse over sloping beds. *Journal of Geophysical* ..., 115(F3):F03040.
- Meakin, P. and Jullien, R. (1985). Structural readjustment effects in cluster-cluster aggregation. *Journal de Physique*, 46(9):1543–1552.
- Mehta, A. (2011). *Granular Physics*. Cambridge University Press.
- Mehta, A. and Barker, G. (1994). The dynamics of sand. *Reports on Progress in Physics*, 57:383.
- Mei, R., Shyy, W., Yu, D., and Luo, L.-S. (2000). Lattice Boltzmann Method for 3-D Flows with Curved Boundary. *Journal of Computational Physics*, 161(2):680–699.
- Meruane, C., Tamburrino, A., and Roche, O. (2010). On the role of the ambient fluid on gravitational granular flow dynamics. *Journal of Fluid Mechanics*, 648:381–404.
- Midi, G. D. R. (2004). On dense granular flows. *European Physical Journal E*, 14(4):341–365.
- Mitchell, J. K. and Soga, K. (2005). *Fundamentals of soil behavior*. John Wiley & Sons.
- Ng, B. H., Ding, Y., and Ghadiri, M. (2008). Assessment of the kinetic-frictional model for dense granular flow. *Particuology*, 6(1):50–58.
- Noble, D. and Torczynski, J. (1998). A lattice-Boltzmann method for partially saturated computational cells. *International Journal of Modern Physics C-Physics and Computer*, 9(8):1189–1202.

- Obrecht, C. and Kuznik, F. (2011). A new approach to the lattice Boltzmann method for graphics processing units. *Computers & Mathematics* 1
2
- Okada, Y. and Ochiai, H. (2008). Flow characteristics of 2-phase granular mass flows from model flume tests. *Engineering Geology*, 97(1-2):1–14. 3
4
- OpenACC-Members (2013). The OpenACC Application Programming Interface Version 2.0 (June, 2013; Corrected: August, 2013). Technical report, OpenMP Standard Group. 5
6
- Pailha, M., Pouliquen, O., and Nicolas, M. (2008). Initiation of Submarine Granular Avalanches: Role of the Initial Volume Fraction. *AIP Conference Proceedings*, 1027(1):935–937. 7
8
- Pan, C., Luo, L., and Miller, C. (2006). An evaluation of lattice Boltzmann schemes for porous medium flow simulation. *Computers & fluids*, 35(8-9):898–909. 9
10
- Peker, S. and Helvacı, (2007). *Solid-liquid two phase flow*. Elsevier. 11
- Pitman, E. B. and Le, L. (2005). A Two-Fluid Model for Avalanche and Debris Flows. *Philosophical Transactions: Mathematical, Physical and Engineering Sciences*, 363(1832):1573–1601. 12
13
14
- Popken, L. and Cleary, P. W. (1999). Comparison of Kinetic Theory and Discrete Element Schemes for Modelling Granular Couette Flows. *Journal of Computational Physics*, 155(1):1–25. 15
16
17
- Potapov, A. and Campbell, C. (1996). Computer simulation of hopper flow. *Physics of Fluids*, 8:2884. 18
19
- Pouliquen, O. (1999). Scaling laws in granular flows down rough inclined planes. *Physics of Fluids*, 11(3):542–548. 20
21
- Pouliquen, O., Cassar, C., Forterre, Y., Jop, P., and Nicolas, M. (2005). How do grains flow: Towards a simple rheology of dense granular flows. 22
23
- Pouliquen, O., Cassar, C., Jop, P., Forterre, Y., and Nicolas, M. (2006). Flow of dense granular material: towards simple constitutive laws. *Journal of Statistical Mechanics: Theory and Experiment*, 2006(07):P07020–P07020. 24
25
26
- Pouliquen, O. and Chevoir, F. (2002). Dense flows of dry granular material. *Comptes Rendus Physique*, 3(2):163–175. 27
28
- Pouliquen, O. and Forterre, Y. (2002). Friction law for dense granular flows: Application to the motion of a mass down a rough inclined plane. *Journal of Fluid Mechanics*, 453:133–151. 29
30
- Radjai, F. and Dubois, F. (2011). *Discrete-element modeling of granular materials*. ISTE Wiley, London; Hoboken, N.J. 31
32
- Radjai, F. and Richéfeu, V. (2009). Contact dynamics as a nonsmooth discrete element method. *Mechanics of Materials*, 41(6):715–728. 33
34
- Radjai, F., Voivret, C., and McNamara, S. (2011). Discrete-element modelling of granular materials. chapter Periodic b, pages 181–198. ISTE Wiley. 35
36

- ¹ Robert, D. (2010). *Soil-pipeline interaction in unsaturated soil*. PhD thesis.
- ² Rondon, L., Pouliquen, O., and Aussillous, P. (2011). Granular collapse in a fluid: Role of the
³ initial volume fraction. *Physics of Fluids*, 23(7):073301–073301–7.
- ⁴ Roux, J. and Combe, G. (2002). Quasistatic rheology and the origins of strain. *Comptes Rendus
Physique*, 3(2):131–140.
- ⁶ Rycroft, C. H., Bazant, M. Z., Grest, G. S., and Landry, J. W. (2006). Dynamics of random
⁷ packings in granular flow. *Physical Review E*, 73(5):051306.
- ⁸ Rycroft, C. H., Orpe, A. V., and Kudrolli, A. (2009). Physical test of a particle simulation
⁹ model in a sheared granular system. *Physical Review E*, 80(3):031305.
- ¹⁰ Savage, S. and Hutter, K. (1991). The dynamics of avalanches of granular materials from
¹¹ initiation to runout. Part I: Analysis. *Acta Mechanica*, 86(1):201–223.
- ¹² Savage, S. and Jeffrey, D. (1981). The stress tensor in a granular flow at high shear rates.
¹³ *Journal of Fluid Mechanics*, 110(1):255–272.
- ¹⁴ Savage, S. and Sayed, M. (1984). Stresses developed by dry cohesionless granular materials
¹⁵ sheared in an annular shear cell. *Journal of Fluid Mechanics*, 142:391–430.
- ¹⁶ Savage, S. B. (1984). The Mechanics of Rapid Granular Flows. *Advances in Applied Mechanics*,
¹⁷ 24(C):289–366.
- ¹⁸ Schaefer, D. G. (1990). Instability and ill-posedness in the deformation of granular materials.
¹⁹ *International Journal for Numerical and Analytical Methods in Geomechanics*, 14(4):253–
²⁰ 278.
- ²¹ Schofield, A. and Wroth, P. (1968). *Critical state soil mechanics*. European civil engineering
²² series. McGraw-Hill.
- ²³ Shin, W. (2010). *Numerical simulation of landslides and debris flows using an enhanced
material point method*. PhD thesis.
- ²⁵ Smagorinsky, J. (1963). General circulation experiments with the primitive equations. *Monthly
weather review*, 91(3):99–164.
- ²⁷ Staron, L. and Hinch, E. J. (2005). Study of the collapse of granular columns using two-
²⁸ dimensional discrete-grain simulation. *Journal of Fluid Mechanics*, 545:1–27.
- ²⁹ Staron, L. and Hinch, E. J. (2006). The spreading of a granular mass: role of grain properties
and initial conditions. *Granular Matter*, 9(3-4):205–217. 3357
- Staron, L. and Hinch, E. J. (2007). The spreading of a granular mass: Role of grain properties 3358
and initial conditions. *Granular Matter*, 9(3-4):205–217. 3359
- Staron, L. and Lajeunesse, E. (2009). Understanding how volume affects the mobility of dry
debris flows. *Geophys. Res. Lett.*, 36(12):L12402. 3360
- 3361

- Staron, L., Radjai, F., and Villette, J. P. (2005). Multi-scale analysis of the stress state in a granular slope in transition to failure. *The European physical journal. E, Soft matter*, 18(3):311–20. 3362
3363
3364
- Steffen, M., Wallstedt, P., Guilkey, J., Kirby, R., and Berzins, M. (2008). Examination and analysis of implementation choices within the material point method. *Computer Modeling in Engineering and Sciences*, 32:107–127. 3365
3366
3367
- Succi, S. (2001). *The lattice Boltzmann equation for fluid dynamics and beyond*. Oxford University Press. 3368
3369
- Succi, S., Foti, E., and Higuera, F. (1989). Three-Dimensional Flows in Complex Geometries with the Lattice Boltzmann Method. *Europhysics Letters (EPL)*, 10(5):433–438. 3370
3371
- Suiker, A., De Borst, R., and Chang, C. (2001). Micro-mechanical modelling of granular material. Part 1: Derivation of a second-gradient micro-polar constitutive theory. *Acta mechanica*, 149(1):161–180. 3372
3373
3374
- Sukop, M. and Thorne, D. (2006). *Lattice Boltzmann modeling: An introduction for geoscientists and engineers*. Springer Verlag. 3375
3376
- Sulsky, D., Chen, Z., and Schreyer, H. (1994). A particle method for history-dependent materials. *Computer Methods in Applied Mechanics and Engineering*, 118(1-2):179–196. 3377
3378
- Sulsky, D., Zhou, S.-J., and Schreyer, H. L. (1995). Application of a particle-in-cell method to solid mechanics, volume 87. 3379
3380
- Sun, X., Sakai, M., and Yamada, Y. (2013). Three-dimensional simulation of a solid–liquid flow by the DEM–SPH method. *Journal of Computational Physics*, 248(0):147–176. 3381
3382
- Topin, V., Dubois, F., Monerie, Y., Perales, F., and Wachs, A. (2011). Micro-rheology of dense particulate flows: Application to immersed avalanches. *Journal of Non-Newtonian Fluid Mechanics*, 166(1-2):63–72. 3383
3384
3385
- Topin, V., Monerie, Y., Perales, F., and Radjaï, F. (2012). Collapse Dynamics and Runout of Dense Granular Materials in a Fluid. *Physical Review Letters*, 109(18):188001. 3386
3387
- Utili, S., Zhao, T., and Houlsby, G. (2014). 3D DEM investigation of granular column collapse: Evaluation of debris motion and its destructive power. *Engineering Geology*. 3388
3389
- Verlet, L. (1967). Computer "Experiments" on Classical Fluids. I. Thermodynamical Properties of Lennard-Jones Molecules. *Phys. Rev.*, 159(1):98. 3390
3391
- Vold, M. J. (1959). A numerical approach to the problem of sediment volume. *Journal of Colloid Science*, 14(2):168–174. 3392
3393
- Volfson, D., Tsimring, L. S., and Aranson, I. S. (2003). Partially fluidized shear granular flows: Continuum theory and molecular dynamics simulations. *Physical Review E*, 68(2):021301. 3394
3395
- Wang, L., Guo, Z., and Mi, J. (2014). Drafting, kissing and tumbling process of two particles with different sizes. *Computers & Fluids*. 3396
3397

-
- Warnett, J. M., Denissenko, P., Thomas, P. J., Kiraci, E., and Williams, M. A. (2013). Scalings of axisymmetric granular column collapse. *Granular Matter*, 16(1):115–124. 3398
3399
- Willis, A., Peixinho, J., Kerswell, R., and Mullin, T. (2008). Experimental and theoretical progress in pipe flow transition. *Philosophical Transactions of the Royal Society A: Mathematical, Physical and Engineering Sciences*, 366(1876):2671. 3400
3401
3402
- Wolfe, M. (2012). PGInsider August 2012: OpenACC Kernels and Parallel Constructs. 3403
- Xiong, Q., Madadi-Kandjani, E., and Lorenzini, G. (2014). A LBM–DEM solver for fast discrete particle simulation of particle–fluid flows. *Continuum Mechanics and Thermodynamics*. 3404
3405
3406
- Xu, H., Louge, M., and Reeves, A. (2003). Solutions of the kinetic theory for bounded collisional granular flows. *Continuum Mechanics and Thermodynamics*, 15(4):321–349. 3407
3408
- Yu, D., Mei, R., Luo, L., and Shyy, W. (2003). Viscous flow computations with the method of Lattice Boltzmann equation. *Progress in Aerospace Sciences*, 39(5):329–367. 3409
3410
- Yu, H., Girimaji, S., and Luo, L. (2005). Lattice Boltzmann simulations of decaying homogeneous isotropic turbulence. *Physical Review E*, 71(1):016708. 3411
3412
- Zenit, R. (2005). Computer simulations of the collapse of a granular column. *Physics of Fluids*, 17(Compendex):031703–1–031703–4. 3413
3414
- Zhang, Y. and Campbell, C. S. (1992). The interface between fluid-like and solid-like behaviour in two-dimensional granular flows. *Journal of Fluid Mechanics*, 237:541–568. 3415
3416
- Zhong, Q. and Olson, M. (1991). Finite element–algebraic closure analysis of turbulent separated-reattaching flow around a rectangular body. *Computer methods in applied mechanics and engineering*, 85(2):131–150. 3417
3418
3419
- Zhou, H., Mo, G., Wu, F., Zhao, J., Rui, M., and Cen, K. (2012). GPU implementation of lattice Boltzmann method for flows with curved boundaries. *Computer Methods in Applied Mechanics and Engineering*, 225-228(null):65–73. 3420
3421
3422
- Ziegler, D. (1993). Boundary conditions for Lattice Boltzmann simulations. *Journal of Statistical Physics*, 71(5):1171–1177. 3423
3424
- Zou, Q. and He, X. (1997). On pressure and velocity boundary conditions for the Lattice Boltzmann BGK model. *Physics of Fluids*, 9(6):1591–1598. 3425
3426